MODELING AND SIMULATION OF THREE-PHASE BIDIRECTIONAL ELECTRIC VEHICLE CHARGER

A Thesis

by

Gorkem Berk Sahinler

Submitted to the
Graduate School of Sciences and Engineering
In Partial Fulfillment of the Requirements for
the Degree of

Master of Science

in the
Department of Electrical and Electronics Engineering

Özyeğin University
June 2021

MODELING AND SIMULATION OF THREE-PHASE BIDIRECTIONAL ELECTRIC VEHICLE CHARGER

Approved by:

Asst. Prof. Gokturk Poyrazoglu, Advisor
Department of Electrical and Electronics Engineering
Ozyegin University

Asst. Prof. Evsen Yanmaz Adam
Department of Electrical and Electronics Engineering
Ozyegin University

Asst. Prof. Ahmet Tekin
Department of Electrical Engineering
Istanbul Technical University (ITU)

Date Approved: 8 June 2021

To all those I love

ABSTRACT

The aim of this research is to investigate how an electric vehicle (EV) charger with controllers performs and affects the EV battery, integrated to the grid. At present, typical applications of EV chargers usually include only charging of the vehicle battery providing unidirectional power flow between the power grid and EV. The proposed three-phase grid connected EV charger system enables bidirectional power flow, sending unused energy in EV battery back to the electricity grid in the scope of V2G operation in addition to conventional charging of the battery. The EV charger circuit consists of two stages, one of which is three-phase AC/DC PWM converter and the other is synchronous DC/DC converter, between which a DC link capacitor having 800V rated bus voltage is inserted. Also, a Li-ion battery pack with the nominal voltage of 500V is used for the system. LCL filter is utilized for AC/DC part of the charger to attenuate line current ripples and the other components are selected based on the theoretical analysis performed as well. Two-loop control algorithms, of which design parameters are calculated using some detailed mathematical analysis, are implemented for both AC/DC converter and DC/DC one to achieve tight voltage & current regulations for the EV charger. Then the performance of the bidirectional EV charger circuit is evaluated via some simulation work in Matlab/Simulink based on closed-loop operation and harmonic contents for grid side. Simulation results are discussed to analyze the closed-loop performance of the EV charger system during various conditions and the developed theory regarding control system design is verified. Harmonics & THD values of line currents are also investigated for various battery voltage levels using the obtained results. In addition, loss analysis is performed to show that the bidirectional EV charger system can operate with high efficiency values.

ÖZETÇE

Bu çalışmanın amacı, şebekeye bağlı bir elektrikli araç şarj devresinin kontrolcü ile birlikte nasıl bir performans gösterdiğini ve araç bataryasını nasıl etkilediğini incelemektir. Günümüzde elektrikli araç şarj istasyonlarının tipik uygulamaları genellikle şebeke ve araç arasında tek yönlü güç transferi sağlayarak sadece araç bataryasını şarj etmeyi içermektedir. Önerilen şebekeye bağlı üç faz elektrikli araç sarj sistemi aracın şarj edilmesinin yanında araç bataryasında kullanılmayan enerjiyi elektrik şebekesine göndermekte ve "araçtan şebekeye" konsepti ile iki yönlü güç transferini mümkün kılmaktadır. Elektrikli araç şarj devresi AC/DC PWM dönüştürücü ve DC/DC senkron çevirici olmak üzere iki kısımdan oluşmaktadır. Bu iki dönüştürücü arasında 800V nominal gerilim değerinde DC link kondansatör bulunmaktadır. Ayrıca sistem için çıkışta 500V değerinde Li-ion batarya kullanılmaktadır. Akım dalgalanmalarını sönümlemek için ise şarj devresinin AC/DC tarafında LCL filtreden yararlanılmıştır. Şarj sisteminin sıkı gerilim ve akım regülasyonunu sağlamak amacıyla çift döngü kontrol algoritması hem AC/DC çevirici hem de DC/DC dönüştürücü için uygulanmaktadır. İlgili kontrol algoritmalarının parametreleri detaylı matematiksel analizlere dayanarak hesaplanmıştır. Daha sonra çift yönlü elektrikli araç şarj sisteminin performansı kapalı çevrim çalışma ve şebeke tarafındaki harmonik içerikleri bakımından bazı simülasyon çalışmaları kapsamında Matlab/Simulink üzerinde incelendi. Simülasyon sonuçları elektrikli araç şarj sisteminin çeşitli koşullar altındaki kapalı çevrim performansını değerlendirmek için ele alındı ve kontrol sistemlerinin tasarımına ilişkin geliştirilen teori doğrulandı. Ayrıca şebeke akımlarının harmonikleri ve THD değerleri elde edilen sonuçlara göre çeşitli batarya gerilim değerleri için incelendi. Ek olarak şarj sisteminin yüksek verimlilikle çalıştığını göstermek için kayıp analizi yapıldı.

ACKNOWLEDGEMENTS

I feel I have been really fortunate in my pursuit of academic career. Firstly, I would like to thank my advisor Prof. Gokturk Poyrazoglu for his endless support, guidance and friendliness. My thesis work could not have been completed without his huge dedication.

I would like to express my sincere gratitude to the professors, giving courses I took during my master's degree program, for providing valuable knowledge as well.

Particularly, I would like to thank my parents and family, who have given me their love and continuous support throughout my thesis work.

Also, I thank the Department of Electrical & Electronics Engineering at Ozyegin University and Vestel Electronics for giving me the opportunity to study my master's degree and write this thesis.

TABLE OF CONTENTS

LIST OF TABLES

LIST OF FIGURES

CHAPTER I

INTRODUCTION

1.1 Overview

In the world, climate change or global warming issues, which have been evident especially since 1980s when it was reported that Ozone layer had been depleted by some pollutants, are mainly due to greenhouse gases such as CO_2 , SO_2 , CO generated by fossil fuel burning. Almost 80% of CO_2 in the atmosphere has been guessed to be produced by burning fossil fuels, of which nearly 50% are caused by electric power generation, that has required a sustainable development all over the world promptly [1-3]. These environmental issues and concerns regarding reduction of carbon emissions have caused a significant improvement in renewable power generation technologies and alternative energy systems in recent years, as well. It is expected that more impacts of power electronics technologies on renewable energy systems, energy conversion, electric vehicles (EVs) and hybrid electric vehicles (HEVs) in addition to industrialization and general energy systems would be observed this century [1, 4, 5]. Specific to transportation, the number of personal automobiles has rapidly increased as a result of more urbanization, industrialization and globalization. Moreover, modern society has significantly depended on transportation which is based on fossil fuels for economic and social development [6]. It is clear that transportation sector has had a significant contribution to global warming, according to trend in CO_2 emissions. As a result, popularity of electric vehicles (EVs) has been increased because of environmental concerns emerged from global warming and lack of fossil fuels, considering that transportation sector in many countries is rapidly being developed [7-10].

Electrification of transportation for mitigation of carburization is also encouraged by public policies. Transition from conventional vehicles with internal combustion engine to EVs is not expected to take long since governments worldwide have already implemented new standards regarding the shift toward EVs to achieve sustainable transportation. To reach the goal of this transition, suitable EV chargers having high efficiency and compatible with electricity grid are needed to be developed to provide efficient and fast battery charging [9]. In the case of grid-to-vehicle (G2V) mode of operation, battery chargers convert AC current distributed by electricity grid into DC one to charge vehicle battery. According to vehicle-to-grid (V2G) concept, which has gained attention recently, energy stored in the battery, not used by the vehicle, can return back to the grid, affecting the power grid significantly, as well [11]. Therefore, EVs and PHEVs can also provide ancillary services, reactive power support for regulations, or tracking of output power generated by renewable energy sources in addition to charging of the vehicle battery when connected to electric power grid [1, 7, 10]. There are two types of EV charging systems, that are on-board and off-board chargers. Generally, off-board charger systems can provide larger amount of power for the vehicle compared to the on-board one. Moreover, off-board chargers include power electronic system required for AC-DC conversion externally, that can be considered as advantageous since they reduce the weight of the vehicle. Thanks to high amount of power that they can provide, off-board charger systems increase the time or miles which EV is used so they can solve range issues for EVs. However, the vehicle can be charged in many locations where AC source is available with on-board chargers, which are more flexible [12, 13]. EV chargers can also be classified into unidirectional chargers and bi-directional chargers according to power flow capability between the vehicle and electric power grid. Typical block diagrams for unidirectional and bidirectional topologies are shown in Figure 1. Unidirectional EV chargers have the advantage of reduced system complexity, fewer circuit components leading to reduced system cost, and small size but they cannot provide ancillary services or reactive power support for load balance in the power grid those would be key to the future of advanced smart grid functionalities [14]. Bi-directional EV chargers

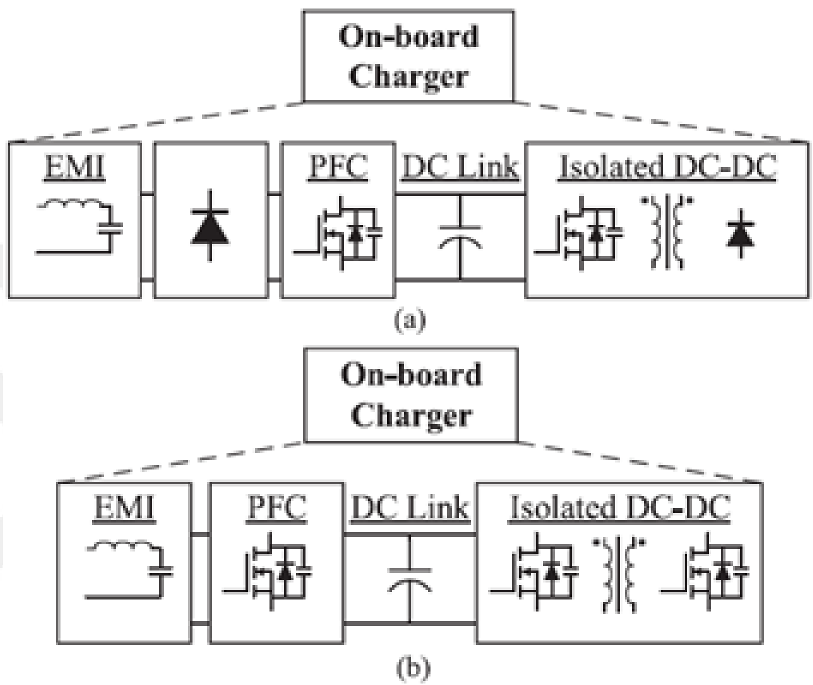

Figure 1: Typical block diagrams for (a) unidirectional and (b) bidirectional EV chargers [14].

enable power flow between the power grid and the vehicle in both directions (G2V or V2G). Also, they can provide load regulation, that is vehicle-to-load (V2L), and back-up power source for households i.e. vehicle-to-house (V2H). Although they have a variety of beneficial functionality especially for smart grids, large number of circuit components, increasing system complexity and cost, cause a disadvantage for them [14, 15].

1.2 Motivation

There has been a significant development in smart grid and an increased interest in its functionality in recent years. The future of smart grid involves a proper integration of renewable or alternative energy systems into the electricity power grid, creating microgrids to increase reliability under the case of disturbances or intermittence. Transportation systems have become more electrified thanks to efforts to mitigate the issues emerged from climate change, as well. Therefore, optimal applications are required to provide the exchange of power between the grid and energy storage systems such as EV batteries or back-up power sources for proper functionality of smart grids. Bidirectional EV chargers, playing important roles for vehicle-to-grid technology, enable not only charging of vehicle battery but also the obvious bidirectional power flow between the electricity grid and the vehicle, providing reactive power support and reverse power for peak-shaving for the grid. Transition to bidirectional EV chargers would enable a significant amount of control and flexibility for the power grid, allowing customers to use energy for their households, vehicles or even sending back to the grid. It also provides support for the electricity grid, balances energy demand and smooths spikes due to consumption of energy with the help of EV batteries for utilities. This thesis presents modeling of a three-phase bidirectional EV charger, of which the performance is analyzed under various conditions and harmonic contents are investigated.

1.3 Objectives

The objective of this thesis is designing a three-phase bidirectional EV charger which can be used for charging, energy storage or V2G applications. Conventional EV chargers generally enable only charging of vehicle battery. The proposed charger system would also be able to supply power back to the power grid from the battery if necessary in addition to providing charging for EV batteries. The system has two stages, including AC/DC PWM and DC/DC bidirectional converters. A DC bus capacitor, having a rated voltage value of 800V, is added between this two converters as well. Rated power of the EV charger is desired to be 5kW and nominal battery voltage value would be 500V as well. To suppress harmonics for the grid side, an LCL filter is inserted between the AC/DC converter of the system and the three phase power grid. Moreover, Clark-Park Transformation and PLL algorithm are utilized to simplify the designing of controllers for AC/DC side of the charger circuit. The following steps would be followed while designing, modeling, simulating and analyzing the complete EV charger system:

- Designing the components such as line filter, DC bus capacitor and output filter of DC/DC side of the charger system.

- Selecting suitable power transistors for the converters of the EV charger circuit.

- Choosing a proper method for modulation signals to generate corresponding gate pulses of AC/DC PWM converter of the EV charger to be modeled.

- Developing the required two-loop control systems based on the equations derived using small signal analysis to achieve tight voltage & current regulations and ensure stability under certain operating conditions.

- Modeling the designed system with the corresponding controllers in MATLAB/Simulink.

- Simulating and analyzing the system under some conditions based on closed loop performance to validate the developed theory regarding control algorithms, harmonic contents of line currents & effects of the power grid on battery voltage/current ripples to be discussed.

- Performing loss analysis for the bidirectional EV charger model confirming that the system is able to operate with high efficiency.

1.4 Main Contributions

This study introduces some significant theoretical approaches especially for control algorithms to be developed for the grid connected three phase bidirectional EV charger to be modeled as well as valuable practical applications for modeling & simulation of the system. Charging and discharging mode of operations are considered separately to design controllers for DC/DC synchronous converter of the bidirectional EV charger circuit in such a way that the control parameters are determined according to buck mode operation of the DC/DC converter while the system operates in G2V mode and they are calculated assuming the converter operates in boost mode while the charger circuit performs V2G mode of operation. Conventionally, the voltage & current controllers of general EV charger topologies given in literature are designed considering the related parameters such as cut-off frequencies, phase margin values and the closed loop performance of systems is analyzed using only compensated loop gains for inner current loop or outer voltage one without taking some other perturbations into account while performing theoretical analysis for stability of the charger circuits. In this research, some additional loop gains for closed loop control are constructed and analyzed theoretically to investigate effects of variation in DC bus voltage, output battery voltage reference or load transient on the other system parameters such as battery voltage & current, line currents, output inductor current or DC link for both G2V and V2G mode of operations regarding the complete EV charger system also taking the interaction between the AC/DC PWM & DC/DC synchronous converters into account. Moreover a few assumptions, that are not common, are made to develop control systems for DC/DC part of the three phase EV charger circuit in a way that no load condition with a very large load resistance value is assumed to simplify the corresponding mathematical procedures derived for boost mode operation since the output of DC/DC converter would be DC link for the charger system operates in the inverter mode.

CHAPTER II

LITERATURE REVIEW AND THEORY

The topics of EV chargers and the related power electronics converters have been studied for years, emphasizing various converter topologies, control algorithms, efficiency, simplicity or cost. Researches have been continuously conducted to develop alternative EV charger topologies, improved grid synchronization schemes or line filters to mitigate harmonic distortions. This chapter covers power electronics converters, various EV charger topologies with battery technologies and design techniques of the related control systems.

2.1 Power Converters

The connection of electric vehicles to the grid is achieved by various power converter chargers enabling energy conversion or power flow between the battery of the vehicle and electric power grid.

2.1.1 Three-Phase AC/DC PWM Converters

Three phase PWM converters or front end converters (FECs) are widely implemented for grid connected electric vehicle chargers (EVCs). Thanks to recent developments and smart grid applications, bidirectional electric vehicle chargers have become more popular since they can enable some facilities having more importance due to emerging technologies including reactive power exchange or load support at the grid side. That is bidirectional EVCs include mainly three phase bidirectional converters that allow power flow in both directions (V2G to provide reactive power or G2V enabling charging of battery) [1, 10]. Gate signals of the switches must be applied to enable power flow between AC source and DC bus sides of a three-phase

PWM converter [16, 17].

2.1.1.1 Switching Techniques for Three-Phase Converters

There are various switching techniques to generate gate signals. Pulse width modulation (PWM) technique is the most common one among them and has become standard technique for three-phase PWM converters in industrial applications. Mostly utilized PWM techniques are sine PWM (SPWM) and space vector PWM (SVPWM) ones as well [18].

For SPWM technique, gate pulses with constant amplitude and variable duty cycle for each period are desired to be generated. By modulating the width of these pulses, a desired voltage at output could be obtained for the converter. Generally three sine waves and a triangular carrier signal with high frequency are implemented to generate PWM signals for gates of the switches using SPWM method. The sine waves are reference signals and they are aparted from each other by 120 phase difference. Moreover the frequency of these reference waves are equal to that of AC source voltages (50/60 Hz). The gate signals are generated by comparing the reference waves with the high-frequency carrier signal (in several kHz to a few MHz) [19]. Block diagram for the algorithm of SPWM generation used in three-phase PWM converters is given in Figure 2, in which g_x represents gate pulses applied to the switches, S_x of the converter (g_x corresponds to S_x, x = 1,2,..6). Moreover, illustrative waveforms for generation of SPWM with the triangular carrier signal and one of the reference sine waves are shown in Figure 3.

Using SVPWM method, space vector concept is utilized to compute duty cycle values and generate the corresponding gate pulses for the switches of three phase PWM converters. The waveform generated by SVPWM technique is realized by combinations of various switching modes of the converters as well. For example, "1" is assumed to be defined as the positive half of the DC bus voltage while "0" as

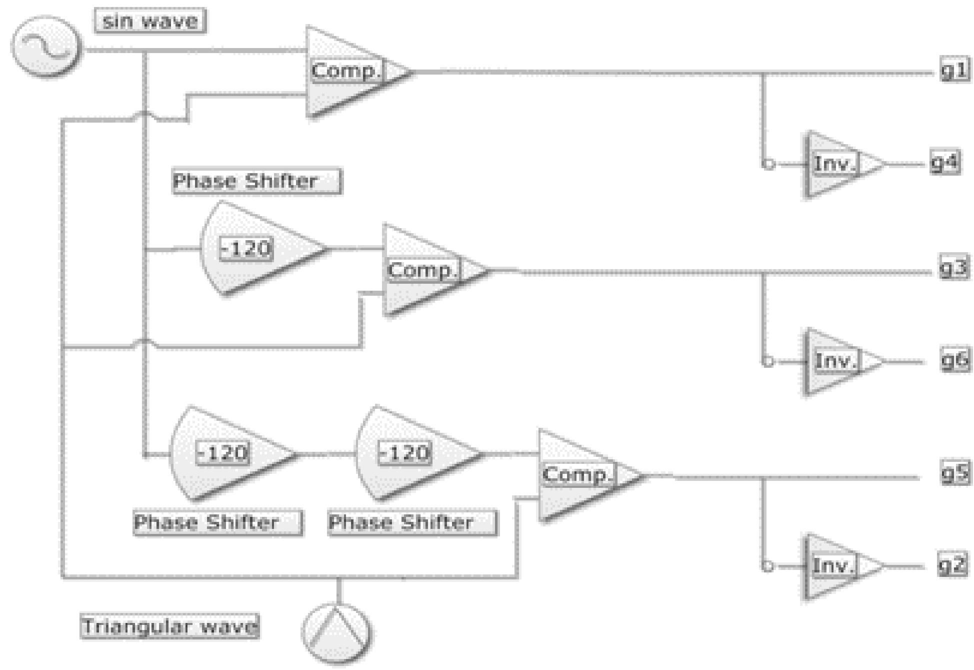

Figure 2: Block diagram for the algorithm of SPWM generation [19].

the negative one, referred to the neutral point, for a three-phase PWM converter. Generally there would be eight switching states for the switches and corresponding eight voltage vectors would be defined, forming a vector space with six sectors for AC/DC PWM converters [18, 21].

SPWM method is used for switching of the gates of three phase AC-DC converter to be modeled as a part of the bidirectional EV charger in this thesis as well.

2.1.1.2 Modulation Techniques for Three-Phase Converters

The operation of PWM can be divided into two modes, which are linear modulation and over-modulation cases. Linear modulation is the modulation for normal steady-state operation while over- modulation occurs when a transient such as load increase is observed for the converter [18, 22]. The waveforms of the carrier signal & reference sine corresponding to linear modulation and over-modulation cases are given in Figure 4 and 5, respectively. The peak value of reference sine wave is represented by V_m

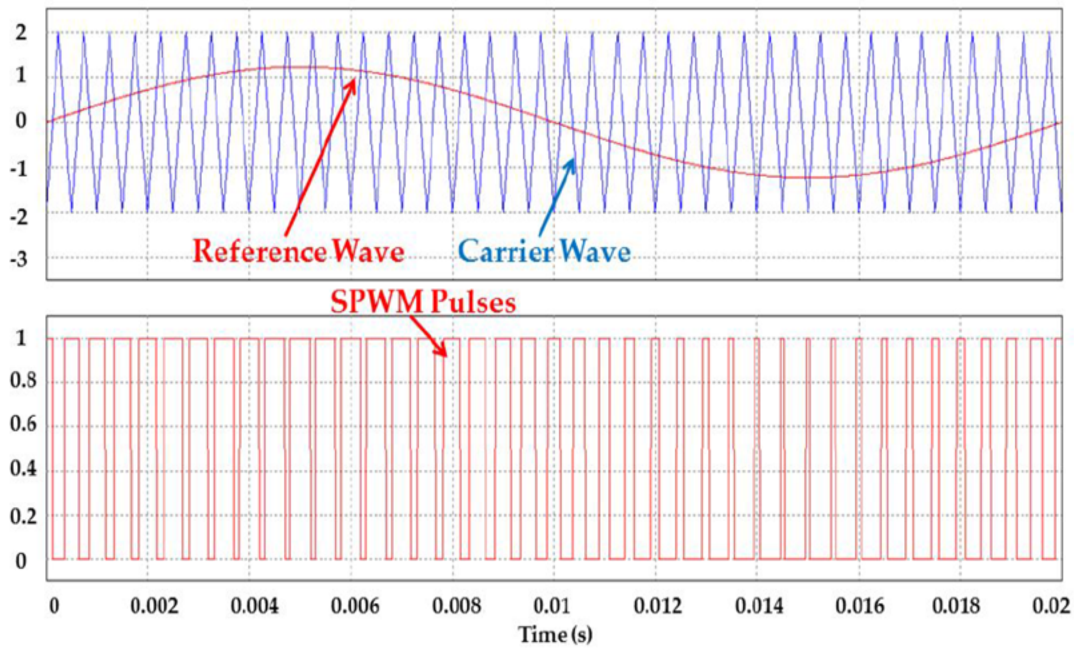

Figure 3: Illustrative waveforms for SPWM generation [20].

while that of triangular carrier wave is notated as V_c.

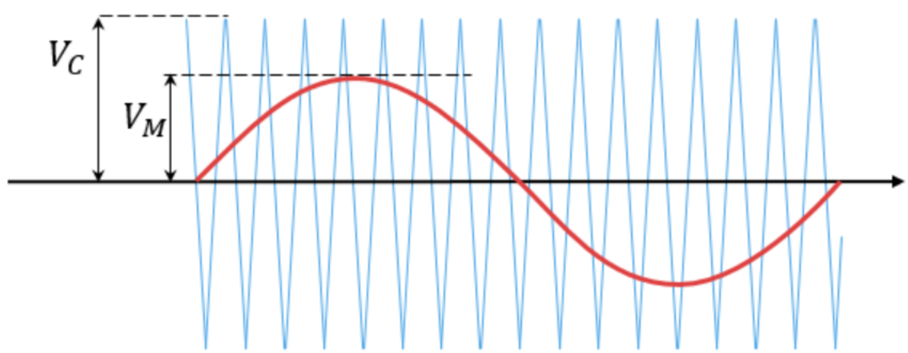

Figure 4: Waveforms of carrier signal and reference for linear modulation case [22].

The modulation index, m_a measuring the ability of the converter to provide a given output voltage, is expressed as;

$$m_a = \frac{V_m}{V_c} \tag{1}$$

- For normal steady-state operation (linear modulation) of power converter, the

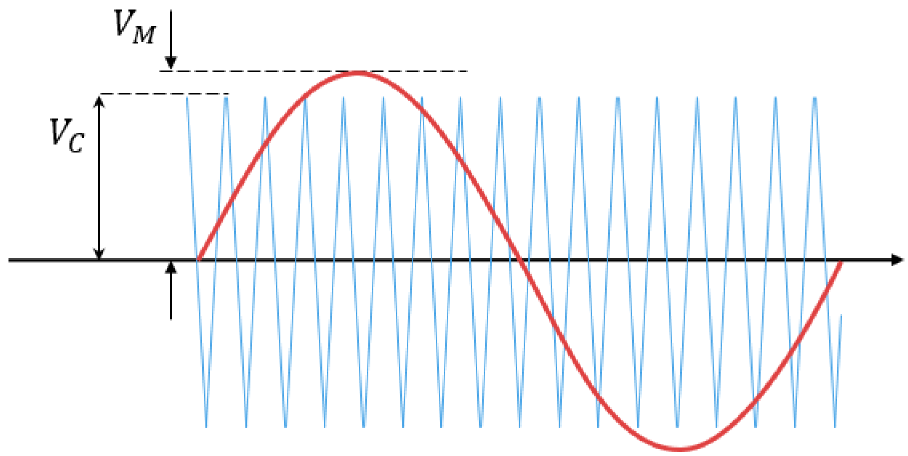

Figure 5: Waveforms of carrier signal and reference for over-modulation case [22].

value of modulation index, m_a is between 0 and 1;

$$0 < m_a \leq 1 \tag{2}$$

- For the case at which a transient occurs (over modulation) the amplitude of V_m exceeds that of V_c and m_a is greater than 1;

$$m_a > 1 \tag{3}$$

For a three-phase PWM converter, switched using SPWM technique, the expression of modulation index, m_a is modified and the following equation can be defined specifically;

$$V_{peak} = m_a \frac{V_{dc}}{2} \tag{4}$$

V_{peak} is peak value of the fundamental component of the phase voltage and V_{dc} represents DC link voltage. The equation given in (4) can be modified a bit and can also be expressed in terms of RMS value of the fundamental component of line-to-line voltage, $V_{1,ll,rms}$ for the converter as;

$$V_{1,ll,rms} = m_a \frac{\sqrt{3}V_{dc}}{2\sqrt{2}} = 0.612 m_a V_{dc} \tag{5}$$

When m_a is greater than 3.24, modulation signal would converge to square or six-step wave as well [18, 22, 23]. Also, duty cycle values of the switches for each of three legs of the PWM converter vary with time, depending on the modulation signals, which are applied for all of three phases [24]. Allowing over-modulation causes harmonics increase for the converter so different injection techniques such as third harmonic or zero sequence injection can be implemented to increase the output voltage of the converter instead of increasing DC bus voltage, that can lead to higher cost [23]. Thanks to these methods, wider linearity range for modulation index would be achieved compared to the case when only conventional SPWM method is used, providing linearity for modulation index values only below 1. Also, they provide low THD for high-voltage applications and reduced switching loses [25].

Using third harmonic injection method, the peak value of the phase voltage can be decreased while that of the fundamental component can be kept as the same. Hence, DC link voltage can be utilized more effectively. Third harmonics would cancel out in the line-to-line voltage thanks to its being injected in all three phases so the utilization of the DC bus voltage would increase by a factor of nearly 1.155. As a result, the PWM operation can also be performed in the over-modulation range to maximize the use of DC bus voltage [23, 26]. The modulation waveforms with third harmonics injected, $V_a^{'}$, $V_b^{'}$ and $V_c^{'}$, corresponding to the legs of the converter can be modified with the following expressions[26, 27];

$$V_a' = V_a + \frac{1}{6}V_m cos(3w_e t) \tag{6}$$

$$V_b' = V_b + \frac{1}{6}V_m cos(3w_e t - \frac{2\pi}{3}) \tag{7}$$

$$V_c' = V_c + \frac{1}{6}V_m cos(3w_e t + \frac{2\pi}{3}) \tag{8}$$

V_a, V_b and V_c are the modulation waves without any injections, w_e represents fundamental angular frequency of the signals and t is time instant of the sine waves.

Usually, the third harmonic injection method is not very simple for practical applications since instantaneous values of phase or frequency of the voltage to be controlled dynamically for three-phase converters would not be known. Therefore, a simpler method is developed, called zero sequence injection, for which half of the minimum and maximum instantaneous values of the three phase voltages is added to the modulation waves of the all three phases. The modulation waveforms with min/max zero sequence injected, V_a'', V_b'' and V_c'', corresponding to the legs of the converter can be written as [27];

$$V_a'' = V_a - V_{mm} \tag{9}$$

$$V_b'' = V_b - V_{mm} \tag{10}$$

$$V_c'' = V_c - V_{mm} \tag{11}$$

where

$$V_{mm} = \frac{1}{2}min(V_a, V_b, V_c) + \frac{1}{2}max(V_a, V_b, V_c) \tag{12}$$

An example algorithm for the implementation of min/max zero sequence injection method is given in Figure 6.

The comparison of the modulation waveforms of the conventional ones without any injection, the ones injected with third harmonics or zero sequence waves for the all three phases are shown in Figure 7 as well.

Moreover, in this thesis the zero sequence injection method is used thanks to its simplicity while PWM modulation is performed for the AC-DC part, which is three phase bi-directional PWM converter, of the EV charger to be modeled.

2.1.1.3 Line Filters for Three-Phase Converters

Line filters are used for harmonics reduction, which is a significant priority of a designer while designing any type of power electronics converters such as AC-DC PWM converters. There are many topologies of such filters, obtained by combining

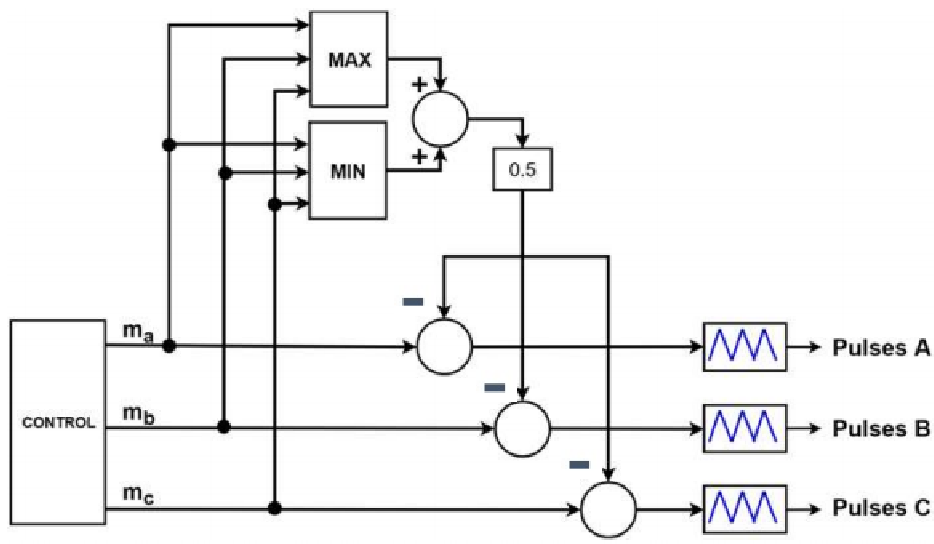

Figure 6: The algorithm of the implementation of min/max zero sequence injection method [23].

inductors and capacitors. For three-phase PWM converters, L, LC LCL filters are usually implemented depending on requirements of the design as well.

L-filter is regarded as the most suitable one for high switching frequency PWM converters but the inductance cause the dynamics of the system to decrease. LC-filter has a more complicated damping behaviour than L-filter does. It is a second order filter, that is a compromise between the values of the inductance and capacitance. Also, the value of inductance is required to be increased to achieve a higher cut-off frequency while a larger value of capacitance is needed to improve voltage quality for this type of filter. For grid connected PWM converters, resonant frequency of LC-filter depends on the impedance of the power grid [28]. Configuration of a LC-filter for three-phase systems is shown in Figure 8.

LCL-filter is a third order filter and suitable for grid-connected AC-DC PWM converters [28]. It provides a higher harmonics attenuation with reduced power consumption, even with smaller component sizes compared to an L or LC-filter. For

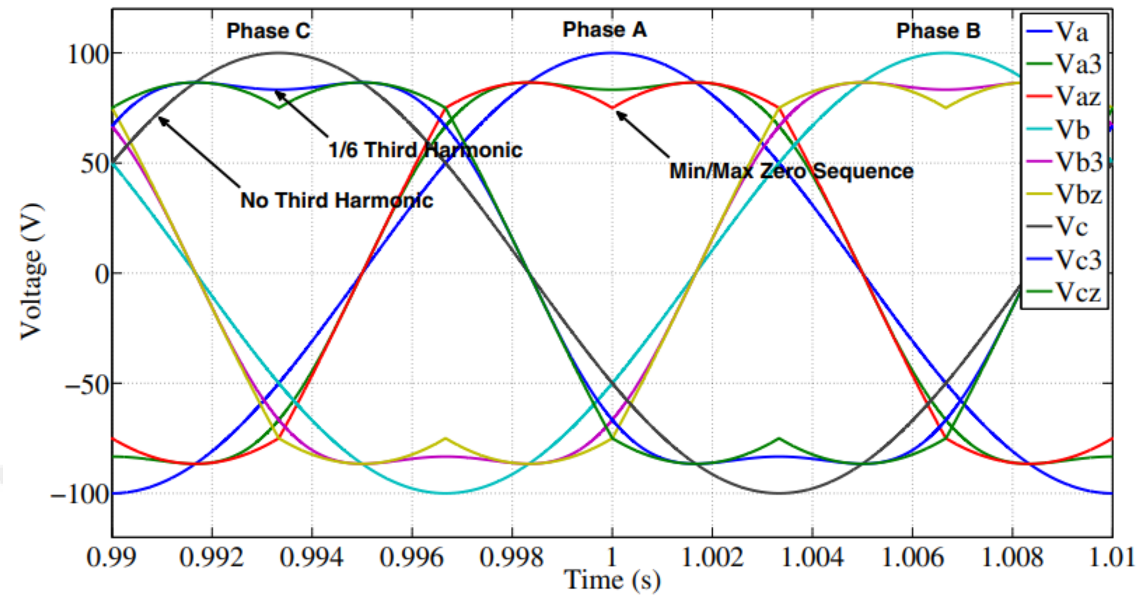

Figure 7: SPWM reference waveforms: normal SPWM, with third harmonic injection and with min/max zero sequence injection [27].

attenuating both low and high order harmonics around the switching frequency, LCL-filter would be an appropriate choice. Also, it is possible to operate the converter with an LCL-filter using relatively low switching frequency for a given harmonics attenuation. LCL filter configuration is given in Figure 9.

While designing this type of filter for AC-DC PWM converters, some constraints such as line current ripple, filter size, switching ripple attenuation etc, are required to be taken into account as well. The converter-side inductance, L_i can be calculated using the equation given in (13).

$$L_i = \frac{V_{DC}}{16 f_s \Delta I_L} \tag{13}$$

f$_s$ is switching frequency of the converter and ΔI_L represents ripple current of the line inductor.

The ripple current of the converter-side inductor, ΔI_L is usually chosen to be 10% of the phase current. Therefore the following expression for ΔI_L is written as;

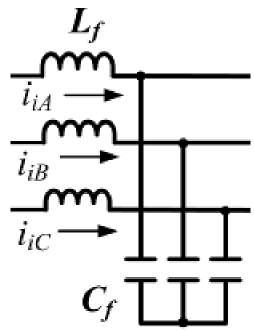

Figure 8: LC-filter for three phase converters [29].

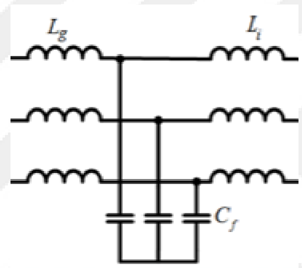

Figure 9: LCL-filter for three phase converters [30].

$$\Delta I_L = 0.1 \frac{\sqrt{2} P_{ph}}{V_{ph(grid)}} \tag{14}$$

P_{ph} represents nominal power of the converter per phase and $V_{ph(grid)}$ is RMS value of single-phase voltage of the grid.

An appropriate selection for value of the grid-side inductance, L_g can also be made using the equation given below.

$$L_g = 0.6 L_i \tag{15}$$

Moreover, in addition to the filter inductance values, the filter capacitance, C_f can be taken as 5% of the base one, C_b according to the expression given in (16).

$$C_f = 0.05 C_b = \frac{P_{ph}}{\omega_{grid} V_{ph(grid)}^2} \tag{16}$$

ω_{grid} is rotational frequency of the grid.

The resonance frequency of the LCL-filter to be designed would be calculated using the equation in (17).

$$f_o = \frac{1}{2\pi}\sqrt{\frac{L_i + L_g}{L_i L_g C_f}} \tag{17}$$

A damping resistor in series with the capacitor of the LCL-filter, C_f could also be added to increase the performance of the filter more as shown in Figure 10.

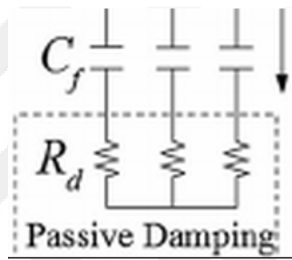

Figure 10: A damping resistor, R_d in series with capacitor, C_f [31].

The value of the damping resistor, R_d is determined using the following equation [32-36].

$$R_d = \frac{1}{6\pi f_o C_f} \tag{18}$$

In this thesis, an LCL-filter is inserted at the grid side of the three-phase bidirectional EV charger to mitigate harmonics of line current as well.

2.1.1.4 Loss Analysis for Three-Phase Converters

Three phase AC/DC bidirectional PWM converters have some losses due to switching transistors to be used for generation of gate signals. When transistors conduct and some amount of current passes through them to provide power flow between the grid side and DC bus, some conduction losses would occur due to on-state voltage drop of the transistor, $V_{on,ac}$ and conduction resistance of it, $R_{on,ac}$. Also, reverse connected internal diodes of the transistor switches can cause some additional conduction losses because of forward voltage drop of the diode, $V_{D,ac}$. The total amount of conduction losses for SPWM method can be predicted using the equations given below;

$$P_{T,ac} = \frac{V_{on,ac} I_m}{2\pi}(1 + \frac{m_a \pi}{4} cos(\phi)) + \frac{R_{on,ac} I_m^2}{2\pi}(\frac{\pi}{4} + \frac{2}{3} m_a cos(\phi)) \tag{19}$$

$$P_{D,ac} = \frac{V_{D,ac} I_m}{2\pi}(1 - \frac{m_a \pi}{4} cos(\phi)) \tag{20}$$

$$P_{tot,cond} = 6(P_{T,ac} + P_{D,ac}) \tag{21}$$

$P_{T,ac}$ & $P_{D,ac}$ are conduction loses due to a single transistor and a single reverse connected diode, respectively. While $P_{tot,cond}$ represents total amount of conduction losses for the converter, I_m is peak value of the line current. ϕ is displacement angle between the fundamental component of the modulation signal and load current.

It is clear that conduction losses of a bidirectional three phase AC/DC PWM converter directly depend on the modulation index value, m_a. By using these analytical equations, some interferences could be made regarding loss analysis or evaluation of efficiency of the converter as well [37].

2.1.2 DC/DC Converters

Bi-directional electric vehicle (EV) chargers mostly include synchronous DC-DC converter parts which can act as buck or boost converter depending on the direction of power flow (condition of charging or discharging). Synchronous converters are mainly selected topology for chargers thanks to their higher efficiency compared to conventional DC-DC ones [38].

2.1.2.1 Analysis of DC/DC Buck Converter

Buck converters are used for reducing the DC voltage via non-dissipative components unlike linear regulators, which helps achieve high efficiency values. Circuit diagram of a simple buck converter for ideal case is shown in Figure 11.

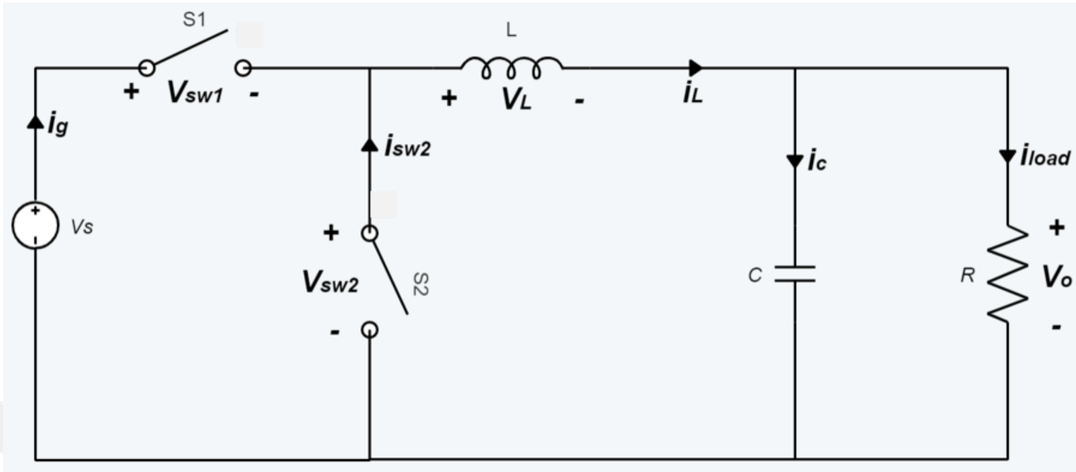

Figure 11: Buck converter circuit diagram for ideal case

V_s corresponds to input DC voltage, I_g is input DC current, V_{sw1} & V_{sw2} represent voltage across switch 1 (S1) & switch 2 (S2) respectively, V_L is inductor voltage, V_C is capacitor voltage, I_L is inductor current, I_c is capacitor current, V_0 is output DC voltage, I_{load} is load current and R represents load resistance.

Steady-state analysis for the converter can be made by investigating the cases at which transistors, S_1 and S_2 are turned on & off. The following expression can be derived

1) when S_1 is on and S_2 is off;

$$v_S(t) - v_0(t) = L\frac{di_L(t)}{dt} \tag{22}$$

$$i_C(t) = i_L(t) - \frac{v_0(t)}{R} \tag{23}$$

$$i_g(t) = i_L(t) \tag{24}$$

2) when S_1 is off and S_2 is on;

$$L\frac{di_L(t)}{dt} = -v_0(t) \tag{25}$$

$$i_C(t) = i_L(t) - \frac{v_0(t)}{R} \tag{26}$$

$$i_g(t) = 0 \tag{27}$$

Assuming the switching period is T_{sw} ,

1) on time duration, t_{on} is (when S_1 is on and S_2 is off.)

$$t_{on} = d(t)T_{sw} \tag{28}$$

2) off time duration, t_{off} is (when S_1 is off and S_2 is on)

$$t_{off} = T_{sw} - d(t)T_{sw} = (1 - d(t))T_{sw} \tag{29}$$

d(t) is duty cycle value.

At steady state, the variables can be assumed to be as time independent and they are equal to their average values. Rearranging the equations;

1) when S_1 is on and S_2 is off;

$$< v_S > - < v_0 >= L\frac{d < i_L >}{dt} \tag{30}$$

$$< i_C >=< i_L > -\frac{< v_0 >}{R} \tag{31}$$

$$< i_g >=< i_L > \tag{32}$$

2) when S_1 is off and S_2 is on;

$$L\frac{d < i_L >}{dt} = - < v_0 > \tag{33}$$

$$< i_C >=< i_L > -\frac{< v_0 >}{R} \tag{34}$$

$$< i_g >= 0 \tag{35}$$

Also;

$$d(t) = d \tag{36}$$

$$1 - d(t) = 1 - d = d' \tag{37}$$

• The average value of inductor voltage during the switching period, T_{sw} would be;

$$\int_0^{T_{sw}} V_L(t)dt = d(< v_g > - < v_0 >) + d'(- < v_0 >) = L\frac{< i_L >}{dt} \tag{38}$$

$$L\frac{d}{dt} < i_L >= d < v_S > - < v_0 > \tag{39}$$

• The average value of output capacitor current during the switching period, T_{sw} would be;

$$\int_0^{T_{sw}} i_C(t)dt = d(< i_L > -\frac{< v_0 >}{R}) + d'(< i_L > -\frac{< v_0 >}{R}) = C\frac{d < v_0 >}{dt} \tag{40}$$

$$L\frac{d}{dt} < v_0 >=< i_L > -\frac{< v_0 >}{R} \tag{41}$$

• The average value of input current during the switching period, T_{sw} would be;

$$< i_g >= d < i_L > \tag{42}$$

If the parasitic effects such as internal resistances, on-state voltage drops etc are included for realistic model, the circuit diagram would be as shown in Figure 12.

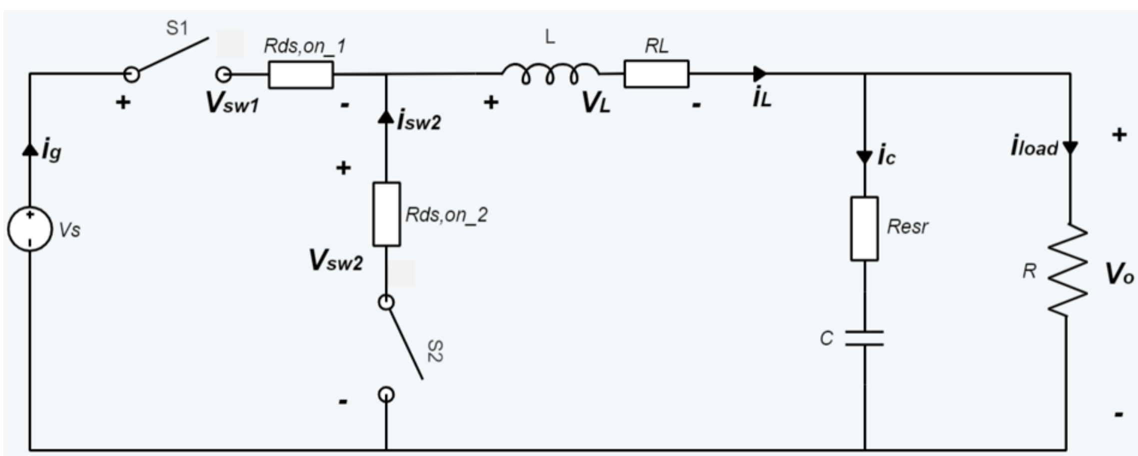

Figure 12: Buck converter circuit including parasitic effects

Additional elements are $R_{ds,on-1}$ & $R_{ds,on-2}$ representing internal resistances of the transistor 1 (S_1) & transistor 2 (S_2) respectively, R_L corresponding internal resistance of the inductor and R_{esr} ESR value of the capacitor.

a. General Analysis of Buck Converter

At steady state, the equations can be rederived according to the realistic buck converter circuit. Rearranging the equations;

1) when S_1 is on and S_2 is off;

$$<v_S> -(R_{ds,on1}+R_L)<i_L> - <v_0> = L\frac{d<i_L>}{dt} \tag{43}$$

$$<i_C> = <i_L> - \frac{<v_0>}{R} \tag{44}$$

$$<i_g> = <i_L> \tag{45}$$

$$<v_0> = R_{esr}<i_C> + <v_C> \tag{46}$$

2) when S_1 is off and S_2 is on;

$$L\frac{d<i_L>}{dt} = -(R_{ds,on2}+R_L)<i_L> - <v_0> \tag{47}$$

$$<i_C> = <i_L> - \frac{<v_0>}{R} \tag{48}$$

$$<i_g> = 0 \tag{49}$$

$$<v_0> = R_{esr}<i_C> + <v_C> \tag{50}$$

• The average value of inductor voltage during the switching period, T_{sw} would be;

$$\int_0^{T_{sw}} V_L(t)dt = d(<v_S> -(R_{ds,on1}+R_L)<i_L> - <v_0>) + d'(-(R_{ds,on2}+R_L)<i_L> - <v_0>) = L\frac{d<i_L>}{dt} \tag{51}$$

$$L\frac{d}{dt}<i_L> = d<v_S> - <i_L>(R_L + dR_{ds,on1} + d'R_{ds,on2}) - <v_0> \tag{52}$$

• The average value of output capacitor current during the switching period, T_{sw} would be;

$$\int_0^{T_{sw}} i_C(t)dt = d(<i_L> - \frac{<v_0>}{R}) + d'(<i_L> - \frac{<v_0>}{R}) = C\frac{d<v_C>}{dt} \tag{53}$$

$$C\frac{d}{dt}<v_C> = <i_L> - \frac{<v_0>}{R} \tag{54}$$

• The average value of input current during the switching period, T_{sw} would be;

$$< i_g >= d < i_L > \tag{55}$$

• The average value of output voltage during the switching period, T_{sw} would be;

$$< v_0 >= d(< v_C > +R_{esr} < i_C >) + d'(< v_C > +R_{esr} < i_C >) \tag{56}$$

$$< v_0 >=< v_C > +R_{esr} < i_C > \tag{57}$$

The parameters, expressed as average values, given in the steady state equations above can be seperated to their large DC components and perturbated AC components as shown below.

$$< v_S >=< v_g >= V_g + \hat{v}_g \tag{58}$$

$$< v_0 >= V + \hat{v} \tag{59}$$

$$< i_L >= I + \hat{i} \tag{60}$$

$$< v_c >= V_c + \hat{v}_c \tag{61}$$

$$< i_g >= I_g + \hat{i}_g \tag{62}$$

$$< i_c >= I_c + \hat{i}_c \tag{63}$$

$$< d >= D + \hat{d} \tag{64}$$

$$< d' >= D' - \hat{d}' \tag{65}$$

Also it is assumed that the converter satisfy the small signal hypothesis. Hence;

$$\hat{v}_g << V_g \tag{66}$$

$$\hat{v} << V \tag{67}$$

$$\hat{i} << I \tag{68}$$

$$\hat{v}_c << V_c \tag{69}$$

$$\hat{i_g} << I_g \tag{70}$$

$$\hat{i_c} << I_c \tag{71}$$

$$\hat{d} << D \tag{72}$$

b. <u>Steady-State DC Analysis of Buck Converter</u>

Firstly, DC analysis would be performed to investigate input-output relationship, inductor current capacitor voltage ripple values and effieciency for the converter. The average values of parameters is reduced to their DC components. Also average value of inductor voltage and capacitor current over a switching period at steady-state is equal to zero.

$$< i_c >= 0 \tag{73}$$

$$< V_L >= 0 \tag{74}$$

Hence the equations would be as shown below for DC analysis;

$$DV_g - I(R_L + DR_{ds,on1} + D'R_{ds,on2}) - V = 0 \tag{75}$$

$$I - \frac{V}{R} = 0 \tag{76}$$

$$I_g = DI \tag{77}$$

$$V_0 = V_c \tag{78}$$

Arranging the equations given above output voltage expression would be;

$$V = \frac{DVg}{1 + \frac{R_L + DR_{ds,on1} + D'R_{ds,on2}}{R}} \tag{79}$$

Assuming $R_{ds,on1} = R_{ds,on2} = R_{ds,on}$ (if two identical transistors are utilized)

$$V = \frac{DV_g}{1 + \frac{RL + Rds,on}{R}} \tag{80}$$

Inductor voltage current waveforms are given in Figure 13-14 as well. Switch1 (S_1) switch2 (S_2) current and voltage waveforms are shown in Figure 15-16 and Figure

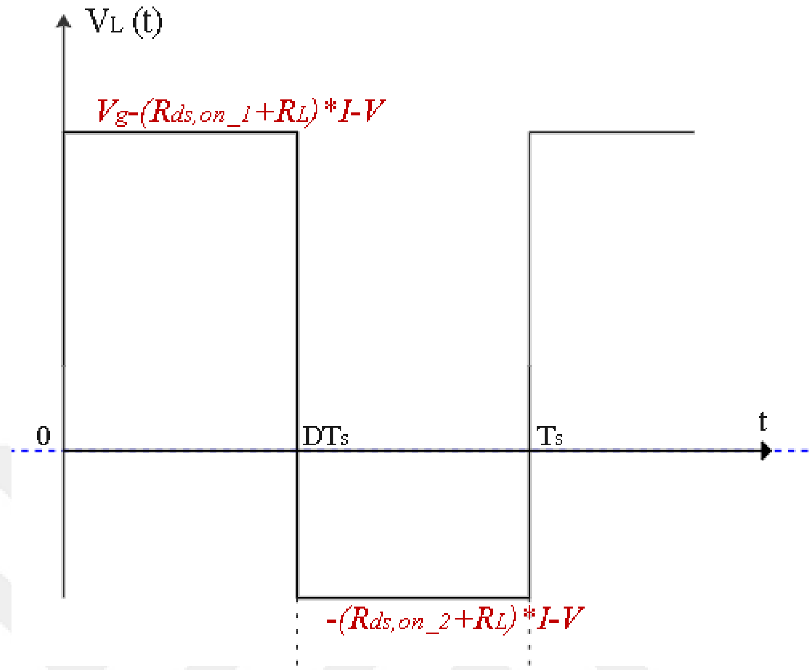

Figure 13: Inductor voltage waveform for buck converter

17-18 respectively. Also, capacitor current voltage waveform is given in Figure 19. (ESR value of the capacitor, R_{esr} is neglected at this stage.)

- For inductor;

$$L\frac{di_L}{dt} = v_L \tag{81}$$

$$L\frac{\Delta i_L}{\Delta t} = v_L \tag{82}$$

Ripple current for inductor is given as;

$$\Delta i_L = \frac{V_L}{L} D' \frac{T_{sw}}{2} \tag{83}$$

$$\Delta i_L = \frac{(R_{ds,on} + R_L)I + V}{2L} D' T_{sw} \tag{84}$$

- For capacitor;

$$C\frac{dv_c}{dt} = i_c \tag{85}$$

$$C\frac{\Delta v_c}{\Delta t} = i_c \tag{86}$$

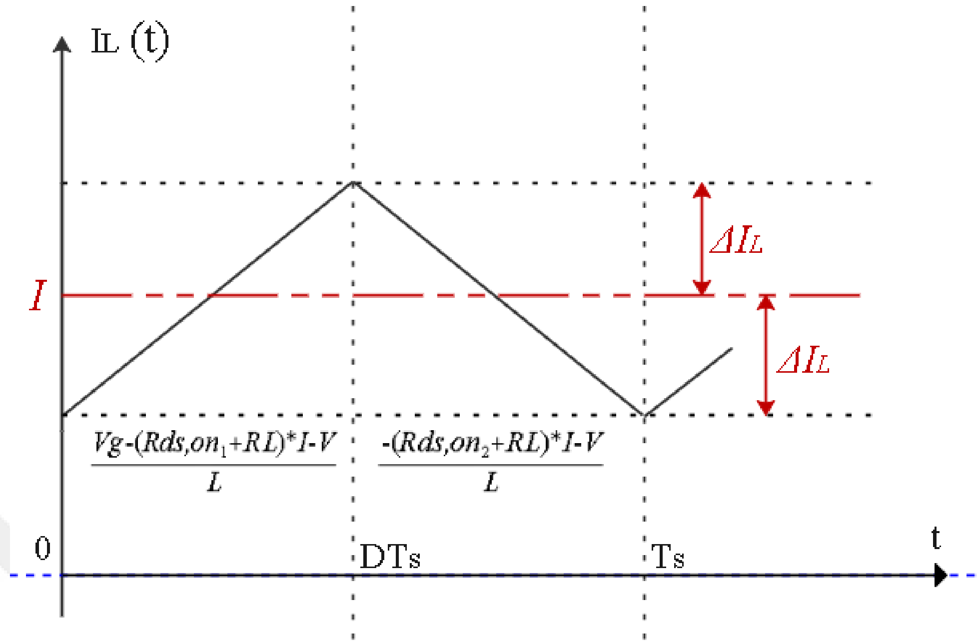

Figure 14: Inductor current waveform for buck converter

According to the plot of capacitor voltage waveform given above;

$$q = C(2\Delta v_c) = \frac{1}{2}\Delta i_L \frac{T_{sw}}{2} \tag{87}$$

q is the total charge.

Ripple voltage for capacitor is given as;

$$\Delta v_c = \frac{\Delta i_L T_{sw}}{8C} \tag{88}$$

Ignoring the switching losses, efficiency of the converter is derived as;

$$\eta_d = \frac{P_{out}}{P_{in}} = \frac{VI}{V_g I_g} = \frac{VI}{V_g DI} = \frac{V}{V_g D} \tag{89}$$

$$\eta_d = \frac{DV_g}{1 + \frac{R_L + R_{ds,on}}{R}} \frac{1}{V_g D} \tag{90}$$

$$\eta_d = \frac{1}{1 + \frac{R_L + R_{ds,on}}{R}} \tag{91}$$

P$_{out}$ represents the output power, P$_{in}$ is the input power and η_d is the efficiency due to conduction losses.

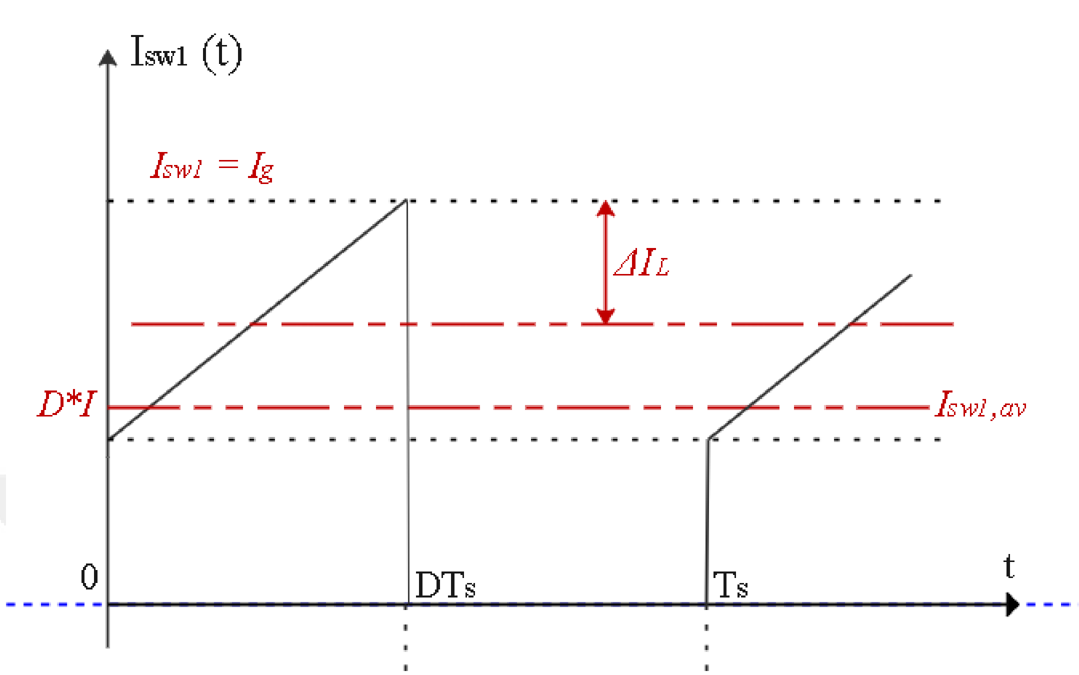

Figure 15: Switch 1, S_1 current waveform for buck converter

c. Small-Signal AC Analysis of Buck Converter

Then small signal AC analysis would be performed to investigate dynamic responses of the converter. By this analysis, effects of change in duty cycle, input voltage/current or load current on output voltage of the converter can be analyzed. Also load is assumed to be resistive for simplicity when the analysis is performed. The parameters, expressed as average values already, given in the steady state equations for the non-ideal synchronous buck converter can be seperated to their large DC components and perturbated AC components as shown below, assuming $R_{ds,on1} = R_{ds,on2} = R_{ds,on}$.

$$L\frac{d}{dt}(I+\hat{i}) = (D+\hat{d})(V_g+\hat{v}_g) - (I+\hat{i})(R_L+R_{ds,on}) - (V+\hat{v}) \tag{92}$$

$$C\frac{d}{dt}(V_c+\hat{v}_c) = (I+\hat{i}) - \frac{(V+\hat{v})}{R} \tag{93}$$

$$(I_g+\hat{i}_g) = (D+\hat{d})(I+\hat{i}) \tag{94}$$

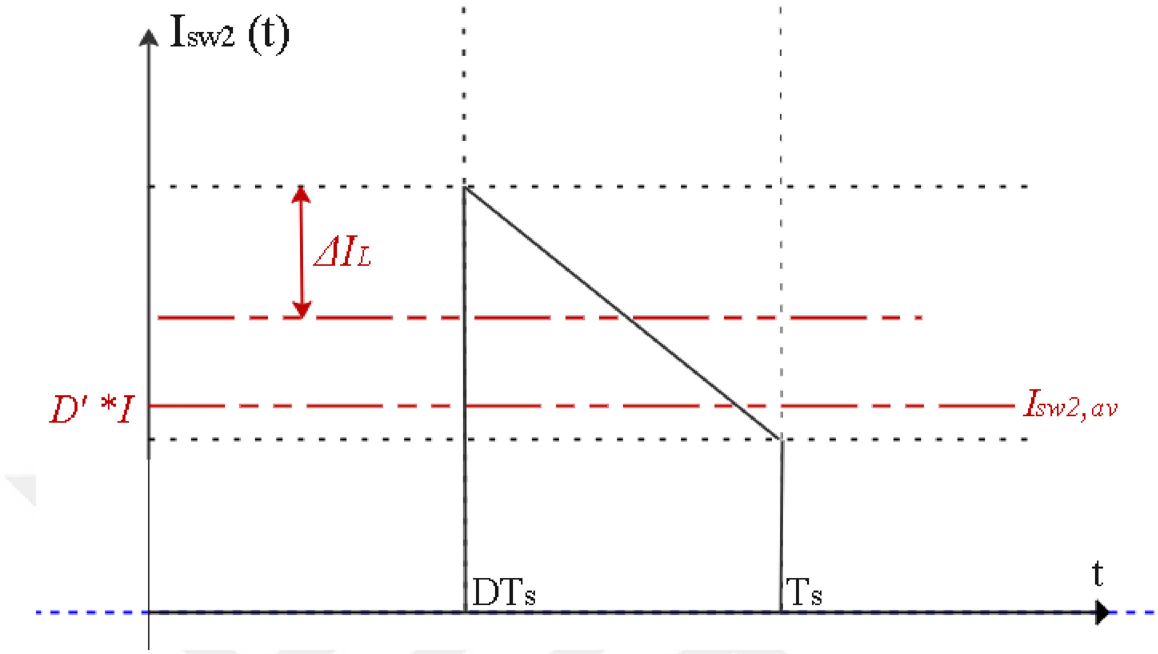

Figure 16: Switch 2, S_2 current waveform for buck converter

$$(V + \hat{v}) = (V_c + \hat{v}_c) + R_{esr}(I_c + \hat{i}_c) \tag{95}$$

Seperating terms related to AC small signal components and neglecting second order AC terms ("$\hat{v}_g\hat{d}$" or "$\hat{i}\hat{d}$");

$$L\frac{d}{dt}\hat{i} = D\hat{v}_g + V_g\hat{d} - \hat{i}(R_L + R_{ds,on}) - \hat{v} \tag{96}$$

$$C\frac{d}{dt}\hat{v}_c = \hat{i}_c = \hat{i} - \frac{\hat{v}}{R} \tag{97}$$

$$\hat{i}_g = D\hat{i} + I\hat{d} \tag{98}$$

$$\hat{v} = \hat{v}_c + R_{esr}\hat{i}_c \tag{99}$$

To investigate effect of small signal perturbation of duty cycle, $\hat{d}$ at output voltage, $\hat{v}$ assuming all other variables are constant and equal to their exact dc values for the converter ($\hat{v}_g = 0$, $\hat{i}_{load} = 0$) transfer function for control-to-output, G_{vd} can be derived. Firstly, rearranging the related equations for the assumption in s- domain;

$$sL\hat{i} = V_g\hat{d} - \hat{i}(R_L + R_{ds,on}) - \hat{v} \tag{100}$$

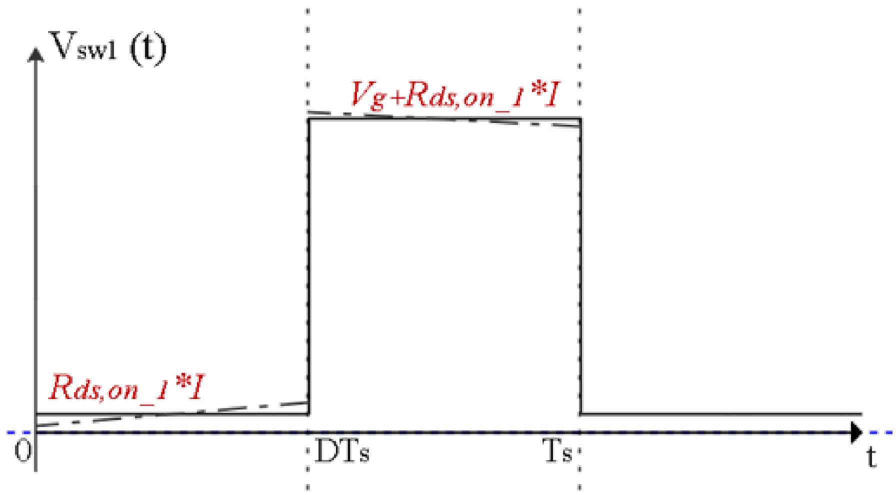

Figure 17: Switch 1, S_1 voltage waveform for buck converter

$$sC\hat{v}_c = \hat{i}_c = \hat{i} - \frac{\hat{v}}{R} \tag{101}$$

$$\hat{v} = \hat{v}_c + R_{esr}\hat{i}_c \tag{102}$$

Making some manipulations from the equations given above, an expression for the relation between small signal output voltage, $\hat{v}$ and duty cycle, $\hat{d}$ would be defined. Then control-to-output transfer function, G_{vd}(s) for the converter is given as;

$$G_{vd}(s) = (V_g\frac{R}{R_e + R})\frac{1 + sCR_{esr}}{(\frac{LC(R+R_{esr})}{R_e+R})s^2 + (\frac{RR_eC+R_{esr}R_eC+R_{esr}RC+L}{R_e+R})s + 1} \tag{103}$$

where

$$R_e = R_L + R_{ds,on} \tag{104}$$

To investigate effect of small signal perturbation of duty cycle, $\hat{d}$ at inductor current, $\hat{i}$ transfer function for control-to-inductor current, G_{id} can be derived. Relationship between G_{id} and G_{vd} can be shown below.

$$G_{id}(s) = \frac{\hat{i}}{\hat{d}} = \frac{\hat{v}}{\hat{d}}\frac{\hat{i}}{\hat{v}} \tag{105}$$

$$G_{id}(s) = G_{vd}(s)\frac{\hat{i}}{\hat{v}} \tag{106}$$

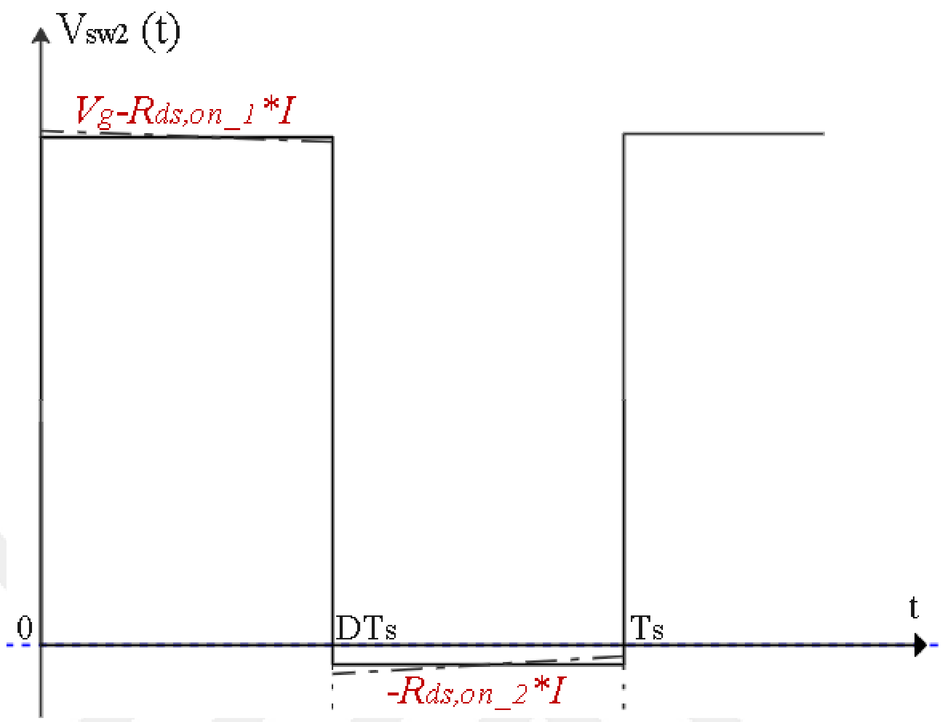

Figure 18: Switch 2, S_2 voltage waveform for buck converter

Relationship between small signal output voltage, $\hat{v}$ and inductor current, $\hat{i}$ can be derived as;

$$sC\hat{v}_c = \hat{i}_c = \hat{i} - \frac{\hat{v}}{R} \tag{107}$$

$$\hat{v} = \frac{1}{sC}(\hat{i} - \frac{\hat{v}}{R}) + R_{esr}(\hat{i} - \frac{\hat{v}}{R}) \tag{108}$$

$$\hat{v} = (\frac{1}{sC} + R_{esr})(\hat{i} - \frac{\hat{v}}{R}) \tag{109}$$

$$\hat{i} = (\frac{1 + \frac{1}{R}(\frac{1}{sC} + R_{esr})}{\frac{1}{sC} + R_{esr}})\hat{v} \tag{110}$$

$$\frac{i}{v} = \frac{1 + sC(R + R_{esr})}{R(1 + sCR_{esr})} \tag{111}$$

Inductor current-to-output transfer function, G_{vi}(s) for the converter can also be defined as (assuming $\hat{i_{load}} = 0$);

$$G_{vi}(s) = \frac{R(1 + sCR_{esr})}{1 + sC(R + R_{esr})} \tag{112}$$

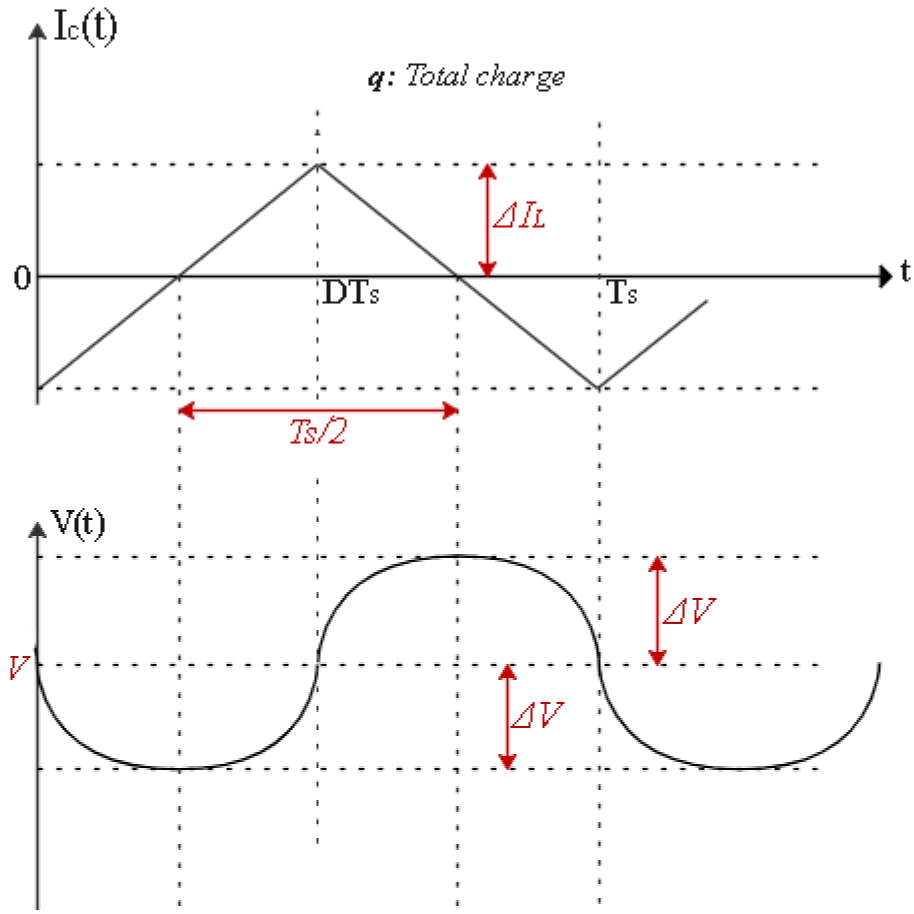

Figure 19: Capacitor current voltage waveform for buck converter

Multiplying G$_{vd}$ by control-to-inductor current transfer function, G$_{id}$(s) for the converter is derived as;

$$G_{id}(s) = (V_g \frac{1}{R_e + R}) \frac{1 + sC(R + R_{esr})}{(\frac{LC(R+R_{esr})}{R_e+R})s^2 + (\frac{RR_eC+R_{esr}R_eC+R_{esr}RC+L}{R_e+R})s + 1} \tag{113}$$

To investigate effect of small signal perturbation of line voltage, at output voltage, $\hat{v}$ assuming all other variables are constant and equal to their exact dc values for the converter ($\hat{d} = 0$, $\hat{i_{load}} = 0$) transfer function for control-to-output, G$_{vg}$ can be derived. Firstly, rearranging the related equations for the assumption in s- domain;

$$sL\hat{i} = D\hat{v}_g - \hat{i}(R_L + R_{ds,on}) - \hat{v} \tag{114}$$

$$sC\hat{v}_c = \hat{i}_c = \hat{i} - \frac{\hat{v}}{R} \tag{115}$$

$$\hat{v} = \hat{v}_c + R_{esr}\hat{i}_c \tag{116}$$

Making some manipulations from the equations given above, an expression for the relation between small signal output voltage, $\hat{v}$ and line voltage, would be defined. Then line-to-output transfer function, G_{vg}(s) for the converter is given as;

$$G_{vg}(s) = (D\frac{R}{R_e + R})\frac{1 + sCR_{esr}}{(\frac{LC(R+R_{esr})}{R_e+R})s^2 + (\frac{RR_eC+R_{esr}R_eC+R_{esr}RC+L}{R_e+R})s + 1} \tag{117}$$

To investigate effect of small signal perturbation of line voltage, at inductor current, $\hat{i}$ transfer function for line-to-inductor current, G_{ig} can be derived in the same way as done previously in deriving control-to-inductor current transfer function, G_{id}. Then line-to-inductor current transfer function, G_{ig}(s) for the converter is derived as;

$$G_{ig}(s) = (D\frac{1}{R_e + R})\frac{1 + sC(R + R_{esr})}{(\frac{LC(R+R_{esr})}{R_e+R})s^2 + (\frac{RR_eC+R_{esr}R_eC+R_{esr}RC+L}{R_e+R})s + 1} \tag{118}$$

To investigate effect of small signal perturbation of load current, at output voltage, $\hat{v}$ assuming all other variables are constant and equal to their exact dc values for the converter ($\hat{d} = 0$ and $\hat{v}_g = 0$) transfer function for load-to-output (output impedance), Z_{out} can be derived. Perturbation of load current is assumed as shown in Figure 20 as well.

Then rearranging the related equations for the assumption in s- domain;

$$sL\hat{i} = -\hat{i}(R_L + R_{ds,on}) - \hat{v} \tag{119}$$

$$sC\hat{v}_c = \hat{i}_c = \hat{i} - \frac{\hat{v}}{R} - \hat{i_{load}} \tag{120}$$

$$\hat{v} = \hat{v}_c + R_{esr}\hat{i}_c \tag{121}$$

Making some manipulations from the equations given above, an expression for the relation between small signal output voltage, $\hat{v}$ and load current, $\hat{i_{load}}$ would be

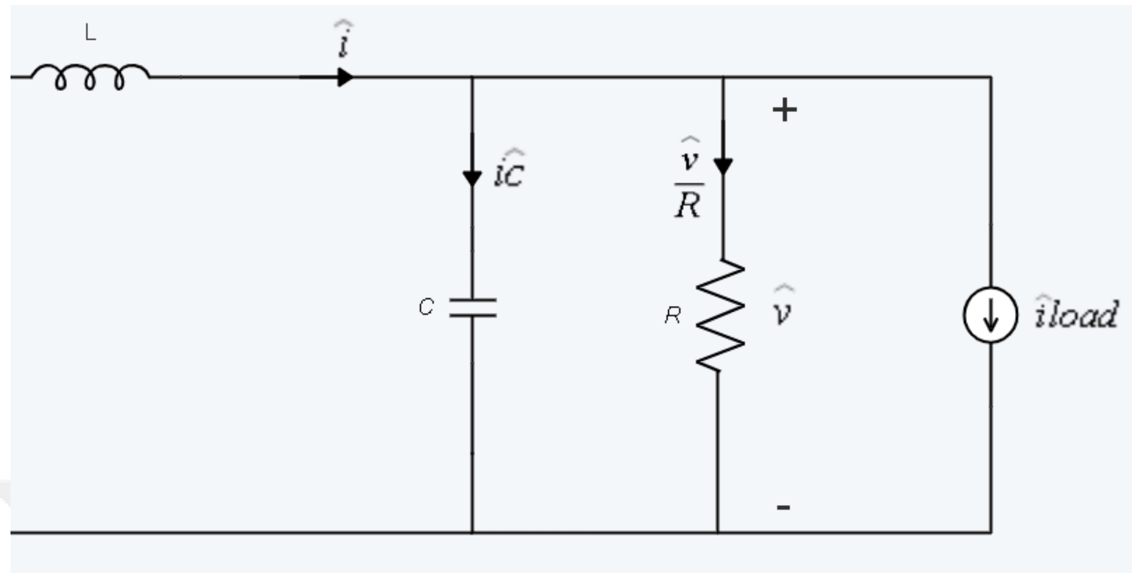

Figure 20: Perturbation of load current at output for buck converter

defined. Then load-to-output (output impedance) transfer function, Z_{out}(s) for the converter is given as;

$$Z_{out}(s) = -(\frac{RR_e}{R_e + R})\frac{(1 + sCR_{esr})(1 + s\frac{L}{R_e})}{(\frac{LC(R+R_{esr})}{R_e+R})s^2 + (\frac{RR_eC+R_{esr}R_eC+R_{esr}RC+L}{R_e+R})s + 1} \tag{122}$$

To investigate effect of small signal perturbation of load current, $\hat{i_{load}}$ at inductor current, $\hat{i}$ transfer function for load-to-inductor current, G_{iz} can be derived in the same way as done previously in deriving control-to-inductor current transfer function, G_{id} and line-to-inductor current transfer function, G_{ig}. Then load-to-inductor current transfer function, G_{iz}(s) for the converter is derived as;

$$G_{iz}(s) = (\frac{R}{R_e + R})\frac{1 + sCR_{esr}}{(\frac{LC(R+R_{esr})}{R_e+R})s^2 + (\frac{RR_eC+R_{esr}R_eC+R_{esr}RC+L}{R_e+R})s + 1} \tag{123}$$

2.1.2.2 Analysis of DC/DC Boost Converter

Boost converters are utilized in applications for which higher DC voltage at output side is required. Circuit diagram of a synchronous boost converter for ideal case is shown in Figure 21.

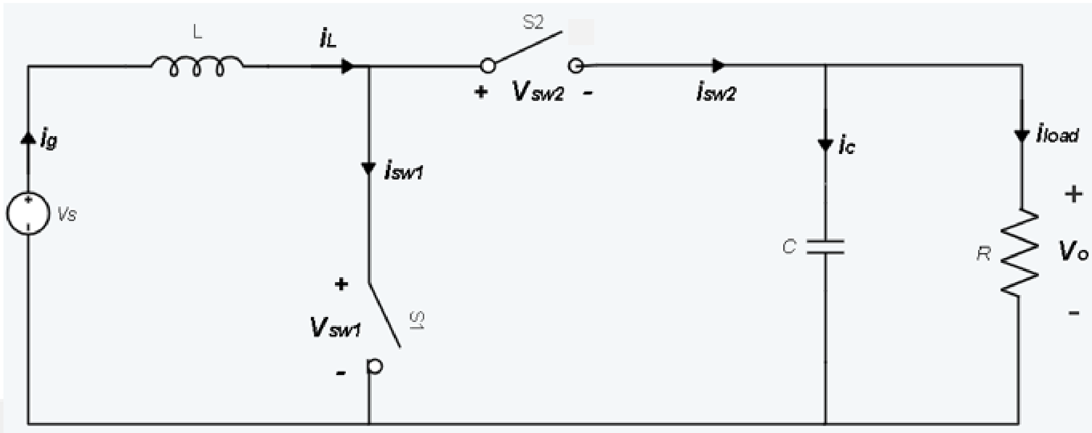

Figure 21: Boost converter circuit diagram for ideal case

Steady-state analysis for the converter can be made by investigating the cases at which transistors, S_1 and S_2 are turned on & off. The following expression can be derived

1) when S_1 is on and S_2 is off;

$$v_S(t) = L\frac{di_L(t)}{dt} \tag{124}$$

$$i_C(t) = -\frac{v_0(t)}{R} \tag{125}$$

$$i_g(t) = i_L(t) \tag{126}$$

2) when S_1 is off and S_2 is on;

$$v_s(t) - v_0(t) = L\frac{di_L(t)}{dt} \tag{127}$$

$$i_C(t) = i_L(t) - \frac{v_0(t)}{R} \tag{128}$$

$$i_g(t) = i_L(t) \tag{129}$$

At steady state, the variables can be assumed to be as time independent and they are equal to their average values. Rearranging the equations;

1) when S_1 is on and S_2 is off;

$$< v_S >= L\frac{d < i_L >}{dt} \tag{130}$$

$$< i_C >= -\frac{< v_0 >}{R} \tag{131}$$

$$< i_g >=< i_L > \tag{132}$$

2) when S_1 is off and S_2 is on;

$$L\frac{d < i_L >}{dt} =< v_S > - < v_0 > \tag{133}$$

$$< i_C >=< i_L > -\frac{< v_0 >}{R} \tag{134}$$

$$< i_g >=< i_L > \tag{135}$$

Also;

$$d(t) = d \tag{136}$$

$$1 - d(t) = 1 - d = d' \tag{137}$$

• The average value of inductor voltage during the switching period, T_{sw} would be;

$$\int_0^{T_{sw}} V_L(t)dt = d(< v_S >) + d'(< v_S > - < v_0 >) = L\frac{< i_L >}{dt} \tag{138}$$

$$L\frac{d}{dt} < i_L >=< v_S > -d' < v_0 > \tag{139}$$

• The average value of output capacitor current during the switching period, T_{sw} would be;

$$\int_0^{T_{sw}} i_C(t)dt = d(\frac{< v_0 >}{R}) + d'(< i_L > -\frac{< v_0 >}{R}) = C\frac{d < v_0 >}{dt} \tag{140}$$

$$C\frac{d}{dt} < v_0 >= d' < i_L > -\frac{< v_0 >}{R} \tag{141}$$

• The average value of input current during the switching period, T_{sw} would be;

$$< i_g >=< i_L > \tag{142}$$

If the parasitic effects such as internal resistances, on-state voltage drops etc are included for realistic model, the circuit diagram would be as shown in Figure 22.

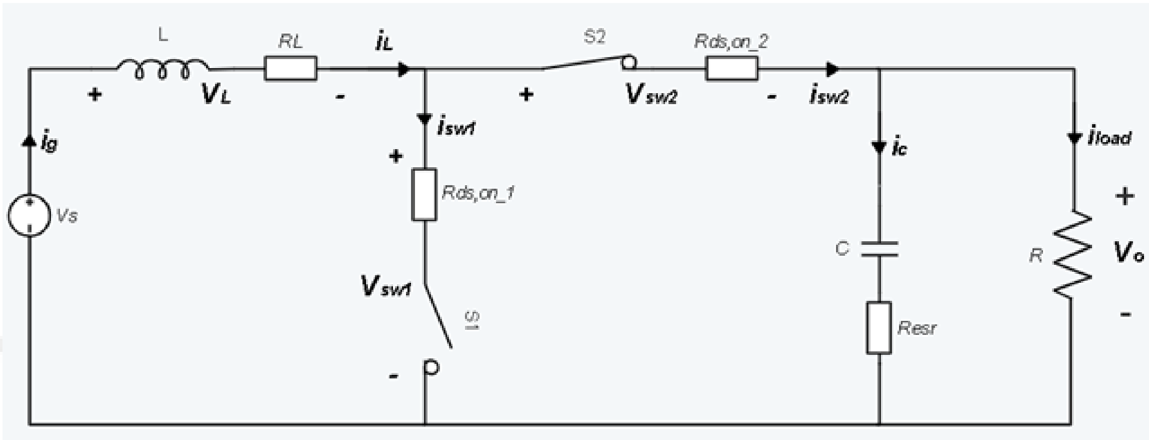

Figure 22: Boost converter circuit including parasitic effects

a. General Analysis of Boost Converter

At steady state, the equations can be rederived according to the realistic buck converter circuit. Rearranging the equations;

1) when S_1 is on and S_2 is off;

$$< v_S > -(R_{ds,on1} + R_L) < i_L >= L\frac{d < i_L >}{dt} \tag{143}$$

$$< i_C >= -\frac{< v_0 >}{R} \tag{144}$$

$$< i_g >=< i_L > \tag{145}$$

$$< v_0 >= R_{esr} < i_C > + < v_C > \tag{146}$$

2) when S_1 is off and S_2 is on;

$$L\frac{d < i_L >}{dt} = -(R_{ds,on2} + R_L) < i_L > + < v_S > - < v_0 > \tag{147}$$

$$< i_C >=< i_L > -\frac{< v_0 >}{R} \tag{148}$$

$$< i_g >=< i_L > \tag{149}$$

$$< v_0 >= R_{esr} < i_C > + < v_C > \tag{150}$$

• The average value of inductor voltage during the switching period, T$_{sw}$ would be;

$$\int_0^{T_{sw}} V_L(t)dt = d(< v_S > -(R_{ds,on1} + R_L) < i_L >) + d'(-(R_{ds,on2} + R_L) < i_L > + < v_S > - < v_0 >) = L\frac{d < i_L >}{dt} \tag{151}$$

$$L\frac{d}{dt} < i_L >=< v_S > - < i_L > (R_L + dR_{ds,on1} + d'R_{ds,on2}) - d' < v_0 > \tag{152}$$

• The average value of output capacitor current during the switching period, T$_{sw}$ would be;

$$\int_0^{T_{sw}} i_C(t)dt = d(-\frac{< v_0 >}{R}) + d'(< i_L > - \frac{< v_0 >}{R}) = C\frac{d < v_C >}{dt} \tag{153}$$

$$C\frac{d}{dt} < v_C >= d' < i_L > - \frac{< v_0 >}{R} \tag{154}$$

• The average value of input current during the switching period, T$_{sw}$ would be;

$$< i_g >=< i_L > \tag{155}$$

• The average value of output voltage during the switching period, T$_{sw}$ would be;

$$< v_0 >= d(< v_C > +R_{esr} < i_C >) + d'(< v_C > +R_{esr} < i_C >) \tag{156}$$

$$< v_0 >=< v_C > +R_{esr} < i_C > \tag{157}$$

The parameters, expressed as average values, given in the steady state equations above can be seperated to their large DC components and perturbated AC components as shown below.

$$< v_S >=< v_g >= V_g + \hat{v}_g \tag{158}$$

$$< v_0 >= V + \hat{v} \tag{159}$$

$$< i_L >= I + \hat{i} \tag{160}$$

$$< v_c >= V_c + \hat{v}_c \tag{161}$$

$$< i_g >= I_g + \hat{i}_g \tag{162}$$

$$< i_c >= I_c + \hat{i_c} \tag{163}$$

$$< d >= D + \hat{d} \tag{164}$$

$$< d' >= D' - \hat{d}' \tag{165}$$

Also it is assumed that the converter satisfy the small signal hypothesis. Hence;

$$\hat{v_g} << V_g \tag{166}$$

$$\hat{v} << V \tag{167}$$

$$\hat{i} << I \tag{168}$$

$$\hat{v_c} << V_c \tag{169}$$

$$\hat{i_g} << I_g \tag{170}$$

$$\hat{i_c} << I_c \tag{171}$$

$$\hat{d} << D \tag{172}$$

b. <u>Steady-State DC Analysis of Boost Converter</u>

Firstly, DC analysis would be performed to investigate input-output relationship, inductor current capacitor voltage ripple values and effieciency for the converter. The average values of parameters is reduced to their DC components. Also average value of inductor voltage and capacitor current over a switching period at steady-state is equal to zero.

$$< i_c >= 0 \tag{173}$$

$$< V_L >= 0 \tag{174}$$

Hence the equations would be as shown below for DC analysis;

$$V_g - I(R_L + DR_{ds,on1} + D'R_{ds,on2}) - D'V = 0 \tag{175}$$

$$D'I - \frac{V}{R} = 0 \tag{176}$$

$$I_g = I \tag{177}$$

$$V_0 = V_c \tag{178}$$

Arranging the equations given above output voltage expression would be;

$$V = \frac{D'Vg}{(D')^2 + \frac{R_L + DR_{ds,on1} + D'R_{ds,on2}}{R}} \tag{179}$$

Assuming R$_{ds,on1}$ = R$_{ds,on2}$ = R$_{ds,on}$ (if two identical transistors are utilized)

$$V = \frac{D'V_g}{(D')^2 + \frac{RL + Rds,on}{R}} \tag{180}$$

Inductor voltage current waveforms are given in Figure 23-24 as well. Switch1 (S$_1$) switch2 (S$_2$) current and voltage waveforms are shown in Figure 25-26 and Figure 27-28 respectively. Also, capacitor current voltage waveform is given in Figure 29. (ESR value of the capacitor, R$_{esr}$ is neglected at this stage.)

- For inductor;

$$L\frac{di_L}{dt} = v_L \tag{181}$$

$$L\frac{\Delta i_L}{\Delta t} = v_L \tag{182}$$

Ripple current for inductor is given as;

$$\Delta i_L = \frac{V_L}{L} D' \frac{T_{sw}}{2} \tag{183}$$

$$\Delta i_L = \frac{V_g - (R_{ds,on} + R_L)I}{2L} DT_{sw} \tag{184}$$

- For capacitor;

$$C\frac{dv_c}{dt} = i_c \tag{185}$$

$$C\frac{\Delta v_c}{\Delta t} = i_c \tag{186}$$

According to the plot of capacitor voltage waveform given above;

$$2\Delta v_c = \frac{1}{C}\frac{V}{R} DT_{sw} \tag{187}$$

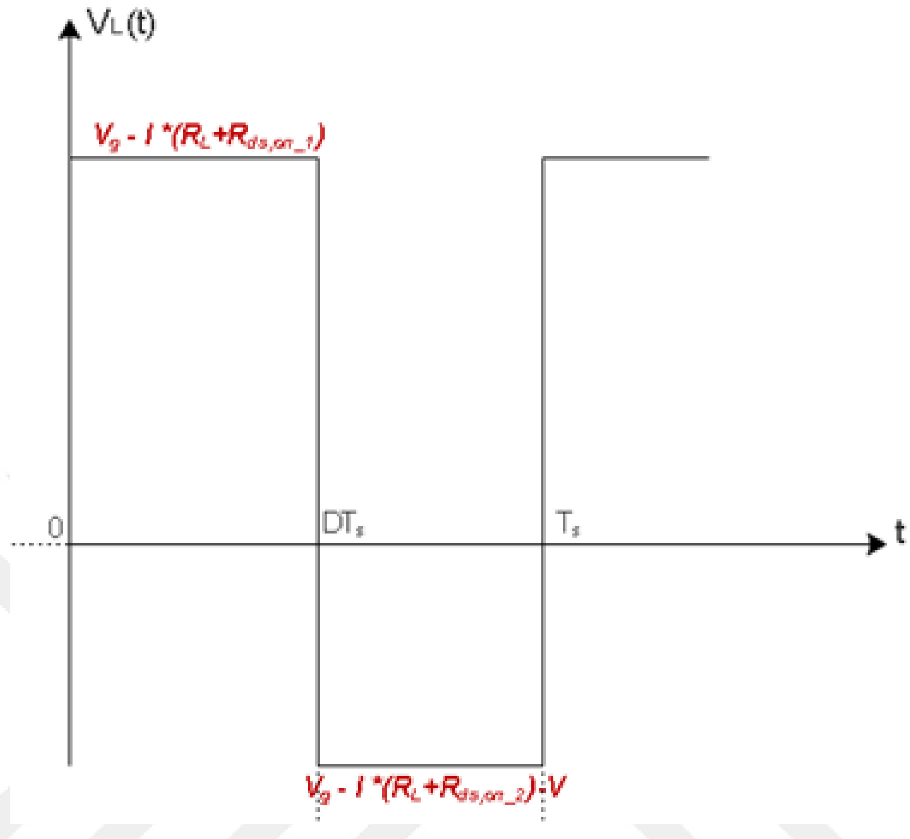

Figure 23: Inductor voltage waveform for boost converter

Ripple voltage for capacitor is given as;

$$\Delta v_c = \frac{VDT_{sw}}{2RC} \tag{188}$$

Ignoring the switching losses, efficiency of the converter is derived as;

$$\eta_d = \frac{P_{out}}{P_{in}} = \frac{V\frac{V}{R}}{V_g I_g} = \frac{VD'I}{V_g I} = \frac{VD'}{V_g} \tag{189}$$

$$\eta_d = \frac{D'V_g}{(D')^2 + \frac{R_L + R_{ds,on}}{R}} \frac{D'}{V_g} \tag{190}$$

$$\eta_d = \frac{1}{1 + \frac{R_L + R_{ds,on}}{R(D')^2}} \tag{191}$$

c. Small-Signal AC Analysis of Boost Converter

Then small signal AC analysis would be performed to investigate dynamic responses of the converter. By this analysis, effects of change in duty cycle, input

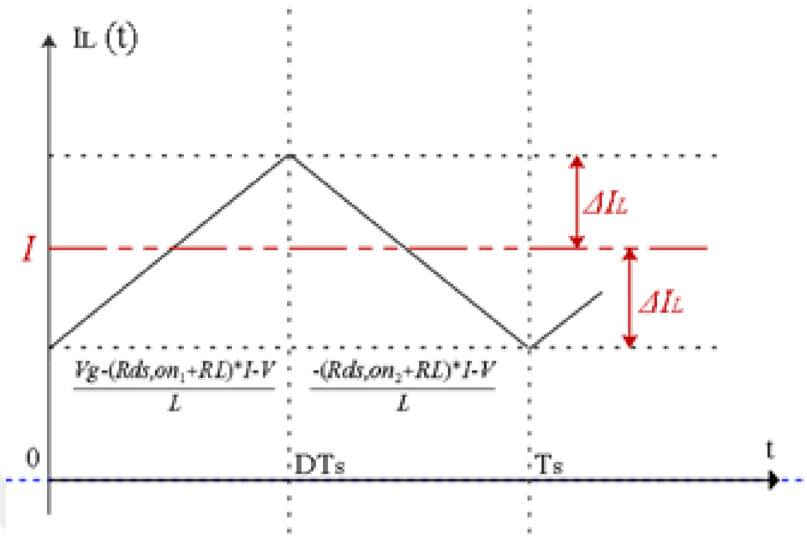

Figure 24: Inductor current waveform for boost converter

voltage/current or load current on output voltage of the converter can be analyzed. Also load is assumed to be resistive for simplicity when the analysis is performed. The parameters, expressed as average values already, given in the steady state equations for the non-ideal synchronous boost converter can be seperated to their large DC components and perturbated AC components as shown below, assuming $R_{ds,on1} = R_{ds,on2} = R_{ds,on}$.

$$L\frac{d}{dt}(I+\hat{i}) = (V_g+\hat{v_g}) - (I+\hat{i})(R_L+R_{ds,on}) - (V+\hat{v})(D'-\hat{d}) \tag{192}$$

$$C\frac{d}{dt}(V_c+\hat{v_c}) = (D'-\hat{d})(I+\hat{i}) - \frac{(V+\hat{v})}{R} \tag{193}$$

$$(I_g+\hat{i_g}) = (I+\hat{i}) \tag{194}$$

$$(V+\hat{v}) = (V_c+\hat{v_c}) + R_{esr}(I_c+\hat{i_c}) \tag{195}$$

Seperating terms related to AC small signal components and neglecting second order AC terms ("$\hat{v_g}\hat{d}$" or "$\hat{i}\hat{d}$");

$$L\frac{d}{dt}\hat{i} = \hat{v_g} - \hat{i}(R_L+R_{ds,on}) + V\hat{d} - D'\hat{v} \tag{196}$$

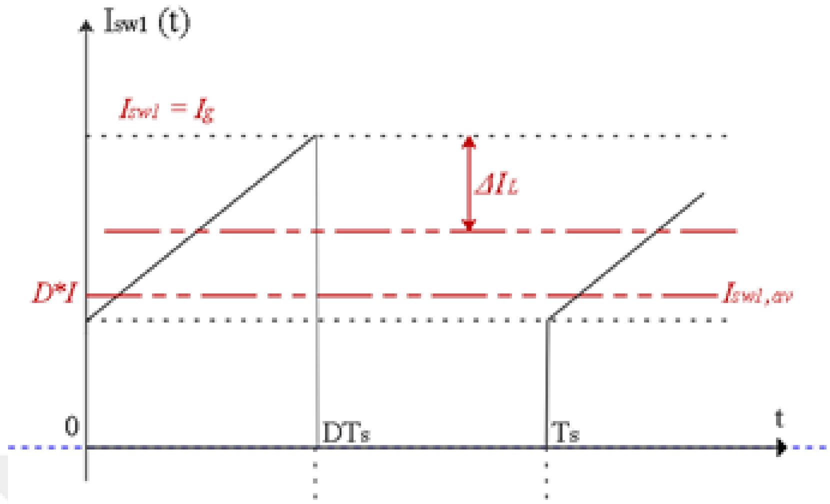

Figure 25: Switch 1, S_1 current waveform for boost converter

$$C\frac{d}{dt}\hat{v}_c = \hat{i}_c = D'\hat{i} - I\hat{d} - \frac{\hat{v}}{R} \tag{197}$$

$$\hat{i}_g = \hat{i} \tag{198}$$

$$\hat{v} = \hat{v}_c + R_{esr}\hat{i}_c \tag{199}$$

To investigate effect of small signal perturbation of duty cycle, $\hat{d}$ at output voltage, $\hat{v}$ assuming all other variables are constant and equal to their exact dc values for the converter ($\hat{v}_g = 0$, $\hat{i}_{load} = 0$) transfer function for control-to-output, G_{vd} can be derived. Firstly, rearranging the related equations for the assumption in s- domain;

$$sL\hat{i} = -\hat{i}(R_L + R_{ds,on}) + V\hat{d} - D'\hat{v} \tag{200}$$

$$sC\hat{v}_c = \hat{i}_c = D'\hat{i} - I\hat{d} - \frac{\hat{v}}{R} \tag{201}$$

$$\hat{v} = \hat{v}_c + R_{esr}\hat{i}_c \tag{202}$$

Making some manipulations from the equations given above, an expression for the relation between small signal output voltage, $\hat{v}$ and duty cycle, $\hat{d}$ would be defined. Then control-to-output transfer function, $G_{vd}(s)$ for the converter is given as;

$$G_{vd}(s) = \frac{D'(1 + sCR_{esr})(V - I(\frac{sL+R_e}{D'}))}{(\frac{LC(R+R_{esr})}{R})s^2 + (\frac{RR_eC+R_{esr}R_eC+R_{esr}RC(D')^2+L}{R})s + (\frac{R_e}{R} + (D')^2)} \tag{203}$$

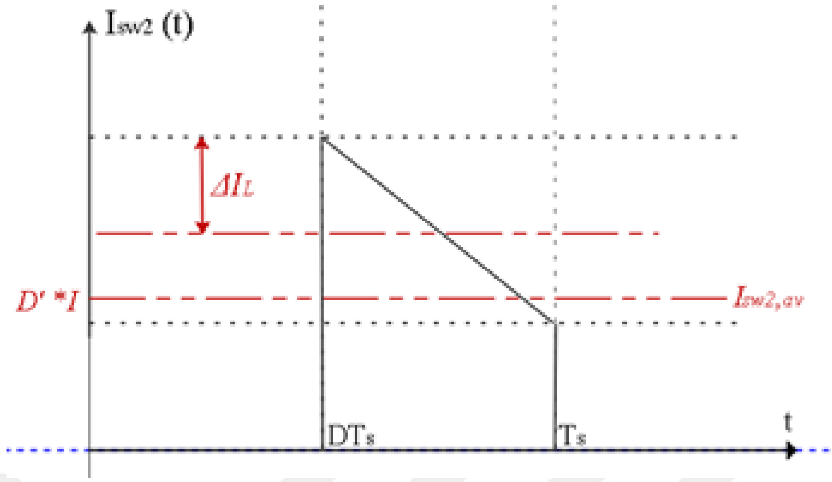

Figure 26: Switch 2, S_2 current waveform for boost converter

where

$$R_e = R_L + R_{ds,on} \tag{204}$$

To investigate effect of small signal perturbation of duty cycle, $\hat{d}$ at inductor current, $\hat{i}$ transfer function for control-to-inductor current, G_{id} can also be derived using the same equations given in (210),(211) and (212)

$$G_{id}(s) = \frac{2\frac{V}{R}(1 + sC(\frac{R}{2} + R_{esr}))}{(\frac{LC(R+R_{esr})}{R})s^2 + (\frac{RR_eC+R_{esr}R_eC+R_{esr}RC(D')^2+L}{R})s + (\frac{R_e}{R} + (D')^2)} \tag{205}$$

To investigate effect of small signal perturbation of line voltage, $\hat{v}_g$ at output voltage, $\hat{v}$ assuming all other variables are constant and equal to their exact dc values for the converter ($\hat{d} = 0$, $\hat{i_{load}} = 0$) transfer function for control-to-output, G_{vg} can be derived. Firstly, rearranging the related equations for the assumption in s- domain;

$$sL\hat{i} = \hat{v}_g - \hat{i}(R_L + R_{ds,on}) - D'\hat{v} \tag{206}$$

$$sC\hat{v}_c = \hat{i_c} = D'\hat{i} - \frac{\hat{v}}{R} \tag{207}$$

$$\hat{v} = \hat{v}_c + R_{esr}\hat{i_c} \tag{208}$$

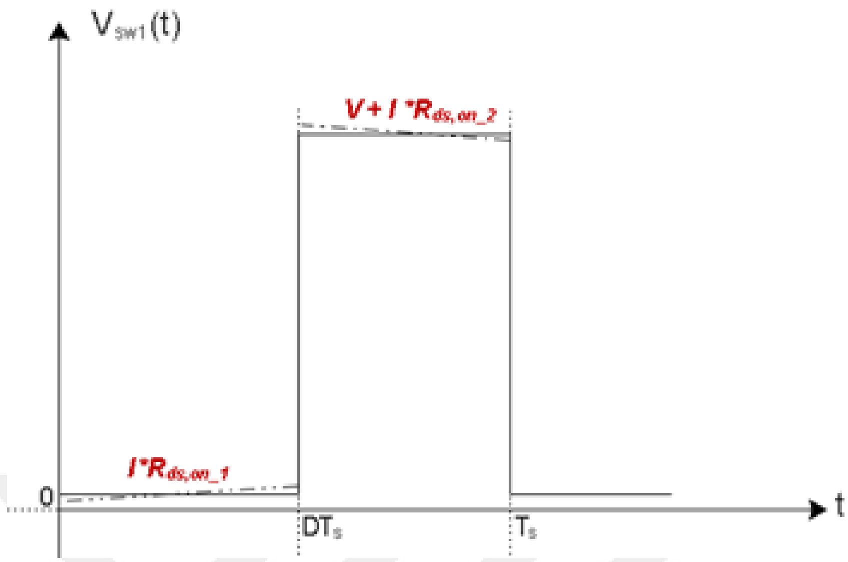

Figure 27: Switch 1, S_1 voltage waveform for boost converter

Making some manipulations from the equations given above, an expression for the relation between small signal output voltage, $\hat{v}$ and line voltage, $\hat{v_g}$ would be defined. Then line-to-output transfer function, $G_{vg}(s)$ for the converter is given as;

$$G_{vg}(s) = \frac{D'(1 + sCR_{esr})}{(\frac{LC(R+R_{esr})}{R})s^2 + (\frac{RR_eC+R_{esr}R_eC+R_{esr}RC(D')^2+L}{R})s + (\frac{R_e}{R} + (D')^2)} \tag{209}$$

To investigate effect of small signal perturbation of line voltage, $\hat{v_g}$ at inductor current, $\hat{i}$ transfer function for line-to-inductor current, G_{ig} can also be derived using the equation given in (216),(217) and (218);

$$G_{ig}(s) = \frac{\frac{1}{R}(1 + sC(R + R_{esr}))}{(\frac{LC(R+R_{esr})}{R})s^2 + (\frac{RR_eC+R_{esr}R_eC+R_{esr}RC(D')^2+L}{R})s + (\frac{R_e}{R} + (D')^2)} \tag{210}$$

To investigate effect of small signal perturbation of load current, $\hat{i_{load}}$ at output voltage, $\hat{v}$ assuming all other variables are constant and equal to their exact dc values for the converter ($\hat{d} = 0$ and $\hat{v_g} = 0$) transfer function for load-to-output (output impedance), Z_{out} can be derived. Perturbation of load current is assumed to be

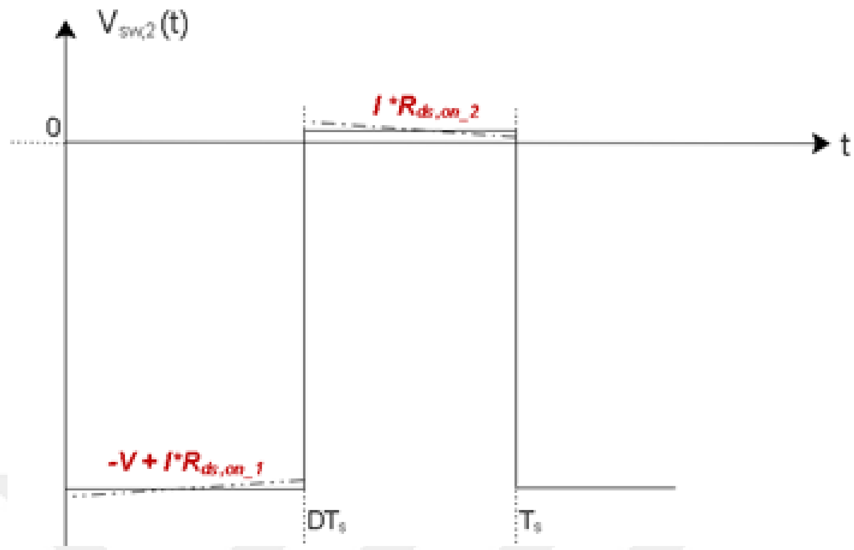

Figure 28: Switch 2, S_2 voltage waveform for boost converter

similar to that as shown in Figure 20 again. Then rearranging the related equations for the assumption in s- domain;

$$sL\hat{i} = -\hat{i}(R_L + R_{ds,on}) - D'\hat{v} \tag{211}$$

$$sC\hat{v}_c = \hat{i}_c = D'\hat{i} - \frac{\hat{v}}{R} - i_{\hat{load}} \tag{212}$$

$$\hat{v} = \hat{v}_c + R_{esr}\hat{i}_c \tag{213}$$

Making some manipulations from the equations given above, an expression for the relation between small signal output voltage, $\hat{v}$ and load current, $i_{\hat{load}}$ would be defined. Then load-to-output (output impedance) transfer function, Z_{out}(s) for the converter is given as;

$$Z_{out}(s) = \frac{-(1 + sCR_{esr})(sL + R_e)}{(\frac{LC(R+R_{esr})}{R})s^2 + (\frac{RR_eC+R_{esr}R_eC+R_{esr}RC(D')^2+L}{R})s + (\frac{R_e}{R} + (D')^2)} \tag{214}$$

To investigate effect of small signal perturbation of load current, $i_{\hat{load}}$ at inductor current, $\hat{i}$ transfer function for load-to-inductor current, G_{iz} can be derived in the same way as done previously in deriving control-to-inductor current transfer function, G_{id}

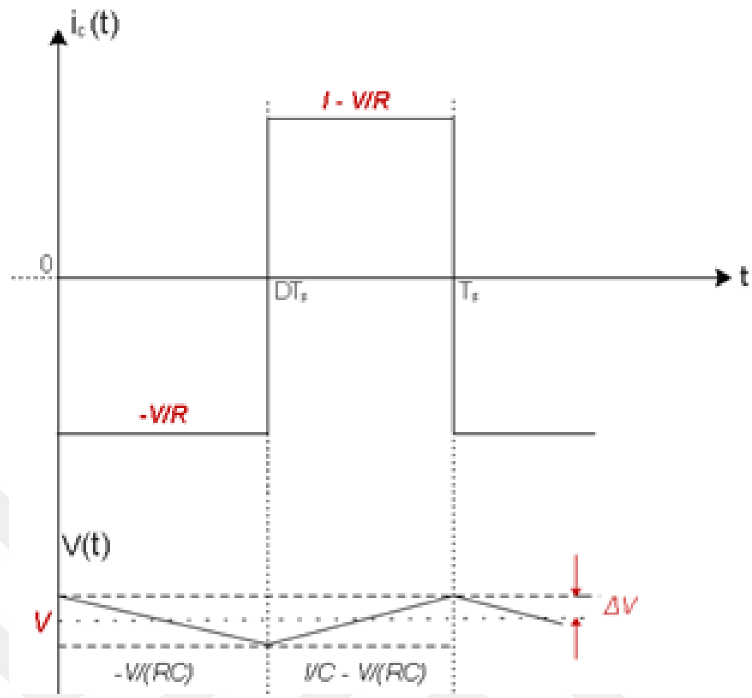

Figure 29: Capacitor current voltage waveform for boost converter

and line-to-inductor current transfer function, G_{ig}. Then load-to-inductor current transfer function, $G_{iz}(s)$ for the converter is derived as;

$$G_{iz}(s) = \frac{D'(1 + sCR_{esr}))}{(\frac{LC(R+R_{esr})}{R})s^2 + (\frac{RR_eC+R_{esr}R_eC+R_{esr}RC(D')^2+L}{R})s + (\frac{R_e}{R} + (D')^2)} \tag{215}$$

The transfer functions derived using small signal analysis in this section are to be used to investigate or gain insight about closed-loop performance and stability of the bidirectional DC/DC converter, which is able to operate as a buck or boost converter depending on the direction of the power flow, as a part of the electric vehicle charger to be developed [38, 39].

2.2 Electric Vehicle Charger Topologies

A battery charger is expected to be efficient and reliable enough providing high power density compared to its low size and weight. The operation of a charger depends on converter topology used, components on it, switching and control algorithm as well. Electric vehicle battery chargers mostly contain a boost converter stage for power factor correction (PFC). Also, for some charger topologies interleaving is proposed to reduce current ripple and inductor size [7, 10, 15]. There are various types of topologies for electric vehicle (EV) charger circuits connected to a single-phase or three-phase power grid depending on power ratings and area of utilization.

Interleaved unidirectional charger topology is a unidirectional configuration with two boost converters in parallel operating 180 out of phase. It consists of paralleled semiconductors providing reduced stress on output capacitor with ripple cancellation at the output [7 ,10 ,15]. However, maximum power level is mostly limited to 3.5 kW for this type chargers since they must provide heat management for the input bridge rectifier [7].

Three level diode-clamped bidirectional charger topology consisting of DC-DC converter and providing low switch voltage stress, reduced component sizes or switching frequency is shown in Figure 30. It is suitable for high power charging applications and can provide power quality in high level at input mains with reduced THD, high power factor and reduced EMI noise leading to ripple-free, regulated DC output voltage. However, its complexity and additional components increse the cost and require more complicated control circuitry [7].

Three-phase full-bridge bidirectional charger topology having more components and higher cost with lower component stresses compared to single-phase one is shown in Figure 31 [7, 40, 41].

An onboard unidirectional full-bridge series resonant charger topology consists of a diode bridge rectifier in conjunction with a filter, PFC stage and resonant DC-DC converter. To limit cost, weight, size and losses for the converter this type of chargers are mostly implemented in a single stage as well [7].

A non-isolated bidirectional two-quadrant charger topology includes an AC-DC

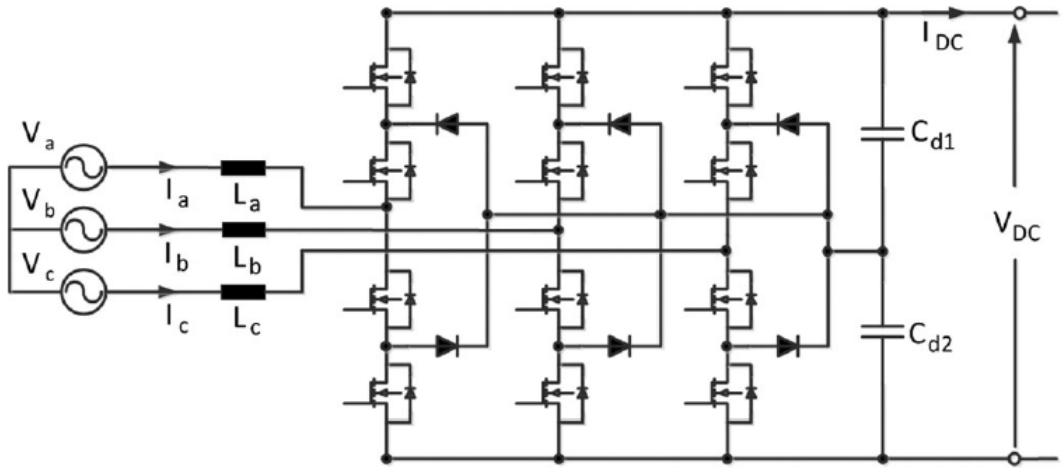

Figure 30: Three-level diode-clamped bidirectional charger topology [7].

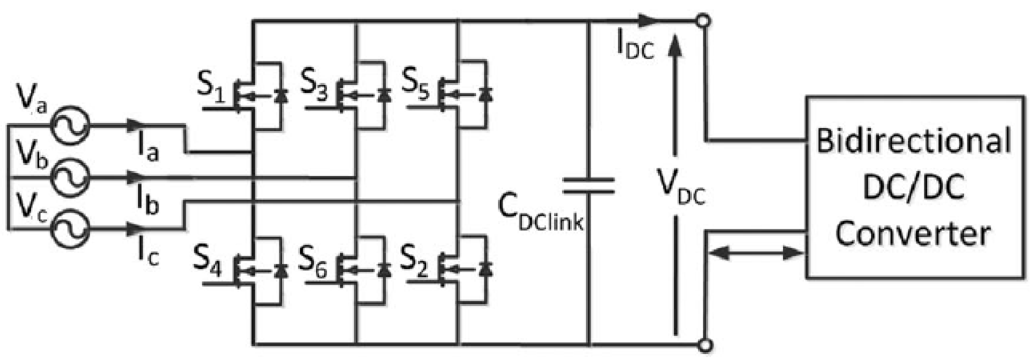

Figure 31: Three-phase full-bridge bidirectional charger topology [7].

converter that enforces power factor and a bi-directional DC-DC converter for regulation of battery current [7, 42]. It has two switches simplifying control circuitry but two inductors with high-current ratings that may be bulky and expensive. Moreover DC-DC converter can operate as a buck or boost converter depending on the direction of power flow. Thus it provides high power density and robust control while causing cost to increase due to large number of components [7].

The circuit topology of the Swiss front-end charger consisting of an active AC-DC front-end converter that sets up parallel DC-DC converter connections inherently is given in Figure 32. It is advantageous thanks to the mains frequency commutation of switches leading to negligible switching losses. Therefore it can provide an onboard charger with reduced size, low weight and high efficiency [14].

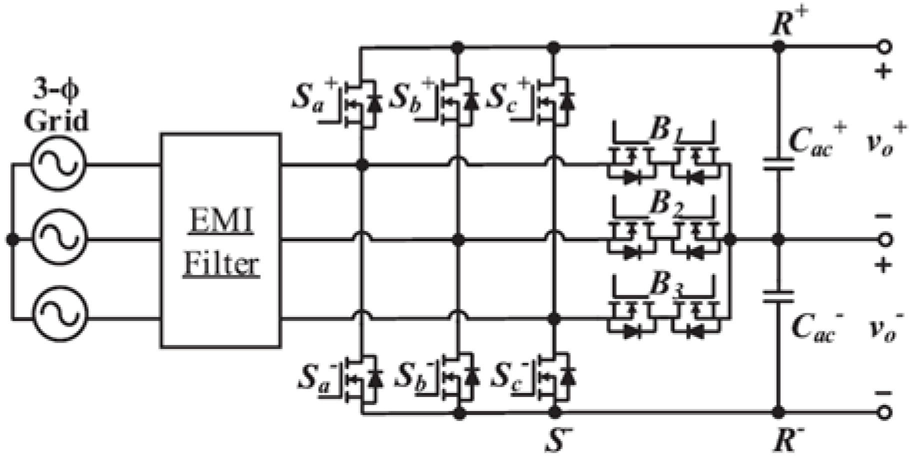

Figure 32: Swiss front-end charger topology [14].

A fast charger topology proposed with AC/DC interleaved three-phase active rectifiers and DC/DC interleaved three-phase choppers (6 x two-level three phase converters in total) is shown in Figure 33. The EV charger with this configuration provides balanced power sharing among each three phase converter (3 x three phase rectifier and 3 x three phase choppper), robustness, low implementation cost or wide range of modulation for switching. Also, it can be upgraded to higher power ratings easily thanks to its homogenous structure and employment of identical modules [9].

The circuit topology of a three phase bidirectional voltage source inverter (VSI) charger is given in Figure 34. The charger consists of a battery bank connected to a DC-DC bidirectional converter and a three phase VSI connected to the power grid. Moreover, LCL filter is inserted between the inverter and the grid to reduce line current harmonics [43, 44]. DC-DC converter can operate as a buck or boost converter depending on the direction of power flow too [35] so the bidirectional VSI charger circuit also enables power transfer from the battery pack to the electricity grid

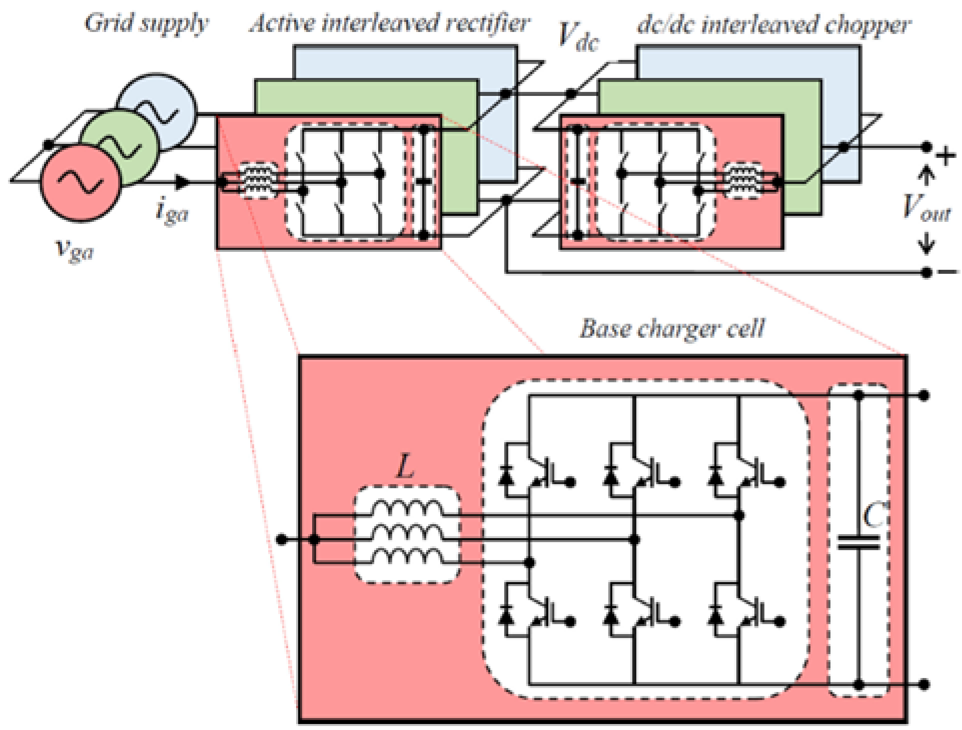

Figure 33: Three-phase interleaved fast charger topology [9].

for mostly reactive power support. Also this EV charger topology is the proposed topology in this thesis for modeling, simulation and analysis of its impacts on the electricity grid and vehicle battery.

2.3 Electric Vehicle Battery Technologies

To energize electric vehicles (EV) or plug-in hybrid electric vehicles (PHEV), energy storage devices providing power source to the vehicle are needed. These devices can be batteries, supercapacitors, ultracapacitors or flywheels. Batteries used in EVs or PHEVs are generally charged by utility power grid. Batteries consist of cells basically. Combination of several cells forms a battery module and that of several modules constitutes a battery pack. In industry, modules consisting of cells are typically 12 V automotive batteries and battery packs made by series and parallel connection of modules are mostly 240 V nominal packs [6].

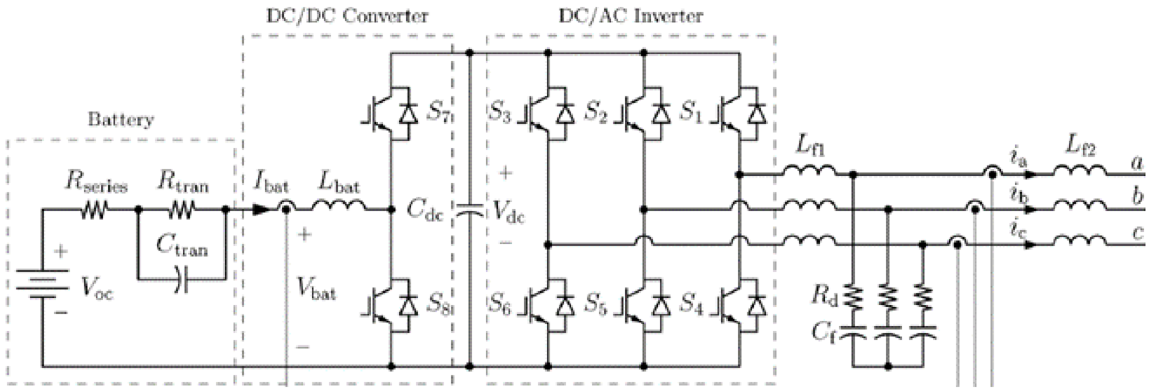

Figure 34: Three-phase bidirectional VSI charger topology [43].

Battery capacity is the amount of charge that a battery can supply before it is fully-discharged that means the voltage falls to a specified value for lower than which it is not able to provide any charge to a load. Unit of battery capacity is the coulomb (C) that is ampere-second or ampere-hour (Ah). Hence unit of Ah is equal to 3600 C. "C-rate" is a term regarding battery charge or discharge process and can be defined as current charging a fully-discharged battery to its rated Ah during charging process, or discharging a fully-charged battery to its completely discharged condition during discharging one.

Energy stored in a battery depends on terminal voltage and the amount of charge stored within it and is defined as (as long as the voltage is not varying substantially);

$$E(Wh) = Ah\ V \tag{216}$$

State of charge (SOC) is the amount of charge a battery has at a particular moment compared to the rated charge of the battery. SOC can be determined by two methods: Amp-hour balancing and EMF based direct measurement. Depth of discharge (DOD) is the amount of depletion the battery has during discharging. Moreover allowable DOD depends on battery chemistry and the usage pattern. While specific power is defined as the rated power of the battery for a given weight or size/volume of the battery, specific energy is energy of the battery for a given weight or size/volume of the battery [1, 6]. Also, the comparison of various devices in terms of specific energy is given in Table 1.

Table 1: The comparison of various devices based on specific energy [6].

Energy source	**Specific energy (Wh/kg)**
Gasoline	12500
Natural gas	9350
Methanol	6200
Hydrogen	28000
Coal	8200
Lead acid battery	35
Nickel metal hydride battery	50
Lithium-polymer battery	200
Lithium-ion battery	120
Sodium sulfur battery	150-300
Flywheel (steel)	12-30
Flywheel (carbon fiber)	30
Ultracapacitor	3.3

Cell voltage is voltage across a battery cell which depends on SOC, age, temperature and charge/discharge rate of the battery. It is mostly defined as rated voltage, that is average voltage over a full discharge cycle, as well [45]. The rated cell voltage ratings of various types of batteries are shown in Table 2. Moreover discharge curves showing change of cell voltage according to capacity for a 33.3 Ah Li-ion battery cell is given in Figure 35.

Battery management is to control the battery current, charge-discharge mechanism, battery voltage and environmental conditions such as ambient temperature or humidity around the battery. It mostly includes data acquisition of temperature, voltage, current, humidity etc via various sensors. It is noted that data acquisition does not cost much while matrix switches for power electronics interface to control charging/discharging may be expensive [6].

Table 2: Cell voltage values of various types of batteries [45].

Chemistry	Symbol	Cell voltage (V)
Lead-acid	PbA	2
Nickel-metal hydride	NiMh	1.2
Lithium-ion	Li-ion	3.8
Lithium-titanate	LiT	2.5
Alkaline	$ZnMnO_2$	1.5

There are various types of battery technologies used in the industry. Lead-acid battery is utilized in automotive industry extensively for starting the engine of vehicle and providing supply for auxiliary loads when the engine is not running. Nickel metal hydride battery is utilized in some hybrid electric vehicles. Lithium-ion batteries can be made with very high energy density and do not have the "memory effect" causing some of the other rechargable batteries to lose their maximum charge level when charged/discharged repeatedly to various capacities which are different from fully rated one. Also this type of batteries impacts environment less compared to the other batteries do. Li-ion batteries have much lower discharge rate than lead-acid ones do, higher efficiency and specific power value (power rating per volume) so they are quite suitable for automotive applications where space is restricted. All of these advantages Li-ion batteries have enable wide usage of them in automotive industry eventhough lead-acid batteries are mostly preferred energy storage device due to their lower cost and safety concerns. However, overcharging or overdischarging Li-ion batteries can cause serious damage on the plates within them or explosions so the life time of these batteries would reduce more compared to that of lead-acid ones [6]. The comparison of energy storage technologies is summarized in Table 3.

Generally batteries accept particular charge current when discharged depending on voltage or SOC at which they are charging. Also charging current may be reduced to ensure the proper charging voltage is applied to the battery when it reaches to a

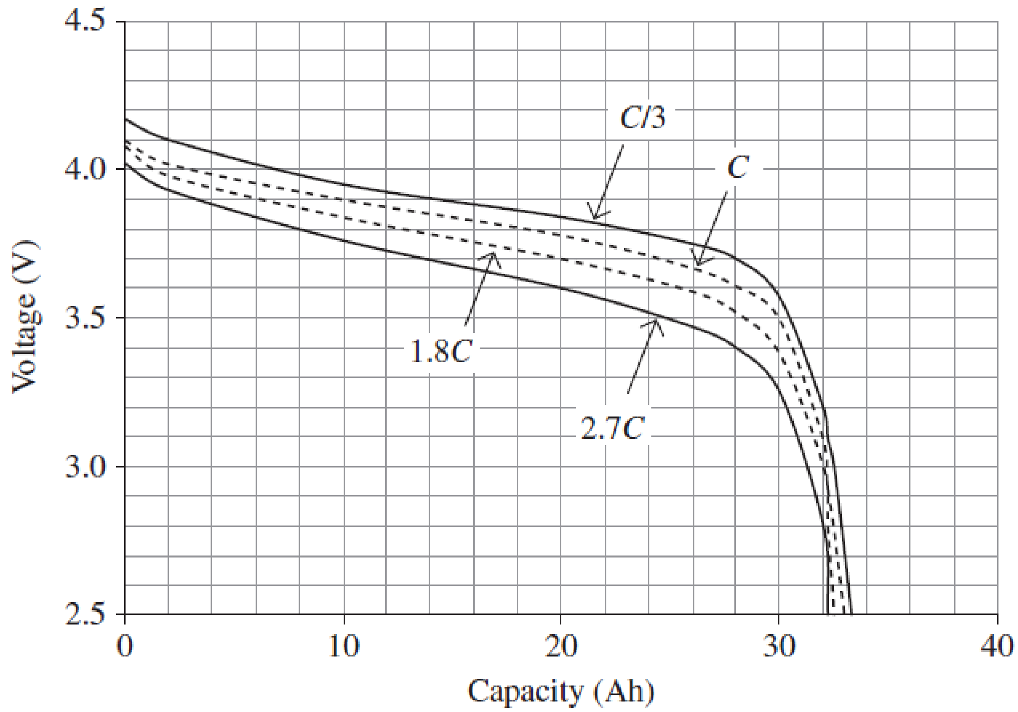

Figure 35: Discharge curves for a 33.3Ah li-ion battery cell with various ratings [45].

certain voltage or SOC value in most applications. It can be said that all types of batteries have a similar charging profile. As an example,the typical charging profile for a Li-ion battery is given in Figure 36. From the figure, the battery charges with a constant current initially when it is fully discharged and voltage increases. The current is reduced when the battery reaches to a particular SOC value, generally around 80 %, or voltage value to ensure that a specific charging voltage would be applied to the battery. After that the charging current is tapered to maintain the constant desired voltage for the battery [45]. This type of charging process is known as constant current-constant voltage (CC-CV) charging as well.

Terminal voltage and current of a battery pack can be determined once the corresponding cell voltage and current values are known [45]. An equivalent circuit of a battery pack consisting of modules connected in series and parallel is shown in Figure 37, for which N_{ser} is the number of cells connected in series for each string of

Table 3: The comparison of energy storage devices [6].

Storage technology	Cycle life	Efficiency (%)	Specific power (W/kg)
Lead-acid battery	500-800	50-92	180
Li-ion polymer battery	500-1000	80-90	>3000
NiMH battery	500-1000	66	250-1000
Ultracapacitor	1000000	90	1000-9000

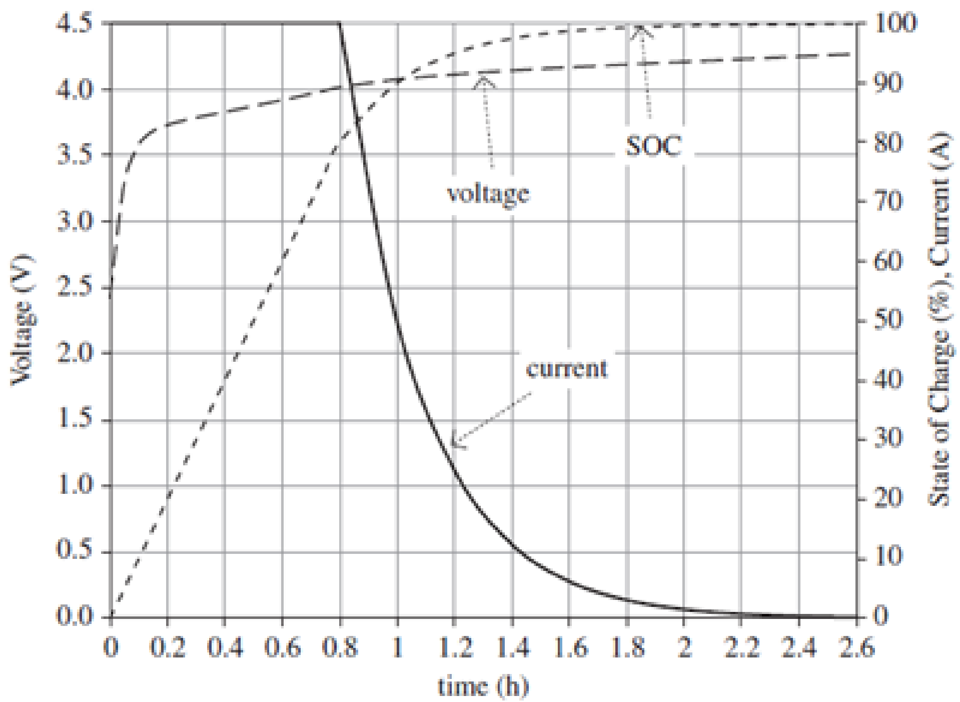

Figure 36: Typical charging profile for a Li-ion battery [45].

the battery pack, N_{par} is the number of strings connected in parallel of the battery pack, V_b represents the cell voltage, I_b corresponds the cell current, V_{bp} is battery pack voltage, $V_{bp(nl)}$ is no load battery pack terminal voltage, I_{bp} is the battery pack current and R_{bp} defines the series internal resistance of the battery pack.

The relationship between battery pack voltage, V_{bp} and cell voltage, V_b can be defined as;

$$V_{bp} = N_{ser} V_b \tag{217}$$

A similar relationship between battery pack current, I_{bp} and cell current, I_b is

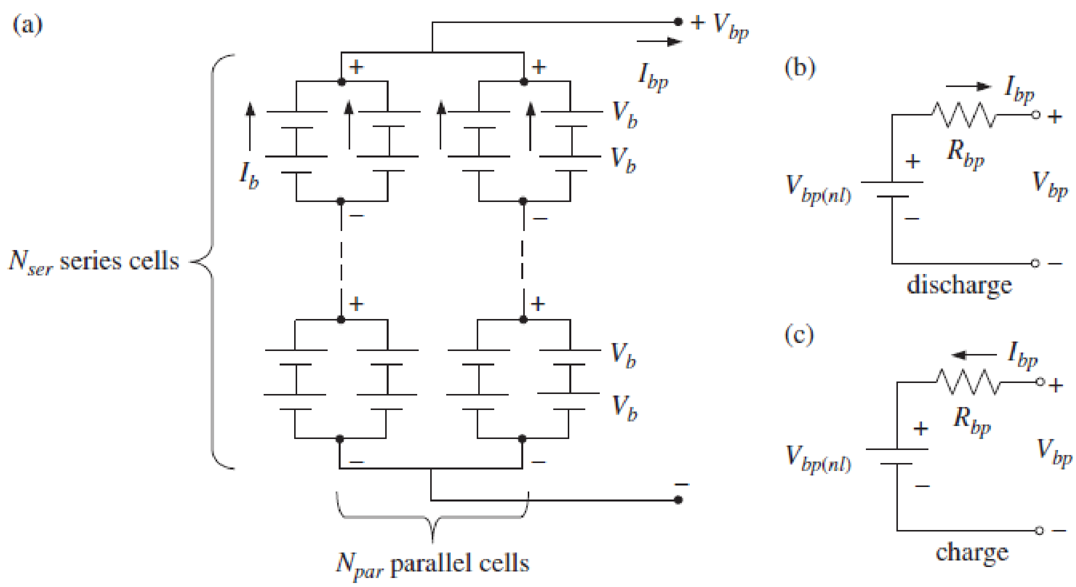

Figure 37: Equivalent circuit of a battery pack: (a) series and parallel connection of modules constituting a battery pack, (b) equivalent simplified circuit for discharging or (c) charging [45].

given as;

$$I_{bp} = N_{par} I_b \tag{218}$$

Moreover the battery pack resistance, Rbp is related by cell resistance, Rb by;

$$R_{bp} = \frac{N_{ser}}{N_{par}} R_b \tag{219}$$

The efficiency of battery pack during discharging, ζ_{dis} is given by;

$$\zeta_{dis} = \frac{V_{bp} I_{bp}}{V_{bp} I_{bp} + R_{bp} I_{bp}^2} = \frac{V_{bp}}{V_{bp(nl)}} \tag{220}$$

That during charging, ζ_{ch} is given by;

$$\zeta_{ch} = \frac{V_{bp} I_{bp} - R_{bp} I_{bp}^2}{V_{bp} I_{bp}} = \frac{V_{bp(nl)}}{V_{bp}} \tag{221}$$

2.4 Clark-Park Transform and Phase-Locked Loop (PLL)

Three-phase PWM converters include three source voltage (or line current) vectors, separated by 120° from each other, in the phasor domain. The phase vectors are defined as:

$$f_a = F_m cos(\omega t + \phi) \tag{222}$$

$$f_b = F_m cos(\omega t + \phi - 120°) \tag{223}$$

$$f_c = F_m cos(\omega t + \phi - 240°) \tag{224}$$

f_a, f_b & f_c represents “a”,”b” & ”c” components for the vector of three phase system (a-b-c), respectively. F_m is the amplitude of vector of three phase system, ω_e is the fundamental angular frequency and ϕ is the phase angle.

Defining;

$$\theta = \omega_e t + \phi \tag{225}$$

Inserting (225) into (222)-(224);

$$f_a = F_m cos(\theta_e) \tag{226}$$

$$f_b = F_m cos(\theta_e - 120°) \tag{227}$$

$$f_c = F_m cos(\theta_e - 240°) \tag{228}$$

Defining;

$$\alpha = e^{j120°} = cos(120°) + jsin(120°) \tag{229}$$

$$\alpha^2 = e^{j240°} = cos(240°) + jsin(240°) \tag{230}$$

Arranging and making some manipulations;

$$f_b\alpha = f_b(cos(120°) + jsin(120°)) = (-\frac{1}{2} + j\frac{\sqrt{3}}{2})f_b \tag{231}$$

$$f_c\alpha^2 = f_c(cos(240°) + jsin(240°)) = (-\frac{1}{2} - j\frac{\sqrt{3}}{2})f_c \tag{232}$$

$$f_{qds} = f_a + \alpha f_b + \alpha^2 f_c = \frac{2}{3}(f_a - \frac{1}{2}(f_b + f_c) + j\frac{\sqrt{3}}{2}(f_b - f_c)) \tag{233}$$

f_{qds} represent the vector of two phase system in stationary frame (qs-ds).

From (231)-(233), the following expression is derived in matrix form.

$$\begin{bmatrix} f_{qs} \\ f_{ds} \end{bmatrix} = \frac{2}{3} \begin{bmatrix} 1 & -\frac{1}{2} & -\frac{1}{2} \\ 0 & \frac{\sqrt{3}}{2} & -\frac{\sqrt{3}}{2} \end{bmatrix} \begin{bmatrix} f_a \\ f_b \\ f_c \end{bmatrix} \tag{234}$$

f$_{qs}$ & f$_{ds}$ are "q" and "d" component vectors of two phase system in stationary frame (qs-ds), respectively.

Making some manipulations for (227) & (228);

$$f_b = F_m cos(\theta_e - 120°) \tag{235}$$

$$f_b = F_m(cos(\theta_e)cos(120°) + sin(\theta_e)sin(120°)) \tag{236}$$

$$f_b = F_m(-\frac{1}{2}cos(\theta_e) + \frac{\sqrt{3}}{2}sin(\theta_e)) \tag{237}$$

$$f_c = F_m cos(\theta_e - 240°) \tag{238}$$

$$f_c = F_m(cos(\theta_e)cos(240°) + sin(\theta_e)sin(240°)) \tag{239}$$

$$f_c = F_m(-\frac{1}{2}cos(\theta_e) - \frac{\sqrt{3}}{2}sin(\theta_e)) \tag{240}$$

$$f_b + f_c = F_m(-cos(\theta_e)) = -F_m cos(\theta_e) \tag{241}$$

$$f_b - f_c = \sqrt{3}F_m sin(\theta_e) \tag{242}$$

Inserting (226),(241) and (242) into (233);

$$f_{qds} = \frac{2}{3}(F_m cos(\theta_e) - \frac{1}{2}(-F_m cos(\theta_e)) + j\frac{\sqrt{3}}{2}(\sqrt{3}F_m sin(\theta_e))) \tag{243}$$

$$f_{qds} = \frac{2}{3}(\frac{3}{2}(F_m cos(\theta_e)) + j\frac{3}{2}(F_m sin(\theta_e))) \tag{244}$$

$$f_{qds} = F_m cos(\theta_e) + jF_m sin(\theta_e) \tag{245}$$

Magnitude of f$_{qds}$ vector can be expressed as;

$$|f_{qds}| = \sqrt{F_m^2 cos^2(\theta_e) + F_m^2 sin^2(\theta_e)} \tag{246}$$

$$|f_{qds}| = \sqrt{F_m^2 [cos^2(\theta_e) + sin^2(\theta_e)]} \tag{247}$$

$$|f_{qds}| = F_m \tag{248}$$

The vector diagram of f$_{qds}$ with its q-d components is given in Figure 38.

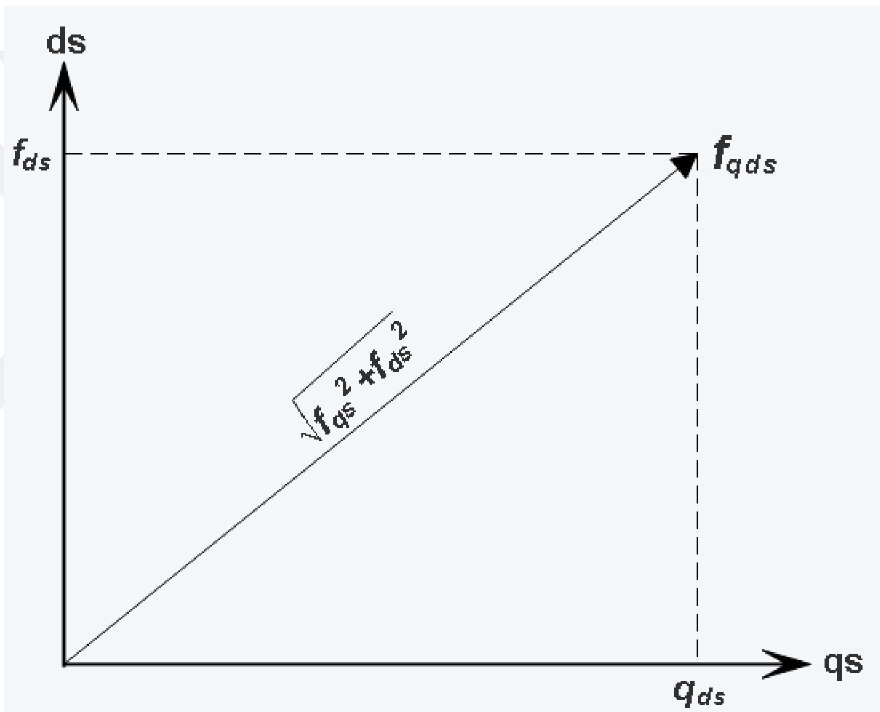

Figure 38: Vector diagram of f$_{qds}$

Transformation from three phase system (a-b-c) to stationary two phase system (d$_s$-q$_s$) can be illustrated using voltage equations for three phase PWM rectifier. General circuit diagram for three phase front-end converter (FEC) is shown in Figure 39.

Three phase voltage equations for the front-end converter are given below.

$$V_{sa} = Ri_a + L\frac{di_a}{dt} + V_{ia} \tag{249}$$

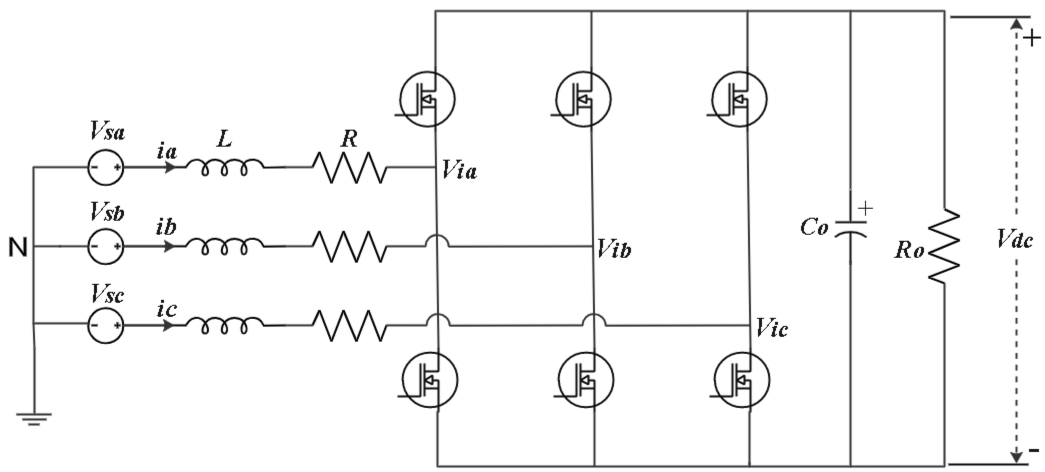

Figure 39: Circuit diagram of three phase front-end converter

$$V_{sb} = Ri_b + L\frac{di_b}{dt} + V_{ib} \tag{250}$$

$$V_{sc} = Ri_c + L\frac{di_c}{dt} + V_{ic} \tag{251}$$

The voltage equations of the converter in two phase stationary reference frame (q_s-d_s) are given below as well.

$$V_{sqds} = Ri_{qds} + L\frac{di_{qds}}{dt} + V_{iqds} \tag{252}$$

V_{sqds} & i_{qds} represent source voltage and line current vector of two phase system in stationary frame (q_s-d_s) respectively.

Real and imaginary parts of the equation given in (252) can be seperated as;

$$V_{sqs} = Ri_{qs} + L\frac{di_{qs}}{dt} + V_{iqs}\ (Real) \tag{253}$$

$$V_{sds} = Ri_{ds} + L\frac{di_{ds}}{dt} + V_{ids}\ (Imagine) \tag{254}$$

Assuming two phase stationary system (q_s-d_s) rotates with an angular frequency of "ω_e" in clockwise direction corresponding an angular position of "θ_e" with a phase angle of "ϕ" ($\theta_e = \omega_e t+\phi$), a two phase system with rotating frame can be obtained.

$$f_{qds} = F_m e^{j\theta_e} = F_m e^{j(\omega_e t+\phi)}\ (stationary) \tag{255}$$

$$f_{qde} = f_{qds} e^{j\theta_e} = F_m e^{j\theta_e} e^{-j\theta_e} \ (rotating) \tag{256}$$

$$f_{qde} = F_m \tag{257}$$

f_{qde} is the vector of two phase system in rotating frame (q_e-d_e) with "$\phi = 0°$".

Transformation from stationary frame to rotating frame in two phase system (q-d) is shown in Figure 40.

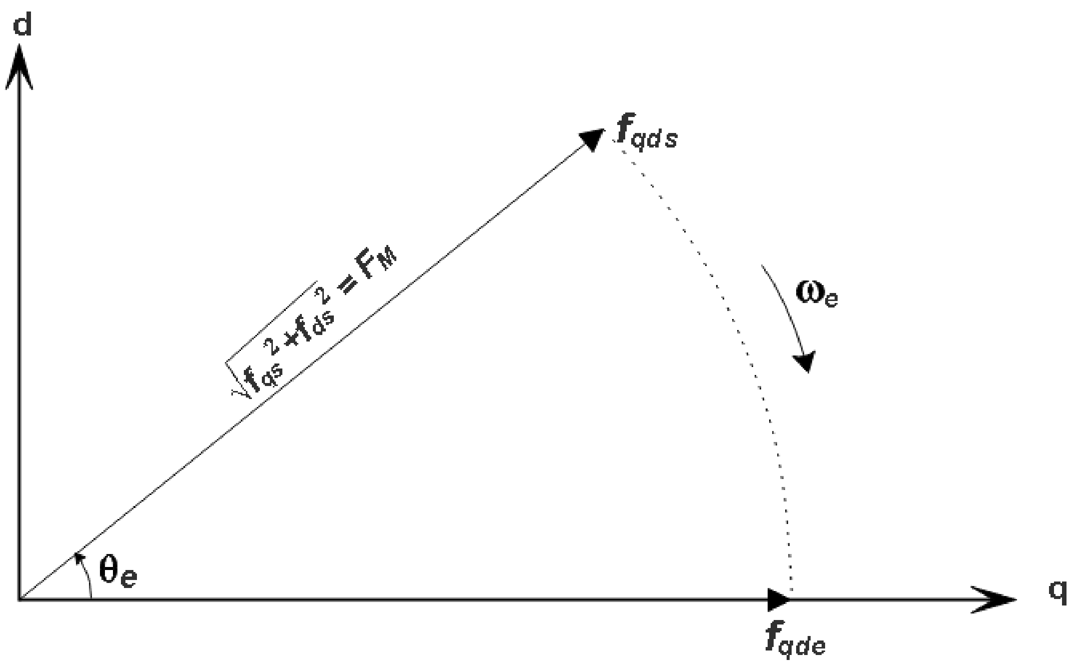

Figure 40: Transformation from stationary frame to rotating frame in two phase system (Vector of "f_{qds}" to vector of "f_{qde}")

To obtain the voltage equations of the converter in two phase rotating reference frame (q_e-d_e), the equation for the stationary reference frame (q_s-d_s) given in (252) is multiplied by "$e^{-j\theta_e}$"

$$V_{sqds} e^{-j\theta_e} = R i_{qds} e^{-j\theta_e} + L \frac{di_{qds}}{dt} e^{-j\theta_e} + V_{iqds} e^{-j\theta_e} \tag{258}$$

An equation can be derived for the term "$L\frac{di_{qds}}{dt}e^{-j\theta_e}$" as shown below.

$$L\frac{d}{dt}[i_{qds}e^{-j\theta_e}] = L\frac{di_{qds}}{dt}e^{-j\theta_e} + i_{qds}L\frac{d}{dt}(-j\theta_e)e^{-j\theta_e} \tag{259}$$

$$L\frac{d}{dt}[i_{qds}e^{-j\theta_e}] = L\frac{d}{dt}i_{qds}e^{-j\theta_e} - j\omega_e Li_{qds}e^{-j\theta_e} \tag{260}$$

$$L\frac{di_{qds}}{dt}e^{-j\theta_e} = L\frac{d}{dt}i_{qde} - j\omega_e Li_{qde} \tag{261}$$

Inserting (261) into (258);

$$V_{sqde} = Ri_{qde} + L\frac{di_{qde}}{dt} - j\omega_e Li_{qde} + V_{iqde} \tag{262}$$

$$V_{sqde} = Ri_{qde} + L\frac{di_{qde}}{dt} + \omega_e Li_{de} - j\omega_e Li_{qe} + V_{iqde} \tag{263}$$

V_{sqde} & I_{qde} are source voltage and line current vectors of two phase system in rotating frame (q_e-d_e), respectively.

Real and imaginary parts of the equation given in (263) can be seperated as;

$$V_{sqe} = Ri_{qe} + L\frac{di_{qe}}{dt} + \omega_e Li_{de} + V_{iqe}\ (Real) \tag{264}$$

$$V_{sde} = Ri_{de} + L\frac{di_{de}}{dt} - \omega_e Li_{qe} + V_{ide}\ (Imaginary) \tag{265}$$

Assuming the voltage vector of two phase system with stationary reference frame ,V_{sqds} has a magnitude of "V_m" and a phase angle of "θ_e" can be expressed as;

$$V_{sqds} = V_m e^{j\theta_e} \tag{266}$$

Hence that with rotating reference frame, V_{sqde} can be derived from (266) as;

$$V_{sqde} = V_{sqds}e^{-j\theta_e} \tag{267}$$

$$V_{sqde} = V_m \tag{268}$$

Real and imaginary parts of V_{sqde} are defined as;

$$V_{sqe} = V_m \tag{269}$$

$$V_{sde} = 0 \tag{270}$$

Similar expressions are also valid for the current vector of two phase system with rotating reference frame, i_{qde} has a magnitude of "I_m" as shown below.

$$I_{qe} = I_m \tag{271}$$

$$I_{de} = 0 \tag{272}$$

The vector diagram of "V_{sqde}" is shown in Figure 41 as well.

Figure 41: Voltage vector diagram of V_{sqde}

Therefore, transformation from three phase system (a-b-c) to two phase system in rotating reference frame (q_e-d_e) reduces the complexity of voltage and current equations for three phase front end converters (FECs). This simplification provides control of three phase PWM rectifiers only for two phase system with constant components.

[($V_{sqe} \sim V_m$ & $V_{sde} \sim 0$)/($i_{qe} \sim I_m$ & $i_{de} \sim 0$)] instead of three phase system with time varying components [46, 47].

Reduction and simplification of source voltage components of three phase time varying system to those of two phase constant system in rotating frame is given in Figure 42.

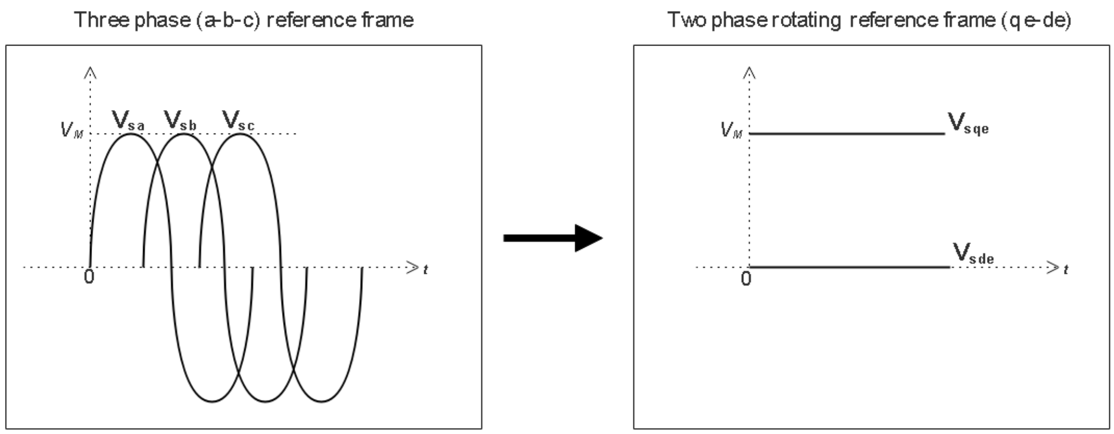

Figure 42: Reduction of voltage components of three phase system to those of two phase system in rotating reference frame

Also expressions for line current components of two phase system in rotating reference frame,"i_{qe} & i_{de}" are given below.

$$i_{qe} = \frac{V_{sqe} - V_{iqe} - \omega_e L i_{de}}{R + sL} \tag{273}$$

$$i_{de} = \frac{V_{sde} - V_{ide} + \omega_e L i_{qe}}{R + sL} \tag{274}$$

The current components given in (273) & (274) can be controlled via current PI controllers. Simplified control diagram for three phase front end converters (without taking transformations between reference frames into account) is shown in Figure 43.

A more detailed control diagram including voltage controller for outer loop in addition to current ones and transformations between three phase "abc" reference frame and two phase "qde" rotating one for three phase front end converters (FECs) is given in Figure 44.

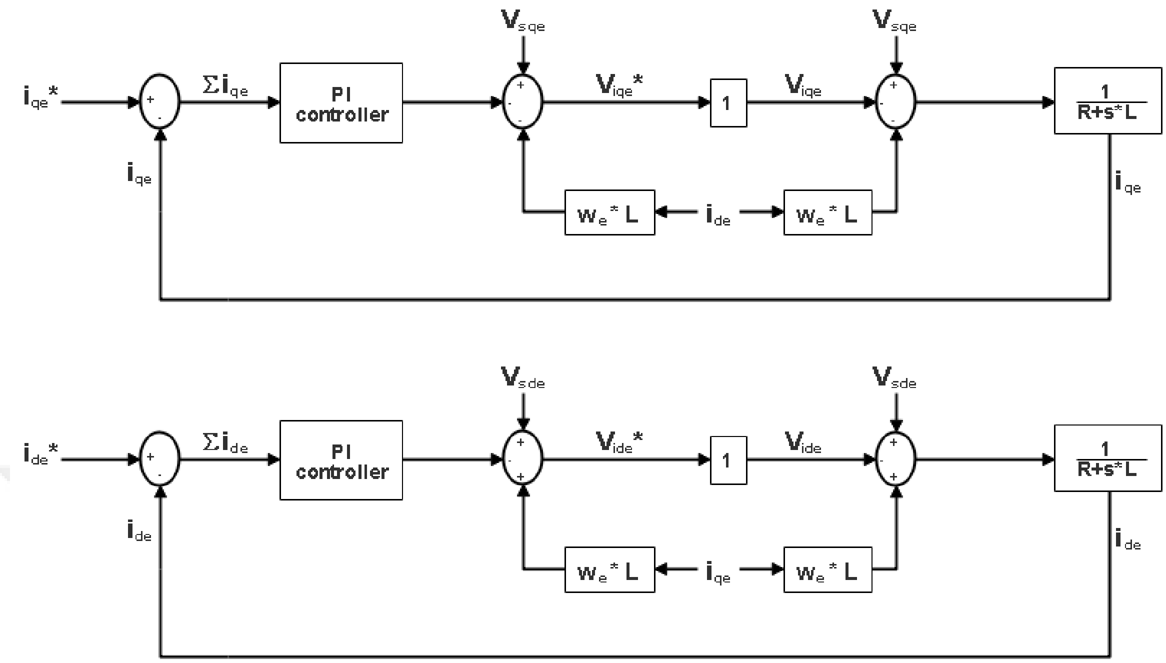

Figure 43: Simplified control diagram for current components in two phase system in rotating reference frame (q_e-d_e)

V_a, V_b & V_c represent phase “a”, ”b” & ”c” components of the reference voltage for modulation and m_a, m_b & m_c are phase “a”, phase ”b” & phase ”c” components of the modulation signal, respectively.

Modulation signals and PWM generation for three phase front end converters are already explained in detail in “Power Converters” section.

The source voltage components of the converter in two phase rotating reference frame (q_e-d_e) can also be derived from those in the stationary reference frame (q_s-d_s) and written as;

$$V_{sqde} = V_{sqds}e^{-j\theta_e} = (V_{sqs} + jV_{sds})e^{-j\theta_e} \tag{275}$$

$$V_{sqde} = (V_{sqs} + jV_{sds})(cos(\theta_e) - jsin(\theta_e)) \tag{276}$$

$$V_{sqde} = (V_{sqs}cos(\theta_e) + V_{sds}sin(\theta_e)) + j(V_{sds}cos(\theta_e) - V_{sqs}sin(\theta_e)) \tag{277}$$

The control diagram of PLL algorithm to track the phase angle of source voltage

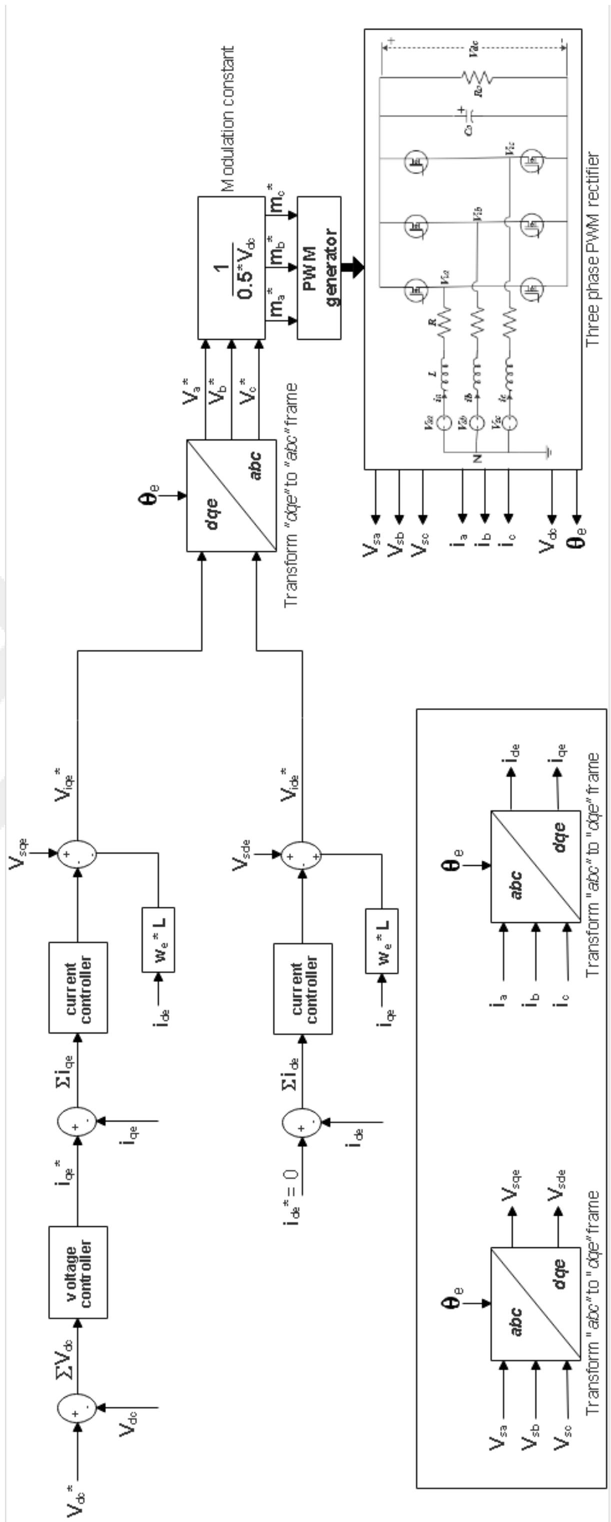

Figure 44: Overall control diagram for three phase front end converters (FECs)

vectors for three phase front end converters (FECs) is shown in Figure 45.

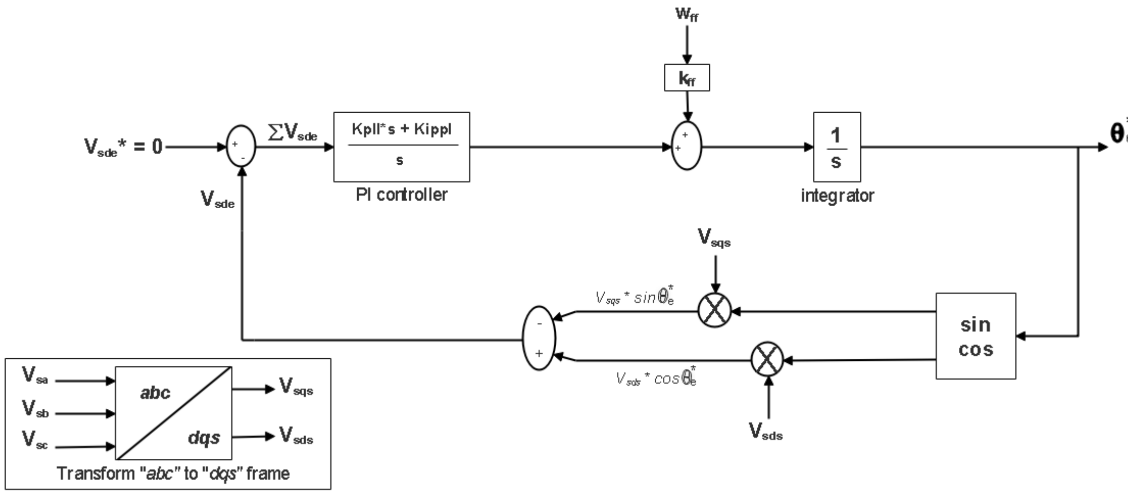

Figure 45: Control diagram of PLL algorithm for three phase front end converters (FECs)

V$_{sde}$* is "d" component of reference source voltage vector of two phase system in rotating frame (q$_e$-d$_e$), θ_e* is reference phase angle of source voltage vector of three phase system (a-b-c), K$_{pll}$ & K$_{ipll}$ are proportional constant (K$_p$) & integrator constant (K$_i$) of PI controller respectively, ω_{ff} is angular feed-forward frequency and k$_{ff}$ defines feed-forward constant value.

From (277), the following expression is derived in matrix form assuming $\theta_e^* \approx \theta_e$

$$\begin{bmatrix} V_{sqe} \\ V_{sde} \end{bmatrix} = \begin{bmatrix} cos(\theta_e^*) & sin(\theta_e^*) \\ -sin(\theta_e^*) & cos(\theta_e^*) \end{bmatrix} \begin{bmatrix} V_{sqs} \\ V_{sds} \end{bmatrix} \tag{278}$$

Investigating "d" component of the source voltage vector in two phase rotating reference frame (q$_e$-d$_e$), V$_{sde}$

$$V_{sde} = V_{sds}cos(\theta_e^*) - V_{sqs}sin(\theta_e^*) \tag{279}$$

From (266), source voltage vector in two phase stationary reference frame can also be defined as;

$$V_{sqds} = V_m cos(\theta_e) + jV_m sin(\theta_e) \tag{280}$$

From (279) and (280)

$$V_{sde} = V_m sin(\theta_e) cos(\theta_e^*) - V_m cos(\theta_e) sin(\theta_e^*) \tag{281}$$

$$V_{sde} = V_m sin(\theta_e - \theta_e^*) \approx 0 \tag{282}$$

Hence, the assumption that phase angle of the three phase system is tracked by PLL algorithm, which means reference angle is almost equal to actual phase angle value measured for front end converters, is verified . PLL control structure would try to equate measured phase angle to the reference value as expected. Difference between actual phase angle value and the reference one can be defined as;

$$\Delta\theta = \theta_e - \theta_e^* \tag{283}$$

$$sin(\Delta\theta) \approx \Delta\theta \tag{284}$$

Therefore the PLL control system can be treated as a linear system for small values of $\Delta\theta$ [47, 48]. The simplified control diagram of PLL algorithm based on this assumption is given in Figure 46.

2.5 Controller Design for Power Electronics Converters

2.5.1 General Controller Design for DC-DC Converters

Regulation of DC-DC converters is critical againts possible variations on input or output side of the circuit so feedback compensator needs to be designed to ensure the stability of the converter for various load current conditions or variations at input voltage.

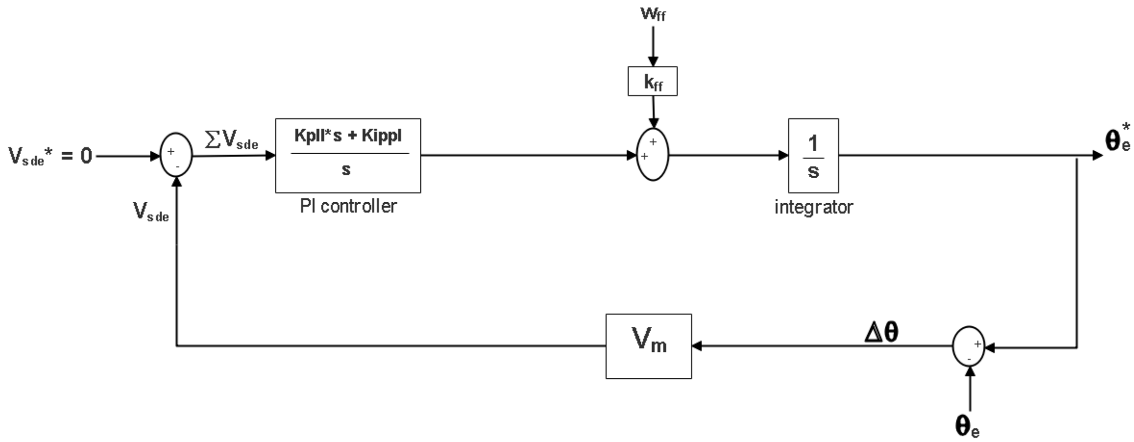

Figure 46: Simplified control diagram of PLL algorithm treated as a linear control system

2.5.1.1 Voltage Mode (Single-Loop) Controller Design

The diagram of a feedback system for output voltage control of a switching power converter is shown in Figure 47.

Also voltage mode control loop can be modelled in small signal dynamics of the converter as shown in Figure 48.

The compensated loop gain of voltage mode control loop can be expressed as;

$$T(s) = G_c(s)\frac{1}{V_M}G_{vd}(s)H(s) \tag{285}$$

It is clear that small signal change occured in input line voltage, $\hat{v_g}$ or load current, $\hat{i_{load}}$ can also affect the response of output voltage in addition to that occured in the reference value, $\hat{v_{ref}}$.

Then perturbation of output voltage, $\hat{v}$ can be derived as;

$$\hat{v} = \frac{\frac{T(s)}{H(s)}}{1+T(s)}\hat{v_{ref}} + \frac{G_{vg}(s)}{1+T(s)}\hat{v_g} + \frac{Z_{out}(s)}{1+T(s)}\hat{i_{load}} \tag{286}$$

To design an appropriate compensator for voltage mode control loop of the converter uncompensated loop gain, T_u(s) must be determined at first. It is given by;

$$T(s) = \frac{1}{V_M}G_{vd}(s)H(s) \tag{287}$$

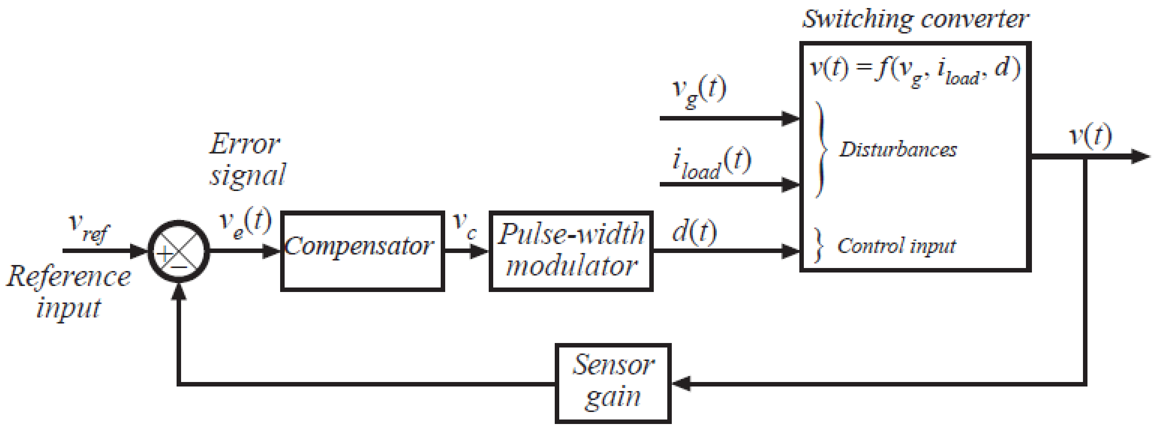

Figure 47: Feedback network of voltage mode control for a switching power converter [39].

Thus the loop is compensated by voltage compensator. Equation for compensated loop is obtained by;

$$T(s) = T_u(s)G_c(s) \tag{288}$$

The voltage compansator can be PI,PD or PID type depending on characteristics of the uncompensated loop gain and some performance parameters (bandwidth,overshoot etc) of the control loop [39, 49]. These types of controllers are analysed in the next sections.

2.5.1.2 Average Current Mode (Cascaded-Loop) Controller Design

Cascaded (outer voltage inner current controller) compensator can provide stability for wider range of operating conditions and better transient responses compared to the conventional single compensator and useful solution for some applications. Generally, two PI controllers for both inner current and outer voltage loops are enough in cascaded mode control. To design cascaded control system for a switching power converter, a compensator for the inner current loop must be designed at first. Feedback system for current control of the converter is given in Figure 49.

V_c is the reference control voltage (v_c = $R_f i_c$), R_f is the sensing resistance for

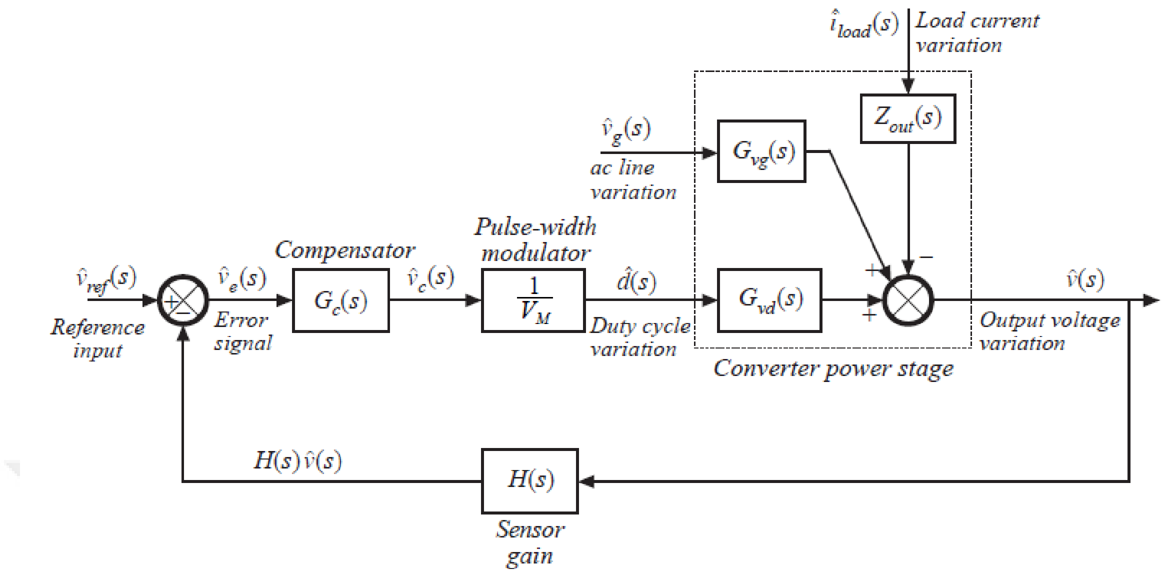

Figure 48: Small signal model of voltage mode control loop for the switching converter [39].

inductor current i, V_M is the peak value of carrier signal generated by PWM block, G_{ci} defines current compensator transfer function, c represents the PWM signal having duty cycle value d.

Also,average current mode control loop can be modelled in small signal dynamics of the converter as shown in Figure 50.

Ti(s) is defined as compensated loop gain and can be expressed as;

$$T_i(s) = R_f G_{ci}(s) \frac{1}{V_M} G_{id}(s) \tag{289}$$

Small signal variations at input line voltage, $\hat{v}_g$ or load current, $\hat{i_{load}}$ can also affect the response of average inductor current in addition to that occured in the reference value, $\hat{v}_c$ as in the case for voltage mode control. Then perturbation of average inductor current, $\hat{i}$ can be derived as;

$$\hat{i} = \frac{\frac{T_i(s)}{R_f}}{1+T_i(s)}\hat{v}_c + \frac{G_{ig}(s)}{1+T_i(s)}\hat{v}_g + \frac{G_{iz}(s)}{1+T_i(s)}\hat{i_{load}} \tag{290}$$

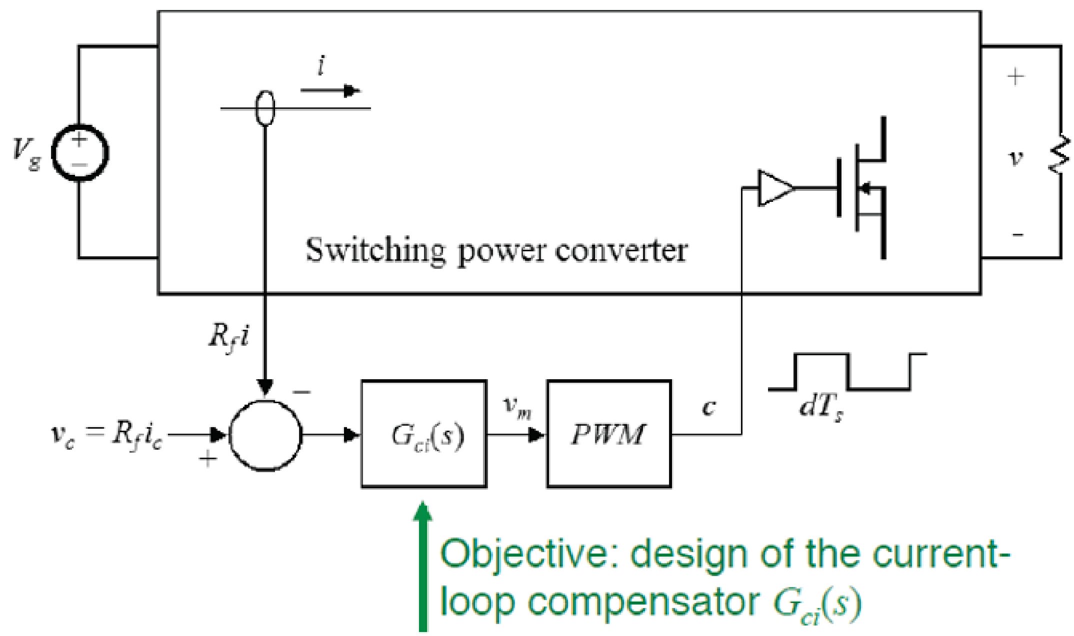

Figure 49: Feedback network for current control loop of the converter [39].

To design current compensator, firstly uncompensated loop gain is obtained, which can be expressed as;

$$T_{iu}(s) = R_f \frac{1}{V_M} G_{id}(s) \tag{291}$$

Therefore the inner loop is compensated by current compensator. Equation for compensated cuurent loop is obtained by;

$$T_i(s) = T_{iu}(s) G_{ci}(s) \tag{292}$$

The current compansator is selected as PI controller which would be enough to obtain a desired response for inductor current in most situations for dynamic variations of the converter as well. After designing inner current compensator, a voltage controller for the outer loop must be designed as well. Feedback system for voltage control around the current control loop of the converter is given in Figure 51, for which V$_{ref}$ is the reference output voltage, H is the sensor gain for output voltage v

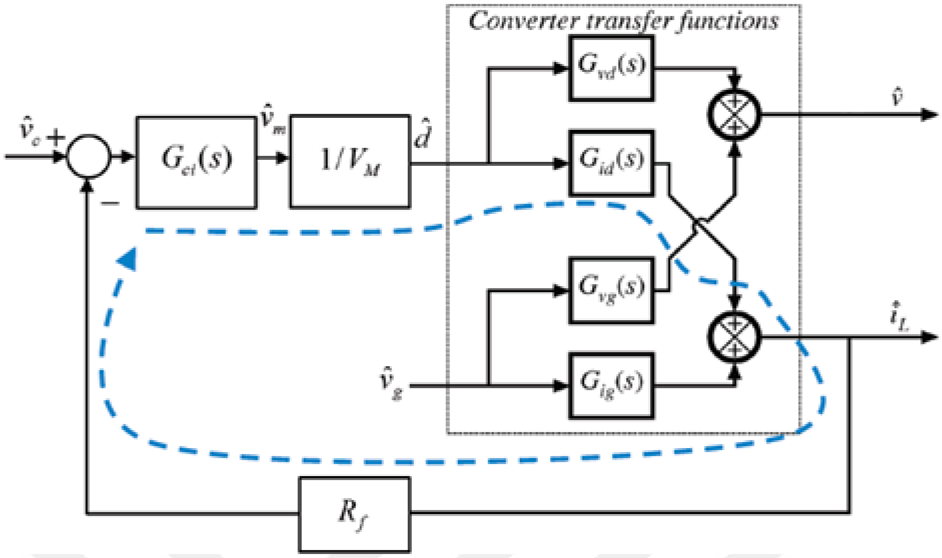

Figure 50: Small signal model of average current mode control loop for the converter [39].

and G_{ci} defines the current compensator transfer function.

Voltage mode control loop can be modelled around the current loop in small signal dynamics of the converter leading to a cascaded control loop as shown in Figure 52.

Small signal perturbations of input line voltage, $\hat{v_g}$ or load current, $\hat{i_{load}}$ can also affect the response of both average inductor current and output voltage. Assuming cross-over frequency of the voltage loop would be well below that of the current loop, inner closed current loop transfer function can be simplified as;

$$\frac{\hat{i}}{\hat{v_c}} = \frac{1}{R_f}\frac{T_i(s)}{1+T_i(s)} \approx \frac{1}{R_f} \tag{293}$$

Simplified model of the cascaded control loop based on the approximation in small signal dynamics of the converter as shown in Figure 53.

Tv(s) is defined as compensated voltage loop gain and can be expressed as;

$$T_v(s) \approx HG_{cv}\frac{1}{R_f}\frac{G_{vd}}{G_{id}} \tag{294}$$

Then perturbation of output voltage, $\hat{v}$ can be derived as;

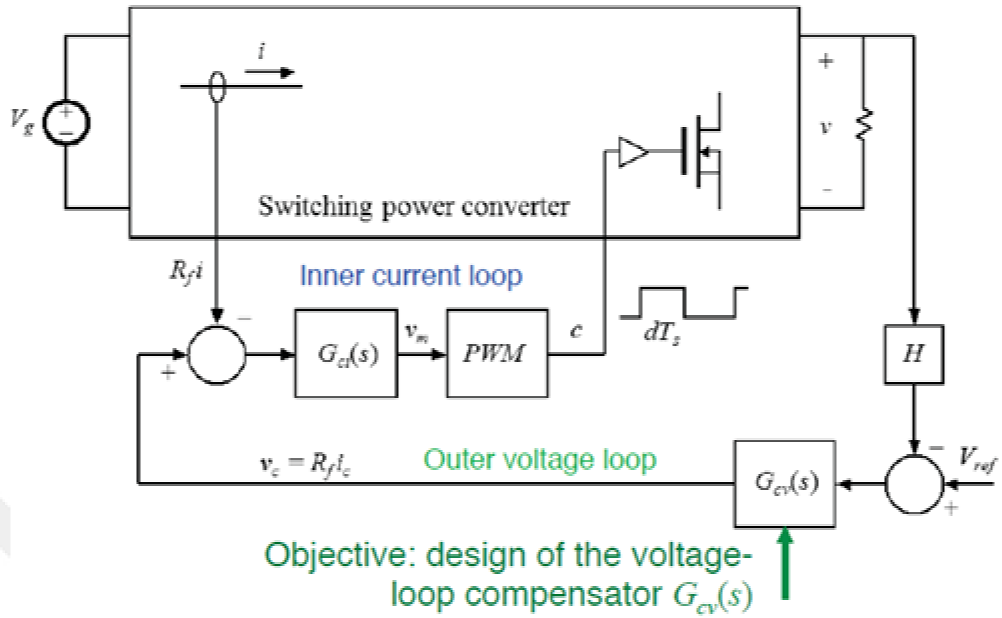

Figure 51: Feedback network for voltage control loop around the inner loop of the converter [39].

$$\hat{v} = (\frac{T_v}{1+T_v}\frac{1}{H})\hat{v_{ref}} + (\frac{G_{vg} - \frac{G_{vd}}{G_{id}}G_{ig}\frac{T_i}{1+T_i}}{1+T_v})\hat{v}_g + (\frac{Z_{out} - \frac{G_{vd}}{G_{id}}G_{iz}\frac{T_i}{1+T_i}}{1+T_v})\hat{i_{load}} \tag{295}$$

To design voltage compensator, firstly uncompensated voltage loop gain is obtained, which can be expressed as;

$$T_v(s) \approx H\frac{1}{R_f}\frac{G_{vd}}{G_{id}} \tag{296}$$

Therefore the outer loop is compensated by voltage compensator. Equation for compensated voltage loop is obtained by;

$$T_v(s) = T_{vu}(s)G_{cv}(s) \tag{297}$$

The voltage compansator can be selected as a PI controller as for the current compensator, too [39, 50].

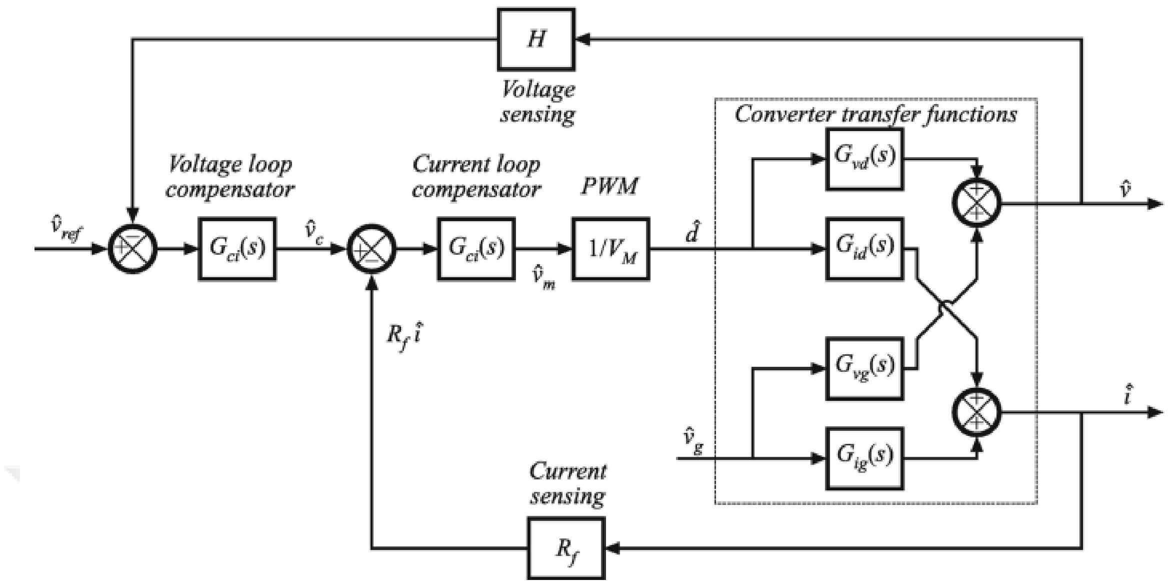

Figure 52: Detailed small signal model of voltage mode control loop around the current loop (cascaded control loop) for the converter [39].

2.5.2 Controller Design for Three-Phase AC-DC Converters

Control systems can be designed for three phase front-end converters (FECs) based on two phase rotating reference frame (q_e-d_e).

2.5.2.1 Current Controller Design

The diagram of a feedback system for control of real component (qe) of line current vector in two phase rotating reference frame for three-phase AC/DC converters is shown in Figure 54.

G is gain of the converter, T_s represents time constant of the inductor ($T_s = L_s/R_s$), T_d is delay time of the converter, K_2 defines gain of the current sensor, T_2 is time constant of the current sensor and $I_{sq,fb}$ represents "q" component of current vector measured by the current sensor.

Moreover following equations are assumed for further analysis of the current control loop.

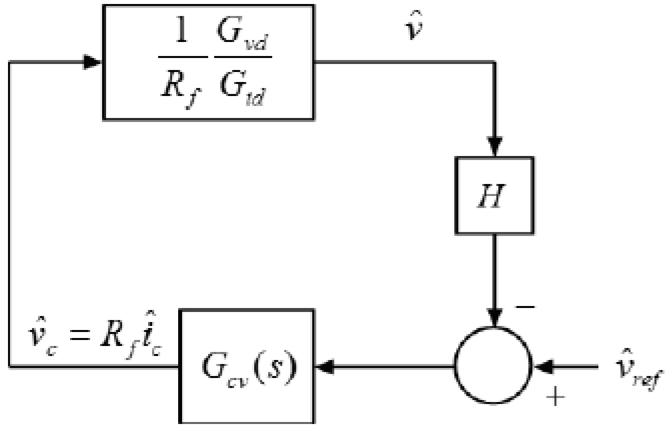

Figure 53: Simplified small signal model of cascaded control loop for the converter [39].

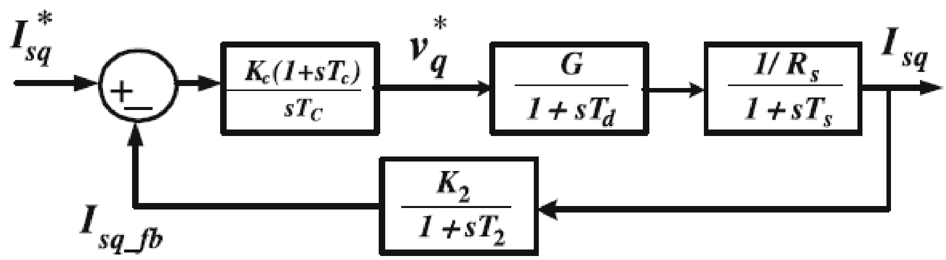

Figure 54: Feedback system for control of current component "q$_e$" [46].

$$I_{sq} = i_{qe} \tag{298}$$

$$V_q = V_{sqe} - V_{iqe} - \omega_e L - i_{de} \tag{299}$$

It can be noticed that PI compensator is implemented for the current control loop. Before analysing the loop, a closed loop system is reviewed briefly. The diagram of a closed loop feedback system is shown in Figure 55.

Output-to-reference input transfer function of the system is derived as;

$$(X(s) - H(s)Y(s))G(s) = Y(s) \tag{300}$$

$$X(s)G(s) - H(s)Y(s)G(s) = Y(s) \tag{301}$$

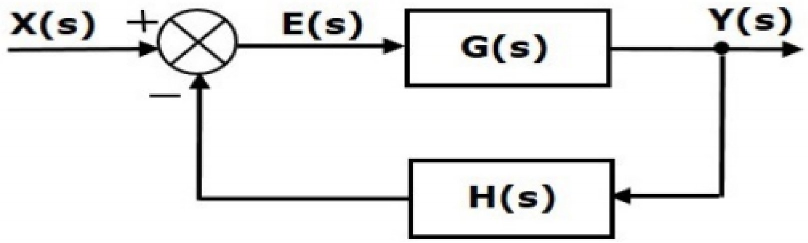

Figure 55: The diagram of a closed loop feedback system [51].

$$X(s)G(s) = (1 + H(s)G(s))Y(s) \tag{302}$$

$$\frac{Y(s)}{X(s)} = \frac{G(s)}{1 + H(s)G(s)} \tag{303}$$

Returning to the current loop, open loop transfer function can be given as;

$$\frac{I_{sq,fb}(s)}{V_q^*(s)} = \frac{GK_2}{R_s}\frac{1}{(1 + sT_s)(1 + sT_d)(1 + sT_2)} \approx \frac{GK_2}{R_s}\frac{1}{(1 + sT_s)(1 + sT_\sigma)} \tag{304}$$

where

$$T_\sigma = T_2 + T_d \tag{305}$$

$$s^2T_2T_d \ << \ 1 + sT_\sigma \tag{306}$$

Transfer function of the closed loop response would be equal to;

$$\frac{I_{sq}^*}{I_{sq}} = \frac{sT_c(1 + sT_d)(1 + sT_s)R_s}{GK_c(1 + sT_c)} + \frac{K_2}{1 + sT_2} \tag{307}$$

Since $T_s >> T_\sigma$, the pole located at $1/T_s$ can be cancelled by selecting;

$$T_c = T_s \tag{308}$$

Then

$$\frac{I_{sq}^*}{I_{sq}} = \frac{sT_s(1 + sT_d)R_s}{GK_c} + \frac{K_2}{1 + sT_2} \tag{309}$$

$$\frac{I_{sq}^{*}}{I_{sq}} = \frac{(1+sT_2)(sT_d + s^2T_sT_d)R_s + GK_2K_c}{GK_c(1+sT_2)} \tag{310}$$

Arranging the terms by assuming $T_\sigma = T_2 + T_d$ and neglecting the term multiplied by T_2T_d for simplicity, the closed loop transfer function of reference input-to-output current can be defined as;

$$\frac{I_{sq}^{*}}{I_{sq}} = \frac{K_cG}{R_sT_sT_\sigma}\frac{(1+sT_2)}{(s^2 + \frac{s}{T_\sigma} + \frac{K_cGK_2}{R_sT_sT_\sigma})} \tag{311}$$

The denominator of the closed loop transfer function has a standard form of a second order transfer function as well. Standard form of a second order transfer function can be expressed as;

$$H(s) = \frac{N(s)}{D(s)} \tag{312}$$

N(s) is the numerator and D(s) is the denominator of the transfer function equation.

$$D(s) = s^2 + 2\zeta\omega_n s + \omega_n^2 \tag{313}$$

Equating D(s) to the denominator term of the closed loop transfer function, the following equations would be obtained.

$$2\zeta\omega_n = \frac{1}{T_\sigma} \tag{314}$$

$$\omega_n^2 = \frac{K_cGK_2}{R_sT_sT_\sigma} \tag{315}$$

So proportional term of PI compensator K_c is defined as;

$$K_c = \frac{R_sT_s}{4\zeta^2GK_2T_\sigma} \tag{316}$$

By selecting a proper value for the damping ratio, ζ a desired response for the closed current loop system can be achieved. To obtain an optimum performance for the current control loop, the damping ratio value is usually taken as;

$$\zeta = \frac{1}{\sqrt(2)} \tag{317}$$

$$K_c = \frac{R_s T_s}{2GK_2T_\sigma} \tag{318}$$

Current loop bandwidth, ω_n would be;

$$\omega_n = \frac{1}{\sqrt(2)T_\sigma} \tag{319}$$

When the parameter of K_c, chosen as given above, is inserted into the closed current loop transfer function equation, the following expression would be obtained;

$$\frac{I_{sq}}{I_{sq}^*} = \frac{1}{K_2}\frac{(1+sT_2)}{(1+2T_\sigma s+2T_\sigma^2 s^2)} \tag{320}$$

2.5.2.2 Voltage Controller Design

A voltage compensator can also be implemented around the current one for control of real component (q_e) of line current vector in two phase rotating reference frame. From the equation of closed current loop transfer function, the zero located at $1/T_2$ due to the current sensor is at a frequency higher than the current loop bandwidth ($1/T_2 >> 0.707/T_\sigma$) so "sT_2" term can be neglected. Moreover the desired bandwidth value for voltage control loop is about tenth of that for the current control one so "$2{T_\sigma}^2 s^2$" term would be ignored for simplicity while designing of voltage controller. Therefore approximated transfer function of the closed current loop is defined as;

$$\frac{I_{sq}}{I_{sq}^*} = \frac{1}{K_2}\frac{1}{(1+2T_\sigma s)} \tag{321}$$

Input-output power balance equation in two-axes rotating reference frame is expressed as;

$$V_{dc}I_{dc} = \frac{3}{2}V_{sqe}i_{qe} \tag{322}$$

The relationship between output DC current, I_{dc} and q_e component of input line current i_{qe} can be derived as;

$$I_{dc} = Ki_{qe} \tag{323}$$

where

$$K = \frac{3}{2}\frac{V_{sqe}}{V_{dc}} \tag{324}$$

The diagram of outer feedback system around the inner current loop for control of output DC voltage for three-phase AC/DC converters is shown in Figure 56.

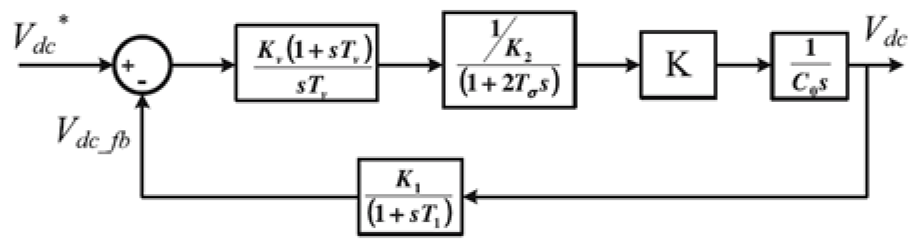

Figure 56: Outer feedback loop for control of output DC voltage [46].

K_1 & T_1 are gain & time constant of the voltage sensor, respectively and $V_{dc,fb}$ defines output voltage measured by the voltage sensor.

The open loop transfer function of the voltage control loop can be given as;

$$\frac{V_{dc,fb}(s)}{V_{dc}^*(s)} = \frac{K_e(1+sT_v)}{sT_v(1+2T_\sigma s)(1+sT_1)C_0 s} \approx \frac{K_e(1+sT_v)}{s^2 T_v C_0(1+sT_\delta)} \tag{325}$$

where

$$T_\delta = T_1 + 2T_\sigma \tag{326}$$

$$2s^2 T_1 T_\sigma << 1 + sT_\delta \tag{327}$$

$$K_e = \frac{KvKK_1}{K_2} \tag{328}$$

An illustrative bode plot of the open voltage loop is shown in Figure 57. The crossover frequency, ω_c is desired to be between the zero located at $\omega_1 = 1/T_v$ and the pole at $\omega_2 = 1/T_\delta$ to obtain a stable loop.

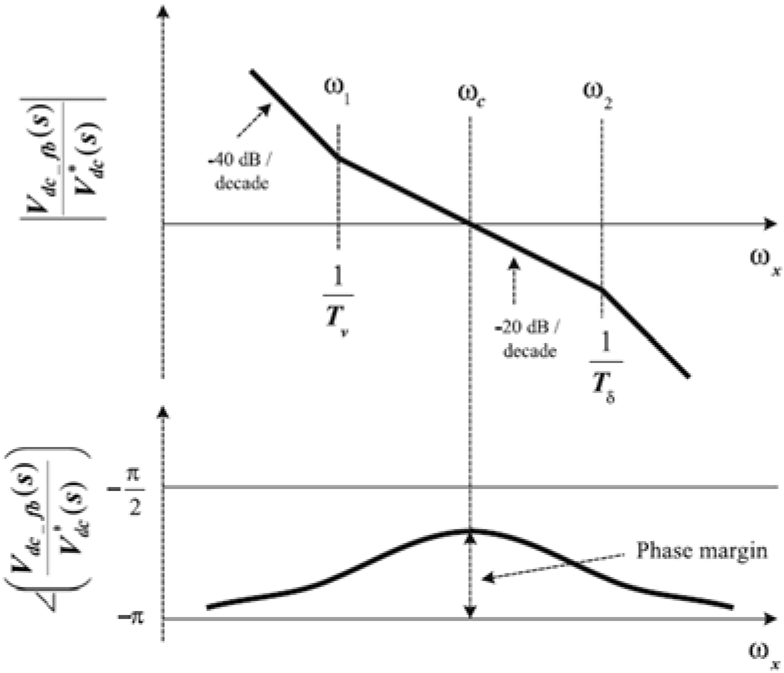

Figure 57: Illustrative bode plot of the compensated open voltage loop [46].

As shown in the illustrative bode plot, the crossover frequency, ω_c would be the geometric mean of two corner frequencies, ω_1 and ω_2 according to symmetrical optimum method. Thus the expression for the crossover frequency, ω_c can be expressed as;

$$\omega_c = \frac{1}{\sqrt{T_v T_\delta}} = \frac{1}{\alpha T_\delta} \tag{329}$$

α is a number showing the relationship between the two corner frequencies as;

$$T_v = \alpha^2 T_\delta \tag{330}$$

Depending on the value of α the parameter, T_v can be determined as well. The gain of the open voltage loop at the crossover frequency, ω_c is equal to 1. The following equation can be derived for the magnitude of gain at $\omega = \omega_c$;

$$|\frac{V_{dc,fb}(s)}{V_{d_c}^*(s)}|_{(\omega=\omega c)} = 1 = \frac{K_e\sqrt{1+(\omega_c T_v)^2}}{\omega_c^2 T_v C_0 \sqrt{1+(\omega_c T_\delta)^2}} \tag{331}$$

$$\frac{K_v K K_1 \sqrt{1+\alpha^2}}{K_2 C_0 \frac{1}{T_\delta} \sqrt{1+\frac{1}{\alpha^2}}} = 1 \tag{332}$$

Arranging the terms, the parameter for the proportional constant, K_v of PI controller can be expresses as;

$$K_v = \frac{C_0 K_2}{K_1 K \alpha T_\delta} \tag{333}$$

Generally, there is no need for a voltage compensator around the current control loop of imaginary component (d_e) since the reference value of "d_e" component for line current vector, $i_{de}{}^*$ can be taken as constant and 0 independent of variations of other parameters for three-phase front end converters (FECs) [46].

2.5.2.3 Controller Design for PLL Algorithm

According to the simplified diagram of PLL control loop shown in Figure 46, open loop transfer function of the control diagram for PLL algorithm, taking the sampling delay into account, is given as;

$$H_{ol} = (K_{pll} + \frac{K_{ipll}}{s})(\frac{1}{1+sT_s})\frac{V_m}{s} \tag{334}$$

$$H_{ol} = \frac{V_m(K_{pll}s + K_{ipll})}{s^2(1+sT_s)} = \frac{V_m K_{ipll}(T_{pll}s+1)}{s^2(1+sT_s)} \tag{335}$$

T_s is sampling time of the PLL control loop and H_{ol} is open loop transfer function of the control loop. Also the ratio between K_{pll} and K_{ipll} can be defines as;

$$T_{pll} = \frac{K_{pll}}{K_{ipll}} \tag{336}$$

It can be noticed that the open loop transfer function of PLL control loop is similar to that given for the voltage control loop in the previous section. Hence the same method to plot an illustrative bode diagram for the system stability and the symmetrical optimum method can be utilized again to determine the parameters of PI controller, K_{pll} and K_{ipll}. An illustrative bode plot of the open loop for PLL algorithm is shown in Figure 58. Also the zero at $\omega_1 = 1/\mathrm{T}_{pll}$ is smaller than the pole at $\omega_2 = 1/\mathrm{T}_s$ since

$$T_s < T_{pll} \tag{337}$$

in practice.

Therefore the expression for the crossover frequency, ω_c can be defined as;

$$\omega_c = \frac{1}{\sqrt{T_s T_{pll}}} = \frac{1}{\alpha T_s} \tag{338}$$

where

$$T_{pll} = \alpha^2 T_s \tag{339}$$

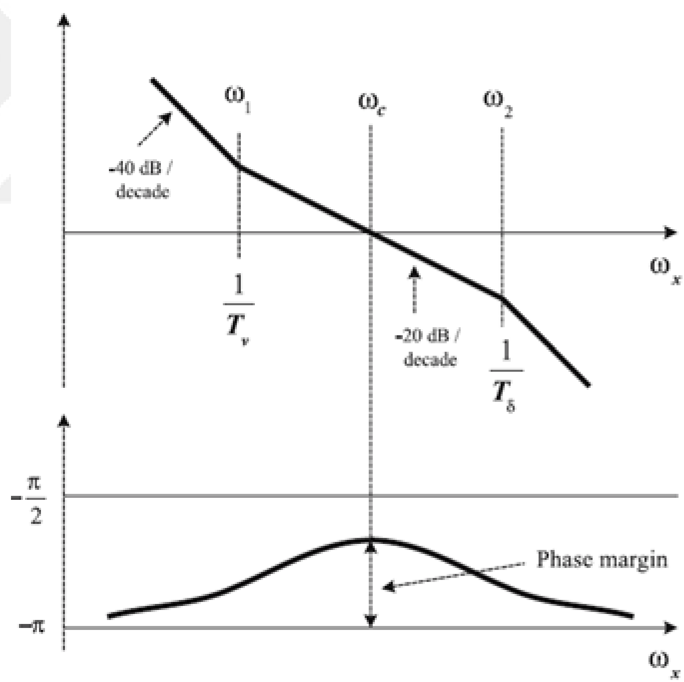

Figure 58: Illustrative bode plot of the compensated open loop for PLL algorithm [46].

The gain of the open loop of the PLL control algorithm at the crossover frequency, ω_c is equal to 1. The following equation can be derived for the magnitude of gain at $\omega = \omega_c$;

$$|H_{ol}(s)|_{(\omega=\omega c)} = 1 = \frac{\sqrt{1+(T_{pll}\omega_c)^2}}{\omega_c^2\sqrt{1+(\omega_c T_s)^2}} K_{ipll} V_m \tag{340}$$

$$\frac{\sqrt{1+\alpha^2}}{\frac{1}{\alpha^2 T_s^2}\sqrt{1+\frac{1}{\alpha^2}}} K_{ipll} V_m = 1 \tag{341}$$

Arranging the terms, the parameter for the integrator constant, K_{ipll} of PI controller can be expresses as;

$$K_{ipll} = \frac{1}{V_m}\frac{1}{\alpha^3 T_s^2} = \frac{K_{pll}}{T_{pll}} \tag{342}$$

Hence the proportional constant, K_{pll} would be;

$$K_{pll} = \frac{1}{V_m \alpha T_s} \tag{343}$$

Hence these controller parameters for PI compensator can be implemented for PLL algorithm [47, 48].

2.5.3 Effect of Sampling Delay in Control Systems

The sampling delay in power converters is considered to be one of the most critical effect to deal with uncertainties for power electronics models, issues in power supplies and corresponding disturbances. Hence, zero order hold (ZOH) can be included in the control system. A pole or zero is added into the control system, which already exists so it only affects a restricted share of the overall delay. In digital control systems, there are two sampling methods basically, that are single updated sampling and double updated one. Modulation index values are updated once in every switching period in single sampling while measurement sampling and calculated values are updated twice in one switching period in double sampling method as well [28]. In Figure 59, the detailed operation of single-update and double-update sampling is shown.

In this thesis, double-update sampling method is implemented while modeling the control algorithms for both AC/DC and DC/DC parts of the bidirectional EV charger

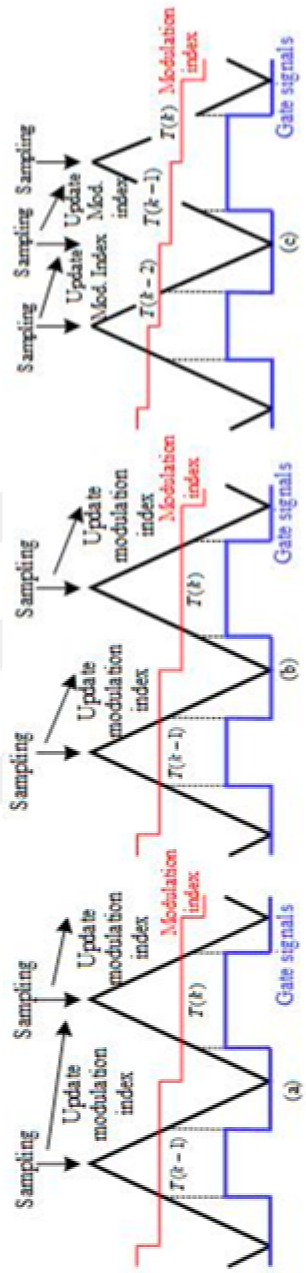

Figure 59: Sampling delay model for a power converter: **(a)** single-update time delay model (sampling at beginning), **(b)** single-update time delay model (sampling at middle), **(c)** double-update time delay model (sampling at beginning) [28].

to be modeled since higher sampling frequency can provide increased bandwidth with larger phase margin value, enhancing stability of the system [52].

CHAPTER III

DESIGN OF THREE-PHASE BIDIRECTIONAL CHARGER

The proposed bidirectional EV charger system consists of two stages, which are three phase AC/DC PWM converter, mostly responsible for regulating DC link voltage, and DC/DC part, enabling charging or discharging of the output battery depending on the direction of power flow. In the case of G2V mode of operation, although it is desired to charge the battery at nominal voltage value of 500V in most cases, charging voltage could sometimes be as low as 300V according to the value of SOC. Hence an additional DC-DC converter is required to step down or regulate charging voltage for the battery. In V2G mode of operation, power in output battery is extracted and send to the electricity grid as well.

3.1 Selection of Components

The values of components utilized in the proposed EV charger model would be calculated according to relevant equations derived from theoretical analysis and given in the previous chapter.

Parameters for LCL filter can be determined based on system power rating. Rated power of the bi-directional EV charger is 15kW. Then the power rating per phase for the three-phase converter would be 5kW. Using (14), ripple current value of the line inductor is calculated and determined as

$$\Delta I_L = 3A \tag{344}$$

Using the calculated ripple current value, converter side filter inductance value is determined using the equation given in (13)

$$L_i = 1.6mH \tag{345}$$

Then grid side filter inductance value from (15) would be

$$L_g = 1mH \tag{346}$$

Also, the filter capacitance value is calculated using the equation, (16) as

$$C_f = 300mF \tag{347}$$

From (17), the resonance frequency of the filter designed with the values determined above would be

$$F_0 = 370Hz \tag{348}$$

Finally, the value for damping resistance from (18), could be determined as;

$$R_d = 0.5\Omega \tag{349}$$

Selection of the power transistors for the bidirectional AC/DC EV charger system is critical since it could affect the efficiency of the system as well. To achieve an EV charger to be operated with a high efficiency value, the values of the parasitic elements for the transistors and the other semiconductor devices are desired to be as low as possible while maintaining stable operation of the charger. Six IGBT's are used in AC/DC side of the system. For the bidirectional three-phase AC/DC converter, an IGBT with on-state resistance value, $R_{on,ac}$ of 10 mΩ and forward voltage drop value, $V_{on,ac}$ of 0.7V is chosen. The same IGBT is also utilized for all six switches to model the AC/DC PWM converter. In DC/DC side, there are two transistors providing synchronous operation of the converter. Two identical MOSFET's with on-state resistance value, $R_{ds,on}$ of 8 mΩ can be selected for the DC/DC converter as well.

Parameters for the bidirectional DC/DC converter to be modeled are also determined based on the design requirements, which are allowable ripple values of inductor current and capacitor voltage. Therefore inductance value can be calculated using the equation given in (84) by considering maximum current ripple value of 4A and neglecting the internal resistance of the inductor. Since the nominal value of output power is 5kW, the inductor current value for buck mode of operation would be determined as;

$$I = \frac{P}{V} = \frac{5000}{500} \tag{350}$$

$$I = 10A \tag{351}$$

An inductor, which has the inductance value of 250μH and the internal resistance with 10mΩ, can be selected for the DC/DC converter. Then the ripple value of the inductor current for buck mode of operation would be calculated as

$$\Delta I = 3.75A \tag{352}$$

That of the capacitor output voltage can also be determined for buck mode of operation from the equation, (88) as

$$\Delta V = 142mV \tag{353}$$

For boost mode of operation, the ripple value of the inductor current using the equation given in (184) would be calculated as

$$\Delta I = 3.75A \tag{354}$$

It is noticed that the inductor current ripple values are the same for both of buck and boost operation of the DC/DC converter. It is expected since the rated values for DC bus voltage and output battery voltage are identical for both of the operation modes, only the direction of power flow is opposite, creating almost the same voltage drop across the inductor, taking some conduction losses for the converter into account.

3.2 System Parameters

The bidirectional charger would be operated at 5kW power condition with a battery pack, having 500V rated value, connected to output. Li-ion battery cells, with 3.7V nominal voltage and 3Ah rated capacitance, are to be utilized to create the battery pack. The three-phase bidirectional EV charger to be modeled has the parameters given in Table 4.

Table 4: System parameters for the three-phase bidirectional EV charger.

Parameter	**Value**
Phase voltage, V_s	$230V_{rms}$
Line frequency, f_{line}	50Hz
Line inductane, L_g	10mH
Line internal resistance, R_g	0.5Ω
Converter side filter inductance, L_i	1.6mH
Grid side filter inductance, L_{grid}	1mH
Filter capacitance, C_f	300mF
Filter damping resistance, R_d	0.5Ω
DC link capacitance, C_0	2mF
DC link voltage, V_{dc}	800V
Switching frequency for AC/DC PWM converter, $f_{sw,ac}$	10kHz
On state resistance of transistors in AC/DC PWM Converter, $R_{on,ac}$	10mΩ
Forward voltage of internal diodes of transistors in AC/DC PWM Converter, $V_{D,ac}$	0.7V
Inductance of DC/DC converter, L	250μH
Internal resistance of inductance in DC/DC converter, R_L	10mΩ
Peak value of PWM generator for DC/DC converter, V_M	4V
On state resistance of transistors in DC/DC converter, $R_{ds,on}$	8mΩ
Rated power, P_{out}	5kW
Output battery voltage, V	500V
Switching frequency for DC/DC converter, $f_{sw,dc}$	100kHz
Number of cells in series for battery pack, N_{ser}	116
Number of cells in parallel for battery pack, N_{par}	10

3.3 Controller Design

3.3.1 Design of Phase-Locked Loop (PLL)

Phase Locked Loop (PLL) algorithm is responsible for achieving in-phase operation keeping the reference angle value equal to actual phase angle value as mention in Chapter 2. The imaginary component of the source voltage (V_{sde}) is used for designing PLL system since the difference between the reference and actual values of the phase angle, which can be used as measured "d" component voltage, V_{sde}, is almost zero as well. Using the design parameters given in (338)-(343), the parameters of PI controller for the PLL algorithm is calculated. In Figure 60, bode plot of the compensated open loop for PLL algorithm is given as well.

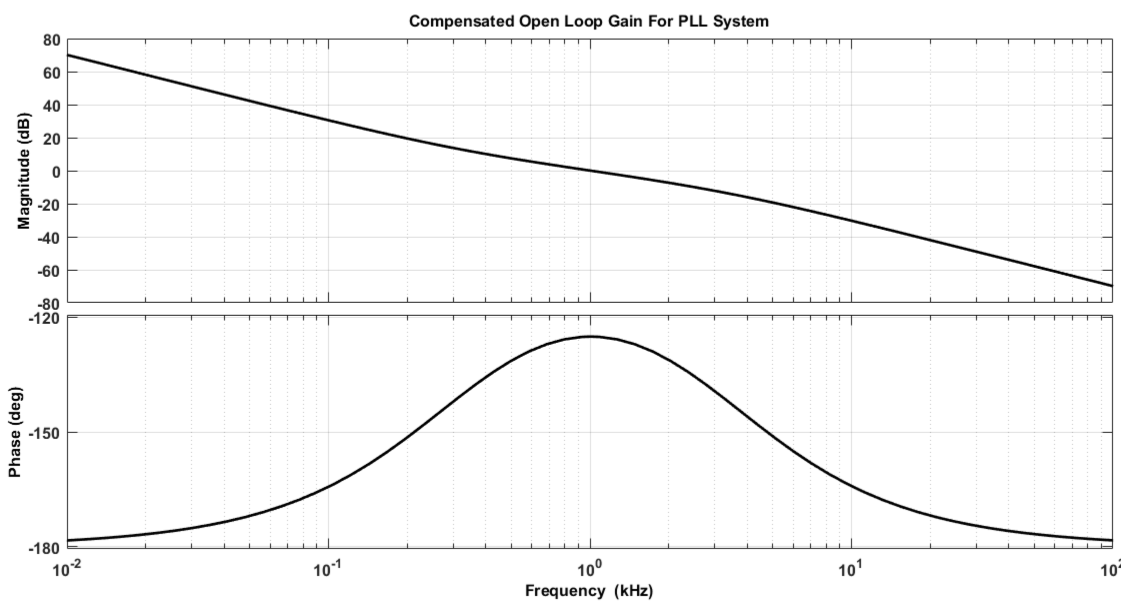

Figure 60: Bode plot of the compensated open loop for PLL system

The value of cross-over frequency of the PLL system, $f_{c,pll}$ is determined as 1kHz from the compensated open loop bode plot, which is equal to the value calculated using the equation (338), selecting the constant parameter α_{pll} as $\sqrt{10}$ to obtain a proper stable operation for the loop;

$$f_{c,pll} = \frac{1}{2\pi}\frac{1}{(\alpha_{pll}T_s)} = 1kHz \tag{355}$$

3.3.2 Design of Decoupled Current Controllers for AC/DC Part

Three-phase line current components are reduced to the two phase ones in rotating reference frame having constant DC values via Clark-Park Transformation as mentioned in Chapter 2. One of these components is desired to be real DC component (i_{qe}), which represents the magnitude value of the line current whereas the other one is intended to be kept as zero (i_{de}). Using the design parameters obtained from the equations, (310)-(320) controller parameters would be determined. The bode plot of the closed current loop designed with the calculated PI controller parameters is shown in Figure 61.

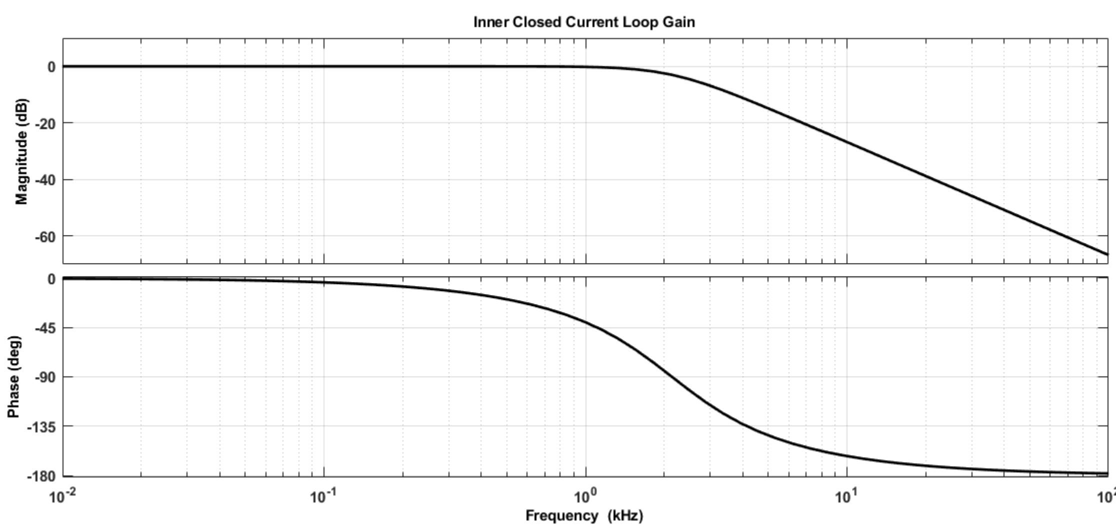

Figure 61: Bode plot of the closed decoupled current loop for AC/DC part of the charger

According to the closed current loop bode plot, -3dB bandwidth, f_n is measured as 2.14 kHz, which is significantly close to the value calculated according to the equation given in (319) and the system parameters given in Table 4;

$$f_n = \frac{1}{2\pi}\frac{1}{(\sqrt{2}T_\sigma)} = 2.05kHz \tag{356}$$

3.3.3 Design of DC Bus Voltage Controller for AC/DC Part

DC link capacitor, responsible for voltage regulation and creating interface between the AC/DC PWM converter and the DC/DC synchronous converter, is desired to be controlled in addition to the decouple current control algorithms to reject possible variations that could occur at the DC bus due to some perturbations and dynamic changes for the EV charger system as well. Using the equations given in (326)-(333) and the parameters for the EV charger system shown in Table 4, the controller parameters for the outer voltage loop could also be determined. The bode plot of the open voltage loop with relevant design parameters is given in Figure 62.

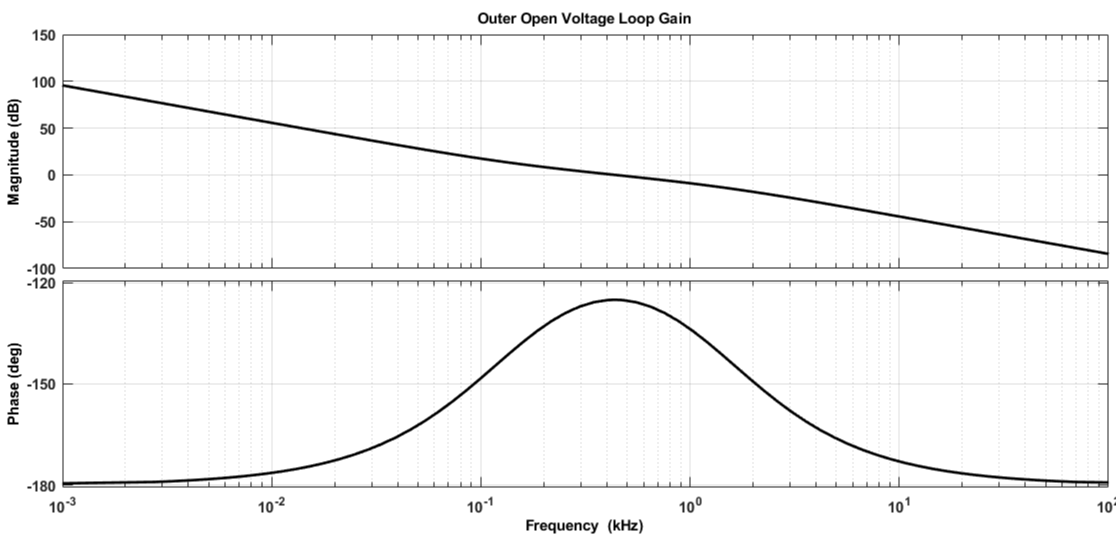

Figure 62: Bode plot of the open voltage loop for AC/DC part of the charger

Also cross-over frequency of the voltage loop, $f_{c,dc}$ is determined as 438 Hz from the open outer voltage loop bode plot, which is equal to the value calculated using the equation (329), selecting the constant parameter α_v as $\sqrt{10}$ as in the case of tuning

PLL system;

$$f_{c,dc} = \frac{1}{2\pi} \frac{1}{(\alpha_v T_\delta)} = 438Hz \tag{357}$$

3.3.4 Design of Inner Current Loop for DC/DC Part

When the bi-directional EV charger performs G2V operation, DC-DC converter operates in buck-mode. The load is a battery bank with a nominal power of 5kW (having 500V, 10A ratings). For simplicity, load is modeled as an equivalent resistance for the battery with;

$$R = \frac{V}{I} = \frac{500}{10} \tag{358}$$

$$R = 50\Omega \tag{359}$$

When the bi-directional EV charger performs V2G operation, DC-DC converter operates in boost-mode, with power flow from the battery pack to the DC bus capacitor. For simplicity, the load side can be assumed as only DC bus capacitor with this mode of operation so nearly no load condition is considered with a large load resistance value of 1 MΩ while designing control loops for the boost mode operation.

In general, cross-over frequency of the current loop is desired to be 1/10 of the switching frequency, so cut-off frequency for inner loop would be

$$f_{ci} = \frac{f_{sw,dc}}{10} \tag{360}$$

$$f_{ci} = 10kHz \tag{361}$$

For buck mode of operation of the DC/DC converter, the compensated open loop bode plot of inner current control system is shown in Figure 63. As mentioned the cross-over frequency of 10 kHz and a phase margin value of 53° are achieved for the case of 5kW power rating according to the compensated current loop gain. Moreover, the loop gain for the power rating value of 500W is also given in the same figure to show the stability of current control loop, that is how much the variation on the system would effect the loop gain.

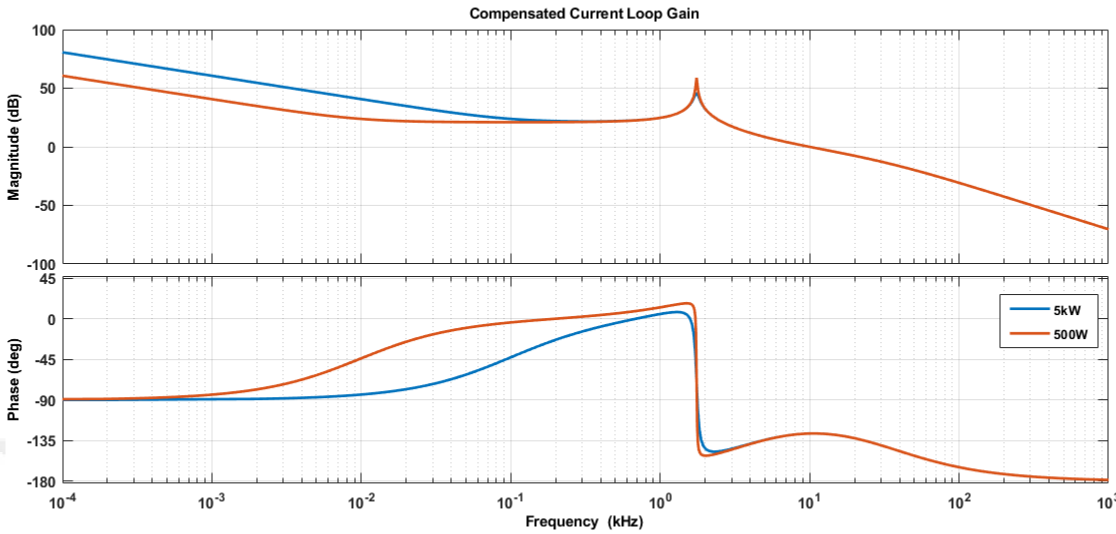

Figure 63: Compensated open loop bode plot of inner current control system for buck mode operation for DC/DC part of the system

The open current loop bode plot for boost mode of operation of the DC/DC converter is also shown in Figure 64. The loop gain has the cross-over frequency of 10 kHz and a phase margin value of 46° for the nominal operating condition according to the compensated current loop gain.

3.3.5 Design of Outer Voltage Loop for DC/DC Part

A voltage loop is usually designed around the inner current loop to regulate output voltage of the converter as well. For outer voltage loop design, cross-over frequency of the voltage loop is usually selected as one tenth of that for current one to prevent undesired interferences between the control loops and guarantee the stability so cut-off frequency for the outer loop is given as

$$f_{cv} = \frac{f_{ci}}{10} \tag{362}$$

$$f_{cv} = 1kHz \tag{363}$$

The bode plot of compensated open outer voltage loop is given in Figure 65 for buck mode of operation of the DC/DC converter. According to the bode plot, the

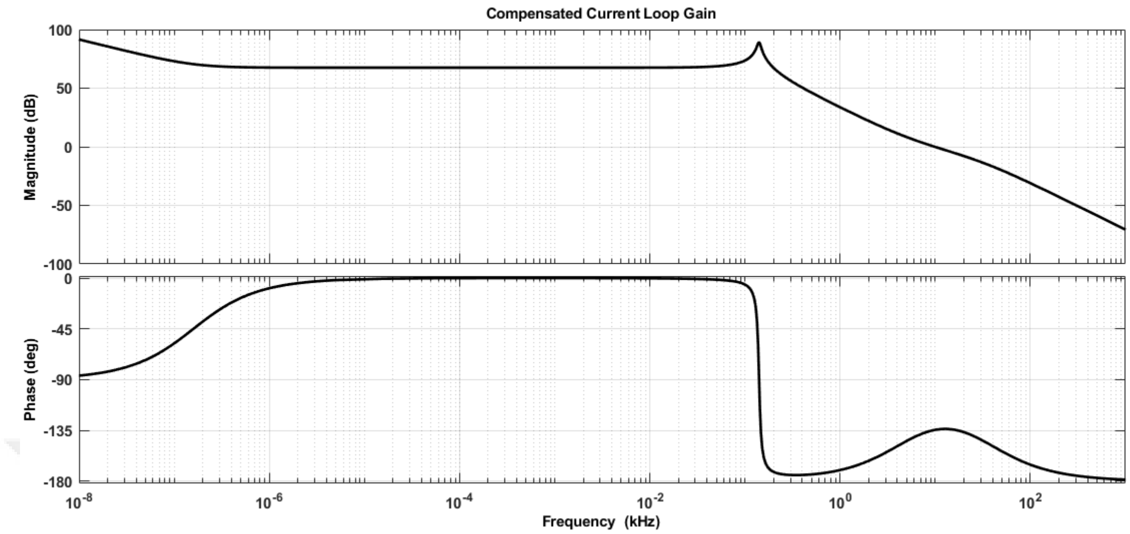

Figure 64: Compensated open loop bode plot of inner current control system for boost mode operation for DC/DC part of the system

compensated voltage loop gain has a cross-over frequency value of 1kHz and a phase margin value of 76° as expected.

For boost mode of operation, the bode plot of the voltage loop can also be constructed assuming that the output side has only DC bus capacitor as mentioned already. In addition, the battery side would be considered as input of the converter due to the direction of power flow reversed according to the case of buck operation. The open voltage loop bode plot for boost mode of operation is shown in Figure 66. The cross-over frequency of 1kHz with a phase margin of 72° are obtained based on the compensated voltage loop gain.

The design parameters of the control systems for both AC/DC and DC/DC converters, constituting the three-phase EV charger to be modeled, are also given in Table 5 as a summary.

There would be some other bode plots to be constructed using the loop gains designed for AC/DC and DC/DC side of the EV charger model to investigate closed loop responses for the complete bidirectional EV charger system including effect of

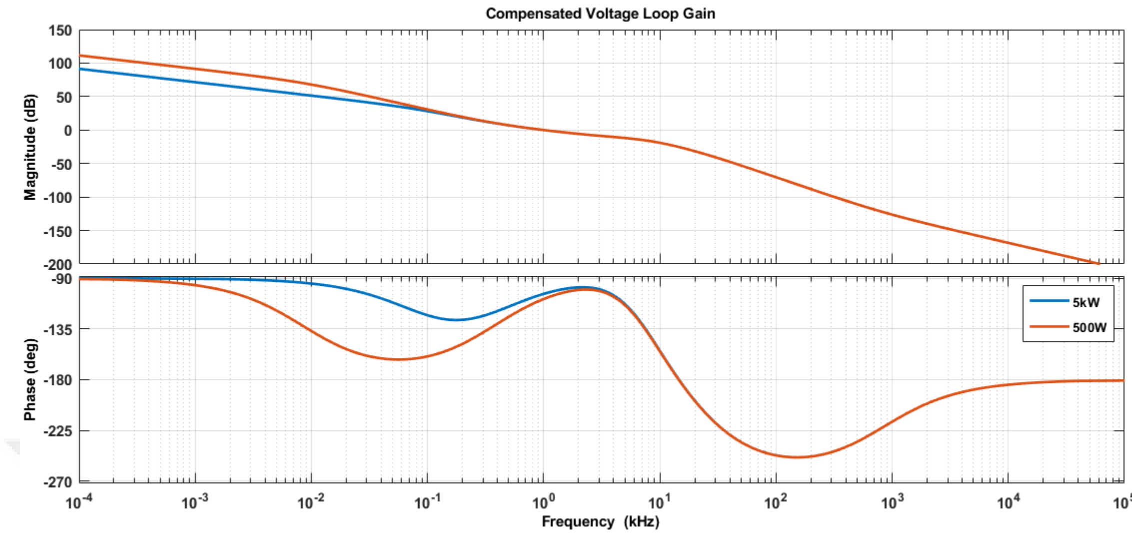

Figure 65: Bode plot of compensated open outer voltage loop for buck mode operation for DC/DC part of the system

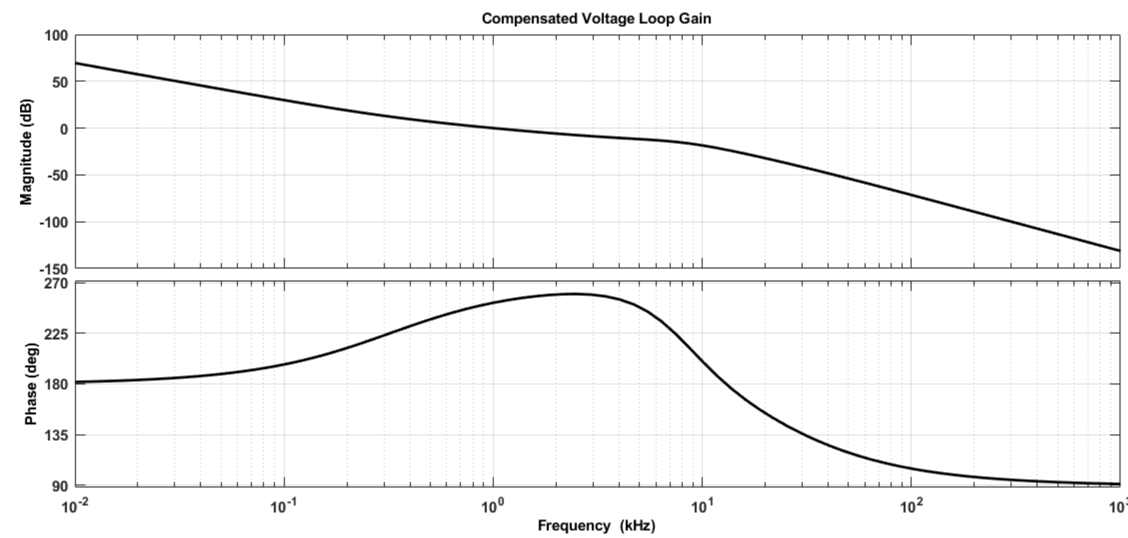

Figure 66: Bode plot of compensated open outer voltage loop for boost mode operation for DC/DC part of the system

variations in DC bus voltage, output battery voltage or load transient on the other system parameters for both G2V and V2G mode of operations. Hence, the closed loop responses can be analyzed individually for rectifier (power flow from the grid

Table 5: Design parameters of the control systems for both AC/DC and DC/DC converters of the three-phase EV charger

	AC/DC PWM Converter Control	**DC/DC Converter Control**	**Phase-Locked Loop (PLL) Control**
Cut-off frequency of inner (current) loop	-	10 kHz	-
Cut-off frequency of outer (voltage) loop	438 Hz	1 kHz	1 kHz
-3dB bandwidth of inner (current) loop	2.1 kHz	-	-

side to battery side) or inverter (power flow from the battery pack to the electricity grid) mode of operations of the EV charger model.

For G2V mode of operation

Some perturbations of load current or DC bus voltage, leading to deviations in battery voltage & inductor current would be evaluated for the rectifier mode of operation of the EV charger. The bode plot of closed loop output impedance gain with the maximum value of 12.7dB (4.3Ω) is given in Figure 67 for G2V mode of operation. It is also possible to investigate the related step response for the same loop. Step function has a wide range of frequency spectrum components, ones of which at the frequencies where output impedance values are maximum would have the most effect of the voltage deviation. Thus output voltage deviation value caused by a step change in load current is guaranteed to be less than the product of the load current step response value and maximum output impedance value of closed loop system for small perturbations. The same concept is also valid for a step change in line voltage, which can be considered as DC bus voltage for the EV charger modeled in this thesis and the deviation value of output caused by would be defined by the product of line voltage step response and the maximum value of closed loop line-to-output transfer function approximately. For load current variation of 1A at some frequency, the deviation at output voltage would be 4.3 V at most according to closed loop output impedance gain bode plot obtained using small-signal variation analysis as well.

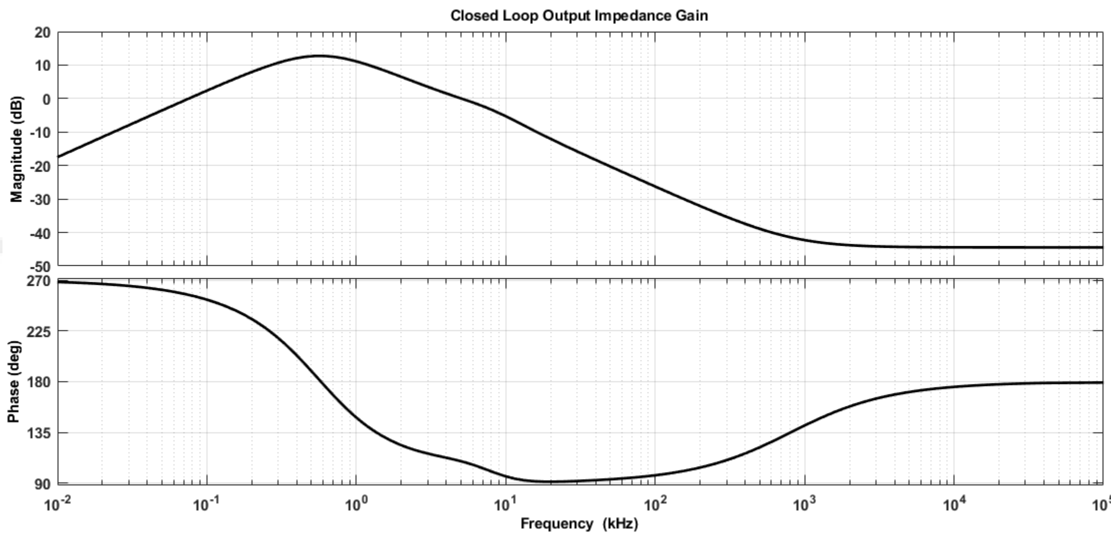

Figure 67: Bode plot of closed loop output impedance for G2V mode of operation

The bode plot of closed loop load-to-current gain for G2V mode of operation with the maximum value of -21.8dB (0.0813A) is given in Figure 68. It is expected that when the load current has the variation of 1A at some frequency, the deviation at inductor current would be 0.0813A at most according to closed loop load-to-current gain bode plot obtained from theoretical analysis using the concept of small-signal variation.

Closed loop line-to-output gain, having the maximum value of -31.9dB (0.0254V), for the rectifier (G2V) mode of operation is shown in Figure 69. For the voltage variation of 1V at DC link at some frequency, maximum possible value of the deviation of output voltage would be expected to be 0.0254 V according to closed loop line-to-output gain bode plot obtained using small-signal variation analysis.

The bode plot of closed loop line-to-current gain with the maximum value of -45.3

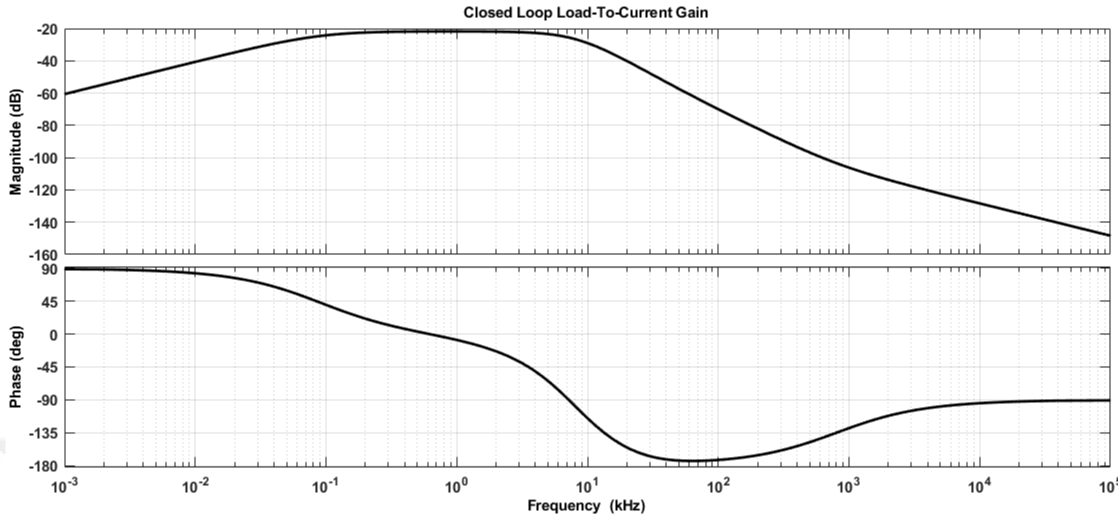

Figure 68: Bode plot of closed loop load-to-current gain for G2V mode of operation

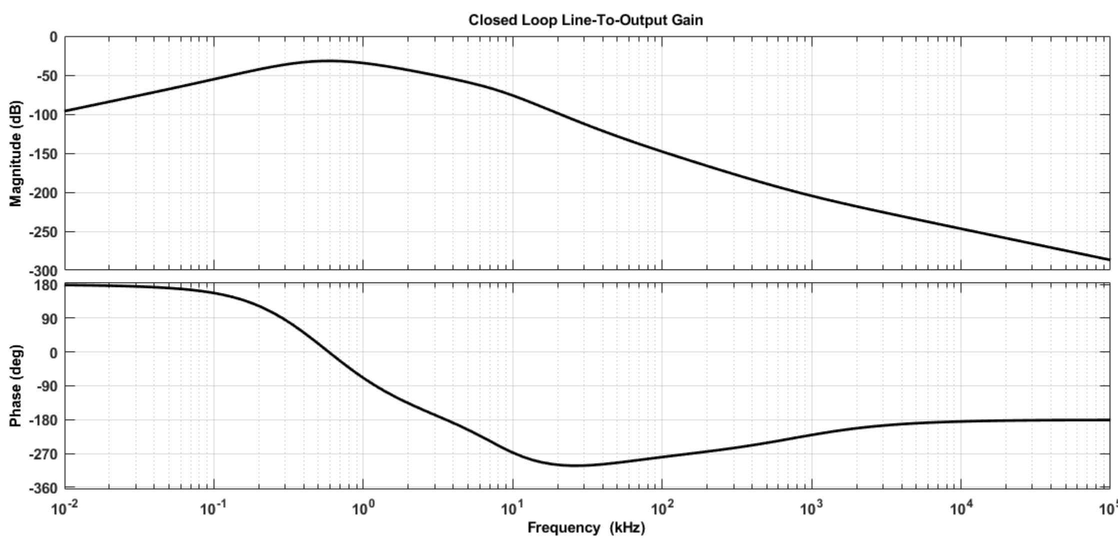

Figure 69: Bode plot of closed loop line-to-output gain for G2V mode of operation

dB (0.00543A) for the rectifier mode of operation is given in Figure 70 as well. It is expected that when the DC bus voltage has the variation of 1V at some frequency, maximum possible value of the deviation of inductor current would be 0.00543A based on closed loop line-to-current gain bode plot obtained with the concept of small-signal analysis again.

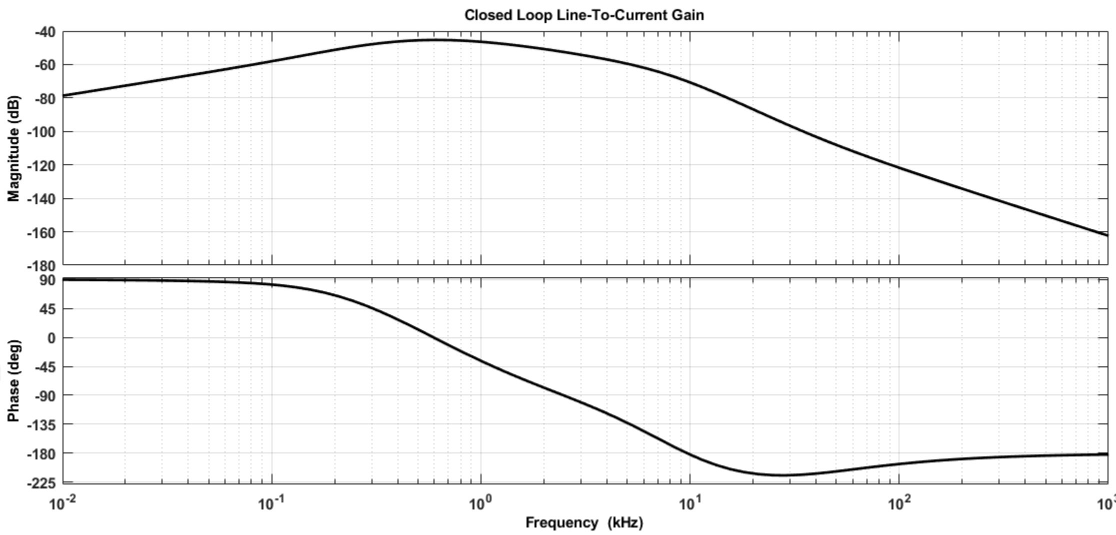

Figure 70: Bode plot of closed loop line-to-current gain for G2V mode of operation

For V2G mode of operation

Some changes in reference value of DC bus voltage or variations in battery voltage, causing deviations in DC link side or inductor current of the DC/DC converter operating as a boost converter, would be analyzed for the inverter mode of operation of the charger system. The bode plot of closed loop line-to-output gain, having the maximum value of -62.9 dB (0.00072 V), for V2G mode of operation is shown in Figure 71. For inverter operation of the EV charger, closed loop line-to-output response would be defined as the deviation observed in DC bus voltage with the variation in battery voltage. For battery voltage variation of 1V at some frequency, the deviation at DC link voltage would be 0.00072 V at most according to closed loop line-to-output gain bode plot obtained using small-signal variation analysis.

Moreover, closed loop line-to-current gain bode plot with the maximum value of -21.3 dB (0.0861A) for inverter (V2G) mode of operation is given in Figure 72. As

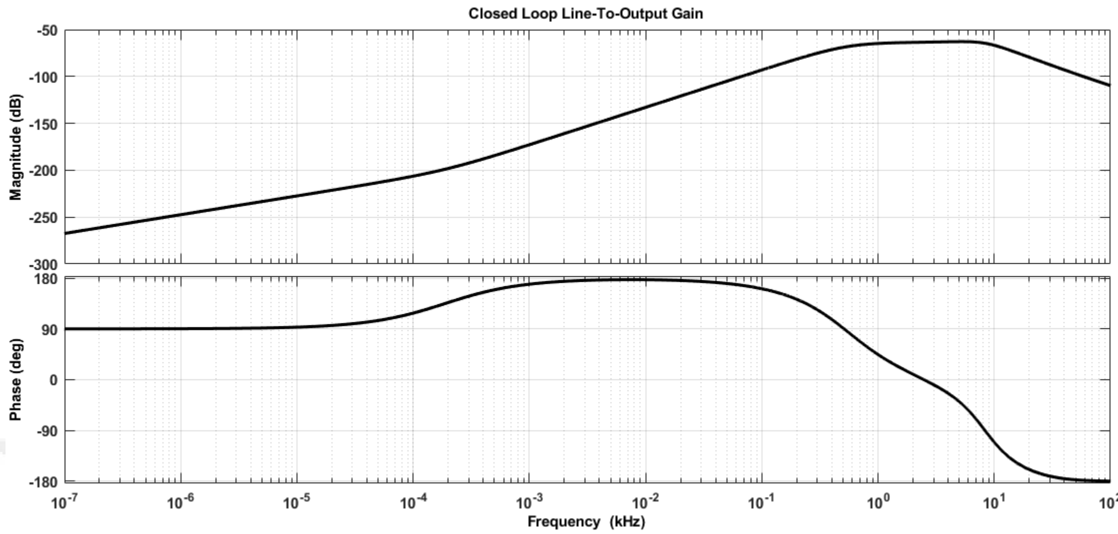

Figure 71: Bode plot of closed loop line-to-output gain for V2G mode of operation

in the case for line-to-output gain, for V2G operation, closed loop line-to-current response can be defined as the deviation observed in inductor current with the variation in battery voltage. It is expected that when the battery voltage has the variation of 1V at some frequency, the deviation at inductor current would be 0.0861A at most according to closed loop line-to-current gain bode plot obtained from theoretical analysis using the concept of small-signal variation.

Finally, the bode plot of closed loop gain for DC bus reference voltage deviation with the maximum value of 7.48 dB (2.37 V) for V2G mode of operation is shown in Figure 73. For the voltage variation of 1V in DC bus reference at some frequency, maximum possible value of the deviation of DC link voltage would be expected to be 2.37 V according to closed loop gain bode plot for DC bus step response obtained using small-signal variation analysis.

All of the bode plots constructed in this section can be considered as reference for analysis of the simulation results obtained under some conditions for the three phase bidirectional EV charger to be modeled

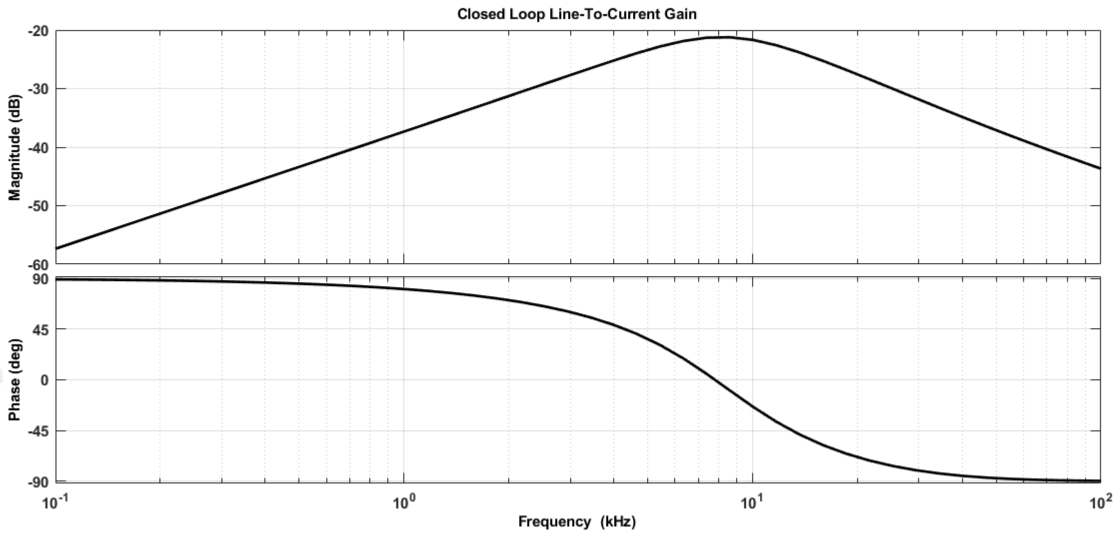

Figure 72: Bode plot of closed loop line-to-current gain for V2G mode of operation

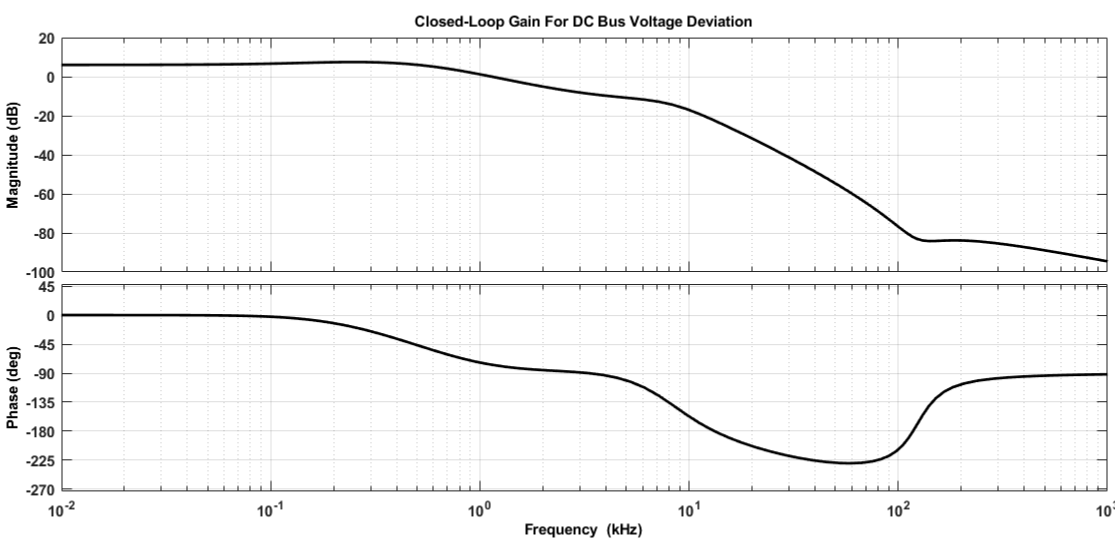

Figure 73: Bode plot of closed loop gain for DC bus reference voltage deviation for V2G mode of operation

CHAPTER IV

MODELING OF THREE-PHASE BIDIRECTIONAL CHARGER IN MATLAB/SIMULINK

The model of the proposed three phase grid-connected bidirectional EV charger circuit, of which the parameters are given in Table 4, can be developed with the corresponding control algorithms using Matlab/Simulink. The EV charger model to be simulated consists of the parts given below;

- Three phase AC/DC PWM converter
- Synchronous DC/DC converter
- Control system for AC/DC converter
- Control system for DC/DC converter

The model of the complete EV charger system constructed in Simulink is shown in Figure 74. DC bus capacitor with the related value is inserted between the models of AC/DC and DC/DC converters, providing regulation for the EV charger, as well. The system is connected to three-phase grid, modeled with three single phase voltage sources. The battery model is selected as Li-ion type since it can provide higher efficieny and has larger specific power value compared to the other types of batteries. Also a switch is inserted into the model, indicating the operation mode of the three phase EV charger. When it is ”1”, direction of the power flow would become from the grid to the battery (G2V mode) and it becomes vice versa (V2G mode) when it is ”0”.

4.1 Modeling of Three-Phase AC/DC PWM Converter

In this section the model for the three-phase AC/DC part of the bidirectional EV charger system is analyzed. Simulink model of the AC/DC PWM converter is given in Figure 75. It is clear that the circuit consists of six IGBT/Diode components, having corresponding internal losses. Also the LCL filter, proposed in the previous chapter, is modeled for the AC/DC converter.

The LCL filter block is given as a subsystem in the AC/DC PWM converter model. In Figure 76, the configuration inside LCL filter block is shown as well. The parameters for the filter components, of which values are determined and given in Table 4, are the same for all of three phases.

Moreover, the algorithm for generation of the gate signals to be applied to the transistors of AC/DC converter is modeled as shown in Figure 77. Since the circuit is operated in closed control loop, the signals obtained in output of the control algorithm, of which the related model is analyzed in next sections, "m_a","m_b", "m_c" are compared with a triangular carrier wave with the frequency, $f_{sw,ac}$ and the gate signals are created according to the model for PWM signal generation.

4.2 Modeling of DC/DC Converter

The Simulink model for the bidirectional DC/DC converter, which is the other part of the proposed EV charger system, would also be investigated. The related DC/DC converter model is shown in Figure 78. It includes two MOSFET/Diode components, providing a synchronous operation. Moreover, the converter can operate in buck or boost mode depending on pattern of the gate signals applied to the transistors. It is noticed that the value of sense voltage of inductor current, which is notated as "$v_s = R_f i_L$", depends on the direction of power flow and can be negative when the converter operates in boost mode. Therefore a minus sign can be inserted to obtain a positive v_s value to be used in the control algorithm whenever the three phase EV charger model operates in V2G mode.

The algorithm of PWM generation would also be implemented for both buck and boost mode operations of the DC/DC converter in Simulink environment as given in Figure 79. When the value of the indicator, determining the direction of power flow, is "1", the gate signals are generated based on the buck mode operation. Whereas they are produced according to the boost one with the indicator value of "0".

It can be noticed that the PWM generator block is inserted as a subsystem into the algorithm in Figure 79 as well. The details of model of PWM generator block, responsible for comparing the signal generated as output of the two-loop controller system for DC/DC converter with the carrier signal having the frequency of $f_{sw,dc}$, is given in Figure 80.

4.3 Modeling of Control Systems

Control systems for both AC/DC PWM converter and synchronous DC/DC converter are constructed in Simulink in addition to the bidirectional EV charger circuit model in this section.

Modeling of Control Algorithm for AC/DC PWM Converter

The control of AC/DC part of the EV charger model is achieved by two DC components, which are voltages & currents in rotating (dqe) reference frame and obtained via Clark-Park Transform. Measurements of three phase voltages and line currents for the bidirectional AC/DC PWM converter would be modeled in Simulink as shown in Figure 81. Transfer functions of voltage and current sensors with the corresponding measurement delay parameters are also given to obtain sensed phase voltage and current values for all of three phases.

Then "q" and "d" components for both of the measured phase voltages and line currents can be obtained applying Clark-Park Transformation. The blocks of this transformation, leading to two DC components from three phase sine waves for the phase voltages & currents, are shown in Figure 82.

Also the mathematical modeling of Clark-Park Transformation block is given in Figure 83. It converts three phase components into two phase ones in rotating reference frame with the related equations, derived in Chapter 2.

Moreover the PLL (Phase Locked Loop) algorithm would be implemented with the corresponding design parameters in Simulink environment. The model of PLL system, for which the imaginary (d) component of the phase voltages in the rotating reference frame, V_{de} is used as reference, is shown in Figure 84. It can be noticed that the value of angular line frequency, notated as "$\omega_{line} = 2\pi f_{line}$", is added as a feedforward into the loop as well.

The complete control algorithm for three phase bidirectional AC/DC PWM converter in Simulink is given in Figure 85. It can be seen that the control system consists of decoupling current compensators for both "q" & "d" components of the line current, forming the inner current loop, and DC bus voltage controller, creating the outer voltage loop. Also the sampling delay for the current loop is taken into account while determining the design parameters of the inner control system in Chapter 2 so blocks for sampling delay for "q" & "d" components of the measured phase currents are inserted into the model. For the activation of inverter mode of operation, a saturation block, forcing the output of voltage PI controller to be some negative value, is included for the DC link voltage controller as well. When the indicator value becomes "0", the EV charger model would operate in V2G mode, causing the real (qe) component of the measured line currents, I_{qe} to flow in the reversed direction (power flow from DC bus to the electricity grid) so the reference value of "q" component of the current is set to a negative value in the case of inverter mode of operation. The voltage components of "V_{iqe}" & "V_{ide}" can be obtained using the related mathematical equations given in (273) and (274) or referring to Figure 44, which are also applied in the control algorithm in Simulink environment. Then three phase voltage waves are formed via inverse Clark-Park Transformation, converting the voltage components in the rotating reference frame to those in three phase system and included for the model as well. After obtaining modulation signals using the equation of (4), the resultant waveforms for modulation are created inserting the block of zero-sequence injection into the model of the control system, which is proposed to increase linearity range of modulation index for the related signals.

Moreover, the detailed modeling of inverse Clark-Park Transformation block is given in Figure 86. It converts two phase voltage components in the rotating (dqe) reference frame into ones given in three phase system via the related equations, which can be obtained rearranging ones derived in Chapter 2, as well.

The subsystem of zero-sequence injection block in the control algorithm of AC/DC PWM converter model is also shown in Figure 87. It is clear that the corresponding equations given in (9)-(12) are implemented in Simulink according to the figure.

Modeling of Control Algorithm for DC/DC Converter

The control of DC/DC part of the three phase bidirectional EV charger model is managed by two-loop control system, having outer voltage loop which regulates the battery voltage or DC bus voltage depending on the mode of operation for the synchronous DC/DC converter and inner current loop that is responsible for tracking the reference value for inductor current. The control algorithm for the DC/DC converter would be implemented in Simulink as shown in Figure 88. It can be noticed that there are two subsystems inserted into the model for current & voltage controllers. One is activated for buck mode of operation when the value of indicator is set to "1" and the other is considered for the DC/DC converter operating in boost mode for which the indicator value is "0". For the rectifier mode of operation (G2V) of the EV charger model, the bidirectional DC/DC converter acts as a buck type so the output voltage can be considered as the battery voltage, which is desired to be sensed and regulated in the two-loop control system. On the other hand, the synchronous

DC/DC converter would operate in boost mode, for which the power flow becomes from the battery side to the DC link, when the three phase charger system is in the inverter mode of operation (V2G). Therefore the output voltage could be regarded as the DC bus voltage, that is regulated in the control system for DC/DC part of the EV charger model for this mode of operation. Furthermore the sensed voltage for the inductor current, v_s is used as measured value for the current controller.

In Figure 89, inside the subsystem of the two-loop controller is shown with voltage and current PI controller blocks, having the related parameters determined based on the design criteria of the control algorithm, in Simulink. As discussed in Chapter 2, the output of voltage compensator is used as the reference for the current one. The output of the current controller is also used for generation of gate signals.

Moreover, the modeling of the current controller block for the DC/DC converter is given in Figure 90. It can be seen that transfer function of sampling delay with the corresponding delay parameter, which is notated as $T_{samp,dc}$, is inserted into the model to take the sampling effect into account for the two-loop control system.

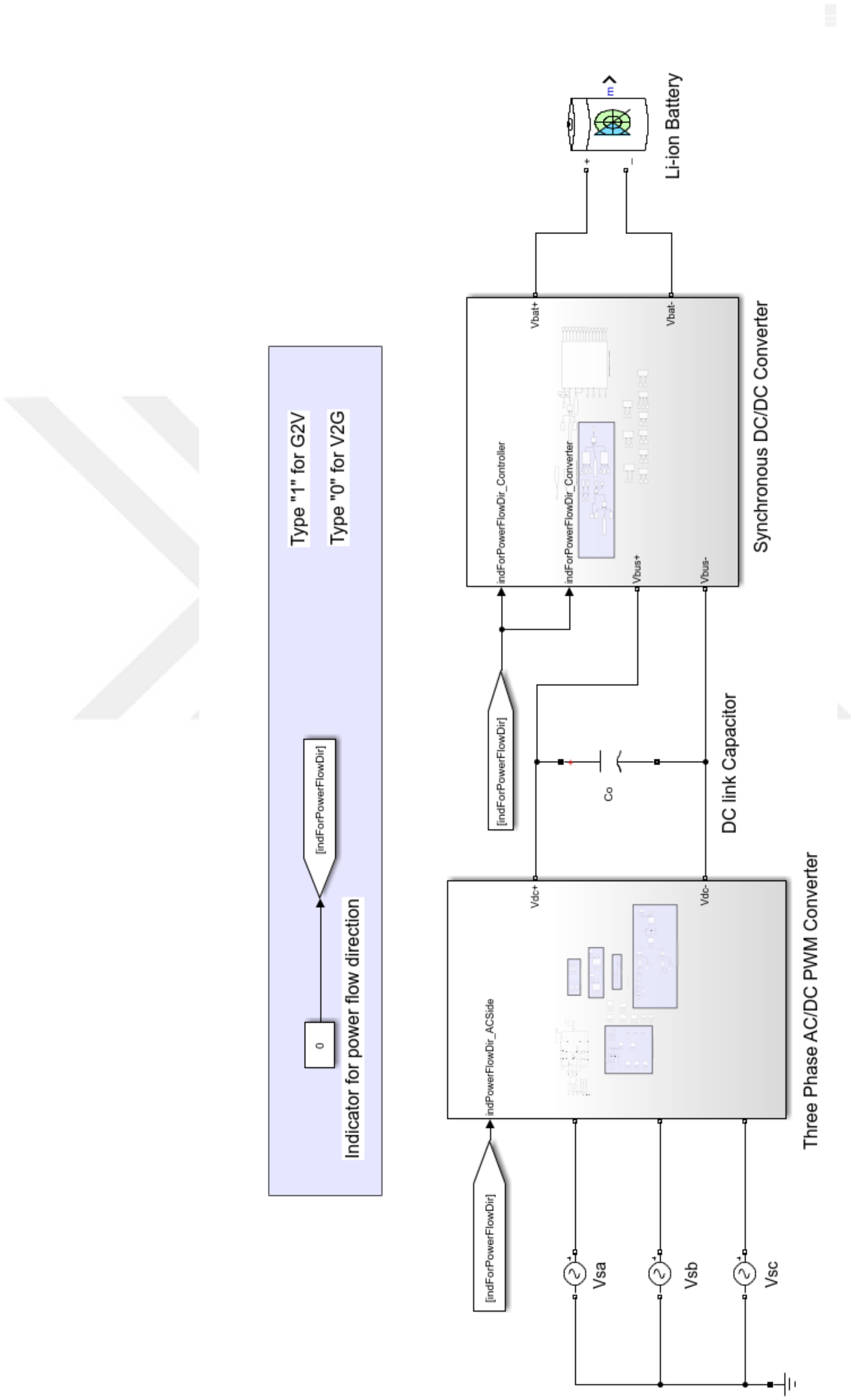

Figure 74: The model of the complete EV charger system in Simulink

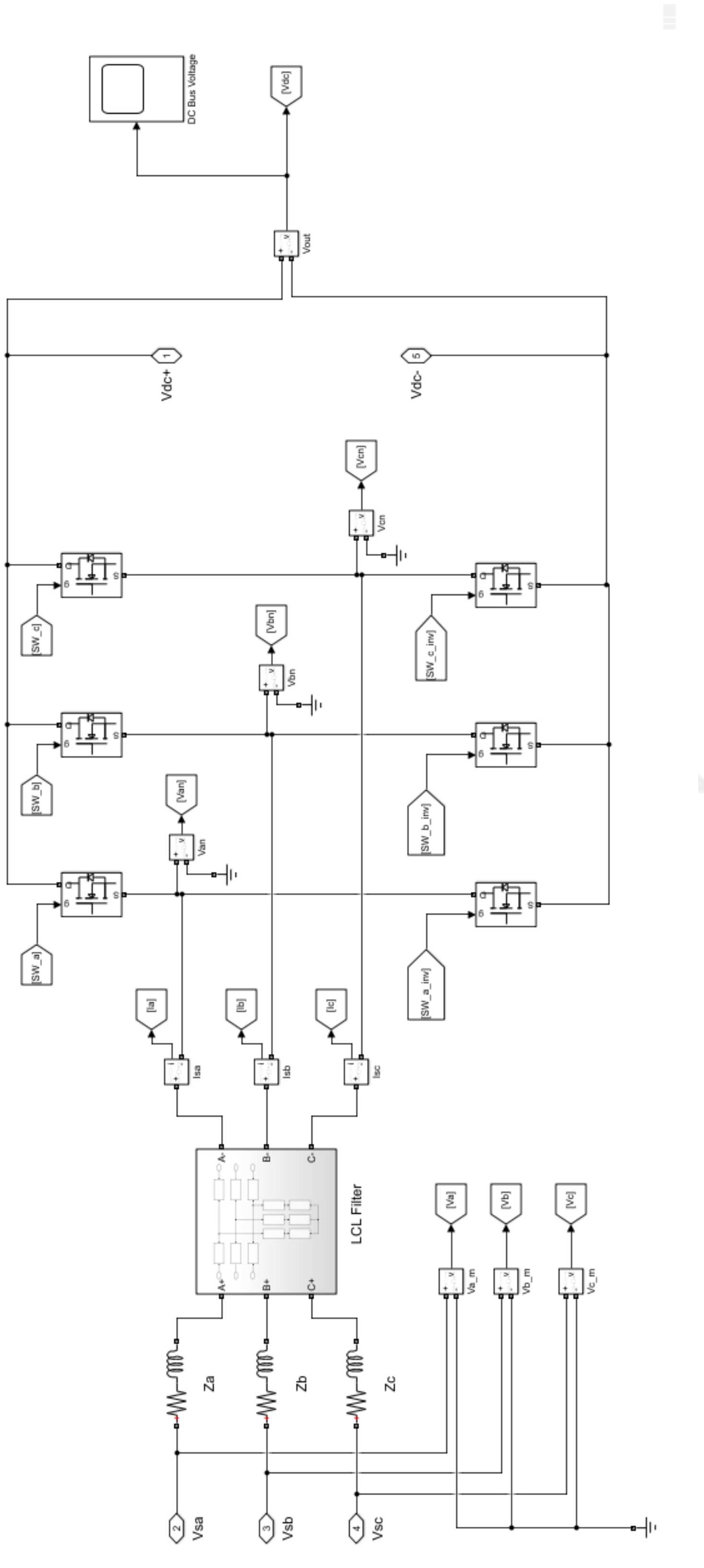

Figure 75: The model of there phase AC/DC PWM converter in Simulink

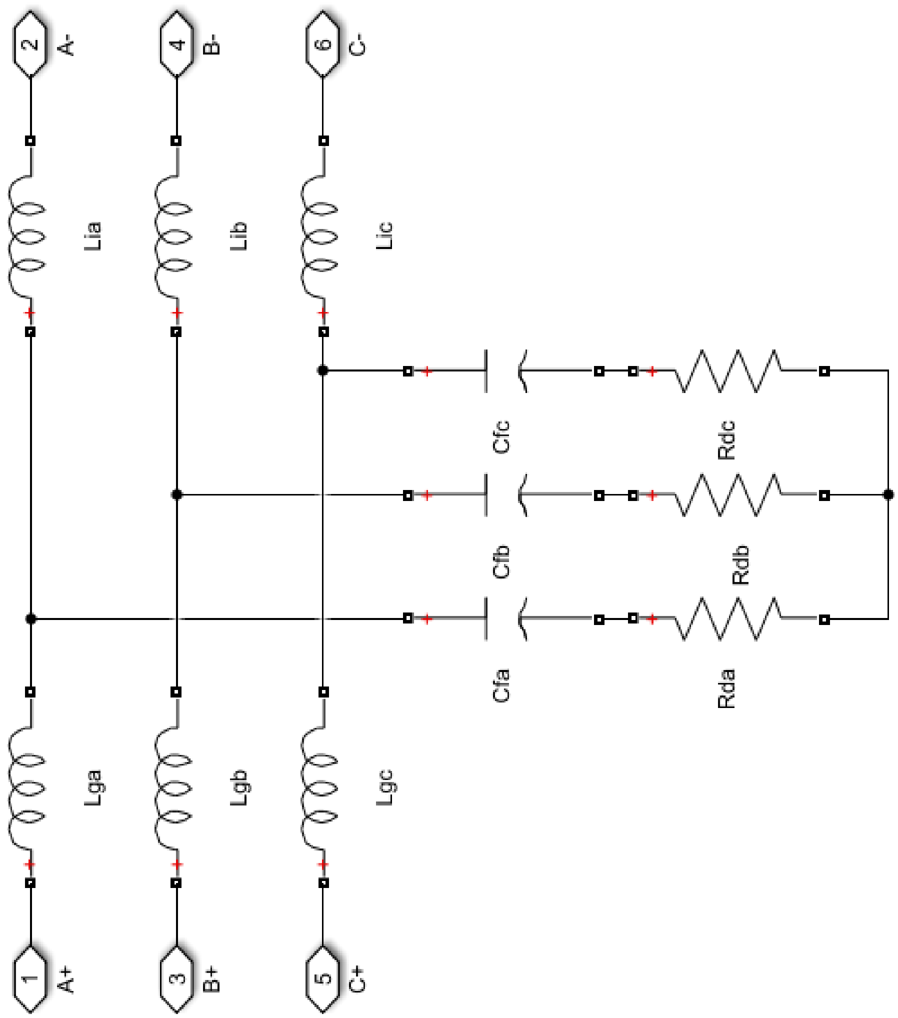

Figure 76: The configuration of LCL filter in Simulink

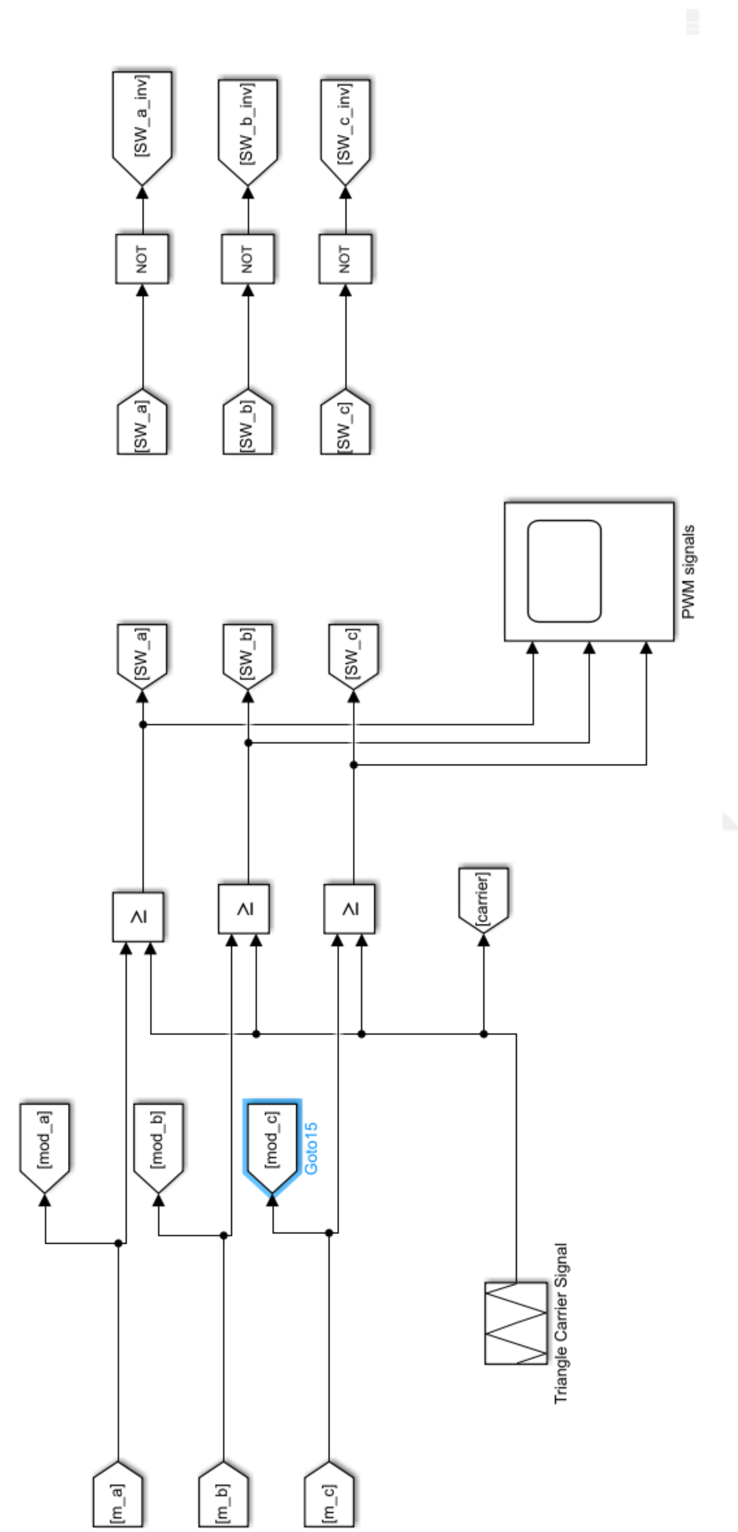

Figure 77: The model of generation of gate signals for AC/DC PWM converter in Simulink

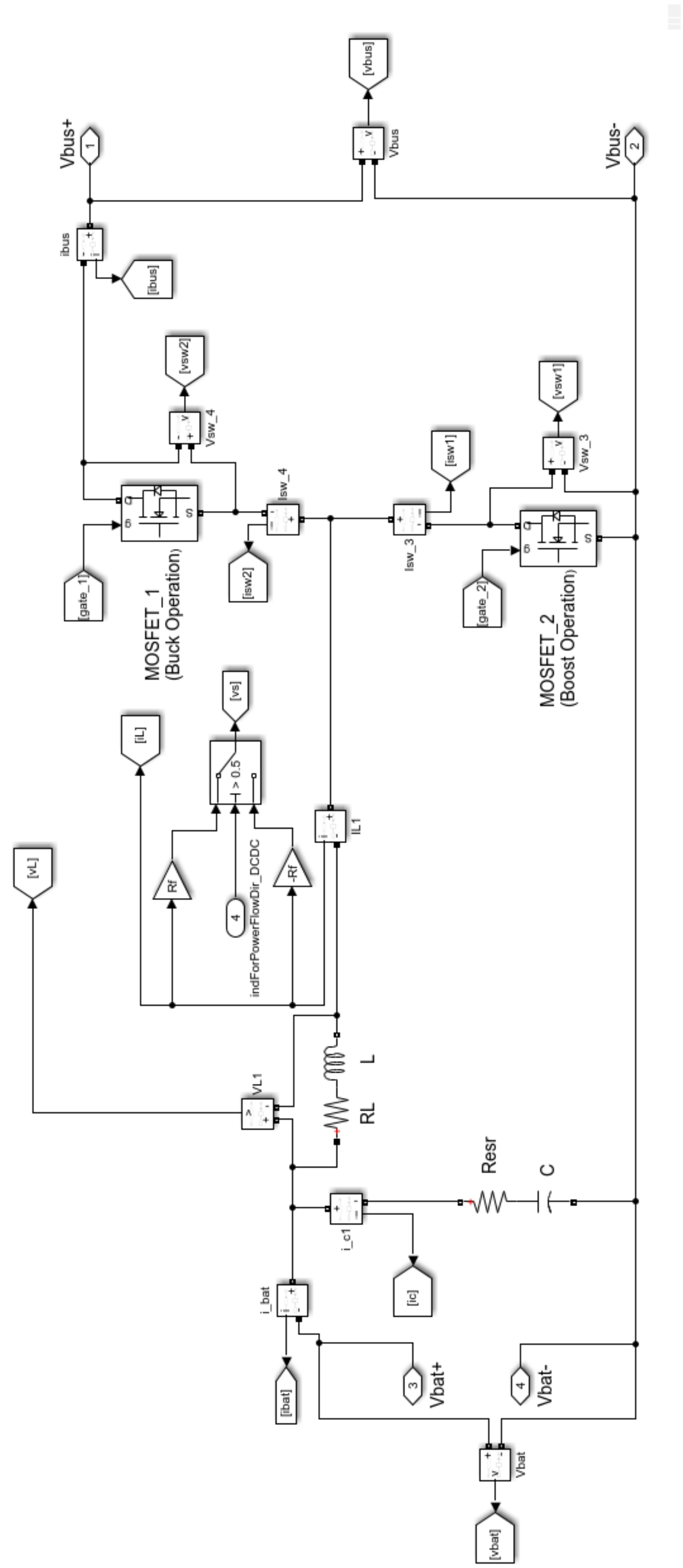

Figure 78: The bidirectional DC/DC converter model in Simulink

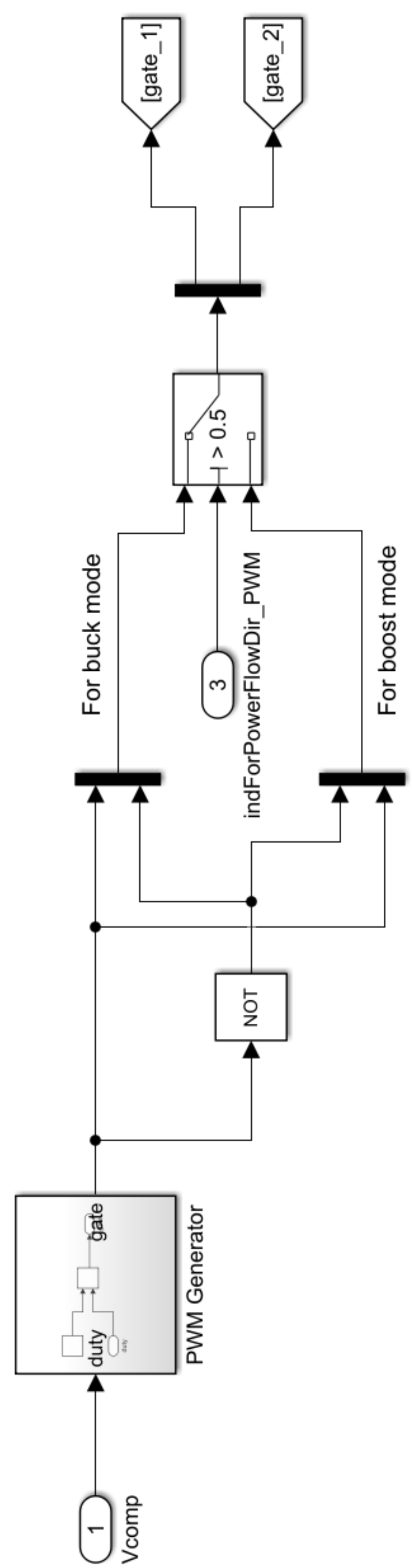

Figure 79: The algorithm of PWM generation for DC/DC converter in Simulink

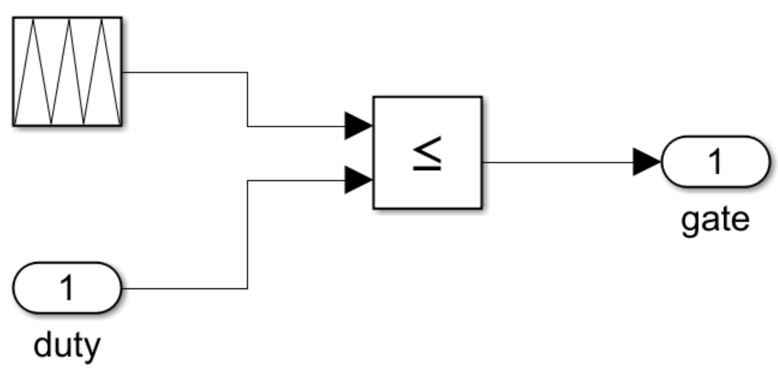

Figure 80: The PWM generator block for DC/DC converter in Simulink

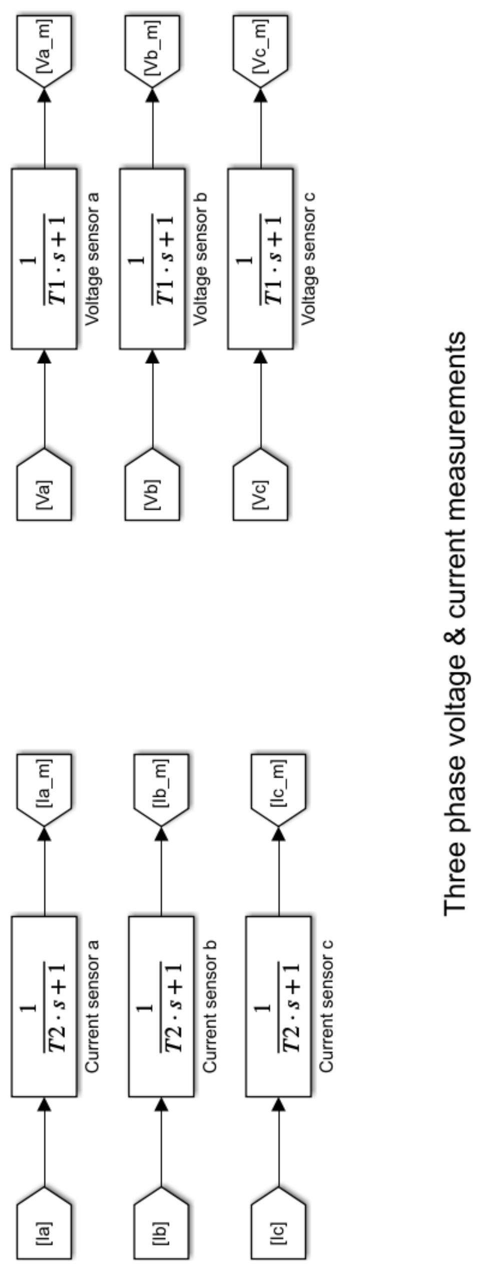

Figure 81: The model of measurements of three phase voltages and line currents for the bidirectional AC/DC PWM converter in Simulink

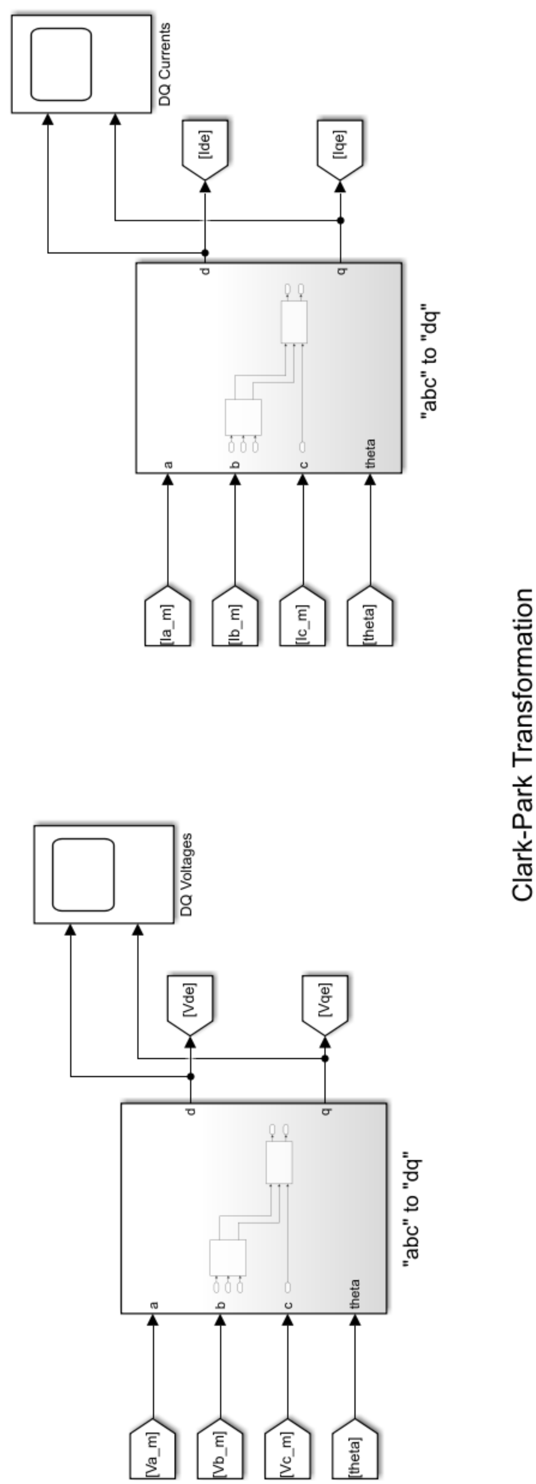

Figure 82: The blocks of Clark-Park Transformation leading to two DC components from three phase sine waves for the phase voltages & currents in Simulink

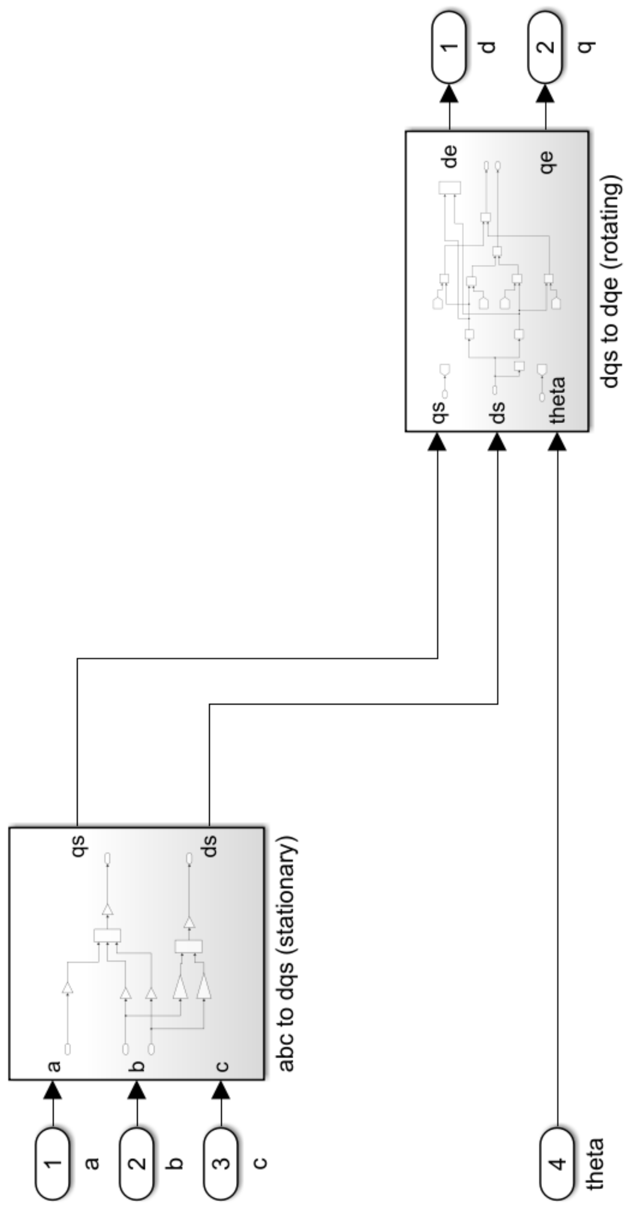

Figure 83: The mathematical modeling of Clark-Park Transformation block in Simulink

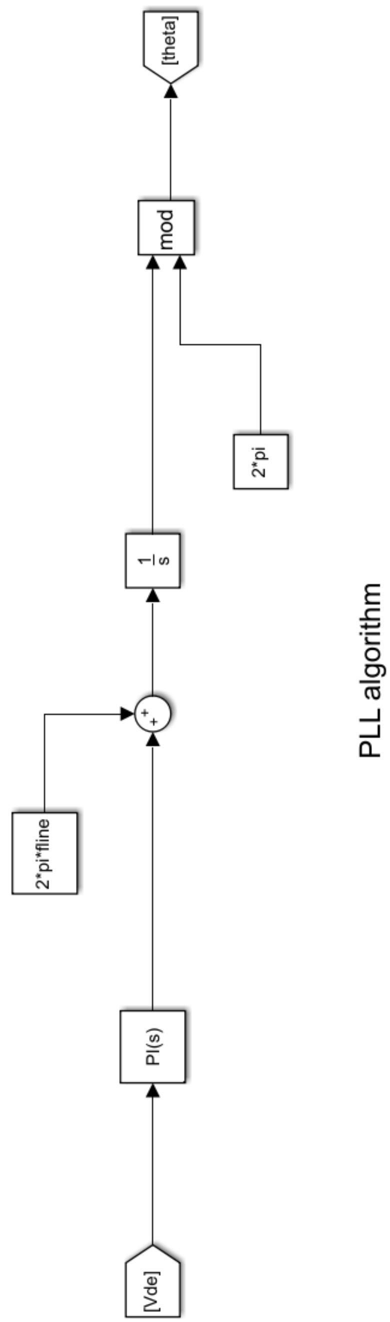

Figure 84: The model of PLL (Phase Locked Loop) system in Simulink

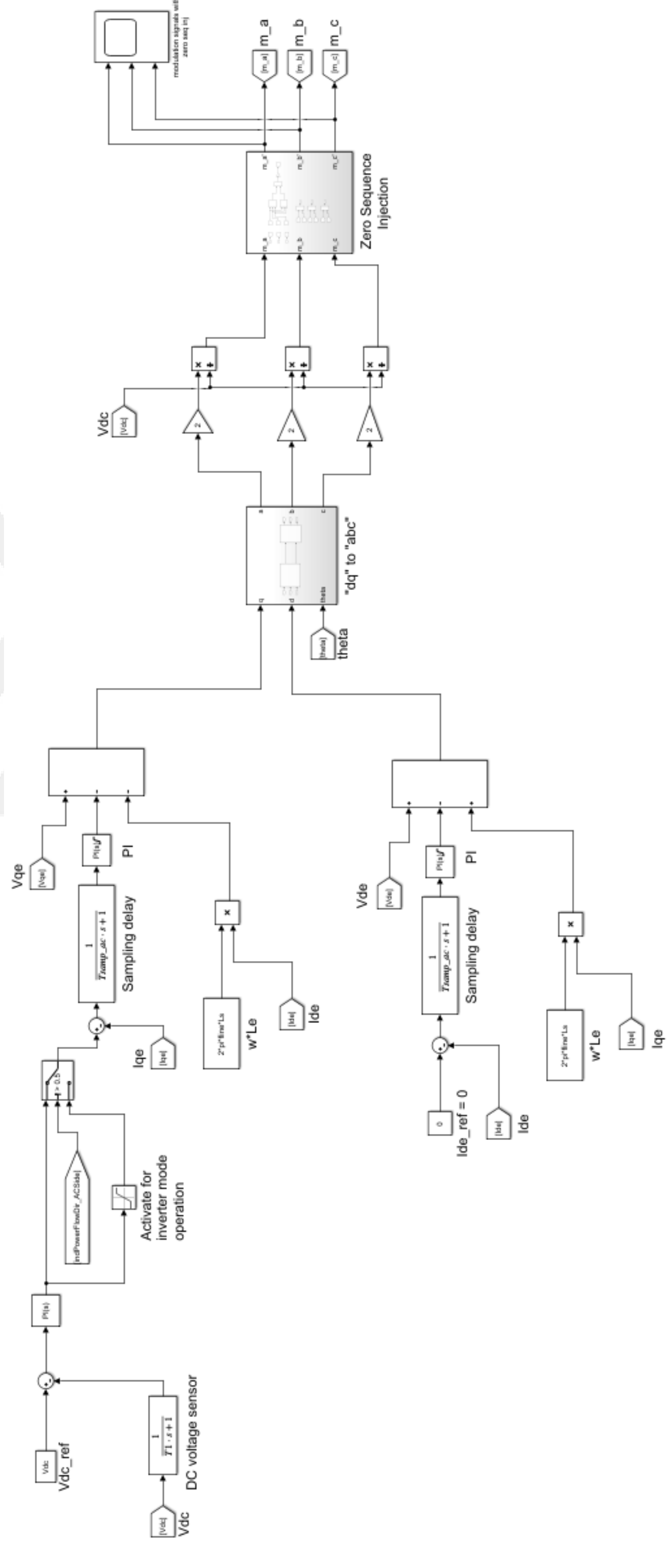

Figure 85: The complete control algorithm for three phase bidirectional AC/DC PWM converter in Simulink

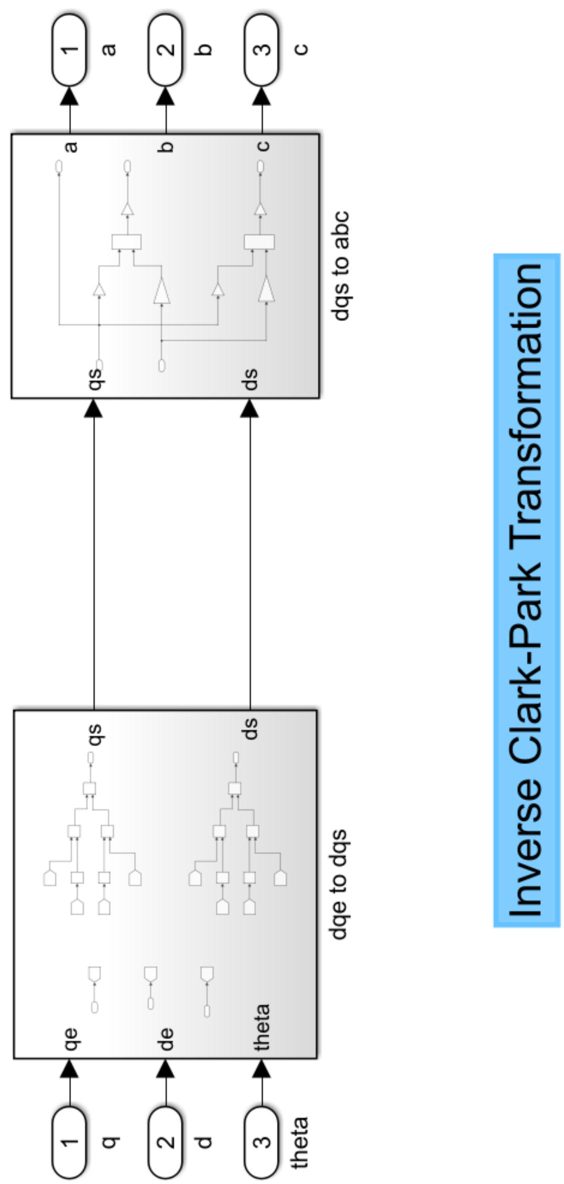

Figure 86: The detailed modeling of inverse Clark-Park Transformation block in Simulink

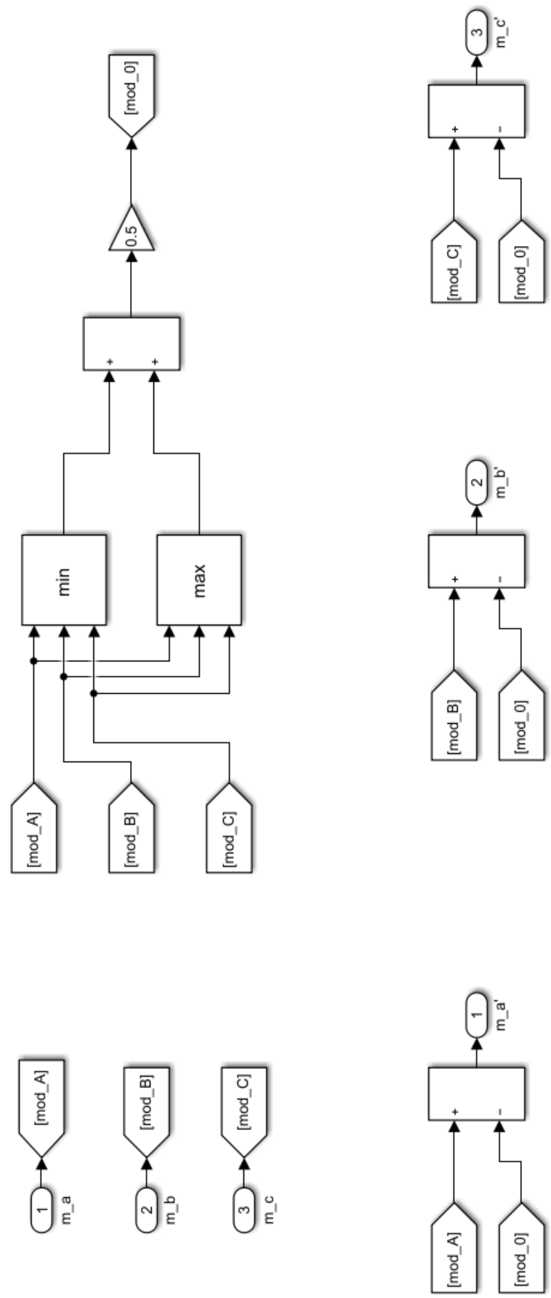

Figure 87: The subsystem of zero-sequence injection block in Simulink

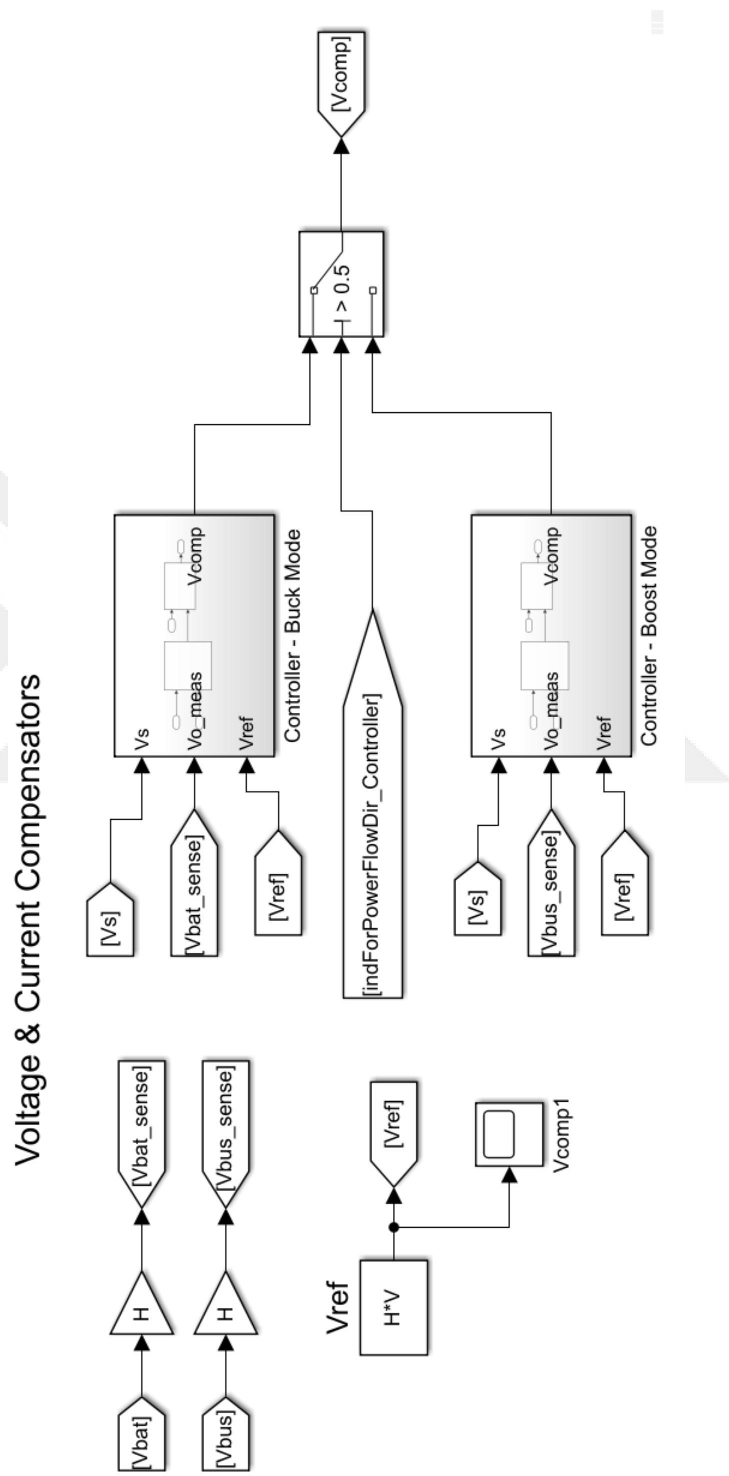

Figure 88: The control algorithm for the DC/DC converter in Simulink

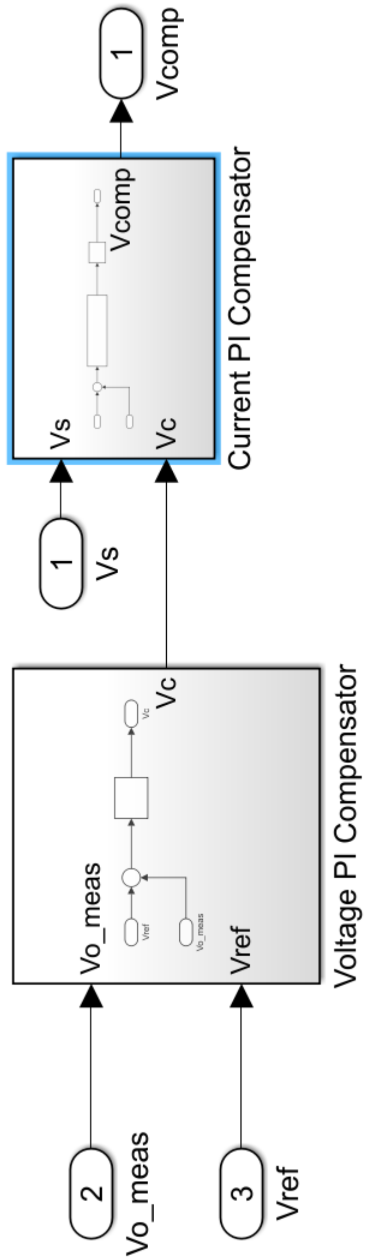

Figure 89: Inside the subsystem of the two-loop controller in Simulink

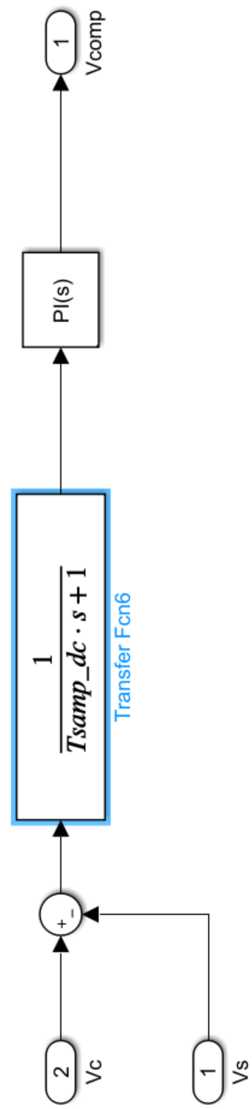

Figure 90: The modeling of the current controller block for the DC/DC converter in Simulink

CHAPTER V

SIMULATION RESULTS AND ANALYSIS

The simulation work for the three-phase bi-directional EV charger, of which the model is presented in the previous chapter, is performed under various operating conditions like steady-state, load transient, line distortion, DC bus variation and variation in battery voltage level.

5.1 Analysis of Closed-Loop System Performance

The EV charger system modelled with the relevant controller blocks, creating a closed loop system, can be evaluated via some simulation study.

5.1.1 Steady-state

In this section, the system is analyzed under steady-state condition for both G2V and V2G mode of operations.

5.1.1.1 In G2V Mode of Operation

The performance of the closed loop system for the EV charger model would be analyzed with various battery voltage charging values.

<u>With 500V battery voltage reference</u>

While the EV charger model is operating at rated conditions (500V, 5kW), steady-state performance of the system would be evaluated. The waveforms of the battery voltage and inductor current in steady-state is shown in Figure 91. The peak-to-peak value of output battery voltage, ΔV is measured as 250mV, which is higher than that calculated by DC analysis as given in the equation (353) due to battery load, including some additional dynamics. Also, that for the inductor current, Δi_L is determined as

3.7A, that verifies the value given in (352) & (354) obtained from theoretical analysis. Hence these values are consistant with the calculated ripple values for selection of the inductor and output capacitor in the Chapter 3 as well. The average value of the inductor current, i_L, equal to battery current, is 10A.

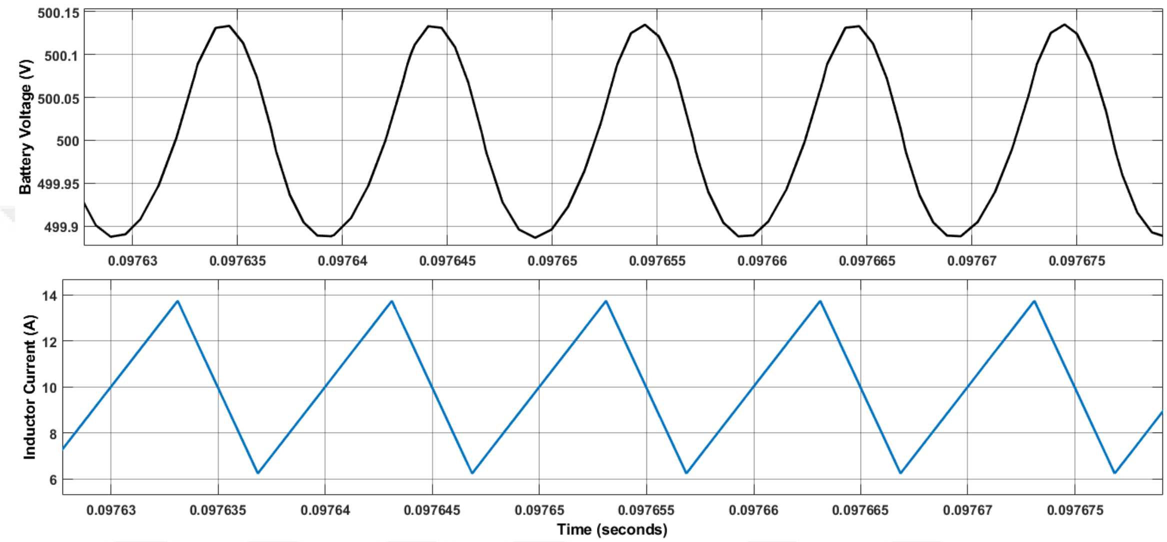

Figure 91: Simulation result for the battery voltage and inductor current in steady-state condition in rectifier mode of operation (with 500V output)

The graph of DC bus voltage, which is able to track the reference value of 800V successfully, is given in Figure 92. The ripple value of the DC link voltage, which is less than 150mV, depending on the DC bus capacitance value, is also very small.

The waveforms of ”q” and ”d” components of line current are also given in Figure 93. The real (q) component of current has the value of 31.5-32 A. The imaginary (d) component is kept to 0A as expected as well.

The waveforms of ”q” and ”d” components of phase voltages are also given in Figure 94. The real (q) component of voltage has the constant value of 325V as expected whereas the value for imaginary component is equal to zero.

Moreover, the phase voltage and line current waveforms corresponding to one of three phases are shown in Figure 95. It is clear that line current is almost in

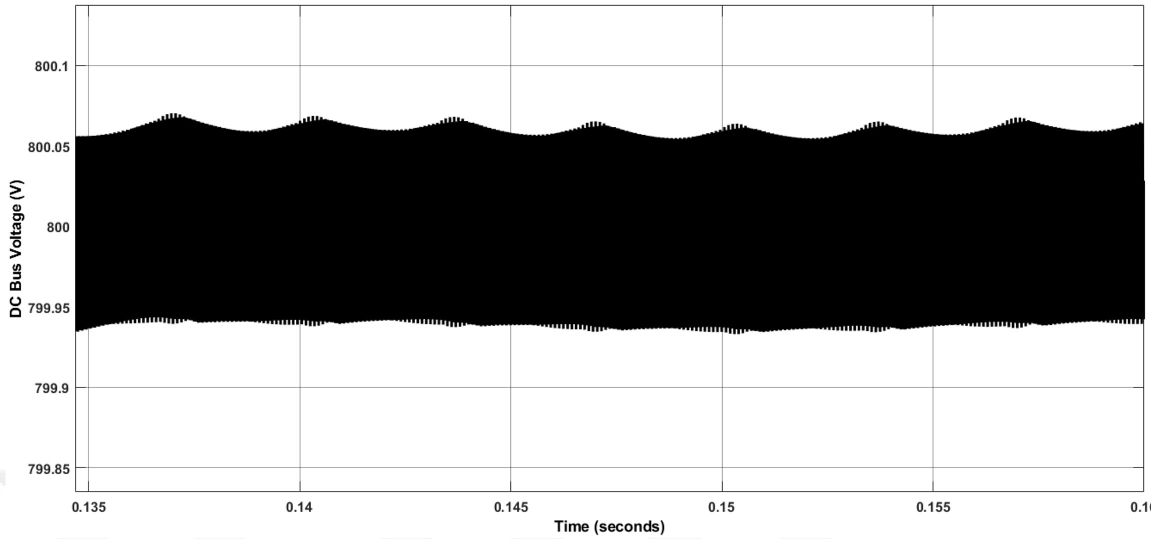

Figure 92: Simulation result for the DC bus voltage in steady-state condition in rectifier mode of operation (with 500V output)

phase with the phase voltage, that indicates the bidirectional EV charger operates in rectifier (G2V) mode. The peak value of the line current, I_m is same with the value of q component current, i_{qe} based on the results.

The waveforms of phase voltage and corresponding phase angle are given in Figure 96. As it can be observed in the plot, in one cycle of the phase voltage, the phase angle value changes from 0 to 2π in rad linearly, determining instantaneous value of the phase voltage, verifying that PLL control algorithm is able to track the phase angle.

The modulation signal waveforms corresponding to all of three phases are also shown in Figure 97. Thanks to zero sequence injection algorithm, the shape of the waveforms are different from pure sine wave as mentioned in Chapter 2. According to the simulation result, RMS value of line-to-line voltage obtained from inverse Clark-Park Transform is measured nearly as 171V. The peak value of the modulation signal waves is expected to be $1/1.115 \approx 0.9$ times of that for the case in which any modulation signal is not applied. Hence the peak of the modulation signal according

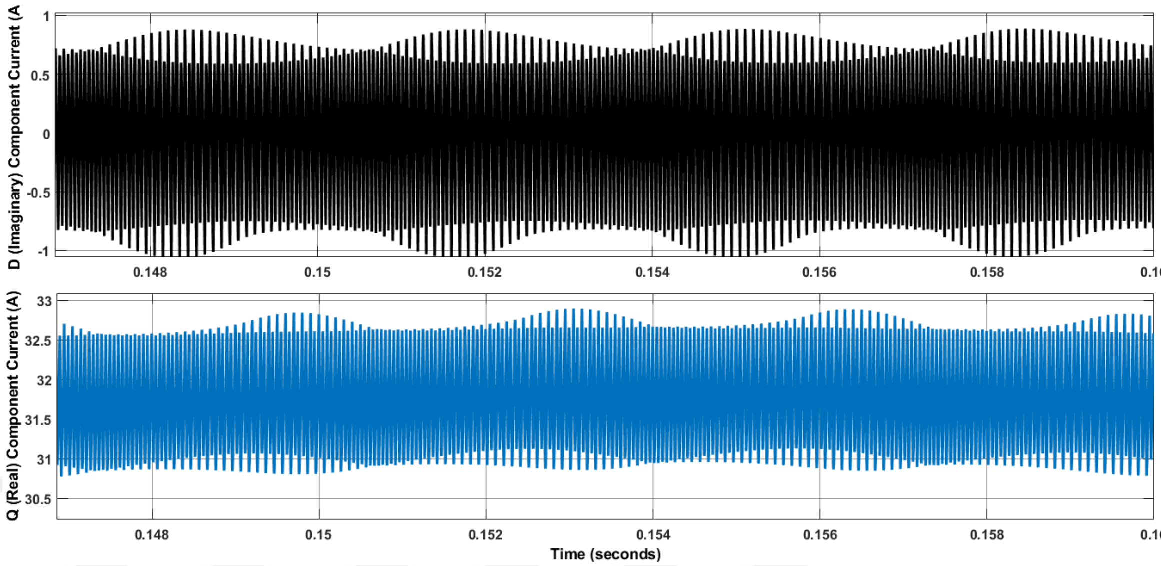

Figure 93: Simulation result for "q" and "d" components of line current in steady-state condition in rectifier mode of operation (with 500V output)

to the equation in (5) would be;

$$m'_a = 0.9\frac{V_{1,ll,rms}}{0.612V_{dc}} = \frac{0.9\ x\ 171}{0.612\ x\ 800} \tag{364}$$

$$m'_a = 0.31 \tag{365}$$

The peak value of modulation signals calculated theoretically is approximately same as that observed in the simulation result as well.

<u>With 400V battery voltage reference</u>

The EV charger system can also be simulated for charging with different battery voltage levels. While the charging of the output battery is performed with 400V, the closed loop performance of the system is analyzed. The waveforms of the battery voltage and current in steady-state with the output reference voltage of 400V is shown in Figure 98.

The waveform of DC link voltage with 800V reference value is also given in Figure 99. The DC bus voltage controller is able to regulate DC link and track the reference voltage value in a desired way according to the plot. The ripple value of DC link

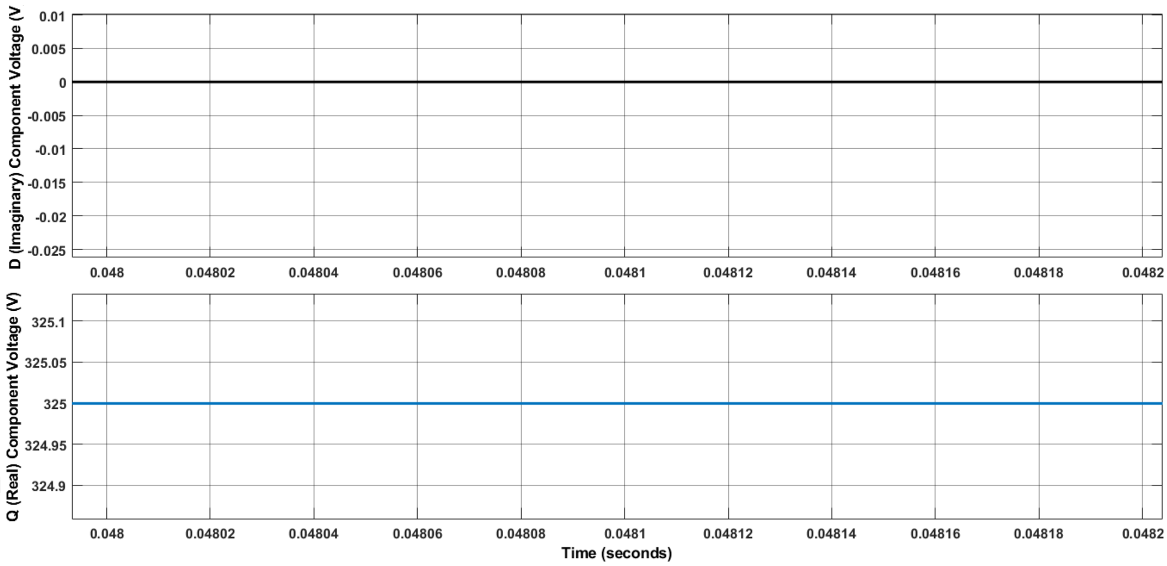

Figure 94: Simulation result for "q" and "d" components of phase voltages in steady-state condition in rectifier mode of operation (with 500V output)

voltage is almost same with that for the case in which the output battery voltage is 500V as well.

The waveforms for line current components in "dq" reference frame are shown in Figure 100. The real (q) component of current has the value of 28-28.5 A for the 400V output voltage case in steady state operation, which is not very different from that for the case of the rated condition with output voltage of 500V. The imaginary (d) component is kept to 0A as desired.

With 300V battery voltage reference

For the charging of the output battery with 300V, the closed loop performance of the system would be evaluated. The waveforms of the battery voltage and current in steady-state with the output reference voltage of 300V is shown in Figure 101. It can be noticed that the average value of inductor current, leading to the value of output battery current, is not very different from those obtained for the cases of 400V and 500V output.

Moreover, the waveform of DC link voltage, having a reference value of 800V, is

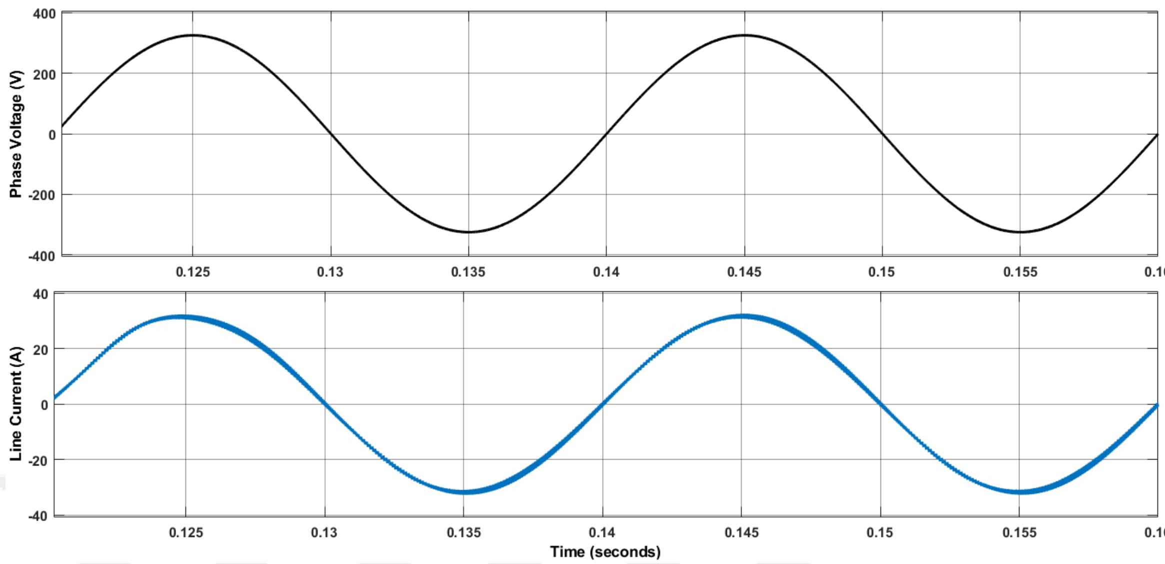

Figure 95: Simulation result for phase voltage and line current waveforms in steady-state condition in rectifier mode of operation (with 500V output)

given in Figure 102. The DC bus voltage value is able to set to the desired one and the ripple value is a bit smaller than those for the cases in which the output voltage are 400V & 500V based on the plot as well.

The waveforms of "q" and "d" components of line current are also shown in Figure 103. For the case of 300V battery voltage, the real (q) component of current has the value of 20.5-21 A in steady state operation, which is smaller than those for the cases with output voltage of 400V and 500V. The imaginary (d) component is set to 0A as well.

5.1.1.2 In V2G Mode of Operation

The performance of the closed loop system for the EV charger model would be analyzed with various battery voltage charging values in inverter (V2G) mode of operation.

With 500V battery voltage reference

While the EV charger model could operate at rated conditions (500V, 5kW) in

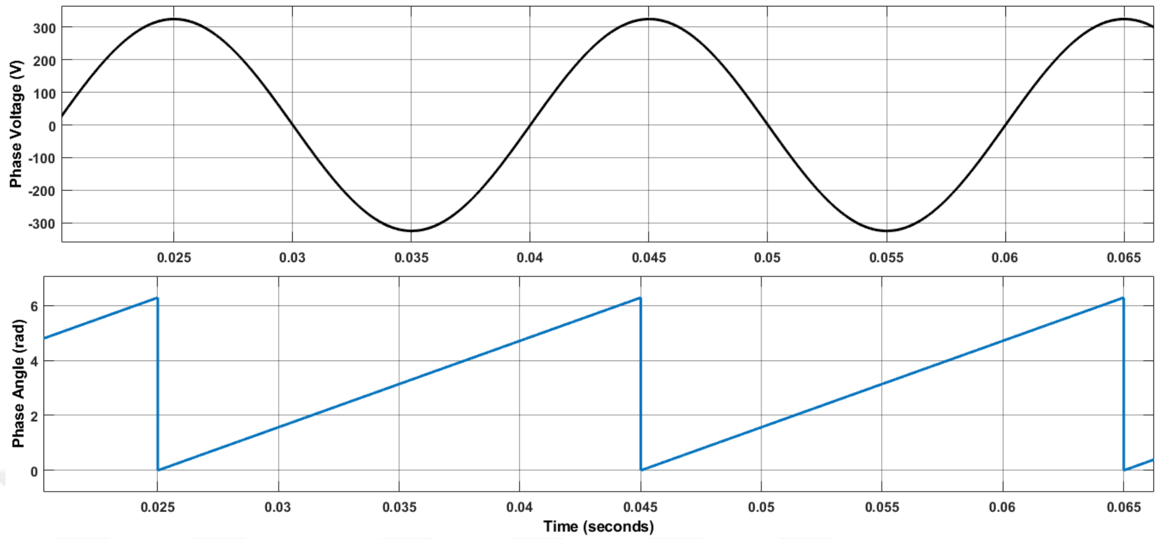

Figure 96: Simulation result for phase voltage and corresponding phase angle waveforms in steady-state condition in rectifier mode of operation (with 500V output)

inverter mode, steady-state performance of the system would be analyzed. The waveforms of the battery voltage and inductor current in steady-state is shown in Figure 104. It can be seen from the figure that the value of inductor current is negative since the direction of power flow for the three phase bidirectional EV charger model is reversed in inverter mode of operation. The peak-to-peak value of the inductor current, Δi_L value is measured as 3.7A, which is very close to the value given in (352) & (354) obtained from DC analysis as in the case for rectifier mode of operation. The average value of the inductor current, i_L, equal to battery current, is around 6A.

The waveform of DC bus voltage for V2G mode of operation, which is able to track the DC link reference voltage of 800V, is given in Figure 105. The ripple value of the DC link voltage is less than 80mV according to the graph, which is almost half of that measured for the case of rectifier mode of operation.

The waveforms of line current in "dq" reference frame are also given in Figure 106. The real (q) component of current has the value of 16-16.5 A. The value is also negative due to the reversed direction of power flow. The imaginary (d) component

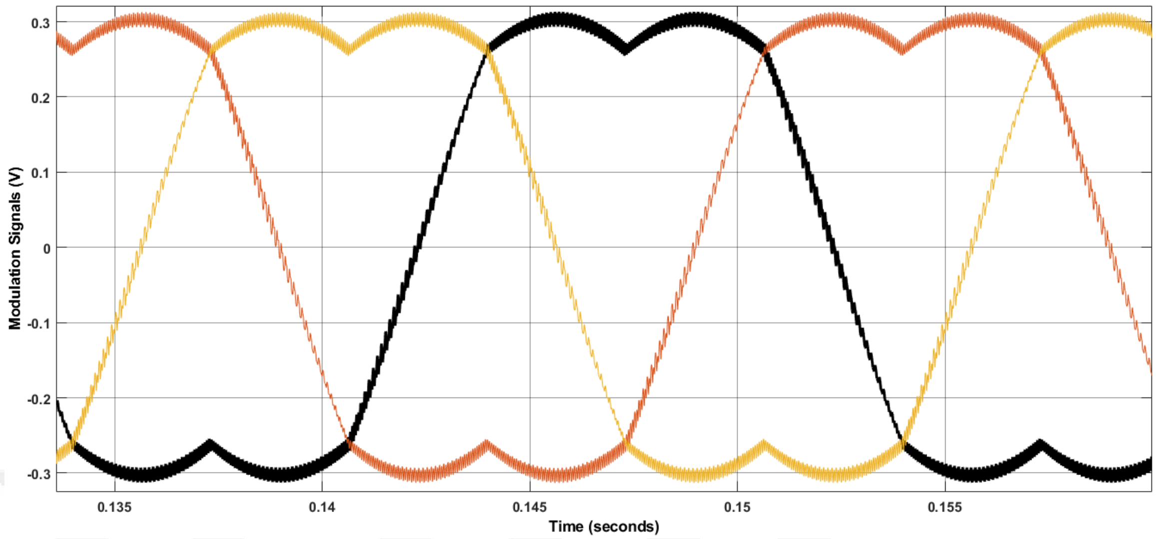

Figure 97: Simulation result for modulation signal waveforms corresponding to all of three phases in steady-state condition in rectifier mode of operation (with 500V output)

is kept to 0A as expected as well.

Moreover, the phase voltage and line current waveforms corresponding to one of three phases for the inverter mode of operation are shown in Figure 107. It is noticed that there is a phase difference of about 180° between line current and the phase voltage, indicating the bidirectional EV charger operates in inverter (V2G) mode. The peak value of the line current, I_m is also same with the value of q component current, i_{qe} based on the simulation result.

For the inverter mode of operation, the modulation signal waveforms corresponding to all of three phases are given in Figure 108 as well. The peak value of modulation signals is almost same with that observed for the case in which the EV charger model operates in rectifier mode as expected.

With 373V battery voltage reference

For the discharging of the output battery in V2G mode of operation when the battery voltage value is about 373V, the closed loop performance of the system could be investigated. The waveforms of the battery voltage and current in steady-state

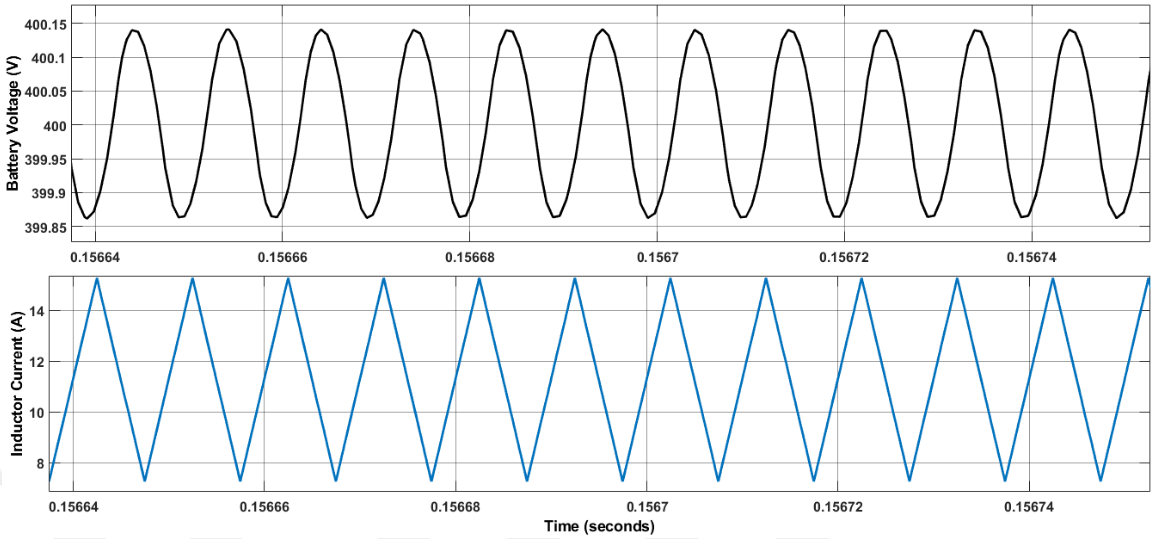

Figure 98: Simulation result for battery voltage and inductor current in steady-state condition in rectifier mode of operation (with 400V output)

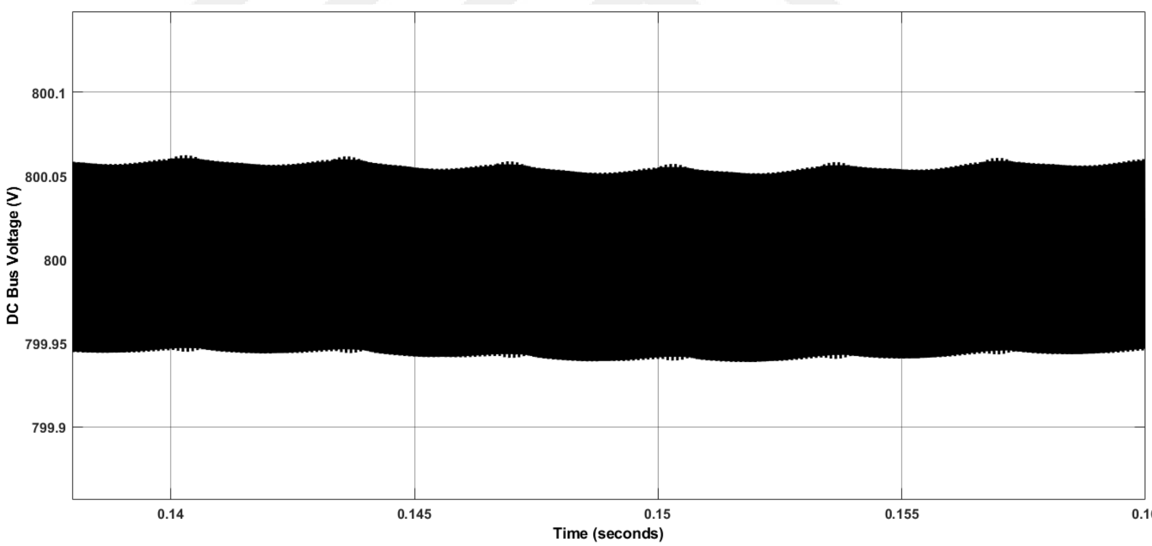

Figure 99: Simulation result for DC link voltage in steady-state condition in rectifier mode of operation (with 400V output)

with the output reference voltage of 373V is given in Figure 109. It can be noticed that the average value of inductor current is nearly 8A, that is equal to the value of output battery current, is larger in magnitude than that obtained for the case of 500V output. Also the ripple value is a bit higher than that observed in the previous

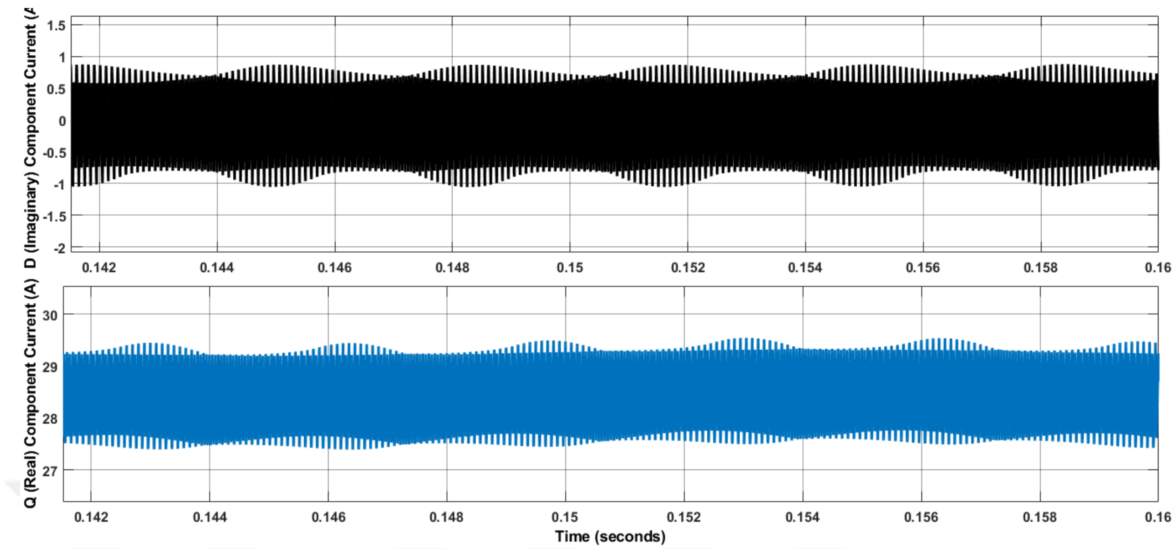

Figure 100: Simulation result for "q" and "d" components of line current in steady-state condition in rectifier mode of operation (with 400V output)

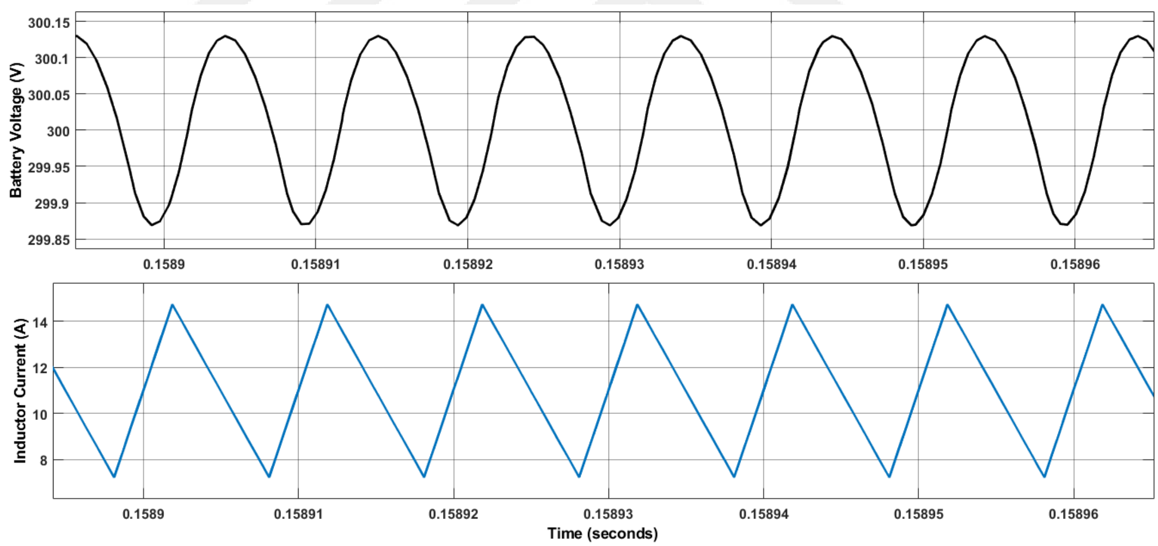

Figure 101: Simulation result for battery voltage and inductor current in steady-state condition in rectifier mode of operation (with 300V output)

case.

Moreover, the waveform of DC link voltage with the reference value of 800V is shown in Figure 110. The DC bus voltage value is able to track the desired value and the ripple value is approximately same with the case in which the output voltage is

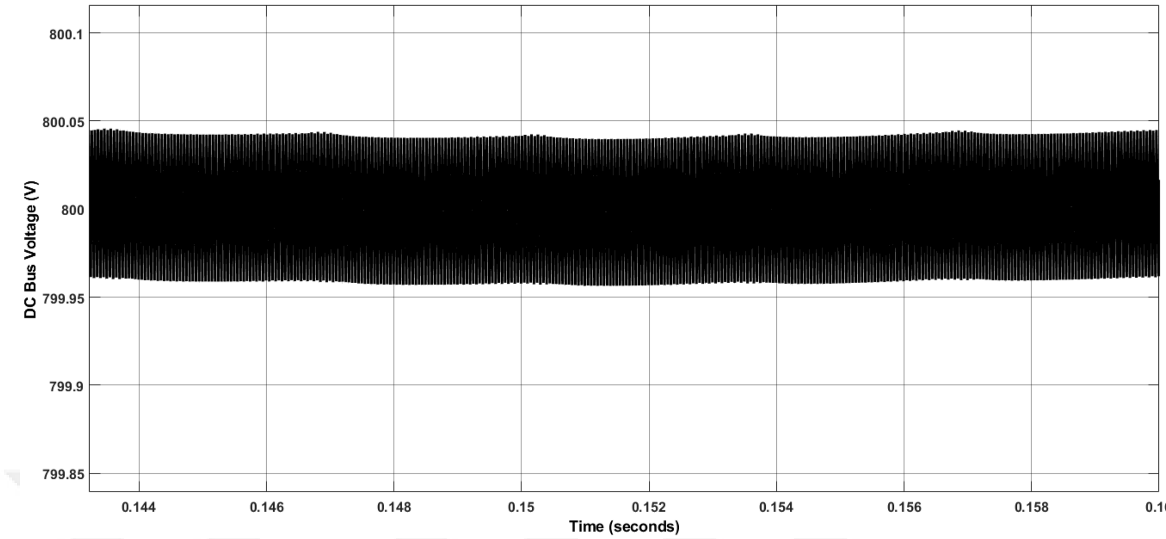

Figure 102: Simulation result for DC link voltage in steady-state condition in rectifier mode of operation (with 300V output)

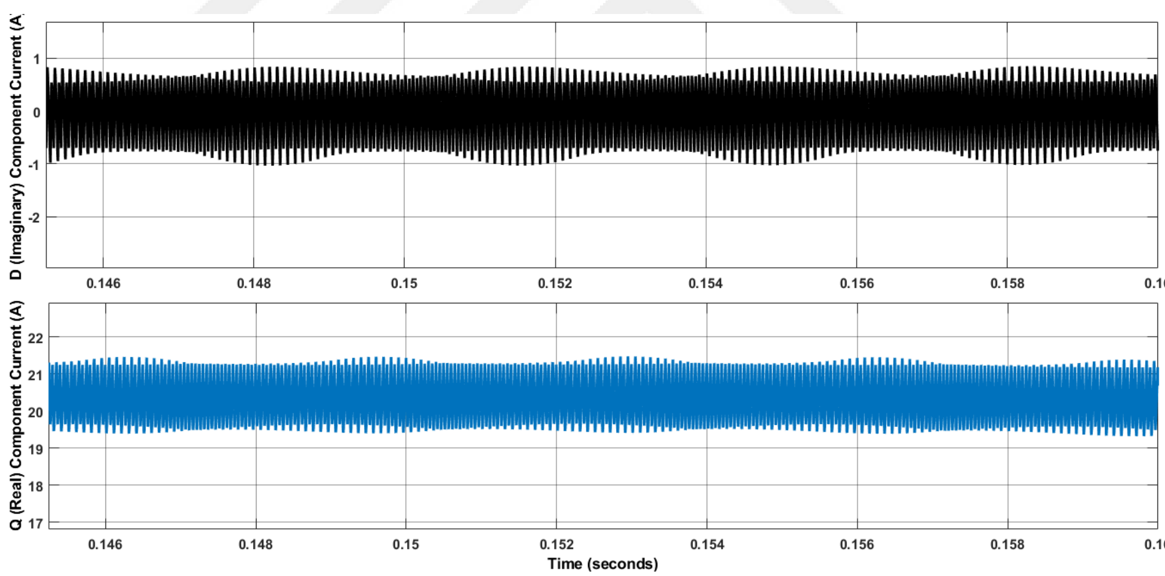

Figure 103: Simulation result for "q" and "d" components of line current in steady-state condition in rectifier mode of operation (with 300V output)

500V based on the simulation result as well.

The waveforms of "q" and "d" components of line current in inverter mode of operation are also given in Figure 111. The real (q) component of line current has the value of 16-16.5 A in magnitude in steady state operation for the case of 373V

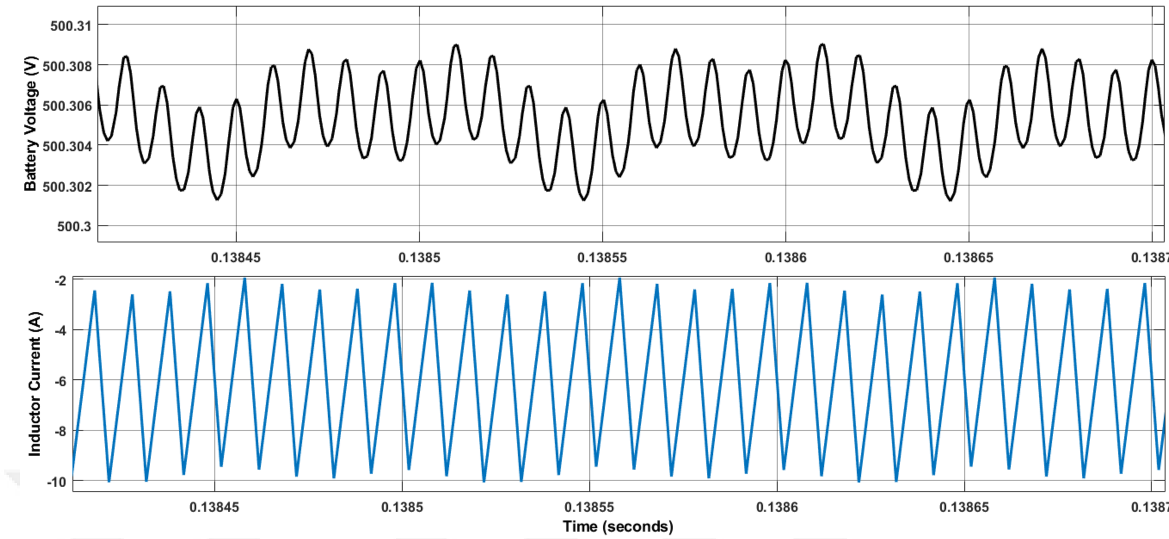

Figure 104: Simulation result for the battery voltage and inductor current in steady-state condition in inverter mode of operation (with 500V output)

battery voltage, which is same as that for the case with output voltage of 500V. The imaginary (d) component is kept at 0A as expected.

5.1.2 DC bus variation

In this section, the system performance is evaluated under DC bus reference voltage variation for both G2V and V2G mode of operations for the rated power condition (5kW & 500V).

5.1.2.1 In G2V Mode of Operation

The closed loop performance for the EV charger model would be analyzed with DC bus reference voltage variation of 1.2V for the rectifier mode of operation. The effect of change in reference value of DC bus voltage would create some deviations in line inductor currents and battery voltage. The responses of the battery voltage and inductor current with the deviation of DC bus reference voltage are shown in Figure 112. At the time t = 0.075s the reference value of DC bus voltage is increased by 1.2V It's clear that the variations of both voltage and current is negligible as

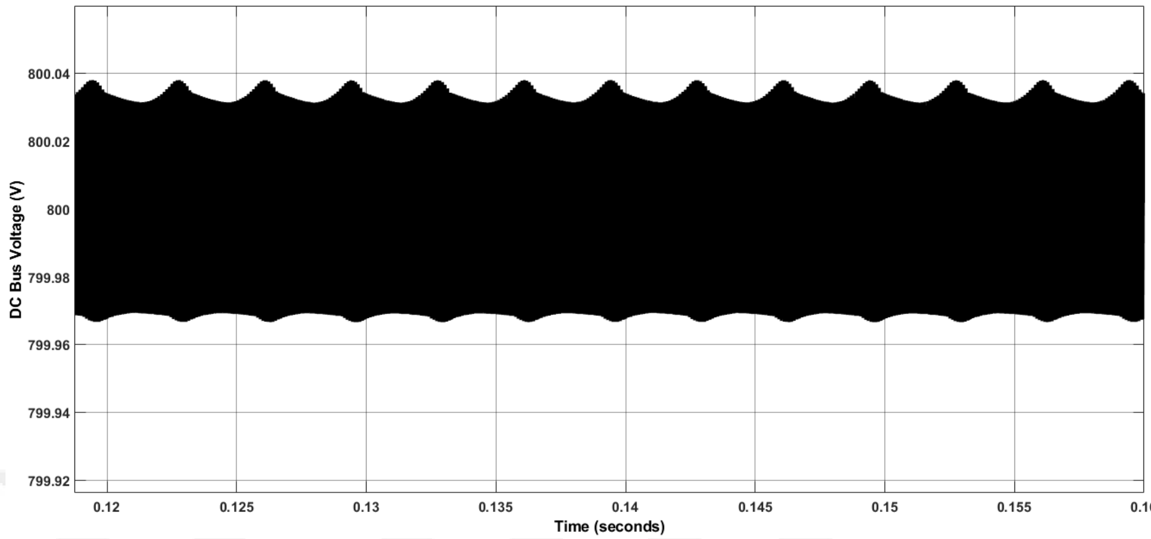

Figure 105: Simulation result for the DC bus voltage in steady-state condition in inverter mode of operation (with 500V output)

expected thanks to the rejection provided by the feedback loop modeled for DC-DC bidirectional converter as well. According to the closed loop line-to-output gain for G2V mode of operation, maximum possible variation in output voltage would be;

$$\Delta V_{bat} = 1.2\ x\ 0.0254 \tag{366}$$

$$\Delta V_{bat} = 0.03V = 30mV \tag{367}$$

Maximum deviation of the value of inductor current can be calculated as;

$$\Delta i_L = 1.2\ x\ 0.00543 \tag{368}$$

$$\Delta i_L = 0.0065A = 6.5mA \tag{369}$$

Hence the calculated values based on the theoretical analysis performed in Chapter 3 validate the results obtained as well.

The step response of DC bus voltage variation could also be evaluated for G2V mode of operation. The response of the DC link voltage with step change of 1.2V in reference value is given in Figure 113. The reference voltage value for DC bus is

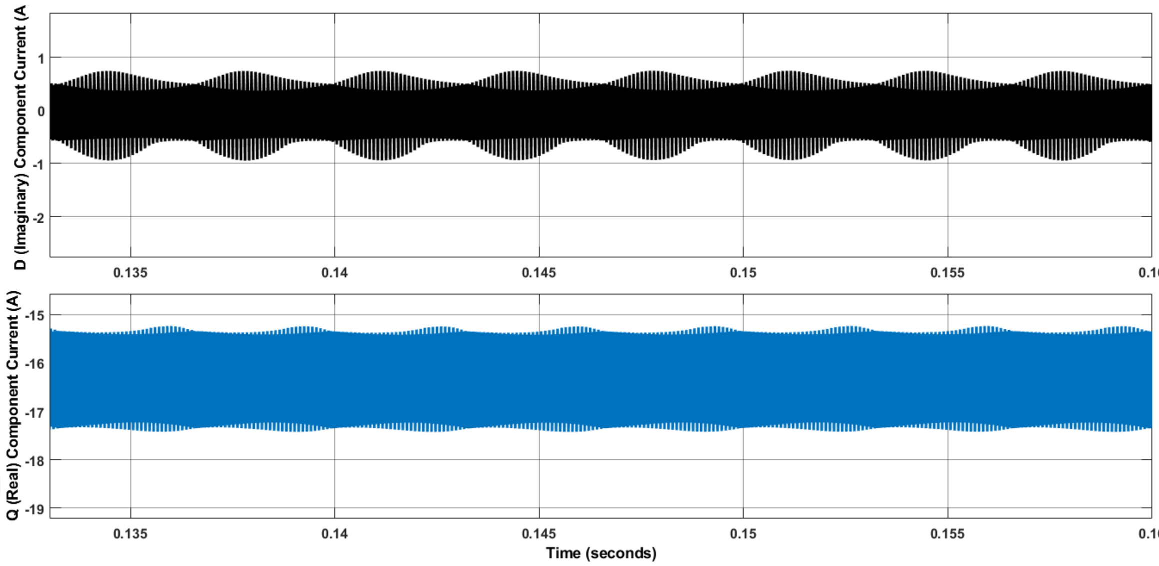

Figure 106: Simulation result for "q" and "d" components of line current in steady-state condition in inverter mode of operation (with 500V output)

increased by 1.2V at the time t = 0.075s and the variation of DC link voltage reaches up to 3.8 V before being set to the new reference value as well.

Finally, the responses of "d" and "q" components of line current with the deviation of DC bus reference voltage are shown in Figure 114. The corresponding variation in the real (q) component of line current is observed as 42A after the reference value of DC bus voltage is increased by 1.2V at t = 0.075s.

5.1.2.2 In V2G Mode of Operation

The performance for the three-phase bidirectional EV charger would be evaluated with DC bus reference voltage variation of 1.2V for the inverter mode of operation as well. The effect of change in reference value of DC bus voltage would create some deviations in battery voltage and inductor currents for V2G mode of operation too. The waveforms showing the responses of the battery voltage and inductor current with the deviation of DC bus reference voltage are given in Figure 115. At the time t = 0.015s the reference value of DC bus voltage is increased by 1.2V The corresponding variations in battery voltage and inductor current are determined as 1.3V and 30A

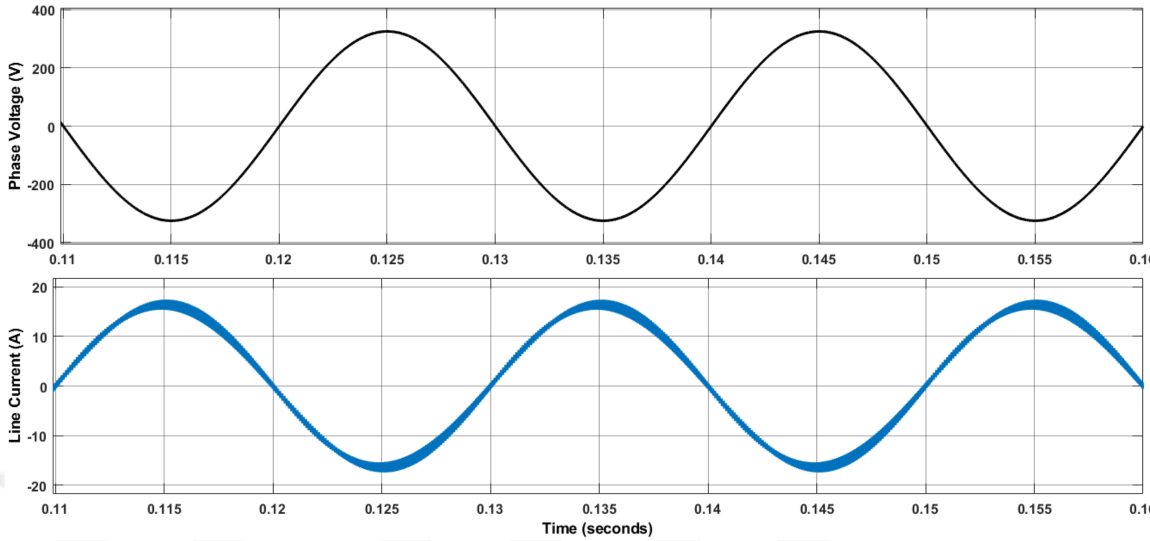

Figure 107: Simulation result for phase voltage and line current waveforms in steady-state condition in inverter mode of operation (with 500V output)

respectively.

The step response of DC bus voltage variation would also be analyzed for the inverter mode of operation. The waveform for the response of DC link voltage with step change of 1.2V in reference value is shown in Figure 116. The reference value of DC bus voltage is decreased by 1.2V at the time t = 0.015s and the maximum value of variation of DC link voltage is measured as 1.4 V before being set to the new reference value. According to the closed loop gain for DC bus reference voltage variation for the inverter mode of operation, maximum possible variation in DC link would be;

$$\Delta V_{dc} = 1.2 \; x \; 2.37 \tag{370}$$

$$\Delta V_{dc} = 2.84V \tag{371}$$

Therefore the measured deviation value based on the simulation result is less than the calculated value according to the theoretical analysis as desired.

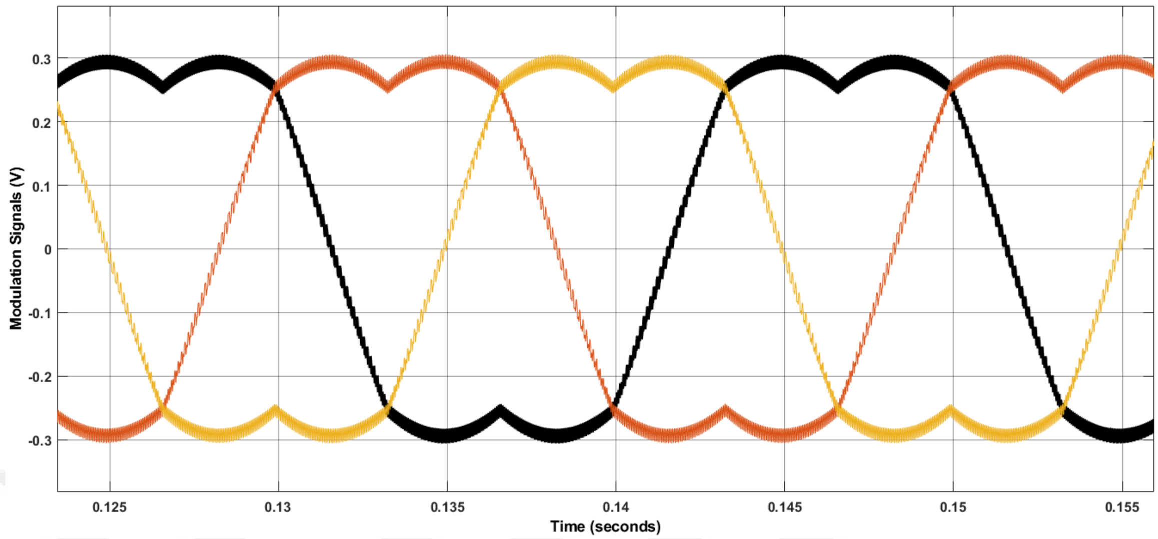

Figure 108: Simulation result for modulation signal waveforms corresponding to all of three phases in steady-state condition in inverter mode of operation (with 500V output)

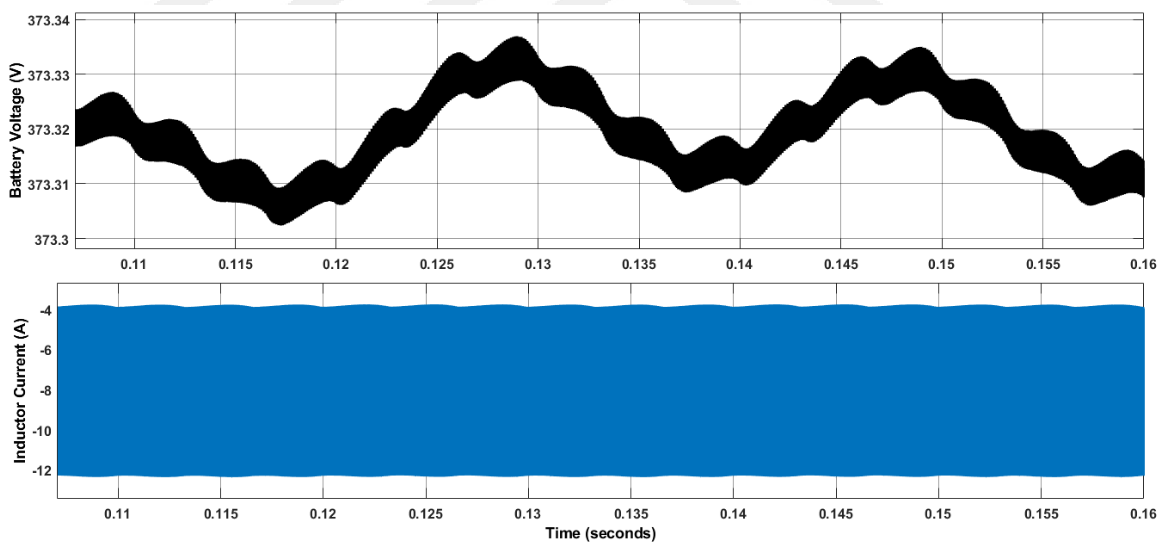

Figure 109: Simulation result for battery voltage and inductor current in steady-state condition in inverter mode of operation (with 373V output)

5.1.3 Line distortion

The performance of the system for the EV charger model can be evaluated with creating some distortions at the grid side in this part.

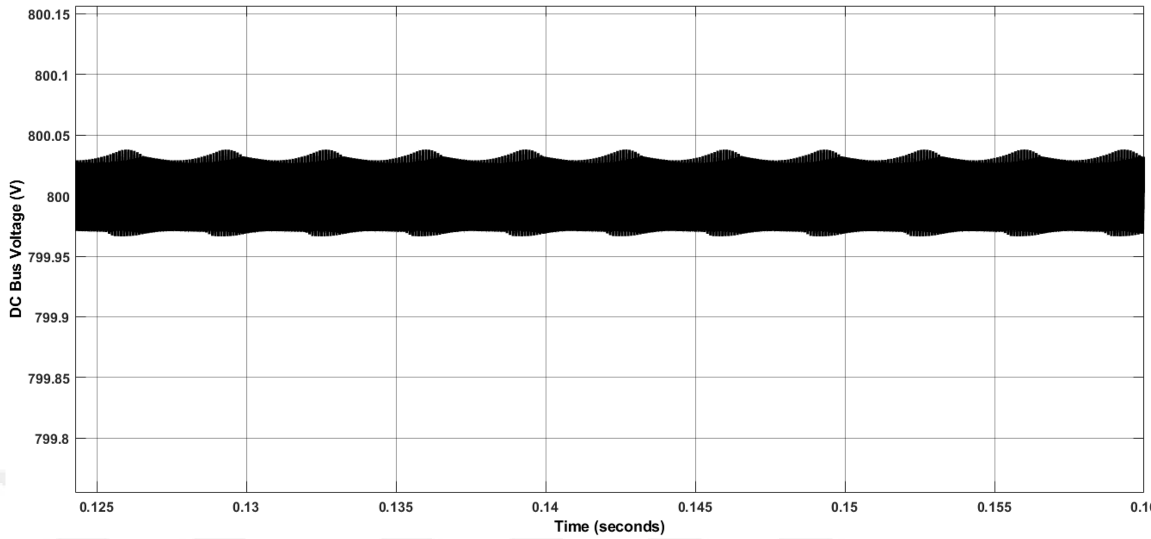

Figure 110: Simulation result for DC link voltage in steady-state condition in inverter mode of operation (with 373V output)

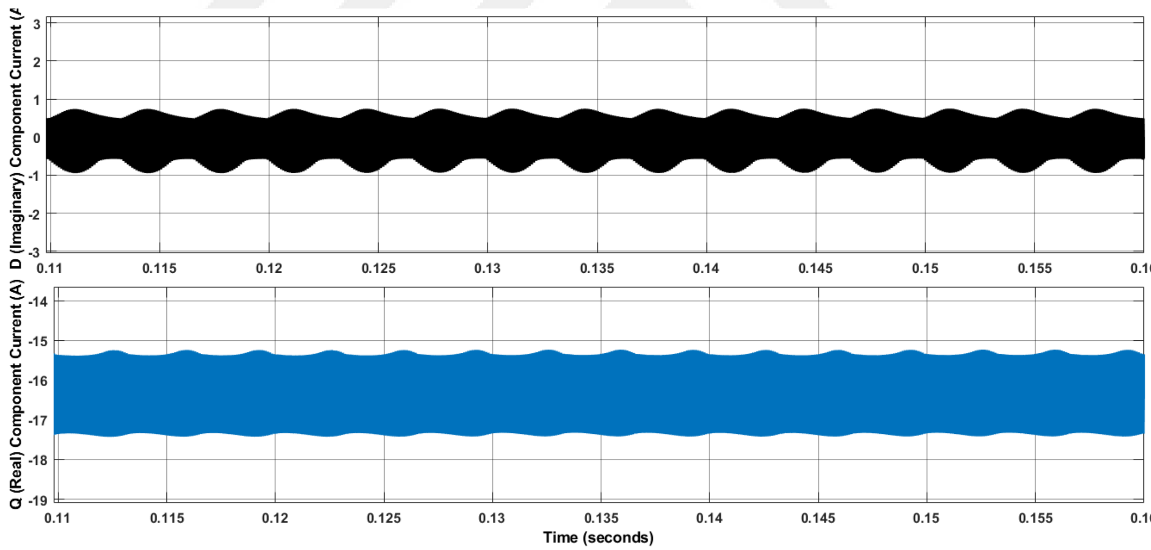

Figure 111: Simulation result for "q" and "d" components of line current in steady-state condition in inverter mode of operation (with 373V output)

5.1.3.1 In G2V Mode of Operation

When the magnitude of one of three phase voltages is decreased to around 270V some deviations could be observed in DC bus voltage, line current components, voltage components in dq reference frame and phase angle for the rectifier mode of operation. The response of DC link voltage with distortion created in grid side is shown

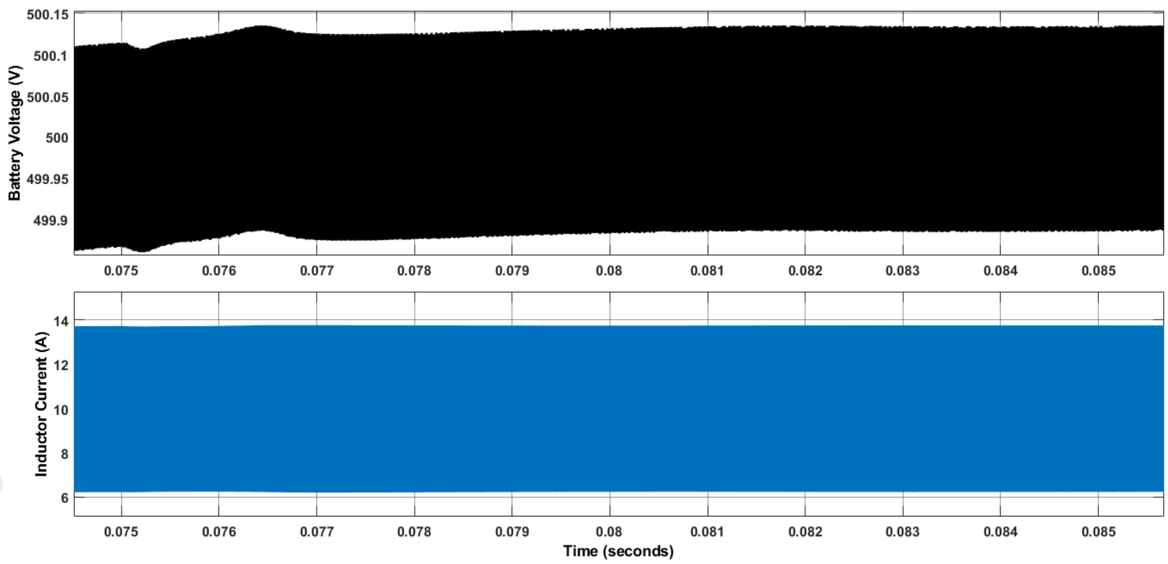

Figure 112: Simulation result for battery voltage and inductor current with DC bus voltage variation of 1.2V in rectifier mode of operation

in Figure 117. At the time t = 0.105s the peak value of one of the phase voltages is changed to 270V then it is increased to 325V again at the time t = 0.12s. It is noticed that some oscillations in DC link voltage occur with the change in magnitude of one of three phase voltages. When the peak value is increased back to 325V, those oscillations are eliminated and the DC bus voltage is set to the desired value as well.

The responses for "q" and "d" components of line current would also be observed with line distortion for G2V mode of operation. The waveforms for the responses of line currents in "dq" reference frame are given in Figure 118 when the peak value of one of three phases is decreased to 270V at the time t = 0.105s and then increased to 325V again at the time t = 0.12s. It is clear that oscillations in real (q) component of line current is observed with the change in peak value of one of the phase voltages as well. As in the case of DC link voltage response, when the peak value is increased back, the oscillations are gone and the q component of line current is able to track the reference value again.

The responses for "q" and "d" components of line voltage can be evaluated with

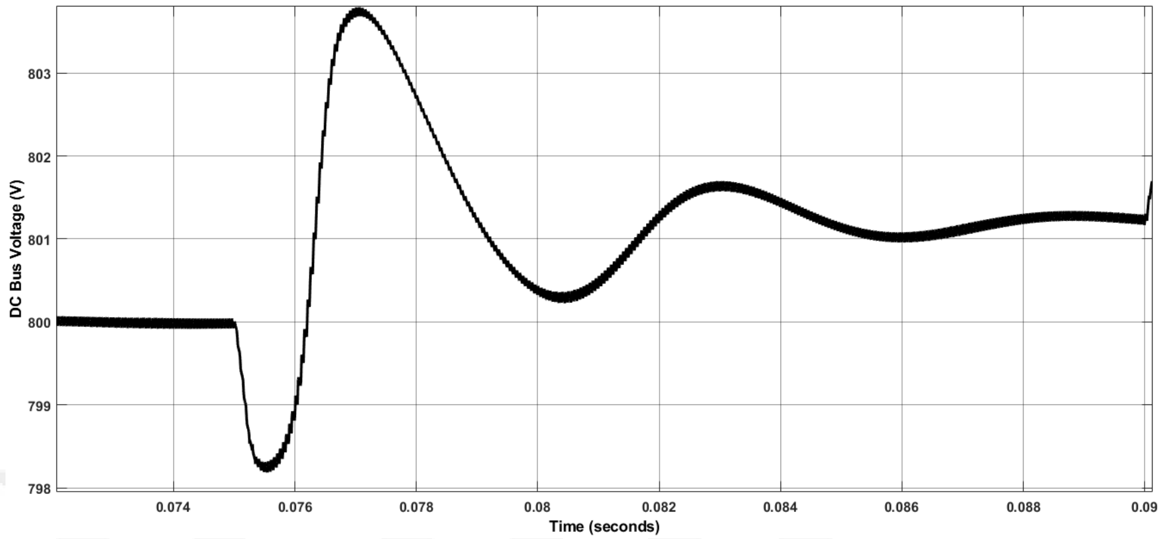

Figure 113: Simulation result for the response of DC link voltage with step change of 1.2V in reference value in rectifier mode of operation

line distortion for rectifier mode of operation in addition to the line current responses. When the magnitude of one of the phase voltages is decreased to 270V at the time t = 0.105s and then increased back to 325V at the time t = 0.12s, the waveforms for the responses of line voltages in "dq" reference frame are shown in Figure 119. It is noticed that some deviations in both real (q) and imaginary (d) components of line voltage are observed with the change in the magnitude of one of three phase voltages as well. As in the previous cases, when the peak value is increased back, the variations observed are eliminated and the line voltage components in "dq" reference frame are set to the desired values again.

Finally, the response of phase angle with the distortion created in the related phase component of three phase voltages for rectifier mode of operation would be analyzed. The waveforms of the corresponding phase voltage, of which the peak value is varied, and the phase angle are shown in Figure 120 as well. Some non-linearity effects in the phase angle waveform could be observed according to the simulation result when the peak value of one of the phase voltages is decreased to 270V at the time t = 0.105s

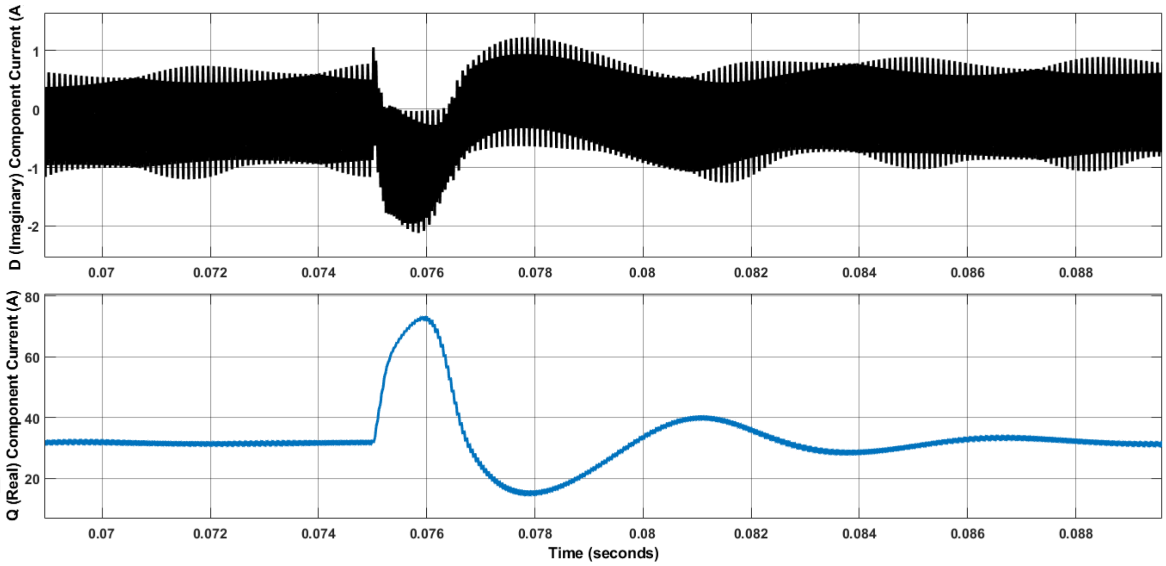

Figure 114: Simulation result for "q" and "d" components of line current with DC bus voltage variation of 1.2V in rectifier mode of operation

and then increased back to 325V at the time t = 0.12s.

5.1.3.2 In V2G Mode of Operation

The closed loop performance for the EV charger model would be analyzed creating line distortion condition with reduction of magnitude value of one of three phase voltages from 325V to about 270V for the inverter mode of operation too. When the magnitude of one of three phase voltages is decreased to about 270V some variations could be observed in DC bus voltage, line current components in dq reference frame, battery voltage & inductor current and phase angle for the inverter (V2G) mode of operation. The response of DC bus voltage with distortion observed in grid side is given in Figure 121 for this mode of operation. At the time t = 0.075s the peak value of one of the phase voltages decreases to 270V then it increases back to 325V at the time t = 0.09s. As it can be concluded from the simulation result, the variation in DC link voltage is very small, which has a negligible value, with the change in magnitude of one of three phase voltages since the EV charger model is operated in the inverter mode, for which most of the parameters is much less sensitive to variations in the

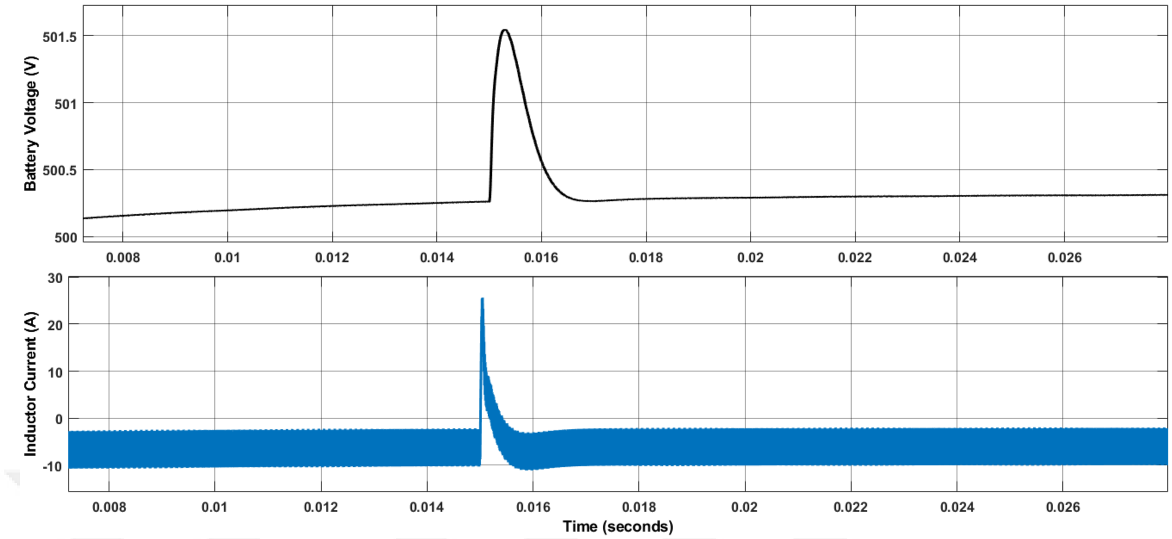

Figure 115: Simulation result for battery voltage and inductor current with DC bus voltage variation of 1.2V in inverter mode of operation

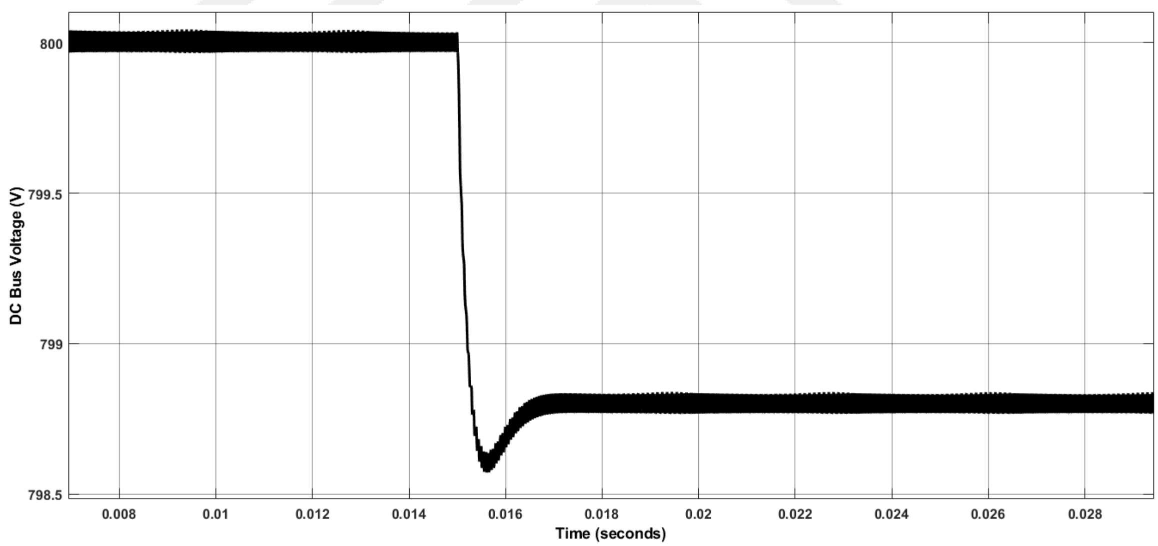

Figure 116: Simulation result for the response of DC link voltage with step change of 1.2V in reference value in inverter mode of operation

grid side compared to the case of rectifier mode of operation.

The responses for "q" and "d" components of line current would also be observed with line distortion for the inverter mode of operation. The waveforms for the responses of line currents in "dq" reference frame are shown in Figure 122 when the

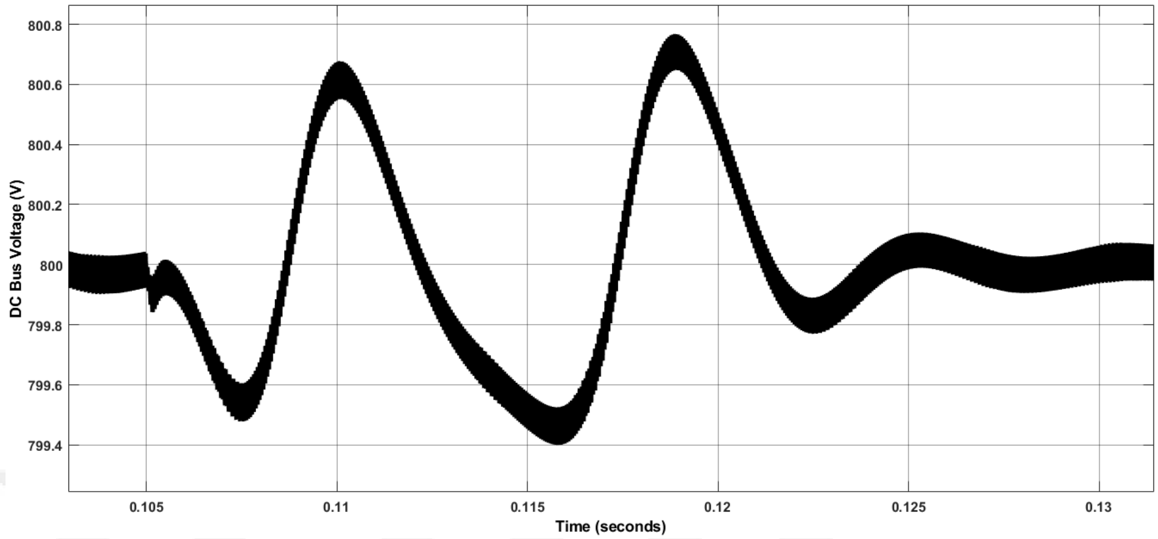

Figure 117: Simulation result for DC link voltage when the magnitude of one of the phase voltages is decreased to 270V and then increased to 325V again for rectifier mode of operation

magnitude of one of three phases is decreased to 270V at the time t = 0.075s and then increased to 325V again at the time t = 0.09s. It is noticed that oscillations observed in the "q" component of line current are much smaller than those in the case for G2V mode of operation with the change in peak value of one of the phase voltages as well.

The waveforms for responses of battery voltage and inductor current with distortion occurring in the grid side are given in Figure 123. At the time t = 0.075s the magnitude of one of the phase voltages is changed to 270V then it is increased to 325V again at the time t = 0.09s. It is clear from the simulation result that some oscillations in output battery voltage and inductor current are observed with the change in the peak value of one of three phase voltages. When the magnitude of the related phase voltage increases back to 325V, those oscillations are gone and the output battery voltage & inductor current are able to track their reference values again as well.

Finally, the waveform for response of phase angle with the distortion observed

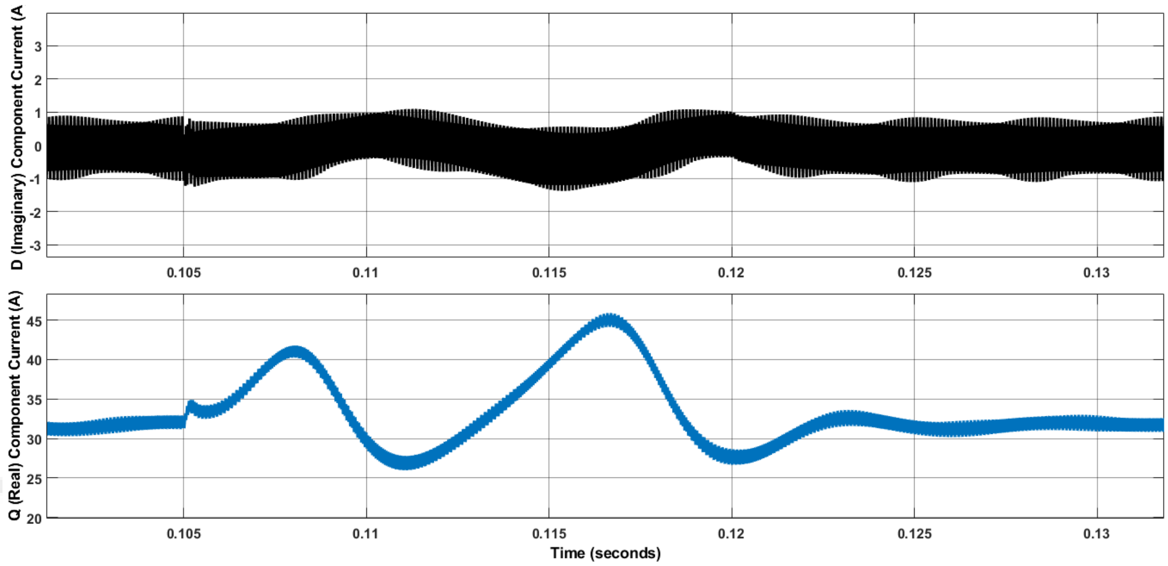

Figure 118: Simulation result for the responses of "q" and "d" components of line current when the magnitude of one of the phase voltages is decreased to 270V and then increased to 325V again for rectifier mode of operation

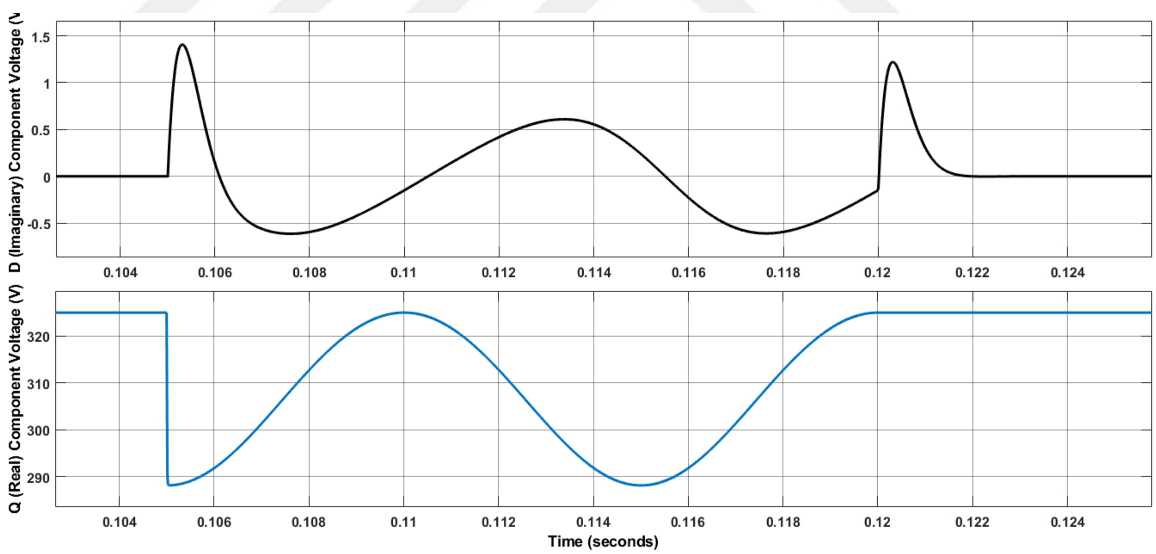

Figure 119: Simulation result for the responses of "q" and "d" components of line voltage when the magnitude of one of the phase voltages is decreased to 270V and then increased to 325V again for rectifier mode of operation

in the corresponding phase component of three phase voltages for inverter mode of operation could be evaluated. The waveforms of the corresponding phase voltage, of which the magnitude is changed, and the phase angle are shown in Figure 124 as

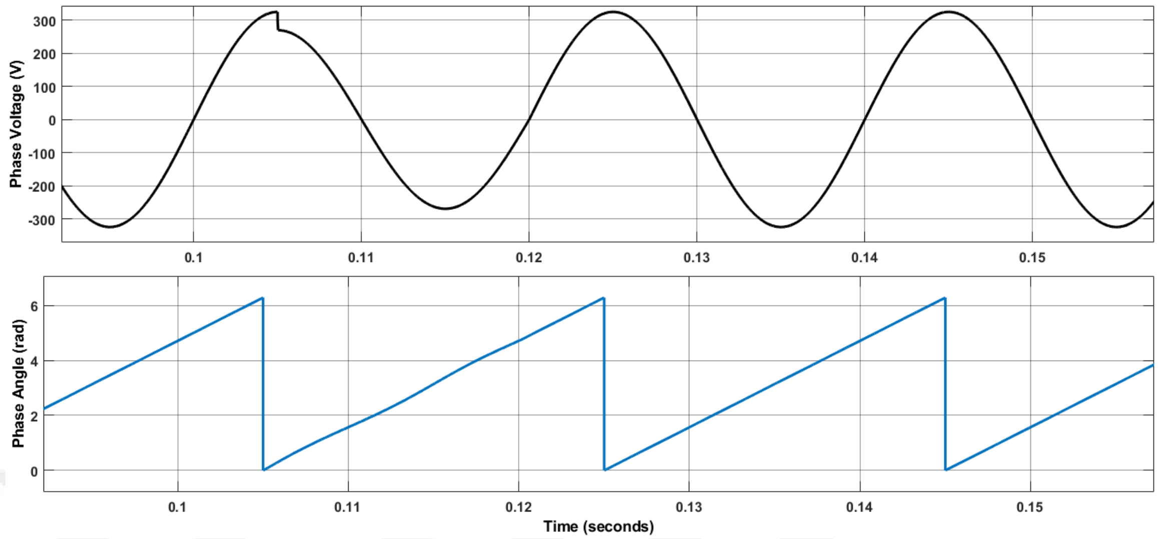

Figure 120: Simulation result for the response of the phase angle when the peak value of the corresponding phase voltage is decreased to 270V and then increased to 325V again for rectifier mode of operation

well. As in the case for G2V mode of operation, some non-linearity effects in the phase angle waveform occur according to the simulation result when the peak value of one of the phase voltages decreases to around 270V at the time t = 0.075s and then increases to 325V again at the time t = 0.12s.

5.1.4 Load transient

The closed loop system performance and functionality for the EV charger model is also analyzed with a load transient of 6.6A for rated operating condition (500V, 5kW).

5.1.4.1 In G2V Mode of Operation

The closed loop performance for the EV charger model would be analyzed performing load transient condition while the system operates in charging mode. The effect of perturbation in load current of the charger can create some deviations in line & inductor currents, battery voltage and DC link voltage. The waveforms for responses of the battery voltage and inductor current with the deviation of load current are

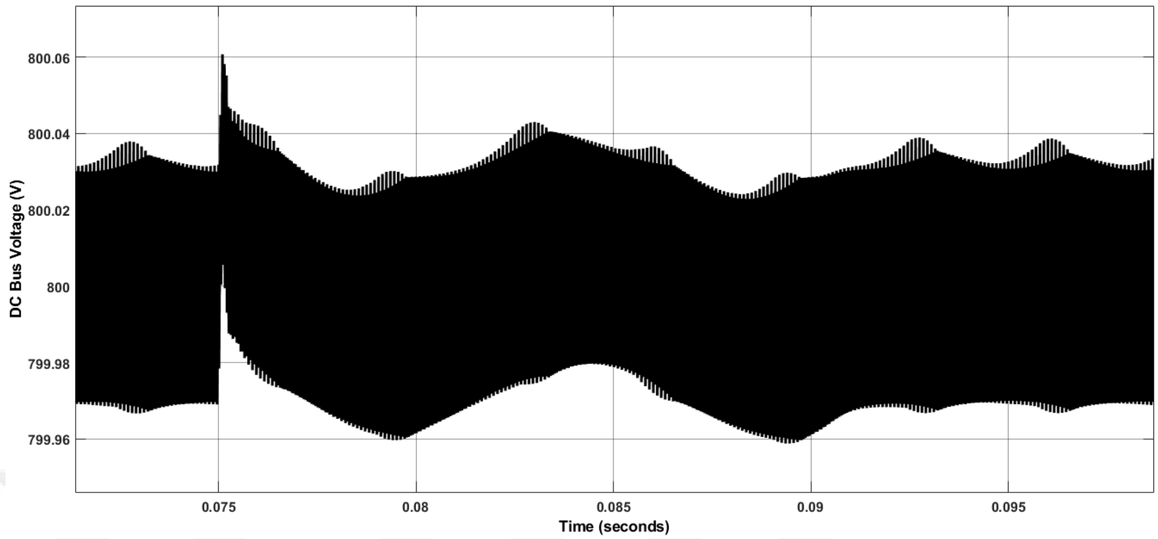

Figure 121: Simulation result for DC link voltage when the magnitude of one of the phase voltages is decreased to 270V and then increased to 325V again for inverter mode of operation

given in Figure 125. At the time t = 0.045s, load current with 6.6A is injected into the battery side of the bidirectional charger system, operating in G2V mode. From the simulation result, the value of change in the battery voltage is determined as nearly 5V. Moreover a small variation can be observed in the inductor current at only the time instant, at which the load current is applied externally, before the average value of the inductor current decreases to around 3.3A. This small deviation of the current, that can be neglected, would be considered due to the effect of closed loop load-to-inductor current gain, derived and analyzed for the rectifier mode of operation in Chapter 3. According to the closed loop output impedance gain for G2V mode of operation, maximum possible variation in output voltage would be;

$$\Delta V_{bat} = 6.6 \ x \ 4.3 \tag{372}$$

$$\Delta V_{bat} = 28.4V \tag{373}$$

Maximum deviation of the value of inductor current can be calculated from closed

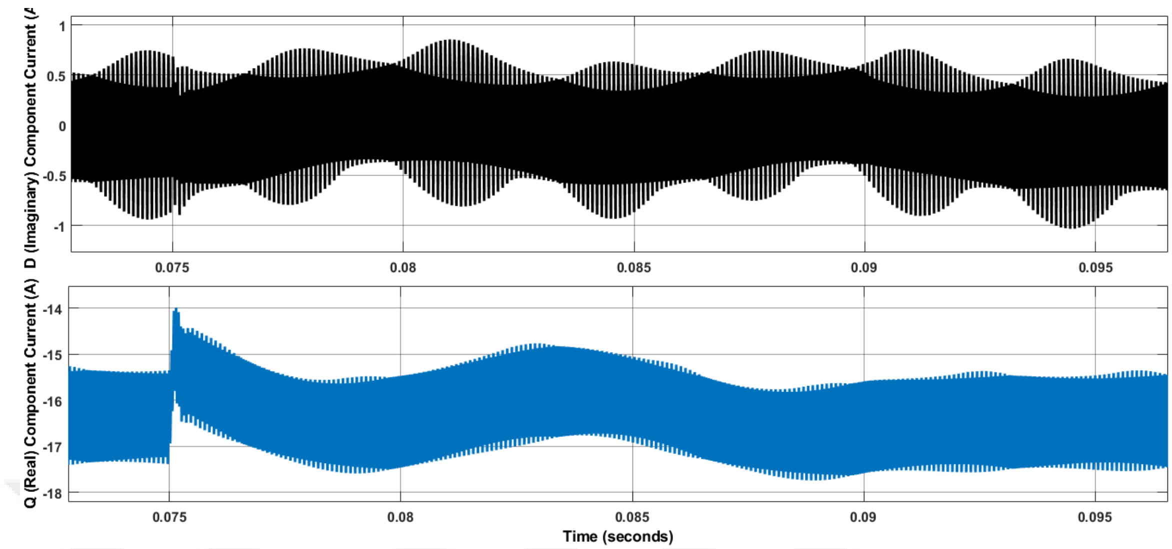

Figure 122: Simulation result for the responses of "q" and "d" components of line current when the magnitude of one of the phase voltages is decreased to 270V and then increased to 325V again for inverter mode of operation

loop load-to-current gain for the rectifier mode of operation as;

$$\Delta i_L = 6.6 \ x \ 0.0813 \tag{374}$$

$$\Delta i_L = 0.54A \tag{375}$$

Therefore the calculated values for the deviations observed in both output voltage and inductor current (the deviation, measured only at the time instant at which load transient occurs, is considered for the current here) based on the theoretical analysis performed in Chapter 3 verify the results obtained as well.

The response of DC link voltage would also be analyzed for the rectifier mode of operation. The waveform showing the change in DC bus voltage with load current transient of 6.6A is given in Figure 126. The value of load current is decreased by 6.6A at the time t = 0.045s and the variation of DC bus voltage reaches up to 0.9V before the controller regulates the DC link back to the reference bus voltage value.

Finally, the responses of "d" and "q" components of line current with the variation of load current are given in Figure 127. The value of real (q) component of line current

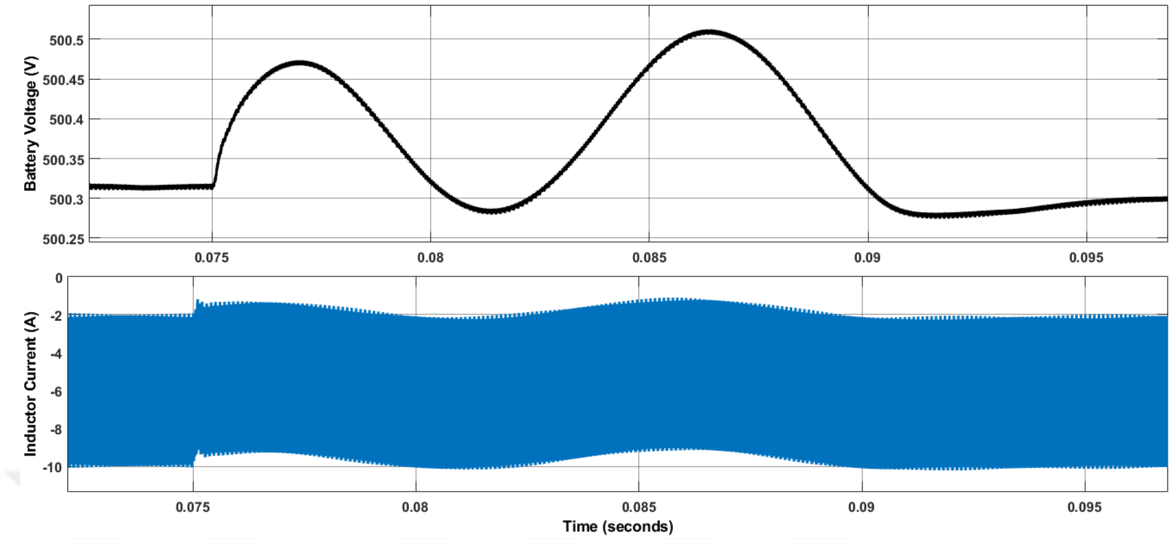

Figure 123: Simulation result for the responses of battery voltage and inductor current when the magnitude of one of the phase voltages is decreased to 270V and then increased to 325V again for inverter mode of operation

decreases to 10-11A from 31-32A after the load current transient with 6.6A is applied at the battery side at the time t = 0.045s.

5.1.5 Variation in desired battery voltage

The performance of the EV charger model would be evaluated via changing reference value of the battery voltage for the rated operation condition (5kW, 500V).

5.1.5.1 In G2V Mode of Operation

For charging mode of operation, effect of variation of 5V in the reference value of output battery voltage on the closed loop system performance would be evaluated. The effect of perturbation in the reference value of battery voltage of the bidirectional EV charger system could cause some variations in line & inductor currents, battery voltage and DC link voltage as in the case for the load transient in rectifier mode of operation. The responses of the battery voltage and inductor current with the deviation of the desired reference value for battery voltage are shown in Figure 128. The reference value of battery voltage for EV charger model is decreased by 5V at the

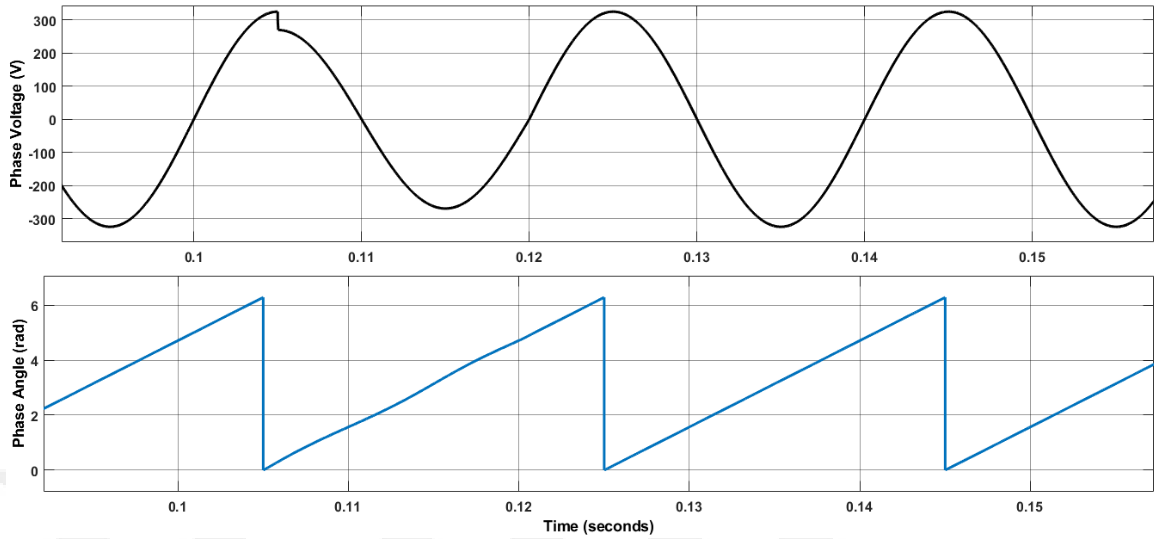

Figure 124: Simulation result for the response of the phase angle when the magnitude of the corresponding phase voltage is decreased to 270V and then increased to 325V again for inverter mode of operation

time t = 0.015s according to the simulation result. It is observed that the response of the output battery voltage with the change of reference value has no overshoot as expected since the outer voltage loop is designed to be operated more slowly compared to the inner current one with a low -3dB bandwidth value in respect to the switching frequency, $f_{sw,dc}$ of the DC-DC converter part of the EV charger system. For the inductor current, an instantaneous jump with some value is observed only at the time instant t = 0.015s, at which the desired reference value is decreased, before the current changes slowly since the response of the inner current control loop is faster compared to the voltage one, which can cause some overshoots, as well.

The response of DC bus voltage with variation of the reference battery voltage can also be evaluated for the G2V mode of operation. The waveform for the change in DC link voltage with decrease of the reference value of the battery voltage is shown in Figure 129. After the value of the desired reference voltage is decreased by 5V at the time t = 0.015s, the variation in DC link voltage reaches up to 0.7V before the controller regulates the DC bus back to the reference bus voltage value.

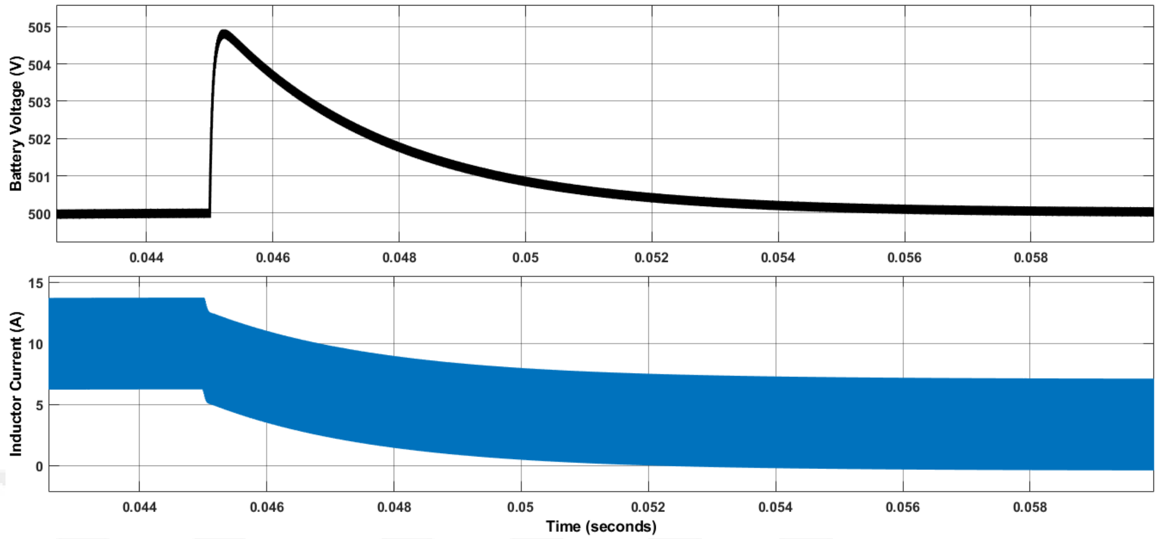

Figure 125: Simulation result for battery voltage and inductor current with load current variation of 6.6A in rectifier mode of operation

Moreover, the waveforms for responses of "d" and "q" components of line current with variation of the reference battery voltage are given in Figure 130. The value of real (q) component of line current changes by nearly 17A after the value of voltage reference is decreased from 500V to 495V at the time t = 0.015s as well.

5.1.5.2 In V2G Mode of Operation

For discharging mode of operation, effect of variation of 20V in battery voltage on the closed loop system performance can be analyzed. The effect of change of the battery voltage value for there phase EV charger model would create some variations in line & inductor currents and DC link voltage in the inverter mode of operation. The waveforms for response of inductor current and the battery voltage, of which the value is decreased by 20V, are shown in Figure 131. The battery voltage value is changed at the time t = 0.045s according to the simulation result for V2G mode of operation. It is noticed that the variation of inductor current with the decrease of the value of battery voltage is very small and can be ignored thanks to the inner current control loop designed for the bidirectional DC-DC converter operating in the boost mode

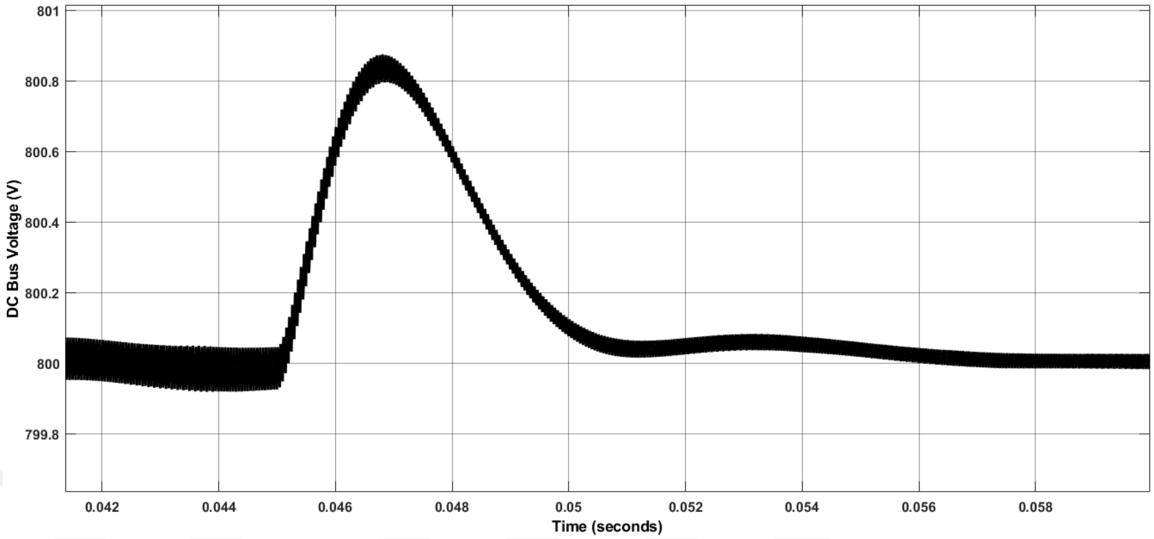

Figure 126: Simulation result for the response of DC link voltage with load current variation of 6.6A in rectifier mode of operation

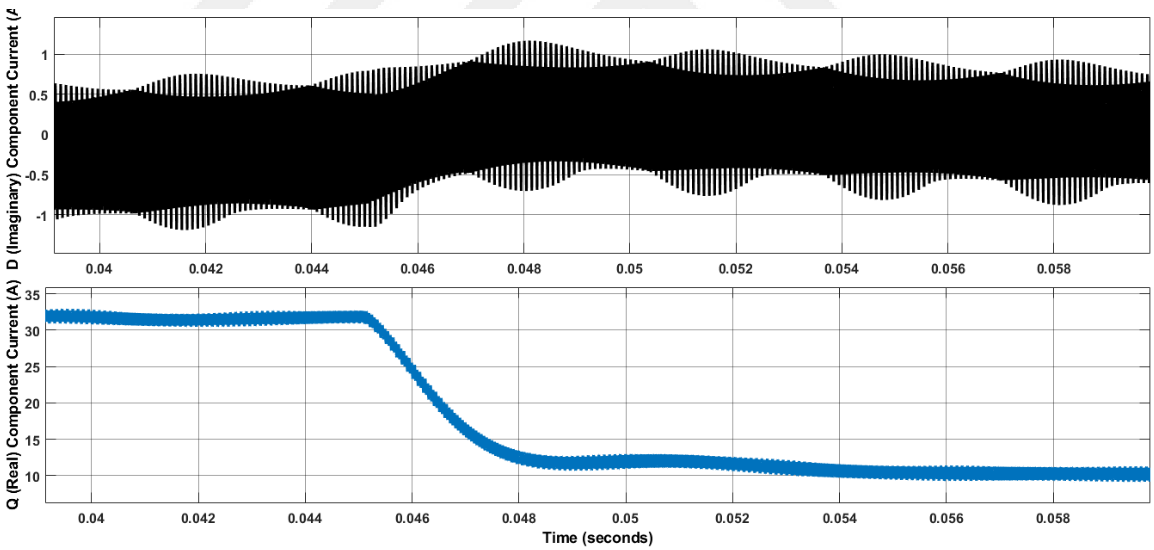

Figure 127: Simulation result for "q" and "d" components of line current with load current variation of 6.6A in rectifier mode of operation

(with power flow from the battery to DC link), which is able to attenuate variations observed in battery voltage for the inductor current with a high ratio as well. Based on the closed loop line-to-current gain for V2G mode of operation, maximum possible variation in inductor current would be;

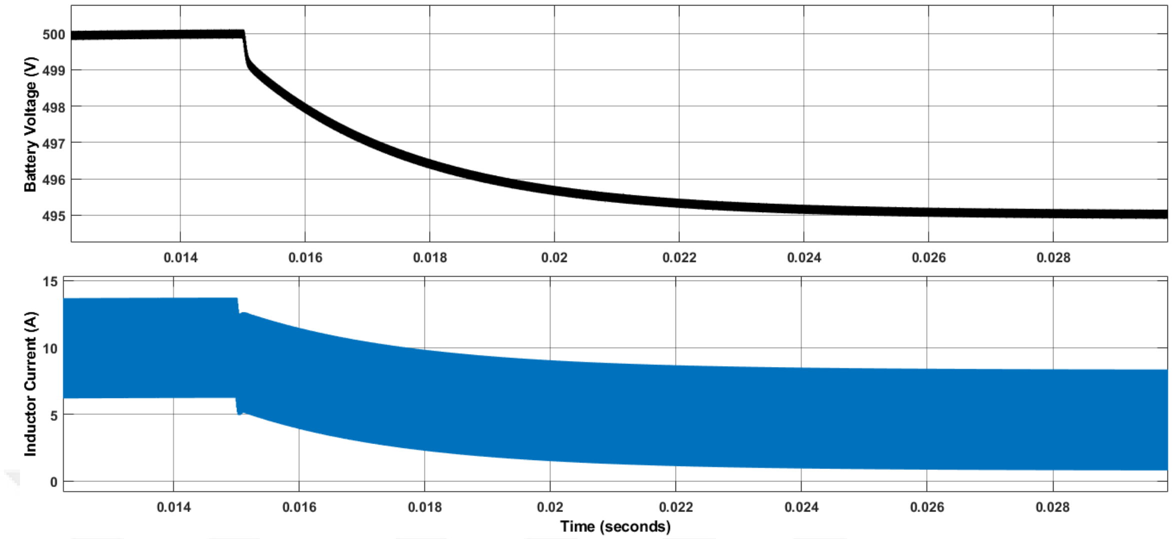

Figure 128: Simulation result for battery voltage and inductor current with the variation of 5V in reference value of battery voltage in rectifier mode of operation

$$\Delta i_L = 20\ x\ 0.0861 \tag{376}$$

$$\Delta i_L = 1.72A \tag{377}$$

It is clear that the change in average value of the inductor current with the decrease of battery voltage value is smaller than 1.72A. Therefore the calculated value for the variation of inductor current, Δi_L according to the theoretical analysis conducted in Chapter 3 verifies the result obtained in the simulation work.

Also the effect of variation in battery voltage value on the DC link voltage can be evaluated for the inverter mode of operation. The response of DC bus voltage with change of the value of battery voltage is given in Figure 132. The command for the battery voltage value to decrease by 20V is applied at the time t = 0.045s according to V2G mode of operation. It is clear that the variation of DC link voltage with the change of the value of battery voltage is negligible based on the simulation result thanks to the closed loop line-to-output gain designed for the synchronous DC-DC converter operating in the boost mode, attenuating variations in battery voltage for

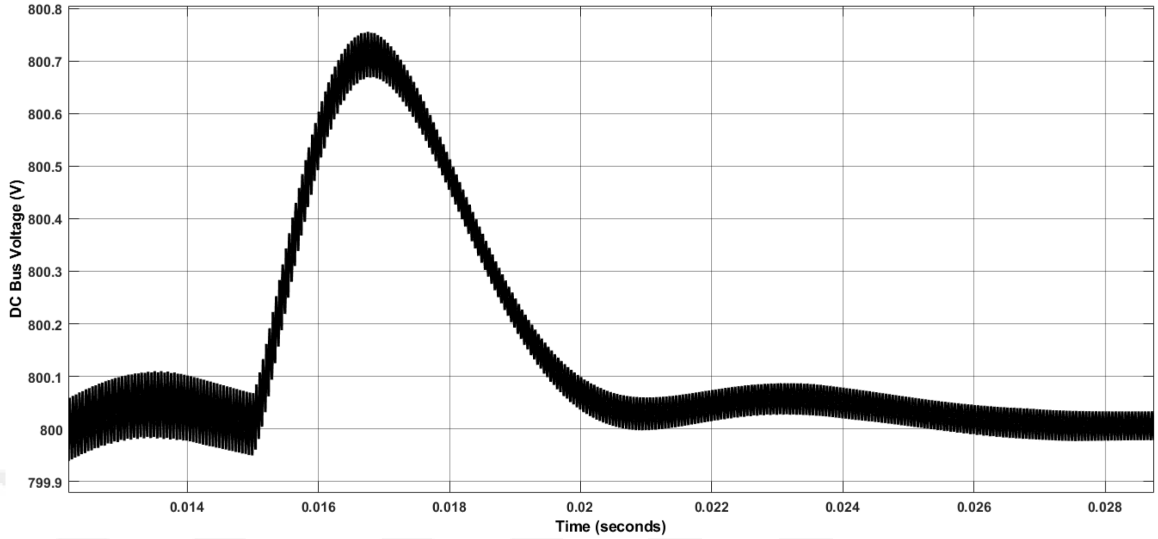

Figure 129: Simulation result for the response of DC bus voltage with the variation of 5V in reference value of battery voltage in rectifier mode of operation

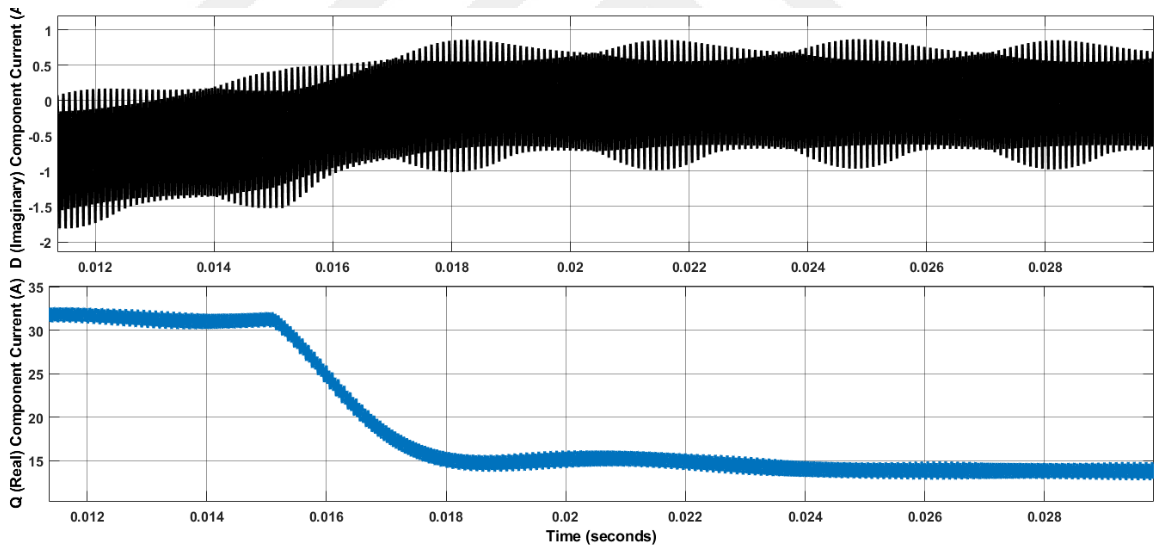

Figure 130: Simulation result for "q" and "d" components of line current with the variation of 5V in reference value of battery voltage in rectifier mode of operation

the DC bus significantly as well. According to the closed loop line-to-output gain for the inverter mode of operation, maximum possible variation in DC link voltage could be;

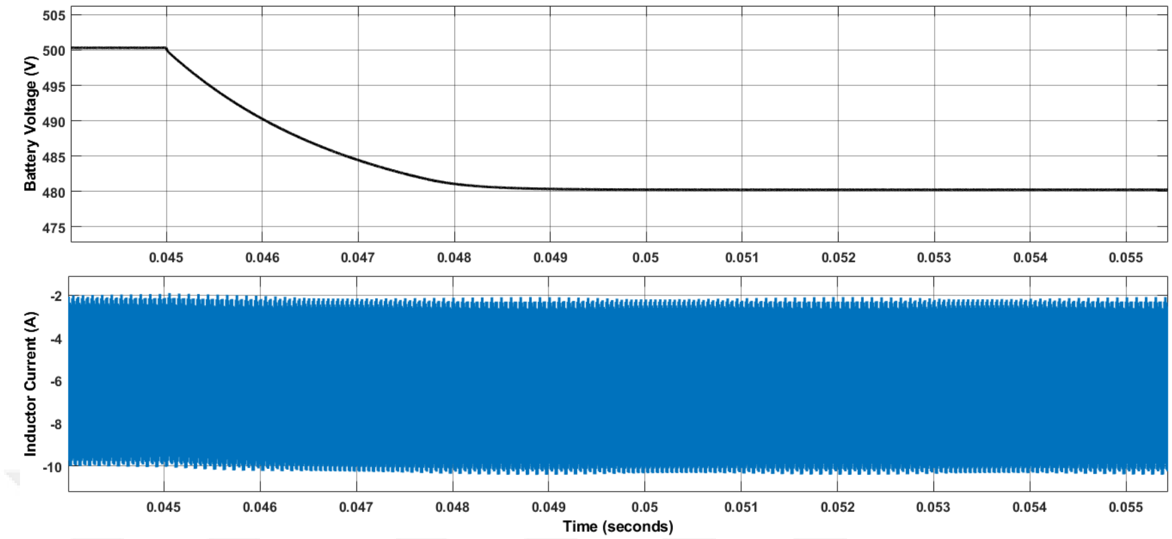

Figure 131: Simulation result for the response of the inductor current with variation of the battery voltage, of which the value is decreased by 20V, in inverter mode of operation

$$\Delta V_{dc} = 20 \ x \ 0.00072 \tag{378}$$

$$\Delta V_{dc} = 0.014V = 14mV \tag{379}$$

Hence the calculated value for the variation of DC bus voltage, ΔV_{dc} is negligibly small based on the theoretical analysis given in Chapter 3, validating the simulation result.

The values obtained from the analysis of simulation results of closed loop system performance for the bidirectional EV charger model under the related conditions are given in Table 6 corresponding to the rated operation conditions with the nominal values for both the rectifier and inverter modes of operation as well.

5.2 Analysis of Harmonic Contents

Connection of power electronics converters to the electricity power grid can cause some harmonics to be observed in line current. Harmonics could be generated due

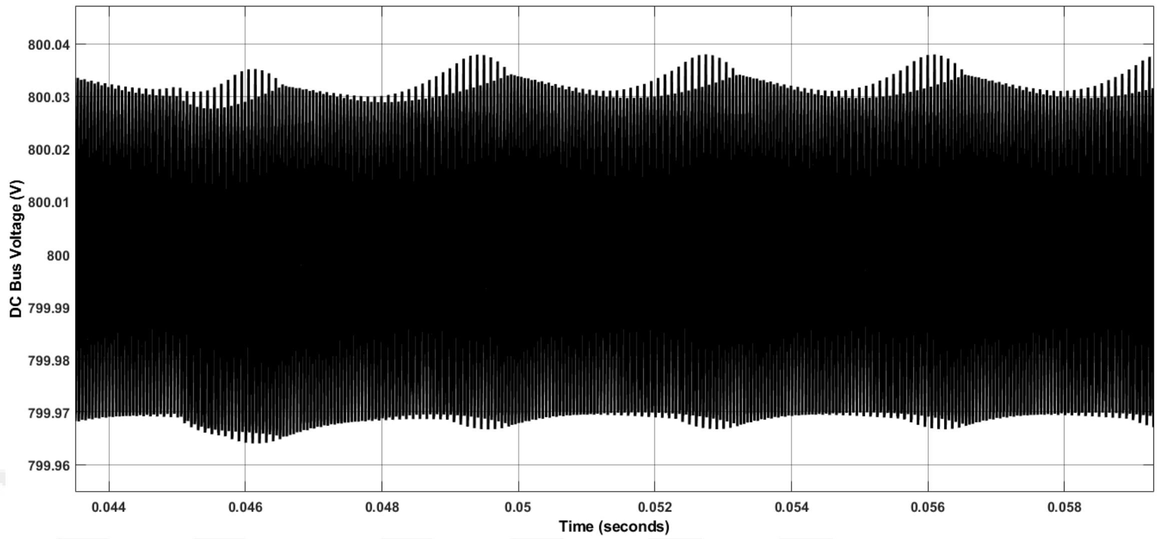

Figure 132: Simulation result for the response of the DC link voltage with variation of the battery voltage, of which the value is decreased by 20V, in inverter mode of operation

to nonlinear loads or switching transistors in power systems. The three-phase bidirectional EV charger model create some harmonics content for line current since it is connected to the grid as well.

5.2.1 Line Current Distortion and Harmonics

In this section, harmonics content evaluation and THD analysis for there-phase line currents for both charging and discharging modes for the bidirectional EV charger system are conducted.

5.2.1.1 In G2V Mode of Operation

Line current distortion and harmonics would be investigated with various charging voltage values for the output battery in the rectifier mode of operation at steady-state condition.

With 500V battery voltage reference

For the rated operating conditions (500V, 5kW) of bidirectional EV charger model, the waveforms of three phase line currents are shown in Figure 133 in steady-state.

Table 6: Values obtained from the analysis of simulation results of closed loop system performance for the EV charger model under the related conditions ($V_{bat} = 500V$ & $V_{dc} = 800V$).

	G2V MODE				V2G MODE		
	Steady-State	**Load Transient (of 6.6A)**	**DC Bus Variation in Reference (of 1.2V)**	**Variation in Battery Voltage Level (of 5V)**	**Steady-State**	**DC Bus Variation in Reference (of 1.2V)**	**Variation in Battery Voltage Level (of 20V)**
Peak-to-peak value of battery voltage	250mV (value according to theory: 142 mV)	-	-	-	-	-	-
Peak-to-peak value of inductor current	3.7A (value according to theory: 3.75 A)	-	-	-	3.7A (value according to theory: 3.75 A)	-	-
Ripple value of DC link voltage	< 150mV	-	-	-	< 80mV	-	-
Deviation in battery voltage	-	5V (max. possible value according to theory: 28.4 V)	Negligible (max. possible value according to theory: 30 mV)	Negligible	-	1.3V	-
Deviation in inductor current	-	Negligible (max. possible value according to theory: 0.54 A	Negligible (max. possible value according to theory: 6.5 mA)	Negligible	-	30A	Negligable (max. possible value according to theory: 1.72 A)
Deviation in DC link voltage	-	0.9V	3.8V	0.7V	-	1.4V (max. possible value according to theory: 2.84 V)	Negligable (max. possible value according to theory: 14 mV)

It can be noticed that line currents are distorted and has some harmonic contents, which cause the current waveforms not to be pure sine waves.

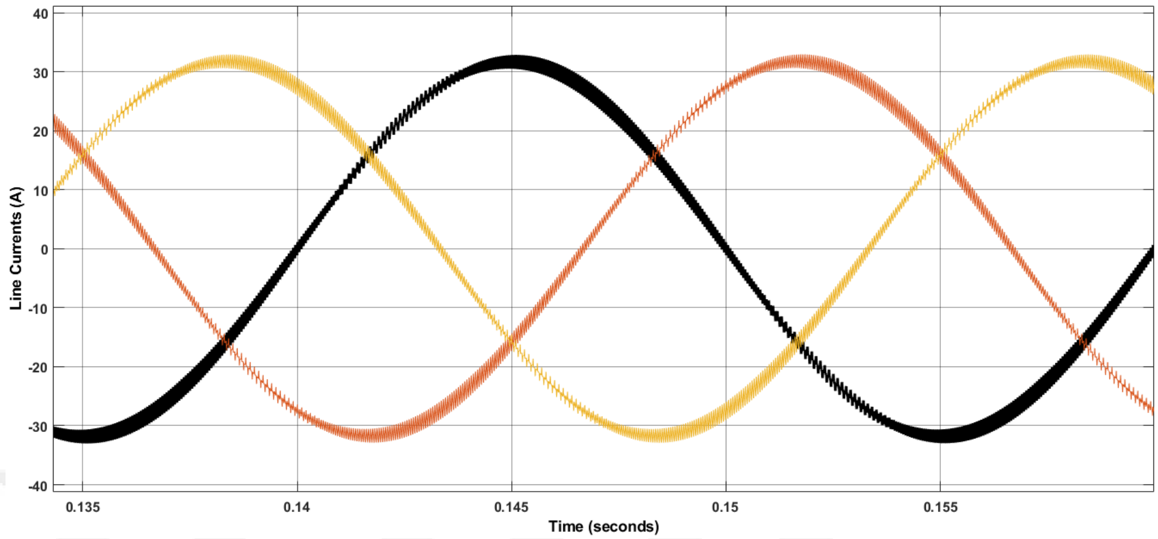

Figure 133: Simulation result for the line currents in steady-state condition in rectifier mode of operation (with 500V output)

Harmonic analysis for one of the three phase currents is performed within one cycle and the related results are shown in Figure 134. THD value of line current is measured as 3.02 %, with fundamental component having the peak value of 31.8 A, according to the harmonic spectrum when the output battery charges with the voltage value of 500V as well. Moreover odd harmonics are more dominant, except ones with order of 3 and multiplies of it, compared to even ones based on the harmonics analysis of the phase current.

With 400V battery voltage reference

While the output battery is charging with 400V, the waveforms of the line currents observed are given in Figure 135 in steady-state. It can be seen that there are some ripples observed in the three phase currents, causing some harmonics to be produced at grid side.

In the rectifier mode of operation, the results of THD analysis for one of the line currents, performed within one cycle, are given in Figure 136 as well. The measured value of THD for the phase current is 3.35 % and the fundamental component has the

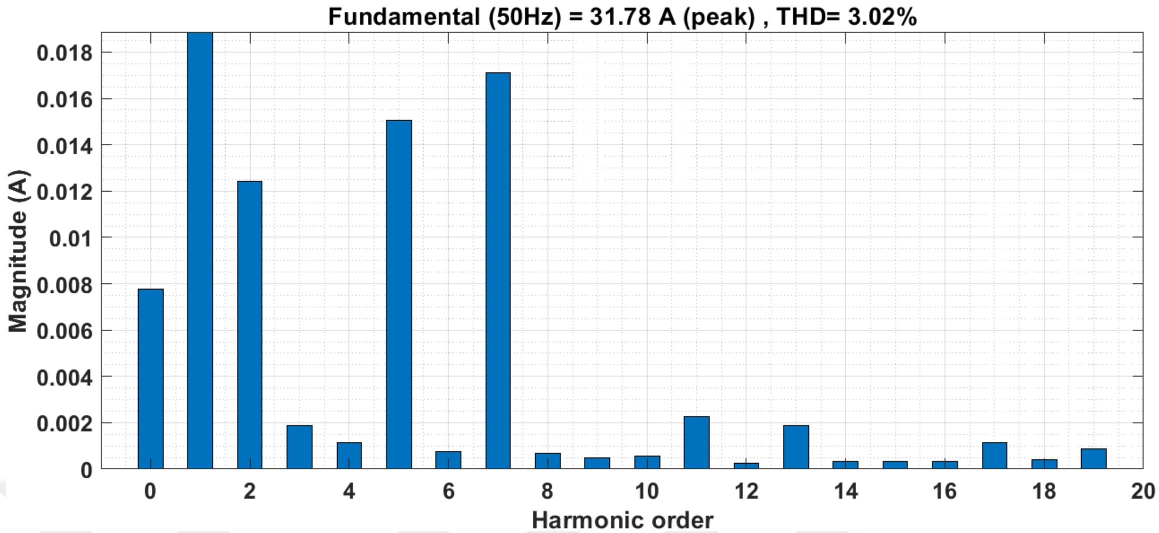

Figure 134: Results of harmonic analysis for one of the line currents in steady-state condition in rectifier mode of operation (with 500V output)

peak value of 28.5A based on the harmonic spectrum with the output battery voltage of 400V. As in the case for the battery voltage value of 500V, the odd harmonic components are also more dominant than the even ones.

With 300V battery voltage reference

Three phase line current waveforms with the charging voltage of 300V for the output battery are shown in Figure 137 in steady-state condition. It is clear that the three phase current waveforms have some distortions, leading to impure sine waves as in the cases in which the battery voltage values are 400V and 500V .

THD analysis for one of the line currents is done within one cycle and the corresponding results are also shown in Figure 138 when the bidirectional EV charger is charged with 300V. The value of harmonic distortion for the line current is observed as 4.52 % according to the harmonic spectrum. Also, the fundamental component of line current has the peak value of 21.1A when the value of battery voltage is 300V. It is clear that THD value is larger compared to those determined in the previous cases in which the output battery is charged with 400V or 500V for the rectifier mode of operation so it can be concluded that line current waveform gets more distorted as

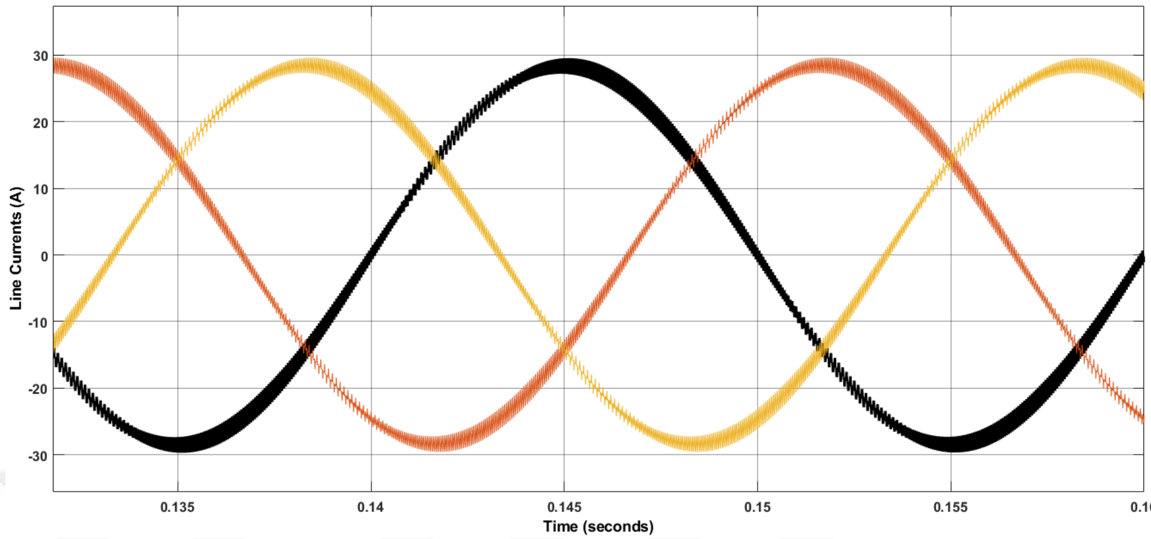

Figure 135: Simulation result for the line currents in steady-state condition in rectifier mode of operation (with 400V output)

the value of phase current drawn from the electricity grid (or total power of three phase system) decreases.

5.2.1.2 In V2G Mode of Operation

For the inverter mode of operation, distortions and harmonics observed in three phase line currents can also be analyzed with various battery voltage values at steady-state condition.

With 500V battery voltage reference

The waveforms of line currents in steady-state are shown in Figure 139 for the rated operating conditions of three phase EV charger system. It is clear that the three phase currents are also distorted with some harmonic contents as in the case of G2V mode of operation.

Harmonic analysis for one of the line currents is performed within one cycle for the inverter mode of operation too and the corresponding results are given in Figure 140. The measured THD value of the line current is 5.73 %, with the fundamental component that has the peak value of 16.4A according to the harmonic spectrum,

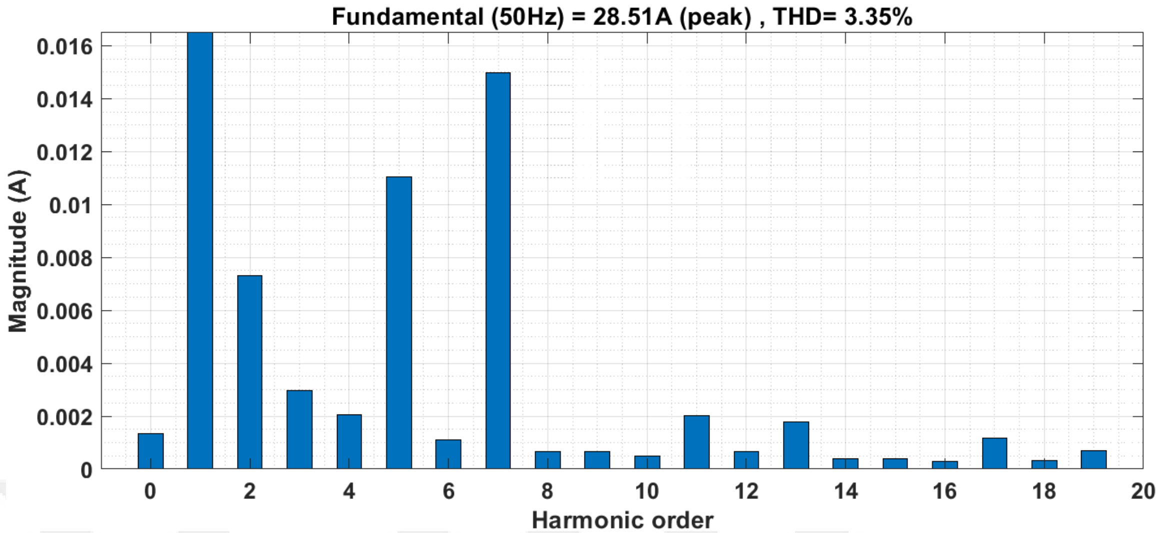

Figure 136: Results of harmonic analysis for one of the line currents in steady-state condition in rectifier mode of operation (with 400V output)

with the battery voltage value of 500V in V2G mode. Odd harmonics are also more dominant, except ones with order of 3 and multiplies of it, than even ones based on the harmonics analysis of the line current as in the case of G2V mode of operation for the EV charger model.

With 373V battery voltage reference

For discharging of the EV battery in V2G mode of operation when the value of battery voltage is about 373V, the waveforms of the three phase currents observed in steady-state are given in Figure 141. Also the line currents has some ripple contents, which can cause some distortions at grid side according to the simulation result as in the previous case.

Moreover, the results of THD analysis for one of the line currents, performed within one cycle, are shown in Figure 142 for the inverter mode of operation. THD value of the phase current is observed as 5.73 %, with the fundamental component having the peak value of 16.4 A, according to the harmonic spectrum when the EV battery discharges with the voltage value around 373V too. The peak values of fundamental sine wave components & THD values for the line current are also the

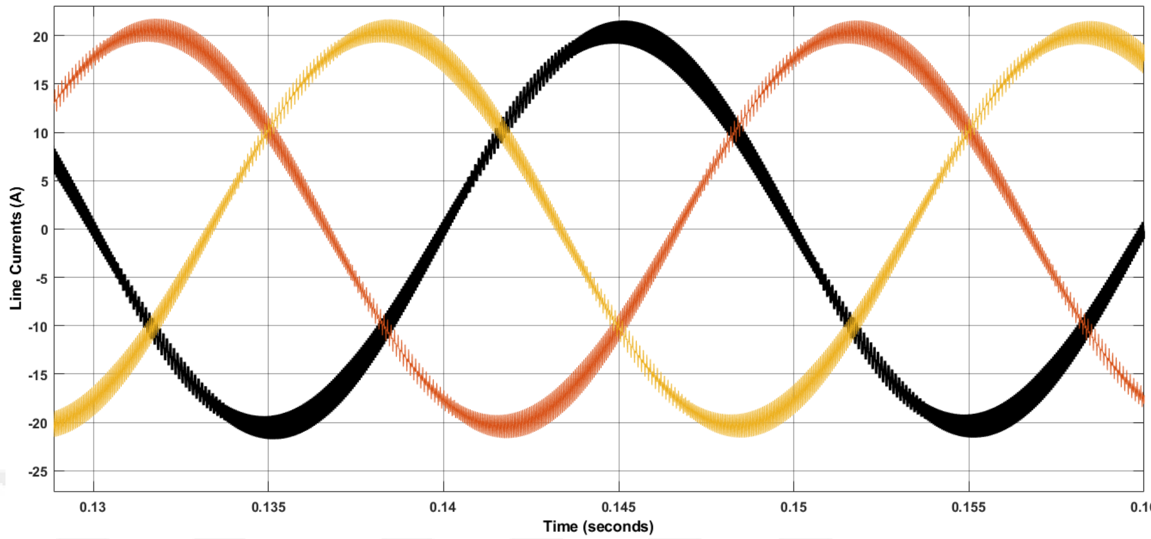

Figure 137: Simulation result for the line currents in steady-state condition in rectifier mode of operation (with 300V output)

same for both the cases of discharge voltage values of 500V and 373V since total power of the EV charger system would not change in spite of varying discharge value of the battery voltage in V2G mode.

Moreover, it can be noticed that more distortions are observed for the waveform of line current when the bidirectional EV charger model operates in the inverter mode compared to those in G2V mode of operation since current is injected into the power grid in V2G mode, for which power flow is achieved from the DC battery to AC line, causing some additional harmonic waves to generate in grid side.

5.2.2 Impact on Performance of Vehicle Battery.

It is predictable that distortions generated at the grid side for the three phase bidirectional EV charger system would cause impurities in DC link and battery side. The ripples observed in waveforms of the battery voltage & current are also due to the distorted line current components in three phase system. Therefore ripple contents can also be studied for the battery voltage & current in addition to the three phase current waveforms for both rectifer and inverter mode of operation for the EV charger

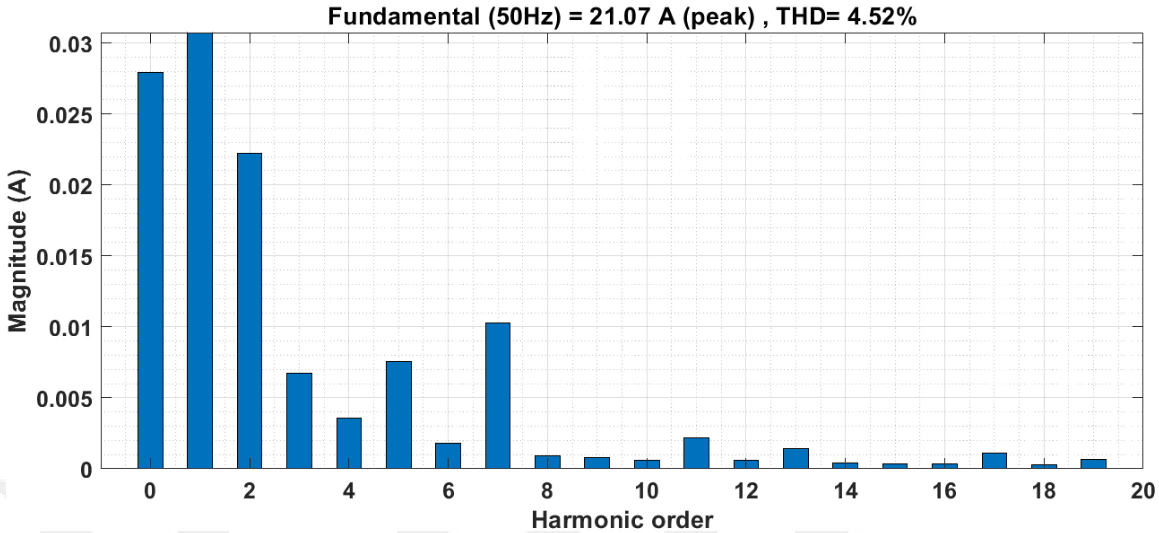

Figure 138: Results of harmonic analysis for one of the line currents in steady-state condition in rectifier mode of operation (with 300V output)

model.

5.2.2.1 *In G2V Mode of Operation*

At steady-state, the waveforms for battery voltage & current could be analyzed with various voltage values and the corresponding ripple values can be measured for the output battery in the G2V mode of operation.

With 500V battery voltage reference

For the rated operating conditions (500V, 5kW) of three phase bidirectional EV charger model, the ripples observed in the waveforms of output voltage and current can be investigated. The steady-state responses of battery voltage & output current are shown in Figure 143 for the rectifier mode of operation with output voltage value of 500V. The ripple value of output voltage, ΔV_{bat} is measured as 250mV while that of battery current, Δi_{bat} is determined as 1.66A based on the simulation result as well.

With 400V battery voltage reference

While the output battery is charging with 400V, the waveforms of the battery

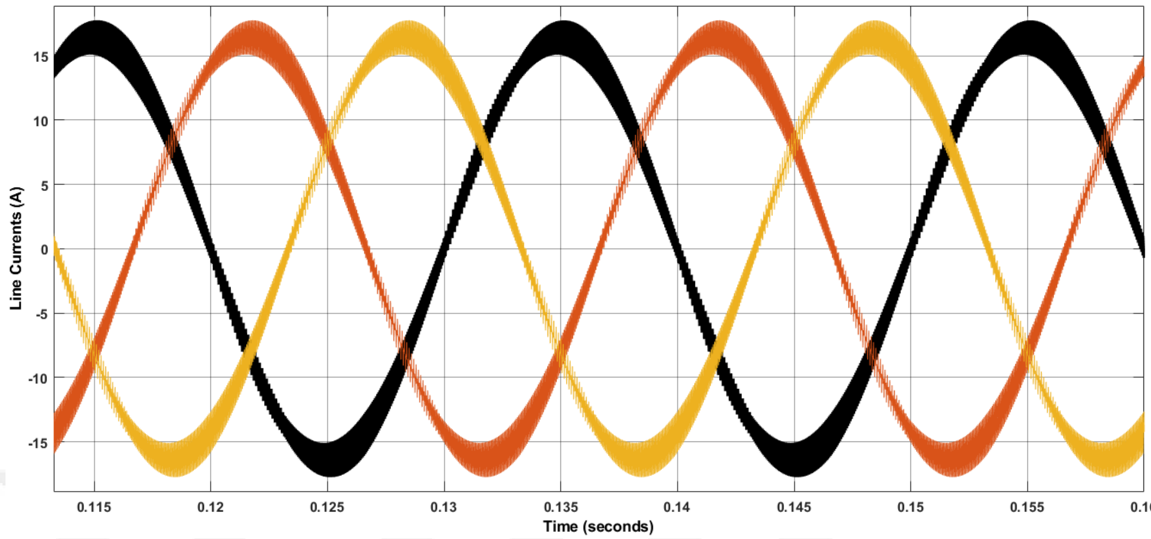

Figure 139: Simulation result for the line currents in steady-state condition in inverter mode of operation (with 500V output)

voltage and current would be analyzed according to the related ripple contents for G2V mode of operation of the charger system. The waveforms of output voltage and battery current are given in Figure 144. Also, the ripple values observed in battery voltage and output current waveforms are measured as 276mV and 1.93A, respectively.

With 300V battery voltage reference

The analysis of ripple contents in the waveforms of battery voltage and output current would also be performed with the charging voltage of 300V for the output battery. The corresponding responses of output voltage & battery current are shown in Figure 145 when the three phase bidirectional EV charger model is charged with 300V in steady-state condition. Moreover, the output battery voltage, ΔV_{bat} has the ripple value of 261mV whereas the output current, Δi_{bat} contains the ripple content, of which the value is determined as 1.82A according to the simulation result.

It can be concluded that the ripple values for both EV battery voltage & current usually tends to increase as line currents get more distorted for the three-phase

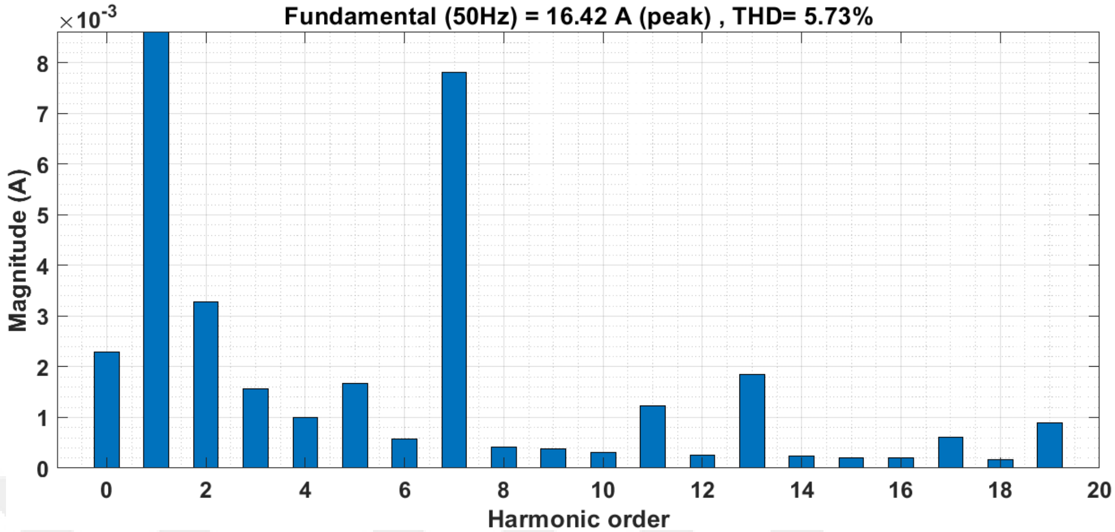

Figure 140: Results of harmonic analysis for one of the line currents in steady-state condition in inverter mode of operation (with 500V output)

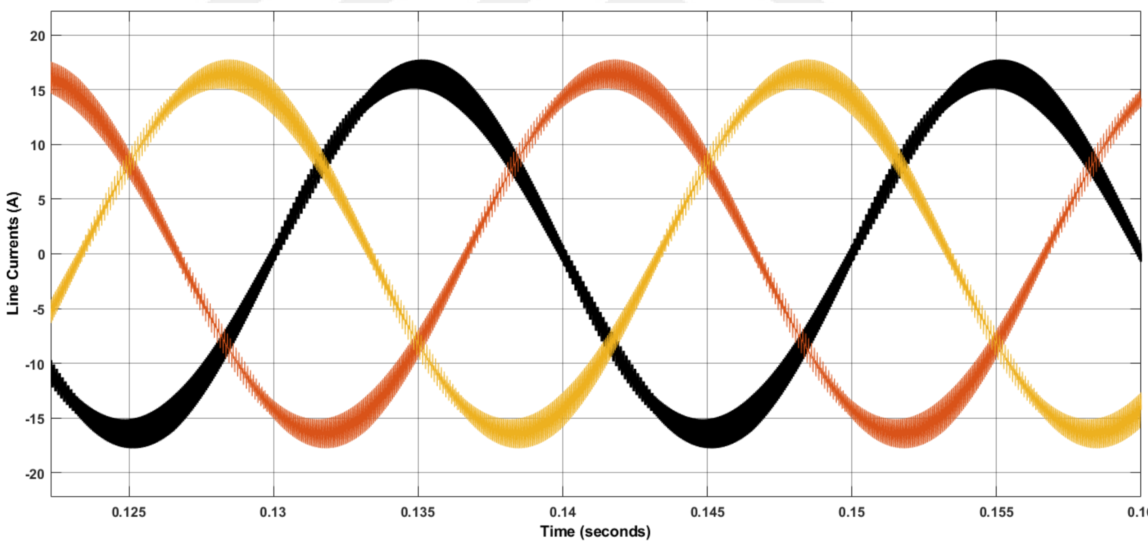

Figure 141: Simulation result for the line currents in steady-state condition in inverter mode of operation (with 373V output)

bidirectional EV charger model, operating in G2V mode, according to the simulation results as expected.

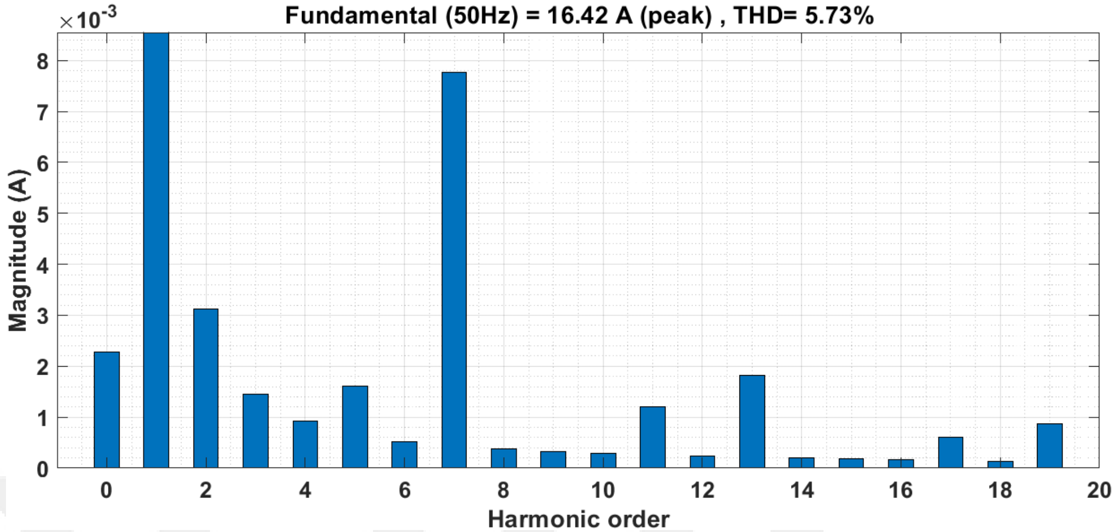

Figure 142: Results of harmonic analysis for one of the line currents in steady-state condition in inverter mode of operation (with 373V output)

5.2.2.2 In V2G Mode of Operation

Ripples observed in the battery voltage & current waveforms would be evaluated with various discharging battery voltage values for the inverter mode of operation at steady-state condition, as well.

With 500V battery voltage reference

The analysis of ripple contents for battery voltage & current can be performed for the V2G mode of operation. The related waveforms of EV battery voltage & current in steady-state are shown in Figure 146 for the rated operating conditions (with a battery voltage value of 500V) of three phase EV charger model. The value of battery voltage ripple, ΔV_{bat} is determined as 9mV while that of the current ripple, Δi_{bat} is measured as 53mA for the inverter mode of operation as well.

With 373V battery voltage reference

Moreover, the steady-state responses of battery voltage & current, with their corresponding ripples, are given in Figure 147 for discharging of the EV battery in the inverter mode of operation when the value of battery voltage is around 373V.

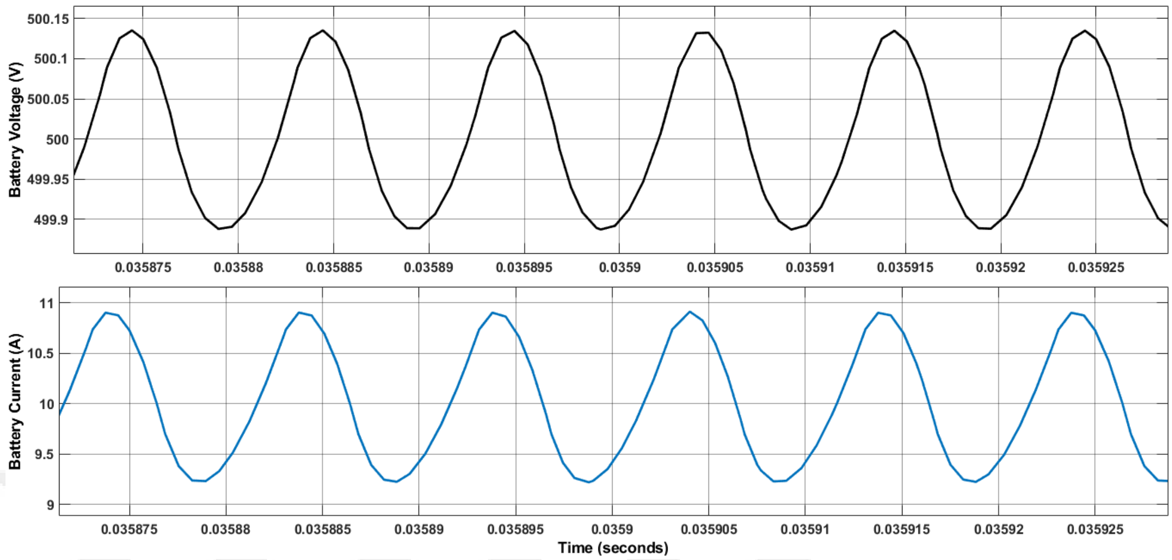

Figure 143: The responses of battery voltage & output current in steady-state condition in rectifier mode of operation (with 500V output)

Furthermore, the EV battery voltage waveform contains a ripple content with the value of 10mV whereas the ripple value of battery current is measured as 31mA according to the corresponding simulation result.

For V2G mode of operation for the EV charger system, it can be noticed that the battery voltage and current waveforms do not be affected by the distortions observed in the grid side significantly based on the simulation results since the battery supplies some power to the electricity grid by discharging instead of accepting current, not influenced by line current harmonics much unlike the case of the rectifier mode of operation.

Furthermore, the obtained simulation results related to harmonic analysis, including THD values of line currents and corresponding ripples observed in battery voltage & current, for steady-state conditions are summarized as given in Table 7 for both charging and discharging mode of operations of the three-phase charger model.

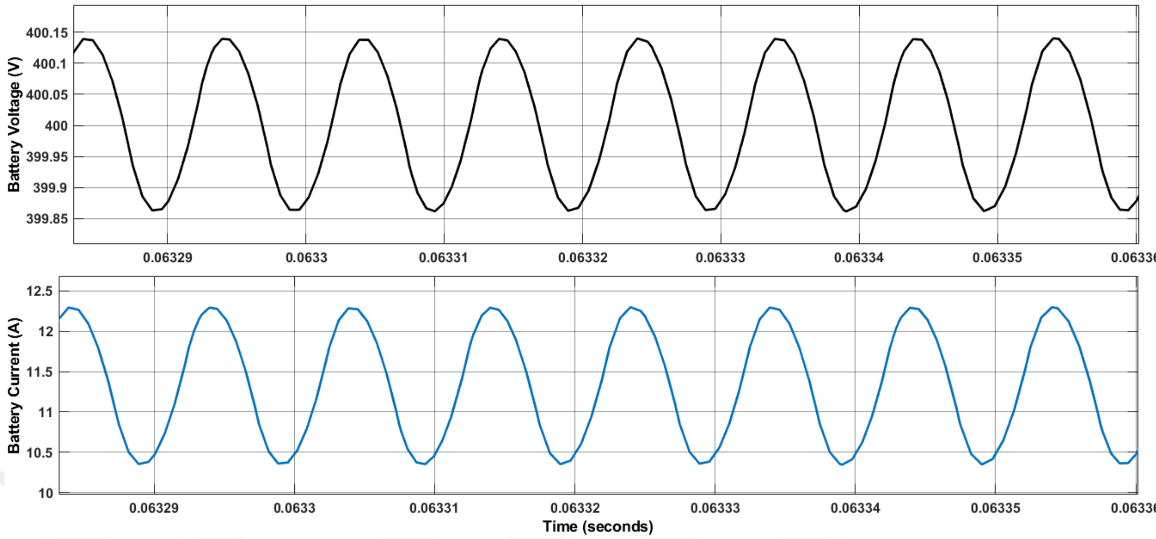

Figure 144: The waveforms of battery voltage & output current in steady-state condition in rectifier mode of operation (with 400V output)

5.3 Power Loss and Efficiency Analysis

Total power loss for the bidirectional three phase EV charger model due to parasitic elements of the transistors or internal resistances of the passive elements such as inductors would be investigated using both simulation results & analytical equations given in Chapter 2 in steady state for the rectifier mode and inverter mode of operations. Also, the efficiency value of the charger system can be calculated for both G2V and V2G mode using total conduction losses for the rated operation condition.

5.3.0.1 In G2V Mode of Operation

In the rectifier mode of operation, the power flow would be from the electricity grid to DC link and battery side so some conduction losses are observed when the power is transmitted to the output battery for the three phase EV charger model, causing the real power of battery side to be less than that measured in the grid side.

Power loss and efficiency calculation from simulation results

From the simulation results of the phase voltage & current waveforms for the nominal value of battery voltage (500V), the power in AC side can be calculated as;

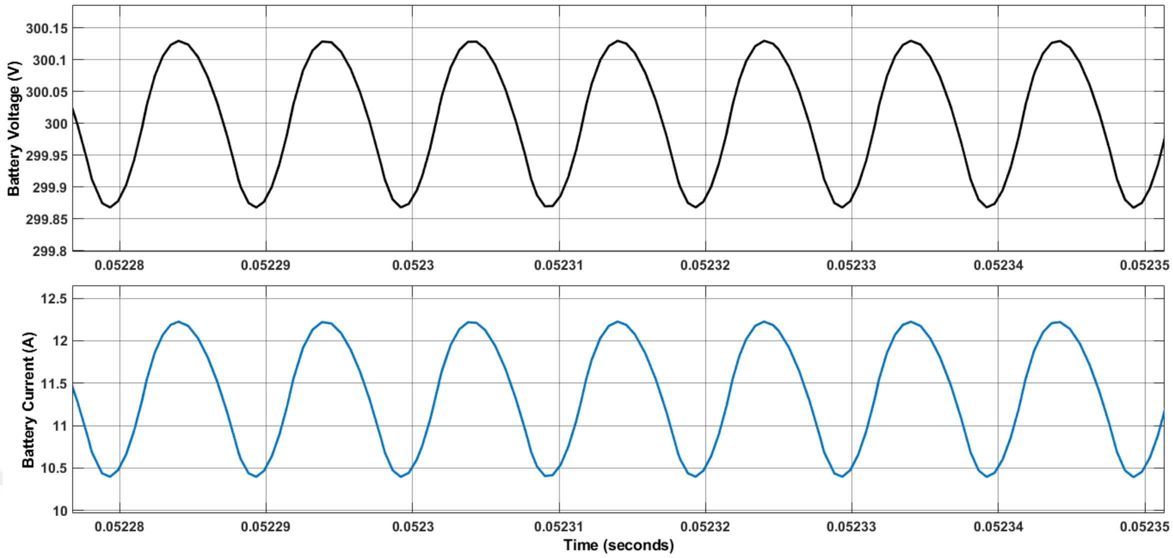

Figure 145: The responses of output voltage & battery current in steady-state condition in rectifier mode of operation (with 300V output)

$$P_{ac} = \frac{3}{2}V_m I_m = \frac{3}{2}\ x\ 325\ x\ 31.8 \tag{380}$$

$$P_{ac} = 15502W \tag{381}$$

Also, the power in DC side would be sum of the EV battery power, P_{bat} and the power value in "dqe" reference frame, P_{dqe} created in the control algorithm for the AC/DC PWM converter as shown in the equation given below;

$$P_{dc} = P_{bat} + P_{dqe} \tag{382}$$

where

$$P_{bat} = 5000W \tag{383}$$

(since the average value of battery current is nearly 10A)

The equation for the value of P_{dqe} can be defined as;

$$P_{dqe} = \frac{3}{2}((V_{sqe} - V_{iqe})i_{qe} + (V_{sde} - V_{ide})i_{de}) \tag{384}$$

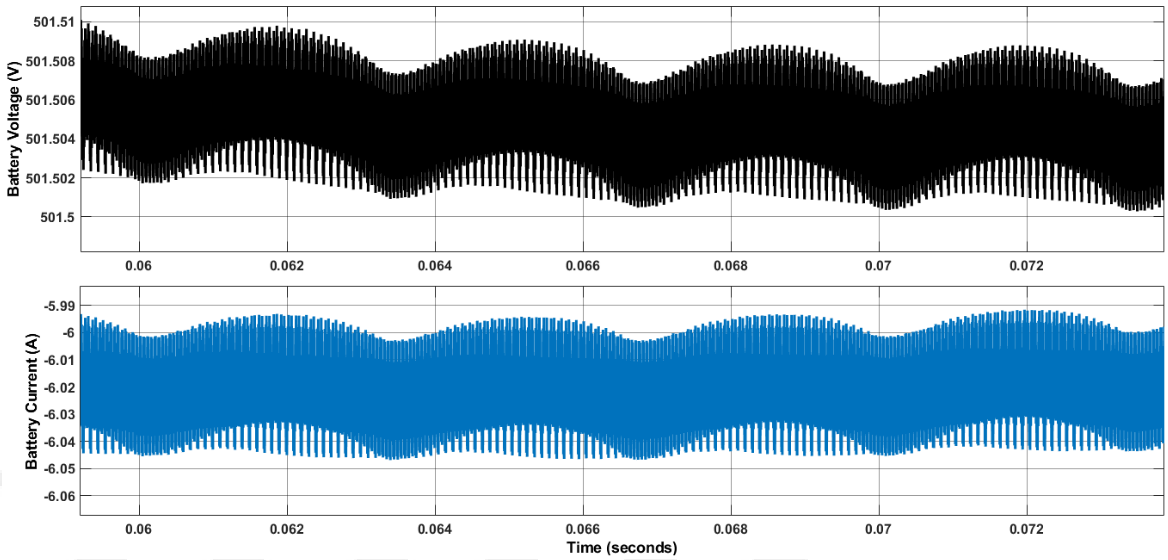

Figure 146: The waveforms of EV battery voltage & current in steady-state condition in inverter mode of operation (with 500V output)

Since the imaginary (d) component of the line current, i_{de} is zero, the equation in (384) is reduced to that given in (385);

$$P_{dqe} = \frac{3}{2}(V_{sqe} - V_{iqe})i_{qe} \tag{385}$$

Thus, the total power in DC side would be calculated as;

$$P_{dc} = 5000 + \frac{3}{2}\ x\ (325 - 105)\ x\ 31.75 \tag{386}$$

$$P_{dc} = 15477W \tag{387}$$

Therefore, the power loss of the system, P_{loss} would become

$$P_{loss} = P_{ac} - P_{dc} = 15502 - 15477 \tag{388}$$

$$P_{loss} = 25W \tag{389}$$

The efficiency of the EV charger model could also be calculated using the total conduction power loss value for the rectifier mode of operation. The expression for efficiency value of the system is given as;

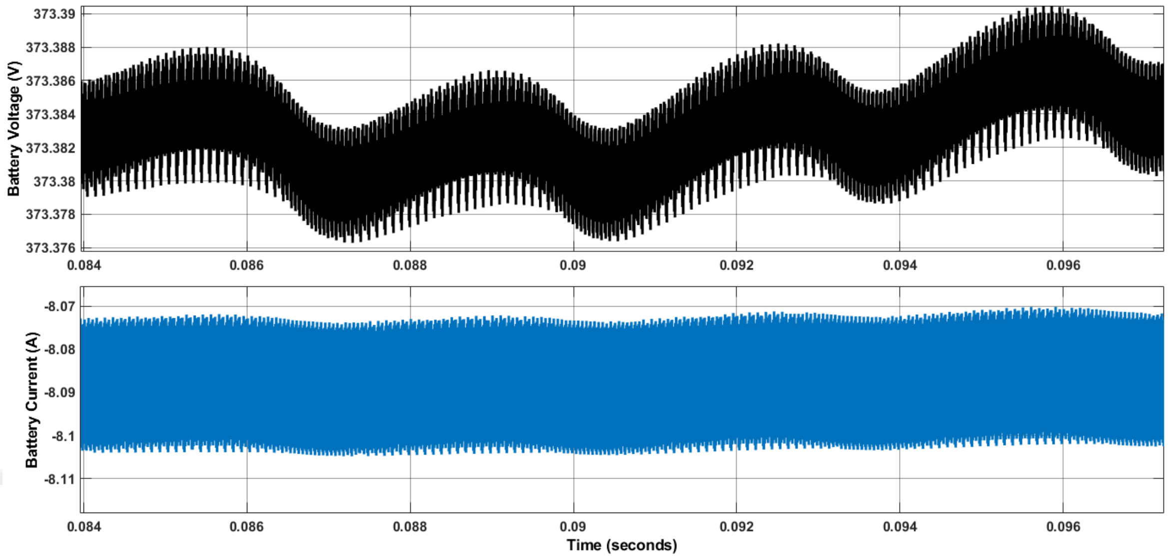

Figure 147: The responses of battery voltage & current in steady-state condition in inverter mode of operation (with 373V output)

$$\eta_{rec} = \frac{P_{ac} - P_{loss}}{P_{ac}} \tag{390}$$

Hence, the value of η_{rec} can be determined as;

$$\eta_{rec} = \frac{15477}{15502} \tag{391}$$

$$\eta_{rec} = 99.8\% \tag{392}$$

Verification of power loss using analytical equations

The power loss value for the three phase bidirectional EV charger model could also be determined using the analytical equations given in (19)-(21) for the AC/DC PWM converter and (91) for the synchronous DC/DC converter, operating in buck mode. Power loss generated in AC/DC side of the charger system can be calculated as;

$$P_{T,ac} = 0 + \frac{0.01 \ x \ 32^2}{2\pi}(\frac{\pi}{4} + \frac{2}{3} \ x \ 0.81) \tag{393}$$

Table 7: Simulation results related to harmonic analysis for steady-state conditions of the EV charger model

	G2V MODE			V2G MODE	
	500V battery voltage reference	**400V battery voltage reference**	**300V battery voltage reference**	**500V battery voltage reference**	**373V battery voltage reference**
THD of line current	3.02%	3.35%	4.52%	5.73%	5.73%
Ripple value of battery voltage	250mV	276mV	261mV	9mV	10mV
Ripple value of battery current	1.66A	1.93A	1.82A	53mA	31mA

$$P_{T,ac} = 2.16W \tag{394}$$

$$P_{D,ac} = \frac{0.7\ x\ 32}{2\pi}(1 - \frac{0.81\pi}{4}) \tag{395}$$

$$P_{D,ac} = 1.3W \tag{396}$$

$$P_{loss,ac} = 6\ x\ (2.16 + 1.3) \tag{397}$$

$$P_{loss,ac} = 20.8W \tag{398}$$

The efficiency value of the DC/DC converter of the three phase EV charger model in G2V mode of operation would be determined as;

$$\eta_d = \frac{1}{1 + \frac{0.01+0.008}{\frac{500}{10}}} \tag{399}$$

$$\eta_d = 0.99964 \tag{400}$$

The power loss created in the DC/DC part of the charger system could be calculated using the efficiency value, η_d as;

$$P_{loss,dc} = \frac{P_{bat}(1-\eta_d)}{\eta_d} = \frac{5000(1-0.99964)}{0.99964} \tag{401}$$

$$P_{loss,dc} = 1.8W \tag{402}$$

Hence the total power loss of the EV charger model would become;

$$P_{loss} = P_{loss,ac} + P_{loss,dc} = 20.8 + 1.8 \tag{403}$$

$$P_{loss} = 22.6W \tag{404}$$

The loss value obtained via the equations ,derived analytically and given in (19)-(21) & (91), is really closed to that calculated using the related simulation results. Therefore, theoretical study regarding power loss analysis verifies the corresponding results observed in simulation for the three phase EV charger model, that operates in the rectifier mode.

5.3.0.2 In V2G Mode of Operation

Direction of the power flow is from the EV battery to the power grid in the inverter mode of operation for the bidirectional charger model and the conduction losses, generated when the power is transmitted to AC side from the battery, causes the real power of the grid side to be less than that measured in the battery side unlike the case of G2V mode.

Power loss and efficiency calculation from simulation results

According to the simulation results of the phase voltage & line current waveforms for the nominal discharging value of battery voltage (500V) in V2G mode of operation, the power in AC side could be calculated as;

$$P_{ac} = \frac{3}{2}V_m I_m = \frac{3}{2}\ x\ 325\ x\ 16.42 \tag{405}$$

$$P_{ac} = 8004W \tag{406}$$

Moreover, the power value measured in DC side is sum of the EV battery power, P_{bat} and the power value in "dqe" reference frame, P_{dqe} as in the case for the rectifier mode of operation. Hence the value of P_{dc} would be expressed as;

$$P_{dc} = P_{bat} + P_{dqe} \tag{407}$$

where

$$P_{bat} = 3000W \tag{408}$$

(since the average value of battery current is about 6A)

The value of P_{dqe} can be defined as given in (385) too and the power in DC side, P_{dc} is determined as;

$$P_{dc} = 3000 + \frac{3}{2}\ x\ (325 - 120)\ x\ 16.3 \tag{409}$$

$$P_{dc} = 8012W \tag{410}$$

Hence, the power loss of the system, P_{loss}, operating in V2G mode, would be;

$$P_{loss} = P_{dc} - P_{ac} = 8012 - 8004 \tag{411}$$

$$P_{loss} = 8W \tag{412}$$

For the inverter mode of operation, the efficiency of the three phase EV charger system would be calculated using the conduction power loss value so the equation for efficiency value of the system is given as;

$$\eta_{rec} = \frac{P_{dc} - P_{loss}}{P_{dc}} \tag{413}$$

Hence, the value of η_{rec} can be determined as;

$$\eta_{rec} = \frac{8004}{8012} \tag{414}$$

$$\eta_{rec} = 99.9\% \tag{415}$$

It can be noticed that the efficiency value of bidirectional EV charger model is slightly larger in V2G mode compared to that in G2V mode since the line or battery current value is smaller, that can lead to less conduction losses, when the charger system operates in the inverter mode.

Verification of power loss using analytical equations

The power loss value for the three phase charger system would also be determined as in the case of the rectifier mode. For V2G mode of operation, power loss generated in AC/DC side of the EV charger model could be calculated as;

$$P_{T,ac} = 0 + \frac{0.01\ x\ 17^2}{2\pi}(\frac{\pi}{4} + \frac{2}{3}\ x\ 0.81) \tag{416}$$

$$P_{T,ac} = 0.61W \tag{417}$$

$$P_{D,ac} = \frac{0.7\ x\ 17}{2\pi}(1 - \frac{0.81\pi}{4}) \tag{418}$$

$$P_{D,ac} = 0.69W \tag{419}$$

$$P_{loss,ac} = 6\ x\ (0.61 + 0.69) \tag{420}$$

$$P_{loss,ac} = 7.8W \tag{421}$$

Since the load resistance value is assumed to be very large, which is selected as 1MΩ, while designing the control loops for the inverter mode of operation in Chapter 3, the efficiency value of DC/DC converter, operating in boost mode, would be nearly 100% so it can be considered there is no conduction losses created in DC/DC side of the EV charger model, which operates in V2G mode. Hence the total power loss of the EV charger model would become;

$$P_{loss} = P_{loss,ac} + P_{loss,dc} = 7.8 + 0 \tag{422}$$

$$P_{loss} = 7.8W \tag{423}$$

To be concluded, the loss value calculated using the analytical equations is almost same with that determined via the corresponding simulation results. As in the case of G2V mode, theoretical study about conduction loss analysis verifies the related results observed in simulation for the bidirectional EV charger system, operating in the inverter mode too.

Total power loss and efficiency values obtained using the related simulation results with the nominal battery voltage value of 500V are given in Table 8 for both G2V and V2G mode of operations for the bidirectional EV charger system.

Table 8: Total power loss and efficiency values obtained using the related simulation results with the nominal battery voltage value of 500V

	G2V mode	**V2G mode**
Total power loss	25W (value according to theoretical analysis: 22.6W)	8W (value according to theoretical analysis: 7.8W)
Efficiency	> 99%	> 99%

5.4 General Discussion

The simulation results for the charger circuit model are investigated in terms of the closed loop system performance and harmonic contents generated at the grid side for both the rectifier and inverter mode of operations. The verification of the performance of the implemented system is done under various operating conditions in simulation work so it is concluded that the control algorithms provide tight current regulation and over-current protection in addition to the control of DC link voltage or battery voltage for the AC/DC PWM converter & DC-DC synchronous converter models. Therefore, the obtained simulation results show that the two-loop control systems are able to achieve a desired closed-loop performance for a wide range of operation for the EV charger system. The evaluation of performance of the model is also carried out for steady-state operating condition in the scope of line current THD and ripple contents observed in battery voltage & current. Moreover, the system operates with line current THD values of less than 5 % in G2V mode for a wide range of output voltage values, between 300V and 500V, in accordance with IEEE-1547 standards for grid connection, whereas it is operated with THD values slightly larger than 5 % in V2G mode, for which the performance could be enhanced a bit more by improving filtering capability of the grid side AC/DC converter. The efficiency value of the EV charger model is guaranteed to be higher than 98 % for both the rectifier and inverter mode of operations when the model operates in nominal conditions so it is clear that the system has really low conduction losses thanks to small values of parasitic elements corresponding to the transistors or passive components as well.

CHAPTER VI

CONCLUSION

A three-phase grid connected bidirectional EV charger model is proposed, designed and simulated to provide both charging of vehicle battery in G2V mode and reactive power support or reverse power for the electricity grid in V2G mode in this thesis. The system consists of two stages, one of which is AC/DC PWM converter responsible for the conversion between AC grid voltage & DC link voltage and the other is synchronous DC/DC converter, able to operate as a buck or boost converter. LCL filter is also added to the grid side of the model to suppress some undesired harmonics generated due to switching operations.

In the first two chapters of this thesis, general overview about the current situation in worldwide is mentioned, why the popularity of EV chargers increases is discussed, the motivation and objectives regarding the study are reported. Then literature review about power electronics converters is given in general, including generation of gate signals, modulation techniques, component design and small-signal analysis. Also, some electric vehicle charger topologies and battery technologies, which are commonly used, are included with the corresponding specifications. From the review of various charger topologies, it can be concluded that the topologies with a diode or diode bridge at output side are able to provide only unidirectional power flow whereas the ones with transistors, across which diodes are connected anti-parallel, have bidirectional power flow capability. For three phase AC/DC converters, the methods of Clark-Park Transformation and PLL control are discussed as well. Lastly, the theory of control system design for both DC/DC and three phase AC/DC converters is mentioned.

In the third chapter, design considerations of the EV charger system are discussed for both AC/DC and DC/DC parts, pointing out the selection of components ,including some calculations to obtain numerical values of system parameters, and the development of control algorithms to form two-loop control systems, consisting of inner current loops, having the bandwidth value about 2kHz for AC/DC part & 10kHz for DC/DC part of the system, and outer voltage loops, with the cut-off frequency value of around 430Hz for AC/DC converter & 1kHz for DC/DC converter of the charger model operated at rated conditions. Theoretical analysis for the control systems are also given for both G2V and V2G mode of operations.

In the forth chapter of the study, the proposed bidirectional EV charger system is implemented with the corresponding control algorithms, proposed for both of the AC/DC and DC/DC parts, in Matlab/Simulink environment. The model is also developed in such a way that it can operate in the inverter mode in addition to the traditional G2V mode and all of the related subsystems are shown.

In the fifth chapter, simulation work of the developed EV charger model is performed in Simulink to evaluate the closed loop performance and harmonic distortion of the complete system. It is observed that while the bidirectional charger model is able to provide a stable operation for various conditions, it may have a line current THD value larger than 5% especially for the inverter mode of operation, which is not in compliance with the related grid connection standards. Hence, there would be need for some improvements of the LCL filter in future to achieve less harmonic distortions for all operating conditions corresponding to the charger model. Finally, the developed model for the charger system can be said to provide really high efficiency values larger than 98% for steady-state operation considering only conduction loses are included for the charger system.

APPENDIX A

MATLAB SCRIPTS

```
% ************************************************
%% PARAMETERS FOR G2V MODE OF OPERATION %%
% ************************************************

%% AC-DC converter ratings

Vm = 325;     % Peak value of phase voltages
Vdc = 800;  % DC bus voltage
fline = 50;    % Line frequency
fsw_ac = 10e3;  % Switching freq
Ls = 1e-3;  % Line inductance
Rs = 0.5;     % Internal resistance of line inductor
Co = 2e-3;  % DC bus capacitance
Lg = 1e-3;  % Grid side filter inductance
Li = 1.6e-3;  % Converter side filter inductance
Cf = 300e-3;  % Filter capacitance
Rd = 0.5;    % Filter damping resistance

Lt = Ls+Lg+Li;  % Total inductance at grid side
Ts = Lt/Rs;  % Time constant of line inductor

Tsw_ac = 1/fsw_ac;  % Switching period
```

```
Tsamp_ac = Tsw_ac/2; % Sampling period
T1 = Tsamp_ac/10;      % Time constant of voltage sensor
                       %(voltage sensor delay)
T2 = Tsamp_ac/10; % Time constant of current sensor
                  % (current sensor delay)

G = 1;  % Converter gain
K1 = 1  % Gain of voltage sensor
K2 = 1; % Gain of current sensor
Tsig = T2 + Tsamp_ac % Effective delay for current control loop
Tdel = T1 + 2*Tsig   % Effective delay for voltage control loop

Ron_ac = 10e-3; % On-state resistance of transistors in AC-DC
                % PWM converter
Von_ac = 0.7;   % Forward voltage drop of internal diode for
                % transistors in AC-DC PWM converter

% PLL parameters %
alfa_pll=sqrt(10); % Constant ratio of Kp and Ki values of PI
                   % controller for PLL loop

Kpll=(1/Vm)*(1/(alfa_pll*Tsamp_ac)) % Kp value of PLL
Tpll=alfa_pll^2*Tsamp_ac            % PLL time constant
Kipll=Kpll/Tpll              % Ki value of PLL

%Compensated open PLL
s= tf('s')
```

```
Gol_pll = (Vm*Kipll*(Tpll*s+1))/(s^2*(1+s*Tsamp_ac))
fc_pll = (1/(alfa_pll*Tsamp_ac))/(2*pi)    % Cross-over freq. of PLL


% Current controller parameters %
Kc = (Rs*Ts)/(2*G*K2*Tsig)
Kpc = Kc;              % Kp value of current controller

Tc = Ts                % Current controller time constant
Kic = Kpc/Tc           % Ki value of current controller

wn = 1/(sqrt(2)*Tsig)  % Current loop bandwidth


% Voltage controller parameters
K = (3/2)*(Vm/Vdc) % Ratio between DC bus current and q component
                   % of line current (K = I_dc/i_sqe)

alfa_volt = sqrt(10);  % Constant ratio of Kp and Ki values of PI
                       % controller for voltage loop
Tv_ac = alfa_volt^2*Tdel      % Voltage controller time constant
Kv = (Co*K2)/(K1*K*alfa_volt*Tdel)

Kpv = Kv                      % Kp value of voltage controller
Kiv = Kpv/Tv_ac                  % Ki value of voltage controller

%%%%%%%%%%%%%%%%%%%%%%%%%%%%%%%%%%%%%%%%%%%%%%%%%%%%%%%%%%%%%%%%
```

```
Idc_max = 10
Iqe_max = -Idc_max/K
%%%%%%%%%%%%%%%%%%%%%%%%%%%%%%%%%%%%%%%%%%%%%%%%%%%%%%%%%%%%%%%%%%%

%Closed current loop
Gc = (Kc*(1 + s*Tc))/(s*Tc)
Gdelay = G/(1+s*Tsamp_ac)
Gind = (1/Rs)/(1+s*Ts)
Gc_sense = K2/(1+s*T2)
Gcl_c = (Gc*Gdelay*Gind)/(1 + (Gc*Gdelay*Gind*Gc_sense))
fn = (1/(sqrt(2)*Tsig))/(2*pi)       % Current loop bandwidth
%%%%%%%%%%%%%%%%%%%%%%%%%%%%%%%%%%%%%%%%%%%%%%%%%%%%%%%%%%%%%%%%%%%

%Open voltage loop
Ke = (Kv*K*K1)/K2
Gol_v = (Ke*(1+s*Tv_ac))/(s^2*Tv_ac*Co*(1+s*Tdel))
fc_v = (1/(alfa_volt*Tdel))/(2*pi)% Cross-over freq. of voltage
                                  % loop
%%%%%%%%%%%%%%%%%%%%%%%%%%%%%%%%%%%%%%%%%%%%%%%%%%%%%%%%%%%%%%%%%%%
%Closed voltage loop
Gv_sense = K1/(1+s*T1)
Gcl_v = (Gol_v/Gv_sense)/(1+Gol_v)
%%%%%%%%%%%%%%%%%%%%%%%%%%%%%%%%%%%%%%%%%%%%%%%%%%%%%%%%%%%%%%%%%%%

figure(1)
bode(Gcl_c)
legend('Inner closed current loop gain')
```

```
figure(2)
bode(Gol_v)
legend('Outer open voltage loop gain')

figure(3)
bode(Gcl_v)
legend('Closed voltage loop gain')

%% DC-DC converter ratings (buck mode)
Vg=800;                  % Input voltage
V=500;                   % Output voltage

P=5000;                 % Output power
P_light = 500

Iload=P/V;               % Load current
Iload_light = P_light/V;

R=V/Iload;               % Load resistance
R_light = V/Iload_light;

fsw_dc=100e3;            % Switching frequency
Tsw_dc=1/fsw_dc;         % Switching period

%Inductor
L=250e-6;                 % Inductance
```

```
RL=10e-3;                % Internal resistance

%Capacitor
C=33e-6;                 % Capacitance
Resr=6e-3;               % ESR value

%Mosfet
Rdson=8e-3;              % On-state resistance
Vf=0.78;                 % Anti-paralel diode forward voltage

VM = 4;                 % Peak value of PWM sawtooth wave

Rf = 0.25;              % Current sensing resistance
H = 0.0075;             % Voltage sensing gain

Vref = H*V;

Tsamp_dc = Tsw_dc/2;     % Sampling delay

%% DC analysis

% Duty cycle
D=(V/Vg)*(1+((RL+Rdson)/R))        % Duty cycle value

% Inductor current
I = V/R
```

```
% Efficiency
nd = 1/(1+((RL+Rdson)/R))

%Inductor ripple current
I_ripple=(((Rdson+RL)*I+V)*(1-D)*Tsw_dc)/(2*L)

%Output voltage ripple (effect of "Resr" is neglected)
V_ripple=(I_ripple*Tsw_dc)/(8*C)

%% Small signal AC analysis
s=tf('s')

Re=RL+Rdson

%Gvd - duty cycle-to-output voltage TF
Gvd=((Vg*R)/(Re+R))*((1+s*C*Resr)/(((L*C*(R+Resr))/(Re+R))*s^2+
((R*Re*C+Resr*Re*C+Resr*R*C+L)/(Re+R))*s+1))

Gvd_light = ((Vg*R_light)/(Re+R_light))*((1+s*C*Resr)/
(((L*C*(R_light+Resr))/(Re+R_light))*s^2+((R_light*Re*C+Resr*Re*C+
Resr*R_light*C+L)/(Re+R_light))*s+1))

%Gvi - inductor current-to-output TF
Gvi=(R*(1+s*C*Resr))/(1+s*C*(R+Resr))

Gvi_light = (R_light*(1+s*C*Resr))/(1+s*C*(R_light+Resr))
```

```
%Gid - duty cycle-to-inductor current TF
Gid=Gvd/Gvi

Gid_light = Gvd_light/Gvi_light

%Gvg - line-to-output voltage TF
Gvg=((D*R)/(Re+R))*((1+s*C*Resr)/(((L*C*(R+Resr))/(Re+R))*s^2+
((R*Re*C+Resr*Re*C+Resr*R*C+L)/(Re+R))*s+1))

%Gig - line-to-inductor current TF
Gig=Gvg/Gvi

%Zout - output impedance TF
Zout=(-(R*Re)/(Re+R))*(1+s*(L/Re))*((1+s*C*Resr)/(((L*C*(R+Resr))
/(Re+R))*s^2+((R*Re*C+Resr*Re*C+Resr*R*C+L)/(Re+R))*s+1))

%Giz - load-to-inductor current TF
Giz=(R/(Re+R))*((1+s*C*Resr)/(((L*C*(R+Resr))/(Re+R))*s^2+
((R*Re*C+Resr*Re*C+Resr*R*C+L)/(Re+R))*s+1))


%% Compensator design

% Sampling delay TF
Hsamp = 1/(1+s*Tsamp_dc)

% Inner current loop design
```

```
Tiu = Rf*(1/VM)*Hsamp*Gid;  % Uncompensated current loop gain
Tiu_light = Rf*(1/VM)*Hsamp*Gid_light

Tiu_fw = Tiu/Rf;             % Forward uncomp. current loop gain
Kpc_dc = 0.3;                % Kp of current controller
Kic_dc = 6749.8;             % Ki of current controller
Gci = Kpc_dc+Kic_dc/s;  % Current controller

Ti = Tiu*Gci;                % Compensated current loop gain
Ti_light = Tiu_light*Gci;    % Compensated current loop gain



Ti_cl = (1/Rf)*(Ti/(1+Ti));     % Inner closed loop gain
Gig_cl = Gig/(1+Ti);             % Closed-loop line-to-current gain
Giz_cl = Giz/(1+Ti);             % Closed-loop load-to-current gain

figure(4)
bode(Ti)
hold on
bode(Ti_light)
legend('5kW','500W')

figure(5)
bode(Ti_cl)
legend('Inner closed loop gain')
```

```
figure(6)
bode(Giz_cl)
legend('Closed-loop load-to-current gain')



% Outer voltage loop design

Gvc = (1/Rf)*(Gvd/Gid)*(Ti/(1+Ti))  % control-to-output
                                     % voltage transfer
                                     % function
Gvc_light = (1/Rf)*(Gvd_light/Gid_light)*(Ti_light/(1+Ti_light))

Tvu = H*Gvc;          % Uncompensated voltage loop gain
Tvu_light = H*Gvc_light;

Kpv_dc = 6.9;                  % Kp of voltage controller
Kiv_dc = 15687;                % Ki of voltage controller
Gcv = Kpv_dc+Kiv_dc/s;  % Voltage controller

Tv = Tvu*Gcv;                  % Compensated voltage loop gain
Tv_light = Tvu_light*Gcv;

Tv_cl = (1/H)*(Tv/(1+Tv));     % Inner closed loop gain
Gvg_cl = (Gvg-(Gvd/Gid)*Gig*(Ti/(1+Ti)))/(1+Tv); % Closed-loop
                                            % line-to-output gain
```

```
Zout_cl = (Zout-(Gvd/Gid)*Giz*(Ti/(1+Ti)))/(1+Tv); % Closed
                                              %-loop output impedance



figure(7)
bode(Tv)
hold on
bode(Tv_light)
legend('5kW','500W')

figure(8)
bode(Tv_cl)
legend('Outer closed loop gain')

figure(9)
bode(Zout_cl)
legend('Closed-loop output impedance bode plot')




Gvg_vcl_tot = Gvg_cl*Gcl_v  % Closed-loop line-to-output gain
                            % for complete system
Gig_vcl_tot = Gig_cl*Gcl_v  % Closed-loop line-to-current gain
                            % for complete system

figure(10)
```

```
bode(Gvg_vcl_tot)
legend('Closed-loop line-to-output gain')

figure(11)
bode(Gig_vcl_tot)
legend('Closed-loop line-to-current gain')

figure(12)
bode(Gol_pll)
legend('Compensated open loop gain for PLL system')



%% Battery parameters (for various voltage values)
CellCap = 3;
Vcell_nom = 3.7;
Nser = 116;
Npar = 10;
Vbat_nom = Nser*Vcell_nom;
BatCap = CellCap * Npar;
T_bat = 1e-4;

% Vbat = 300V %
SOC_1 = 0.03;
% Vbat = 400V %
SOC_2 = 2.4;
% Vbat = 500V %
SOC_3 = 98.5;
```

```
% ************************************************
%% PARAMETERS FOR V2G MODE OF OPERATION %%
% ************************************************

%% AC-DC converter ratings
Vm = 325;     % Peak value of phase voltages
Vdc = 800;  % DC bus voltage
fline = 50;   % Line frequency
fsw_ac = 10e3;  % Switching freq
Ls = 1e-3;  % Line inductance
Rs = 0.5;     % Internal resistance of line inductor
Co = 2e-3;  % DC bus capacitance
Lg = 1e-3;  % Grid side filter inductance
Li = 1.6e-3;  % Converter side filter inductance
Cf = 300e-3;  % Filter capacitance
Rd = 0.5;   % Filter damping resistance

Lt = Ls+Lg+Li;  % Total inductance at grid side
Ts = Lt/Rs;  % Time constant of line inductor

Tsw_ac = 1/fsw_ac;  % Switching period
Tsamp_ac = Tsw_ac/2; % Sampling period
T1 = Tsamp_ac/10;      % Time constant of voltage sensor
                       % (voltage sensor delay)
T2 = Tsamp_ac/10; % Time constant of current sensor
                  % (current sensor delay)
```

```
G = 1;  % Converter gain
K1 = 1  % Gain of voltage sensor
K2 = 1; % Gain of current sensor
Tsig = T2 + Tsamp_ac   % Effective delay for current
                       % control loop
Tdel = T1 + 2*Tsig     % Effective delay for voltage
                       % control loop

Ron_ac = 10e-3;        % On-state resistance of transistors
                       % in AC-DC PWM converter
Von_ac = 0.7;          % Forward voltage drop of
                       % transistors in AC-DC PWM converter

% PLL parameters %
alfa_pll=sqrt(10);     % Constant ratio of Kp and Ki values
                       % of PI controller for PLL loop

Kpll=(1/Vm)*(1/(alfa_pll*Tsamp_ac)) % Kp value of PLL
Tpll=alfa_pll^2*Tsamp_ac            % PLL time constant
Kipll=Kpll/Tpll                % Ki value of PLL

%Compensated open PLL
s= tf('s')
Gol_pll = (Vm*Kipll*(Tpll*s+1))/(s^2*(1+s*Tsamp_ac))
fc_pll = (1/(alfa_pll*Tsamp_ac))/(2*pi)
% Cross-over freq. of PLL
```

```
% Current controller parameters %
Kc = (Rs*Ts)/(2*G*K2*Tsig)
Kpc = Kc;     % Kp value of current controller

Tc = Ts       % Current controller time constant
Kic = Kpc/Tc % Ki value of current controller

wn = 1/(sqrt(2)*Tsig)  % Current loop bandwidth


% Voltage controller parameters
K = (3/2)*(Vm/Vdc)  % Ratio between DC bus current
                    % and q component of line current
                    % (K = I_dc/i_sqe)

alfa_volt = sqrt(10);  % Constant ratio of Kp and Ki
                       % values of PI controller for
                       % voltage loop
Tv_ac = alfa_volt^2*Tdel  % Voltage controller time
                          % constant
Kv = (Co*K2)/(K1*K*alfa_volt*Tdel)

Kpv = Kv          % Kp value of voltage controller
Kiv = Kpv/Tv_ac  % Ki value of voltage controller

%%%%%%%%%%%%%%%%%%%%%%%%%%%%%%%%%%%%%%%%%%%%%%%%%%%%%%%%
```

```
Idc_max = 10
Iqe_max = -Idc_max/K
%%%%%%%%%%%%%%%%%%%%%%%%%%%%%%%%%%%%%%%%%%%%%%%%%%%%%%%%

%Closed current loop
Gc = (Kc*(1 + s*Tc))/(s*Tc)
Gdelay = G/(1+s*Tsamp_ac)
Gind = (1/Rs)/(1+s*Ts)
Gc_sense = K2/(1+s*T2)
Gcl_c = (Gc*Gdelay*Gind)/(1 + (Gc*Gdelay*Gind*Gc_sense))
fn = (1/(sqrt(2)*Tsig))/(2*pi) % Current loop bandwidth
%%%%%%%%%%%%%%%%%%%%%%%%%%%%%%%%%%%%%%%%%%%%%%%%%%%%%%%%

%Open voltage loop
Ke = (Kv*K*K1)/K2
Gol_v = (Ke*(1+s*Tv_ac))/(s^2*Tv_ac*Co*(1+s*Tdel))
fc_v = (1/(alfa_volt*Tdel))/(2*pi) % Cross-over freq.
                                   % of voltage loop
%%%%%%%%%%%%%%%%%%%%%%%%%%%%%%%%%%%%%%%%%%%%%%%%%%%%%%%%
%Closed voltage loop
Gv_sense = K1/(1+s*T1)
Gcl_v = (Gol_v/Gv_sense)/(1+Gol_v)
%%%%%%%%%%%%%%%%%%%%%%%%%%%%%%%%%%%%%%%%%%%%%%%%%%%%%%%%

figure(1)
bode(Gcl_c)
legend('Inner closed current loop gain')
```

```
figure(2)
bode(Gol_v)
legend('Outer open voltage loop gain')

figure(3)
bode(Gcl_v)
legend('Closed voltage loop gain')

%% DC-DC converter ratings (boost mode)
Vg=500;                 % Input voltage
V=800;                  % Output voltage

R=1e6;     % Load is assumed to be nearly as no load

fsw_dc=100e3;            % Switching frequency
Tsw_dc=1/fsw_dc;         % Switching period

%Inductor
L=250e-6;               % Inductance
RL=10e-3;               % Internal resistance

%Capacitor
C=Co;                   % Capacitance
Resr=0;                 % ESR value

%Mosfet
```

```
Rdson=8e-3;             % On-state resistance
Vf=0.78;                % Anti-paralel diode forward voltage

VM = 4;                 % Peak value of PWM sawtooth wave

Rf = 0.25;              % Current sensing resistance
H = 0.0075;             % Voltage sensing gain

Vref = H*V;

Tsamp_dc = Tsw_dc/2;     % Sampling delay

%% DC analysis

% Duty cycle
D=1-((Vg+sqrt(Vg^2-4*V^2*((RL+Rdson)/R)))/(2*V))

% Inductor current
I = V/(R*(1-D))

% Efficiency
nd = 1/(1+(RL+Rdson)/(R*(1-D)^2))

%Inductor ripple current
I_ripple=((Vg-(Rdson+RL)*I)*D*Tsw_dc)/(2*L)
%% Small signal AC analysis
s=tf('s')
```

```
Re=RL+Rdson

%Gvd - duty cycle-to-output voltage TF
Gvd=((1-D)*(1+s*C*Resr)*(V-I*((s*L+Re)/(1-D))))/
(((L*C*(R+Resr))/R)*s^2+((R*Re*C+Resr*Re*C+Resr
*R*C*(1-D)^2+L)/R)*s+((Re/R)+(1-D)^2))

%Gid - duty cycle-to-inductor current TF
Gid=(2*V*(1+s*C*((R/2)+Resr)))/((L*C*(R+Resr))*s^2+
(R*Re*C+Resr*Re*C+Resr*R*C*(1-D)^2+L)*s+
(Re+R*(1-D)^2))

%Gvg - line-to-output voltage TF
Gvg=((1-D)*(1+s*C*Resr))/(((L*C*(R+Resr))/R)*s^2
+((R*Re*C+Resr*Re*C+Resr*R*C*(1-D)^2+L)/R)*s+
((Re/R)+(1-D)^2))

%Gig - line-to-inductor current TF
Gig=(1+s*C*(R+Resr))/((L*C*(R+Resr))*s^2+
(R*Re*C+Resr*Re*C+Resr*R*C*(1-D)^2+L)*s+
(Re+R*(1-D)^2))

%Zout - output impedance TF
Zout=(-(1+s*C*Resr)*(s*L+Re))/(((L*C*(R+Resr))
/R)*s^2+((R*Re*C+Resr*Re*C+Resr*R*C*(1-D)^2+L)
/R)*s+((Re/R)+(1-D)^2))
```

```
%Giz - load-to-inductor current TF
Giz=((1-D)*(1+s*C*Resr))/(((L*C*(R+Resr))/R)*s^2+
((R*Re*C+Resr*Re*C+Resr*R*C*(1-D)^2+L)/R)*s+
((Re/R)+(1-D)^2))


%% Compensator design

% Sampling delay TF
Hsamp = 1/(1+s*Tsamp_dc)

% Inner current loop design

Tiu = Rf*(1/VM)*Hsamp*Gid;  % Uncompensated current loop gain
Tiu_fw = Tiu/Rf;        % Forward uncomp. current loop gain
Kpc_dc = 0.29;                % Kp of current controller
Kic_dc = 9270.6;              % Ki of current controller
Gci = Kpc_dc+Kic_dc/s;        % Current controller
Ti = Tiu*Gci;           % Compensated current loop gain

Ti_cl = (1/Rf)*(Ti/(1+Ti));     % Inner closed loop gain
Gig_cl = Gig/(1+Ti);    % Closed-loop line-to-current gain
Giz_cl = Giz/(1+Ti);    % Closed-loop load-to-current gain

figure(4)
bode(Ti)
```

```
legend('Compensated current loop gain')

figure(5)
bode(Gig_cl)
legend('Closed-loop line-to-current gain')



% Outer voltage loop design

Gvc = (1/Rf)*(Gvd/Gid)*(Ti/(1+Ti))
% Control-to-output voltage transfer function
Tvu = H*Gvc;% Uncompensated voltage loop gain
Kpv_dc = 625.3;      % Kp of voltage controller
Kiv_dc = 1.26e6;     % Ki of voltage controller
Gcv = Kpv_dc+Kiv_dc/s;  % Voltage controller
Tv = Tvu*Gcv;  % Compensated voltage loop gain

Tv_cl =  (Tv/(1+Tv)); % Inner closed loop gain
Gvg_cl = (Gvg-(Gvd/Gid)*Gig*(Ti/(1+Ti)))/(1+Tv);
% Closed-loop line-to-output gain

Zout_cl = (Zout-(Gvd/Gid)*Giz*(Ti/(1+Ti)))/(1+Tv);
% Closed-loop output impedance



figure(6)
bode(Tv)
```

```
legend('Compensated voltage loop gain')

figure(7)
bode(Gvg_cl)
legend('Closed-loop line-to-output gain')



Tv_cl_tot = Tv_cl + Gcl_v % Closed-loop gain for DC bus
                          % voltage deviation

figure(8)
bode(Tv_cl_tot)
legend('Closed-loop gain for DC bus voltage deviation')



figure(9)
bode(Gol_pll)
legend('Compensated open loop gain for PLL system')

%% Battery parameters (for various voltage values)
CellCap = 3;
Vcell_nom = 3.7;
Nser = 116;
Npar = 10;
Vbat_nom = Nser*Vcell_nom;
BatCap = CellCap * Npar;
```

```
T_bat = 1e-4;


% Vbat = 373V %
SOC_1 = 2.3;

% Vbat = 500V %
SOC_3 = 99.1;
```

Bibliography

[1] H. Abu-Rub, M. Malinowski, and K. Al-Haddad, *Power Electronics for Renewable Energy Systems, Transportation and Industrial Applications.* Chichester, West Sussex, United Kingdom: Wiley/IEEE, 2014.

[2] D. S. Matawal and D. J. Maton, "Climate change and global warming: Signs, impact and solutions," *International Journal of Environmental Science and Development*, p. 62–66, Feb. 2013.

[3] Z. Hu, C. Li, Y. Cao, B. Fang, L. He, and M. Zhang, "How smart grid contributes to energy sustainability," *Energy Procedia*, vol. 61, pp. 858–861, Dec. 2014.

[4] J. Xian, H. Zhang, and L. Tan, "Decouple control strategy of three-phase grid-connected inverter with lcl filter," in *2018 13th IEEE Conference on Industrial Electronics and Applications (ICIEA)*, pp. 238–242, IEEE, 2018.

[5] S. Abolhosseini, A. Heshmati, and J. Altmann, "A review of renewable energy supply and energy efficiency technologies," April 2014.

[6] C. Mi and M. A. Masrur, *Hybrid electric vehicles: principles and applications with practical perspectives.* Hoboken, NJ, USA: John Wiley & Sons, Inc., 2018.

[7] M. Yilmaz and P. T. Krein, "Review of battery charger topologies, charging power levels, and infrastructure for plug-in electric and hybrid vehicles," *IEEE Transactions on Power Electronics*, vol. 28, p. 2151–2169, May 2013.

[8] M. Ehsani, Y. Gao, and A. Emadi, *Modern electric, hybrid electric, and fuel cell vehicles: fundamentals, theory, and design.* Boca Raton: CRC Press, 2010.

[9] K. Drobnic, G. Grandi, M. Hammami, R. Mandrioli, M. Ricco, A. Viatkin, and M. Vujacic, "An output ripple-free fast charger for electric vehicles based on grid-tied modular three-phase interleaved converters," *IEEE Transactions on Industry Applications*, vol. 55, pp. 6102–6114, Nov. 2019.

[10] A. Emadi, *Advanced Electric Drive Vehicles.* Boca Raton, FL, USA: Taylor and Francis, an imprint of CRC Press, 2015.

[11] J. Gallardo-Lozano, M. I. Milanés-Montero, M. A. Guerrero-Martínez, and E. Romero-Cadaval, "Three-phase bidirectional battery charger for smart electric vehicles," in *2011 7th International Conference-Workshop Compatibility and Power Electronics (CPE)*, pp. 371 – 376, IEEE, 2011.

[12] N. C. K. Colombage, *Design and Control of On-board Bidirectional Battery Chargers with Islanding Detection for Electric Vehicle Applications.* PhD thesis, The University of Sheffield, Dec. 2015.

[13] M. Kesler, M. C. Kisacikoglu, and L. M. Tolbert, "Vehicle-to-grid reactive power operation using plug-in electric vehicle bidirectional offboard charger," *IEEE Transactions on Industry Electronics*, vol. 61, pp. 6778–6784, Dec. 2014.

[14] A. Khaligh and M. D'Antonio, "Global trends in high-power onboard chargers for electric vehicles," *IEEE Transactions on Vehicular Technology*, vol. 68, pp. 3306–3324, Apr. 2019.

[15] G. Abad, *Power Electronics and Electric Drives for Traction Applications*. Chichester, West Sussex, United Kingdom: Wiley, 2017.

[16] W. S. Im, J. J. Moon, J. M. Kim, D. C. Lee, and K. B. Lee, "Fault tolerant control strategy of 3-phase ac-dc pwm converter under multiple open-switch faults conditions," in *2012 Twenty-Seventh Annual IEEE Applied Power Electronics Conference and Exposition (APEC)*, pp. 789 – 795, IEEE, 2012.

[17] J. Han, X. Zhou, S. Lu, and P. Zhao, "A three-phase bidirectional grid-connected ac/dc converter for v2g applications," *Journal of Control Science and Engineering*, pp. 1–12, Sept. 2020.

[18] T. Erfidan, S. Urgun, and B. Hekimoğlu, "Low cost microcontroller based implementation of modulation techniques for three-phase inverter applications," in *MELECON 2008 - The 14th IEEE Mediterranean Electrotechnical Conference*, pp. 541 – 546, IEEE, 2008.

[19] N. I. Raju, M. S. Islam, and A. A. Uddin, "Sinusoidal pwm signal generation technique for three phase voltage source inverter with analog circuit simulation of pwm inverter for standalone load micro-grid system," *International Journal of Renewable Energy Research*, vol. 3, pp. 647–658, Jan. 2013.

[20] P. N. Kapil and C. M. Dhrangadharia, "Design and simulation of three-phase voltage source based converter for hvdc applications," *International Journal of Electronic and Electrical Engineering*, vol. 7, pp. 573–580, Jan. 2014.

[21] Infineon, "Xc164 different pwm waveforms generation for 3-phase ac induction motor with xc164cs," July 2006.

[22] Mathworks, "Pwm generator (three-phase, three-level): Generate three-phase, three-level pulse width modulated signal or waveform for gating switching devices," 2016.

[23] Udemy, "Power electronics: Control and simulation of pwm inverters," Sep 2019.

[24] A. M. Hava, R. J. Kerkman, and T. A. Lipo, "Simple analytical and graphical methods for carrier-based pwm-vsi drives," *IEEE Transactions on Power Electronics*, vol. 14, pp. 573–580, Jan. 1999.

[25] D. Baimel, R. Rabinovici, and S. Tapuchi, "Phase shifted pwm with third harmonic injection for over-modulation range operation," in *2014 International Symposium on Power Electronics, Electrical Drives, Automation and Motion*, pp. 753 – 757, IEEE, 2014.

[26] T. Midtsund, "Control of power electronic converters in distributed power generation systems," Master's thesis, Norwegian University of Science and Technology, Trondheim, Norway, July 2010.

[27] S. Haghbin and T. Thiringer, "Dc bus current harmonics of a three-phase pwm inverter with the zero sequence injection," in *2014 IEEE Transportation Electrification Conference and Expo (ITEC)*, pp. 1 – 6, IEEE, 2014.

[28] S. Tahir, J. Wang, M. H. Baloch, and G. S. Kaloi, "Digital control techniques based on voltage source inverters in renewable energy applications: A review," *Electronics*, vol. 7, no. 2, 2018.

[29] H. T. Nguyen, E. Kim, I. Kim, H. H. Choi, and J. Jung, "Model predictive control with modulated optimal vector for a three-phase inverter with an lc filter," *IEEE Transactions on Power Electronics*, vol. 33, no. 3, pp. 2690–2703, 2018.

[30] J.-Y. Lee, Y.-P. Cho, H.-S. Kim, and J.-H. Jung, "Design methodology of passive damped lcl filter using current controller for grid-connected three-phase voltage-source inverters," *Journal of Power Electronics*, vol. 18, pp. 1178–1189, 07 2018.

[31] R. Peña-Alzola, M. Liserre, F. Blaabjerg, R. Sebastian, J. Dannehl, and F. Fuchs, "Analysis of the passive damping losses in lcl-filter-based grid converters," *Power Electronics, IEEE Transactions on*, vol. 28, 06 2013.

[32] M. N. Mustafa, "Design of a grid connected photovoltaic power electronic converter," Master's thesis, Universitet i Tromsø, Tromsø, Norway, June 2017.

[33] K. Frisfelds and O. Krievs, "Design of a three-phase bidirectional pwm rectifier with simple control algorithm," *Latvian Journal of Physics and Technical Sciences*, vol. 56, pp. 3–12, 06 2019.

[34] E. Bayoumi, *Design of Three-Phase LCL-Filter for Grid-Connected PWM Voltage Source Inverter Using Bacteria Foraging Optimization*, pp. 199–219. 03 2016.

[35] A. Arancibia and K. Strunz, "Modeling of an electric vehicle charging station for fast dc charging," in *2012 IEEE International Electric Vehicle Conference*, pp. 1 – 6, IEEE, 2012.

[36] A. Reznik, "Analysis and design of a smart-inverter for renewable energy interconnection to the grid," Master's thesis, Colorado School of Mines, Soccer Field, Golden, CO 80401, USA, 2013.

[37] M. Bierhoff and F. Fuchs, "Semiconductor losses in voltage source and current source igbt converters based on analytical derivation," in *2004 IEEE 35th Annual Power Electronics Specialists Conference (IEEE Cat. No.04CH37551)*, vol. 4, pp. 2836–2842 Vol.4, 2004.

[38] L. Zhao, J. Qian, and T. Instruments, "Dc-dc power conversions and system design considerations for battery operated system," *Texas Instruments Seminar*, 01 2006.

[39] R. Erickson and D. Maksimovic, *Fundamentals of Power Electronics*. Boulder, CO, USA: Springer International Publishing, 2020.

[40] B. Wu, H. Chen, G. Guan, and L. Yin, "Simulation model of three-phase pwm rectifier charging station and harmonic analysis on grid," in *2017 IEEE Innovative Smart Grid Technologies - Asia (ISGT-Asia)*, pp. 1 – 6, IEEE, 2017.

[41] J. W. Kolar, "Vienna rectifier beyond...," March 2018.

[42] K. Fahem, D. E. Chariag, and L. Sbita, "On-board bidirectional battery chargers topologies for plug-in hybrid electric vehicles," in *2017 International Conference on Green Energy Conversion Systems (GECS)*, pp. 1 – 6, IEEE, 2017.

[43] A. Arancibia, K. Strunz, and F. M. David, "A unified single- and three-phase control for grid connected electric vehicles," *IEEE Transactions on Smart Grid*, vol. 4, p. 1780–1790, Dec. 2013.

[44] V. L. Nguyen, T. T. Quoc, and S. Bacha, "Harmonic distortion mitigation for electric vehicle fast charging systems," in *2013 IEEE Grenoble Conference*, pp. 1 – 6, IEEE, 2013.

[45] J. G. Hayes and G. A. Goodarzi, *Electric Powertrain: Energy Systems, Power Electronics and Drives for Hybrid, Electric and Fuel Cell Vehicles*. Hoboken, NJ, USA: John Wiley & Sons, 2018.

[46] J. Prasad, T. Bhavsar, R. Ghosh, and G. Narayanan, "Vector control of three-phase ac/dc front-end converter," *Sadhana*, vol. 33, pp. 591–613, 10 2009.

[47] S.-K. Chung, "Phase-locked loop for grid-connected three-phase power conversion system," *Electric Power Applications, IEE Proceedings -*, vol. 147, pp. 213 – 219, 06 2000.

[48] V. Kaura and V. Blasko, "Operation of a phase locked loop system under distorted utility conditions," *Industry Applications, IEEE Transactions on*, vol. 33, pp. 58 – 63, 02 1997.

[49] M. G. Simoes and F. A. Farret, *Modeling Power Electronics and Interfacing Energy Conversion Systems*. Hoboken, NJ, USA: Wiley/IEEE, 2017.

[50] H. Zhang, T. Wu, H. Dong, C. An, and H. Zhai, "Design of double closed loop control system for beam supply," in *2019 2nd International Conference of Intelligent Robotic and Control Engineering (IRCE)*, pp. 56–61, 2019.

[51] "Transfer function of closed loop system - derivation."

[52] Y.-T. Chang and Y.-S. Lai, "Effect of sampling frequency of a/d converter on controller stability and bandwidth of digital-controlled power converter," pp. 625 – 629, 11 2007.

VITA

Gorkem B. Sahinler attended Trabzon High School in September 2007 and graduated from there with a honor in June 2011. He entered Middle East Technical University (METU) in September 2011 and earned the degree of Bachelor of Science in Electrical and Electronics Engineering in January 2017. He also attended Ozyegın University in January 2019 and received the degree of Master of Science in Electrical and Electronics Engineering in July 2021.